ELECTROCATALYTIC AND OPTOELECTRONIC BEHAVIOR OF COLLOIDALLY FUNCTIONALIZED TRANSITION METAL (HYDR)OXIDES

by

Eve Yaret Martinez

A Dissertation

Submitted to the Faculty of Purdue University

In Partial Fulfillment of the Requirements for the degree of

Doctor of Philosophy

Department of Chemistry

West Lafayette, Indiana

May 2021

THE PURDUE UNIVERSITY GRADUATE SCHOOL
STATEMENT OF COMMITTEE APPROVAL

Dr. Christina W. Li, Chair

Department of Chemistry

Dr. Corey M. Thompson

Department of Chemistry

Dr. Shelley A. Claridge

Department of Chemistry &

Weldon School of Biomedical Engineering

Dr. Letian Dou

Davidson School of Chemical Engineering

Approved by:

Dr. Christine A. Hrycyna

Dedicated to my mother, Maria Alejandra Gomez

Todo lo que logre fue posible por tu esfuerzo. Gracias mami.

ACKNOWLEDGMENTS

I would like to thank my research advisor, Professor Christina W. Li, for shaping me into the researcher I've become. I am grateful to have worked under such a bright and talented woman. I will never be able to thank her enough for her mentorship, friendship and support. I'd also like to thank Professor Shelley A. Claridge, Professor Letian Dou and Professor Corey M. Thompson for serving as my committee members.

Next, I want to thank my mother, Maria, and my sister, Nayelly, for their unwavering love and support. Nayelly, I've enjoyed our "study sessions", charcuterie board feasts and our many ramen and hot pot meals. Dad and Mario, thank you for constantly reminding me that I was capable of getting through graduate school.

I'd like to thank the phenomenal women who supported me throughout my undergraduate studies, Dr. Mary Crawford and Dr. Helen Hoyt. They both planted the seed that led me towards pursuing my Ph.D. and they've been extremely supportive throughout my time in undergraduate and graduate school. I also want to thank the late Honorable Judge Jack K. Mandel and Judy Mandel. I will miss you forever Judge. Thank you for taking an interest in mentoring me.

I'd like to thank my amazing and lovely friends, Jordan, Chou, Colby and Andre. I'm so glad you were all a part of my Indiana family. I'd also like to thank my closest friend, Kaity, for being my rock, for always thinking of me and for sending me encouraging messages throughout my time in graduate school.

I'd like to thank all my co-workers for making my graduate school experience a memorable one. Vamakshi, thank you for always being willing to get bubble tea with me and talk through problems I was experiencing with my science. Dan, thanks for helping me with the glovebox and for being my friend. Kuixin, I've had so much fun working with you. It's been a great experience watching you grow as a researcher. Will, thank you for always being willing to grab a meal, for our adventures outside of lab and for your friendship.

A huge thank you to everyone who has supported me through my academic journey as a Latina chemist.

Lastly, I want to thank my husband, Dr. Michael J. Behlen, for giving me nothing but love and happiness during our time together. I am excited for our next journey together.

TABLE OF CONTENTS

LIST OF TABLES

LIST OF FIGURES

ABSTRACT

Transition metal oxides and hydroxides have utility in electrochemical catalysis and electronic applications due to their unique structural and electronic properties. In this dissertation, transition metal (hydr)oxides were studied in two veins which highlight the versatility of these nanomaterials: electrochemical CO oxidation and electron-doping. This work demonstrates how the structure and electronics of transition metal (hydr)oxides impact their electronic and catalytic applications.

In order to move toward renewable energy sources, fuel cells have been sought out as an alternative electrical energy source. Platinum has been utilized as a catalyst in fuel cells due to its high catalytic behavior. However, the small amounts of carbon monoxide found in hydrogen gas will slowly saturate the platinum surface and effectively poison the catalyst. Fortunately, previous work has shown transition metal hydr(oxy)oxides of Ni, Co, Mn, and Fe on a Pt surface decreased the overpotential for CO oxidation by working in a bifunctional manner by activating H_2O on the oxide surface while reacting with CO bound to platinum.

In our work, we developed a synthetic method for depositing a monolayer metal halide shell onto platinum nanoparticles. Using a solution-phase method, a series of colloidal first-row and post-transition metal halides on Pt were studied in electrochemical CO oxidation. Through this work, the CO oxidation activity was strongly dependent on the identity of the metal oxide shell and a ~200 mV shift towards lower overpotential relative to platinum was observed. Furthermore, this synthetic method allowed us to access core-shell nanostructures that had not been previously reported and study them as potential catalysts in fuel cells.

In more recent work, transition metal (hydr)oxides were investigated for their electron-doping properties. Ambipolar doping of transition metal (hydr)oxides is highly desirable for applications in electronic and optoelectronic devices. However, developing a transition metal oxide that is stable to both n-type defects (oxygen vacancies) and p-type defects (metal vacancies) is difficult. NiO and CoO are known p-type semiconductors with high conductivities; however, very little is known about their n-doped form.

By turning to layered hydrotalcite and brucite $Co(OH)_2$ and $Ni(OH)_2$, we discovered that the n-doped form is accessible. By treating the metal hydroxide nanosheets with electron donor,

n-butyllithium, the conductivity increased from 10^{-12} S/cm to 10^{-6} S/cm. Using an array of X-ray spectroscopic techniques, the nanoplatelets were found to compensate doped-electrons through lithium adsorption, oxygen vacancy formation, and metal-centered reduction. This work highlights the importance of understanding the role of crystal structure, defect formation, and structural environment in accessing ambipolar forms of transition metal (hydr)oxides.

CHAPTER 1. SURFACE FUNCTIONALIZATION OF PLATINUM NANOPARTICLES WITH METAL CHLORIDES FOR BIFUNCTIONAL CO OXIDATION

Reprinted from Polyhedron, Martinez, E. Y.; Li, C. W. Surface functionalization of Pt nanoparticles with metal chlorides for bifunctional CO oxidation. *Polyhedron,* **2019**, *170*, 239–244. (DOI: 10.1016/j.poly.2019.05.048)

1.1 Abstract

Incorporation of a metal oxide or hydroxide species into Pt-based electrocatalysts has been shown to lower the overpotential required to oxidatively remove carbon monoxide from the catalyst surface, a reaction that is critical to preventing catalyst poisoning and deactivation in fuel cell devices. In this work, we report a general synthetic method toward Pt-metal oxide composite nanoparticles via the adsorption of metal halide ligands onto 1–2 nm colloidal Pt nanoparticles. Pt-metal oxide composite nanoparticles spanning across the first-row transition metals and post-transition metals are synthesized and characterized with transmission electron microscopy and energy dispersive X-ray scattering. CO stripping and steady-state CO oxidation experiments reveal that Mn, Fe, Co, Ni, and In oxides are capable of participating in the catalysis as a bifunctional partner and reduce the overpotential required for CO electrooxidation by ∼200 mV relative to pure Pt.

1.2 Introduction

Metal oxide supported platinum nanoparticles are among the most important heterogeneous catalysts for both thermal and electrochemical catalysis.[1-6] The role of the metal oxide, as a ligand that can tune the electronic and steric properties of the active site or as an active bifunctional participant in the catalytic reaction, is a key question for catalyst design in a wide range of reactions.[7-13] In this study, we utilize nanoparticle ligand interactions to synthesize colloidal core-shell and supported Pt nanoparticles with metal oxides across the first-row transition metal series in order to systematically probe the influence of the oxide shell on alkaline electrochemistry.

We focused on alkaline CO electrooxidation as a probe reaction for bifunctional participation of the metal oxide shell layer. The oxidative desorption of CO on Pt is hypothesized to proceed through a Langmuir-Hinshelwood mechanism, in which adsorbed surface hydroxides on adjacent metal oxide surfaces facilitate the desorption of CO.[14] Electrodeposited metal hydroxide layers of Ni, Co, Fe, and Mn on Pt single crystals have been studied for the alkaline hydrogen evolution and CO oxidation reactions, in which the rates of both reactions were enhanced by the metal hydroxide overlayer.[15-17] Here, our solution-phase synthetic method allows us to thinly coat 1-2 nm colloidal Pt nanoparticles with a wide range of metal oxide shells while maintaining high Pt electrochemical surface area (ECSA). The CO oxidation peak potential shifts to lower overpotential by over 100 mV in the presence of a submonolayer Fe, Co, Ni, and In hydroxide shell and by smaller degrees for earlier transition metal or post-transition metal oxides. While previous work demonstrated the promotional effect of late transition-metal hydroxides on Pt single crystals, we are now able to controllably deposit a broader swath of metal oxides onto very small Pt nanoparticles and systematically study their effects on reactivity. We postulate that these 1-2 nm core-shell Pt-metal oxide (Pt-MO_x) nanoparticles may be relevant as CO-resistant electrocatalysts for alkaline fuel cells and electrolyzers.

1.3 Results and Discussion

1.3.1 Pt-MO_x Synthesis

We first synthesized 1-2 nm "unprotected" platinum nanoparticles based on a literature method.[18] As-synthesized, these nanoparticles are colloidally stabilized via a surface layer of hydroxide anions and ethylene glycol. A metal halide ligand is then adsorbed by stirring a solution of the unprotected platinum nanoparticles with the appropriate metal precursor in dimethylformamide (DMF) at room temperature for 12 hours (**Figure 1.1**). Nanoparticles were then precipitated and washed three times with acetone and formamide to fully remove excess metal halide, leaving behind only metal halide or hydroxide species that are specifically adsorbed to the Pt surface. Residual hydroxide anions associated with the Pt surface likely react with the metal chloride precursor to form the metal hydroxide, which should limit shell formation to the immediate vicinity of the Pt nanoparticle surface. Alternatively, direct adsorption of the metal halide without hydrolysis would also result in self-limiting submonolayer and monolayer shells.

The adsorption of metal halide and metal oxide complexes as colloidal nanoparticle ligands is precedented for noble metal cores, and both hydroxide and chloride binding modes are likely represented on our colloidal Pt-$MCl_x(OH)_y$ nanoparticles.[19-22] Both possibilities should result in a Pt-MO_x or $M(OH)_x$ core-shell structure once immersed in the aqueous alkaline environment needed for electrochemistry. In the case of the most readily hydrolysable metal chlorides, secondary nucleation of the metal oxide may also occur due to adventitious water, resulting in a combination of supported Pt nanoparticles in addition to core-shell nanostructures. Using this method, we have synthesized the Pt-metal oxide composite structures for metal oxides across the first-row transition series from Sc to Zn as well as post-transition metals Ga and In. After metal halide functionalization, the particles are completely dissolved in DMF and remain colloidal for over 30 days in the presence of surfactant tetrabutylammonium chloride (TBACl). The synthetic method is highly reproducible by all characterization methods and electrochemical measurements, and all subsequent electrochemical data represents an average of at least three separate synthetic batches for each Pt-metal oxide composite material.

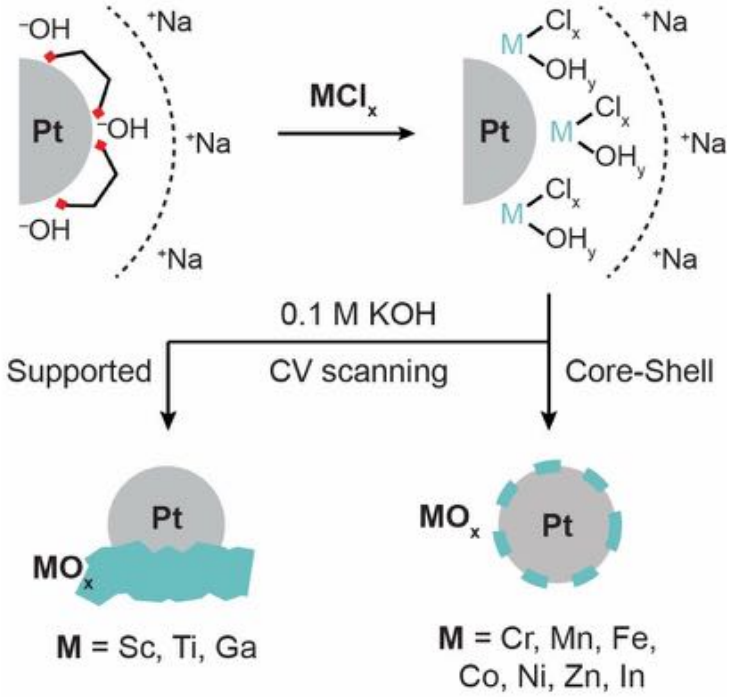

Figure 1.1. Schematic for the synthesis of Pt-metal oxide colloidal nanoparticles via adsorption of metal halide ligands to the Pt surface followed by hydrolysis under electrochemical scanning.

1.3.2 Structural Characterization

Characterization of the Pt-metal oxide composite nanoparticles was carried out using transmission electron microscopy (TEM) coupled with elemental mapping using energy dispersive X-ray spectroscopy (EDS). In all cases, platinum nanoparticles before and after metal oxide addition remained spherical and 1-2 nm in diameter (**Figure 1.2**).

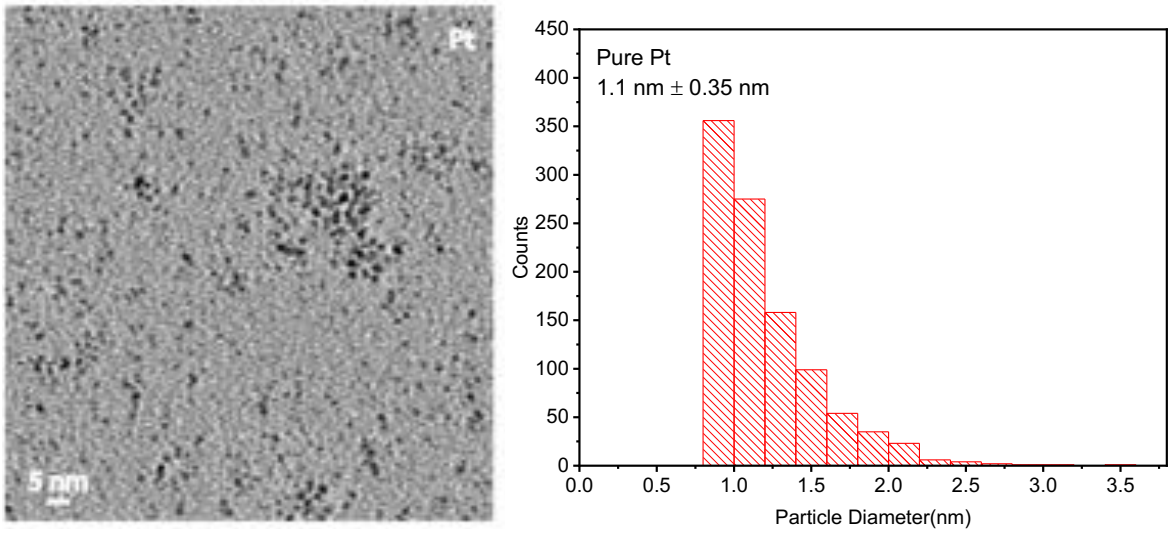

Figure 1.2. TEM and histogram of particle sizes for pure Pt nanoparticles based on 1015 nanoparticles.

In the cases of Sc, Ti, and Ga, obvious secondary nucleation of the metal oxide was observed with areas of lighter contrast corresponding to pure metal oxide that are unassociated with the Pt nanoparticles (**Figure 1.3, 1.5**). In all other samples, no distinct areas of lighter contrast were observed in the TEM, and the STEM-EDS mapping shows that the metal oxide is completely co-localized with the Pt nanoparticles (**Figure 1.3b, A.1-A.4**).

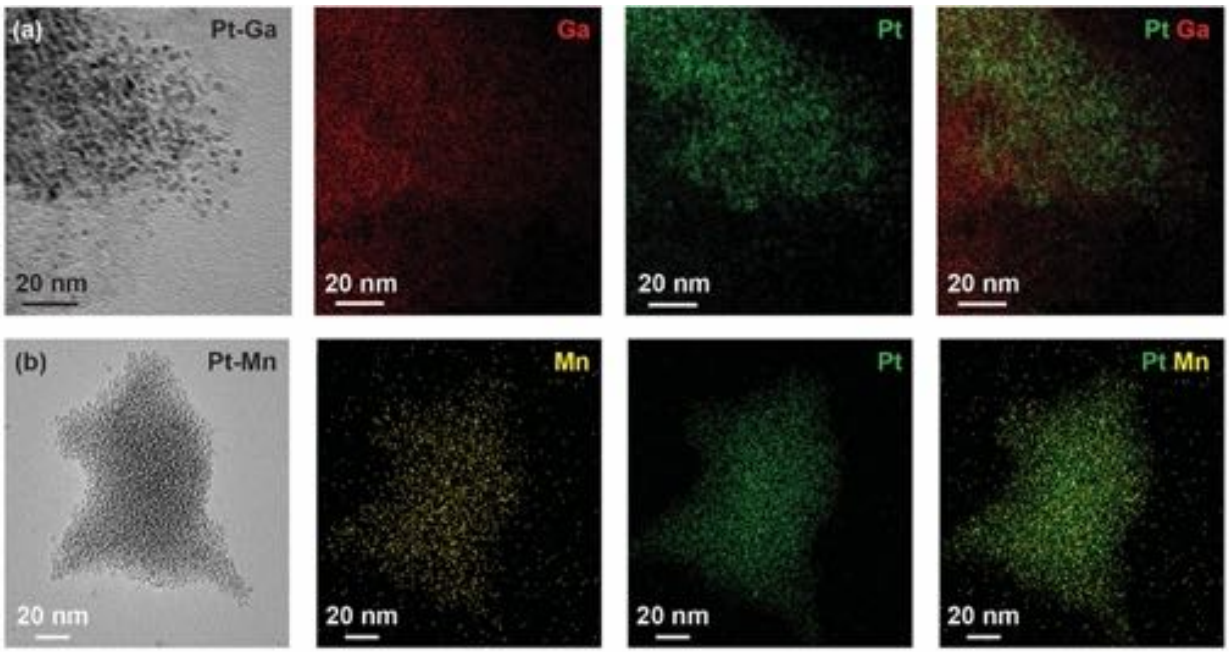

Figure 1.3. TEM images and EDS maps for each metal atom showing (**a**) supported Pt NPs with secondary nucleated GaO_x and (**b**) colocalization of Mn and Pt in Pt-MnO_x nanoparticles.

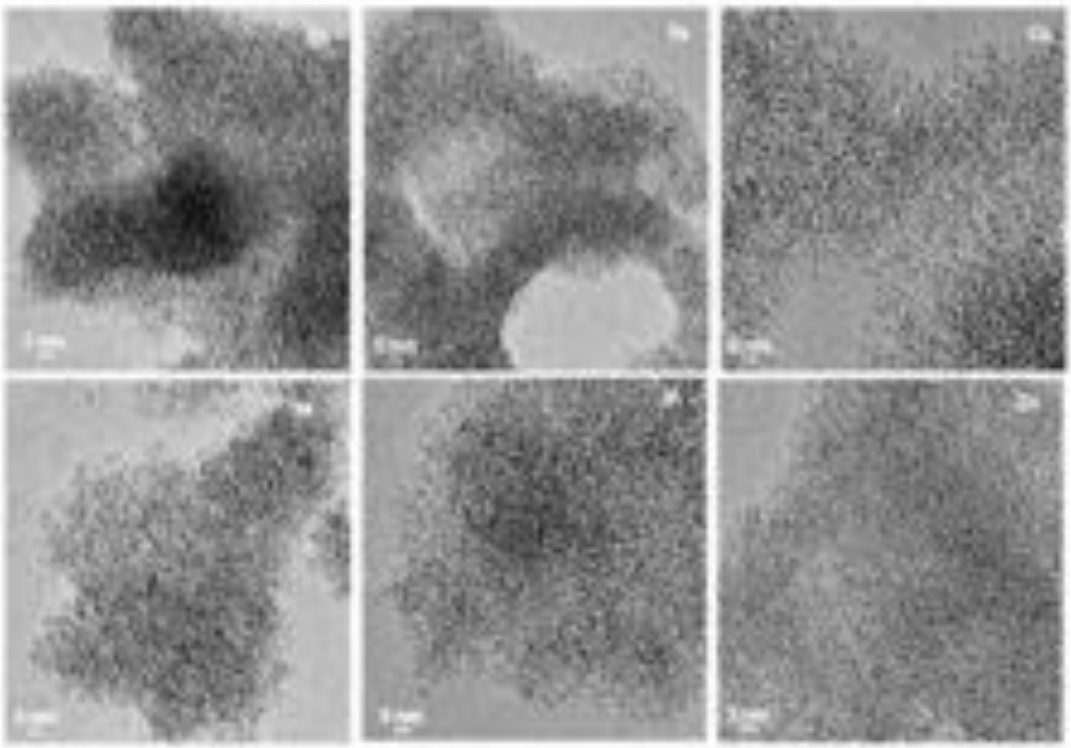

Figure 1.4. TEM images for Pt-MO_x composite nanoparticles (M=Cr, Fe, Co, Ni, In, Zn) and pure Pt used in electrochemical studies. All scale bars are 5 nm.

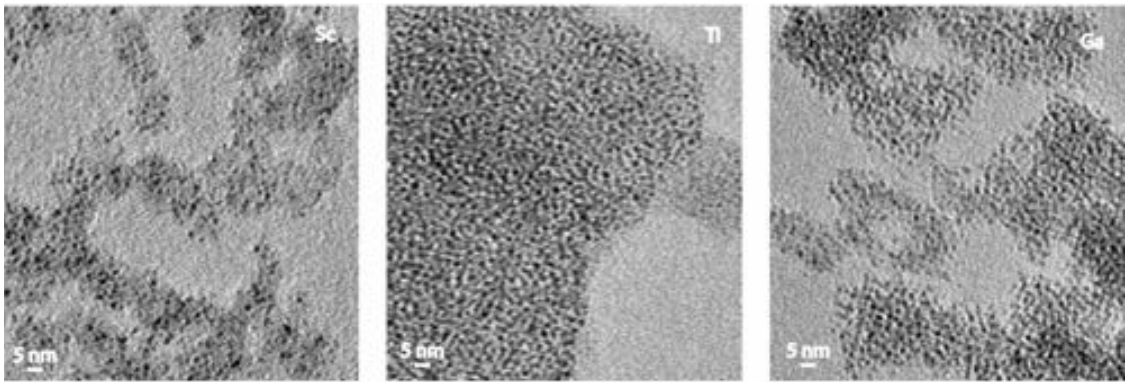

Figure 1.5. Transmission electron microscopy (TEM) images for MO_x-supported Pt nanoparticles (M=Sc, Ti, Ga) used in electrochemical studies. All scale bars are 5 nm.

Inductively coupled plasma-mass spectrometry (ICP-MS) and EDS were used to obtain the atomic ratio of platinum and the second metal (**Table 1.1, A.6**). Based on a simplified calculation assuming 1.5 nm Pt core nanoparticles and spherical close packing of metal chloride complexes, we estimate that a single monolayer of surface metal halide should exhibit an atomic percent ranging from 15% to 19% depending on the Van der Waal's radius of the complex. For the supported samples (M = Sc, Ti, Ga), the atomic percent of the metal oxide is well above monolayer coverage, ranging from 32% to 81%, consistent with significant secondary nucleation of the metal oxide. For all of the samples where a core-shell structure is postulated (M = Cr, Mn, Co, Ni, Zn, In), the atomic percent falls below monolayer coverage. While the core-shell structure could not be directly visualized in HR-TEM due to the very thin amorphous oxide (**Figure 1.6**), the EDS mapping data and ICP-MS atomic ratios suggest that the structure comprises Pt core nanoparticles in close contact with metal chloride or oxide shell at submonolayer levels.

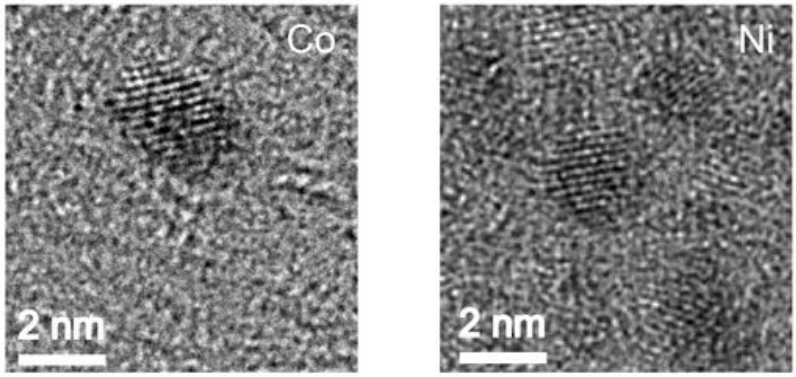

Figure 1.6. High-resolution TEM images Pt-CoO_x and Pt-NiO_x before catalysis.

Table 1.1. EDS and ICP-MS atomic ratios of Pt to the second metal in composite nanoparticle samples.

Sample	EDS Atomic Pt:M Ratio		ICP-MS Atomic Pt:M Ratio	
	% Pt	**% M**	**% Pt**	**% M**
Sc	19.0	81.0	18.7	81.3
Ti	58.9	41.1	68.2	31.8
Cr	89.6	10.4	90.1	9.9
Mn	93.2	6.8	89.8	10.2
Fe	72.2	27.8	17.5	82.5**
Co	91.1	8.9	90.8	9.2
Ni	89.8	10.2	93.3	6.7
Zn	--*	--*	96.4	3.6
Ga	62.7	37.3	57.6	42.4
In	95.3	4.7	87.5	12.5

**Zn K peaks overlap with Cu K peaks, and an accurate percentage could not be determined.*

***Significant Fe is observed in the blank sample, and an accurate percentage could not be determined.*

X-ray photoelectron spectroscopy (XPS) was used to determine the identity and oxidation state of the metals present in as-synthesized Pt-$MCl_x(OH)_y$ nanoparticles. In all cases, the binding energy of the second metal was consistent with the oxidation state of the metal halide precursor used in synthesis (**Figure A.7-A.16**).[23-26] We also observe that significant chloride remains in the sample after three cleaning cycles, with the Cl:M atomic ratio ranging from 0.6 to 3, suggesting that surface-adsorbed complexes exhibit mixed hydroxide and chloride coordination (**Table 1.2**).

Table 1.2. Summary of processed XPS data with Pt:M ratio, Pt^{2+}:Pt^0 ratio and X:M Ratio for all Pt samples.

Sample	Pt:M Atomic Ratio		Pt^{2+}:Pt^0 Oxidation State Ratio		X:M Atomic Ratio
	% Pt	% M	% Pt^{2+}	% Pt^0	X:M
Sc	14	86	66	34	0.31
Ti	32	68	71	29	0.72
Cr	90	10	36	64	0.0*
Mn	78	22	44	56	1.1
Fe	83	17	44	56	2.2
Co	94	6	39	61	7.0**
Ni	48	52	39	61	0.62
Zn	98	2	48	52	330**
Ga	68	32	41	59	0.30
In	83	17	43	57	1.3
Pt	14	86	40	60	0.31

**Precursor did not contain chlorine.*

***Intensity of M peaks were too low to obtain an accurate X:M ratio.*

1.3.3 Electrochemical Characterization

In order to assess the effect of the metal oxide shell on Pt adsorbate binding and redox properties, cyclic voltammetry (CV) was conducted in 0.1 M KOH. On all samples, the first scan exhibits a higher oxidation current between 0.8 V and 1.7 V vs. RHE and a negatively shifted Pt-O reduction feature at ~0.6 V (**Figure 1.7a**). These CV features shift significantly in the next few scans, likely due to removal of residual ligands on the surface including ethylene glycol, chlorides, and hydroxides. In the presence of the oxide shell, the Pt-hydride (0.1–0.4 V) and Pt-oxide (0.4–0.9 V) features become more clearly defined in the first 3-5 scans of the CV (**Figure 1.7b, A.17**). The interface between the Pt and the shell metal oxide likely rearranges significantly upon immersion into KOH electrolyte and in the first several CV scans due to hydrolysis of residual metal halide ligands. TEM images taken after CV scanning show some particle aggregation, consistent with hydrolysis of the ligand responsible for colloidal stability.

After 10 scans, the underpotential deposited hydride (Pt-H_{upd}) oxidation and Pt-O reduction regions are stable in both peak shape and current density. On the bare platinum nanoparticles, the platinum oxide reduction comprises a single peak at 687 mV vs. RHE, and the Pt-H_{upd} oxidation shows a distinctive double feature with a more intense peak at 308 mV derived from Pt (111) and (110) facets and a second feature at 413 mV comprising Pt (100) facets, consistent with literature reports (**Figure 1.7c**).[27-29] While many of the metal oxide shelled materials show fairly similar profiles in the CV, Pt capped with Ni, Co, Fe, and Mn oxide show clear differences. In these samples, the Pt (100) H_{upd} feature at 0.41 V becomes significantly broader and weaker such that it becomes nearly indistinguishable in the CV (**Figure 1.7c**). This suggests that a fraction of Pt-H_{upd} binding sites present on the bare nanoparticles are now covered by the oxide shell. In contrast, the Pt-O reduction peak has a clear second peak that emerges as a positive shoulder at 830 mV vs. RHE. This shoulder feature may be indicative of interfacial sites between the Pt and metal oxide submonolayer that exhibit more reducible Pt-O bonds due to bifunctionality or electronic perturbation. Finally, evidence of the electroactive metal hydroxide is clear in the Ni(II/III) redox feature as well as in the significant oxygen evolution current observed in the presence of the first-row transition metal hydroxides (**Figure A.17**). Together, these perturbations in the Pt-H_{upd} and Pt-O regions suggest that the metal oxide shell masks a small fraction of Pt surface sites as well as creates new interfacial sites with altered adsorbate binding properties.

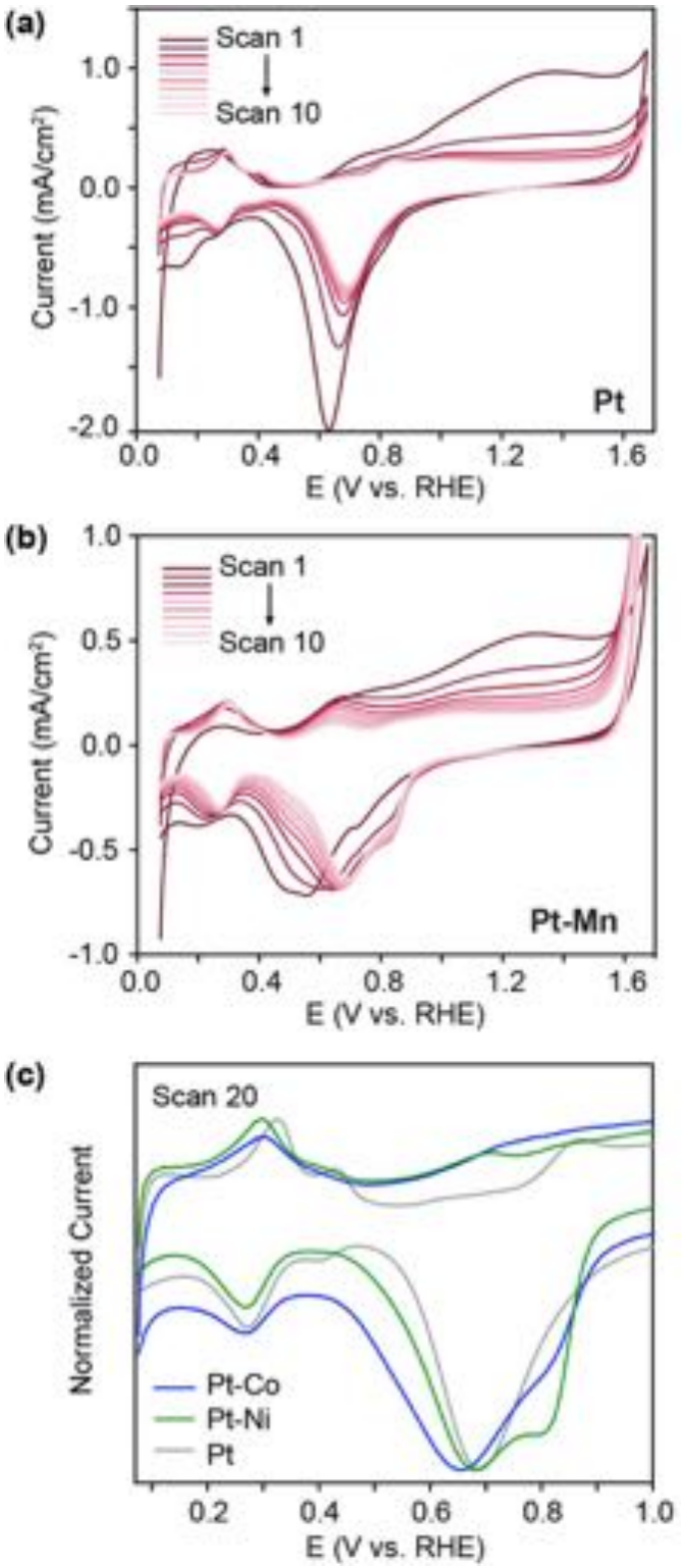

Figure 1.7. Evolution of initial CVs in 0.1 M KOH over the first 10 cycles for (**a**) pure Pt nanoparticles and (**b**) Pt-MnO_x composite nanoparticles. (**c**) Stabilized CV for pure Pt, Pt-NiO_x, and Pt-CoO_x illustrating changes in the Pt-H_{upd} and Pt-O features.

1.3.4 Electrochemical CO Oxidation

Electrochemical CO stripping is a useful probe reaction to assess bifunctionality in Pt alloy and multimetallic catalysts. In particular, numerous Pt alloys with more oxophilic metals have been studied as alcohol oxidation catalysts, and the CO stripping peak potential is shifted negatively by ~0.3 V due to the participation of $M(OH)_x$ species in the rate-determining oxidation of CO.[30-34] Several examples of composite structures with $Ni(OH)_x$ as both a support and overlayer have also shown lower overpotential peaks in the CO stripping profile.[15-17, 35] On the unprotected Pt nanoparticles, the CO stripping profile consists of three features (**Figure 1.8a**). The most prominent feature at 0.75 V vs. RHE (peak 3) matches well to previously measured CO stripping potentials on Pt (111) single crystals.[36-39] The intermediate peak at 0.67 V vs. RHE (peak 2) corresponds to either the low-index facets, Pt (110) and Pt (100), or to a stepped surface, and the broad peak at 0.58 V (peak 1) does not appear on single crystals. This lowest overpotential peak likely corresponds to undercoordinated sites found only on the surfaces of small nanoparticles.[40]

In the metal hydroxide shelled Pt nanoparticles, particularly in $Pt@Fe(OH)_x$, $Pt@Co(OH)_x$, and $Pt@Ni(OH)_x$, the CO stripping features appear markedly different (**Figure 1.8b**). At least three features still exist, including peaks 2 and 3 that loosely correspond to the single-crystal facets of Pt. The peak positions of those single-crystal CO stripping peaks shift slightly (<40 mV) relative to the bare Pt nanoparticles, but the most striking differences occur at low overpotential. The defect feature on the bare Pt nanoparticles at 0.58 V vs. RHE is now buried underneath a new sharp peak centered at 0.46-0.48 V vs. RHE. We postulate that this low overpotential CO stripping feature comes from Pt atoms immediately adjacent to metal hydroxide sites. On these three samples, the low overpotential peak is also significantly increased in intensity relative to pure Pt, suggesting that a significant fraction of Pt surface atoms are proximal to the metal oxide layer.

To further understand the role of bifunctionality in the oxidative desorption of CO, we compared the CO stripping profile on all of the first-row transition metals from Sc to Zn and the post transition metals, Ga and In. On several Pt-metal oxide composite samples (Sc, Ti, Cr, Zn, Ga), the peak shape matches closely to that of pure Pt nanoparticles (**Figure 1.8a, A.18**). The defect feature shifts slightly to lower overpotential by ~40 mV, but the ratio of peak heights for peak 1 to peak 3 remain essentially unchanged (**Figure 1.8c-d**). The total electrochemically active surface area for Pt, obtained from integration of the CO stripping region, shows that all oxides suppress total Pt surface area to some degree, but the effect is most dramatic on the oxides that

exhibit significant secondary nucleation (**Figure A.18**). We hypothesize that these samples do contain shell metal oxides and interfacial sites between the oxide and Pt core, but these interfacial sites do not strongly perturb the binding strength or oxidative stripping of adsorbed CO.

In contrast, Mn, Fe, Co, Ni, and In oxides clearly show much greater changes to the CO stripping profile (**Figure 1.8a-b**). In the Mn and In samples, the relative ratios of peak 1 to peak 3 remain similar to that of pure Pt, but the position of the defect feature shifts by >100 mV to lower overpotential (**Figure 1.8c**). In the Fe, Co, and Ni samples, the entire profile changes dramatically in shape. While the lowest overpotential peak remains fairly clear, peaks 2 and 3 merge into a broad asymmetric feature (**Figure 1.8b**). Unlike the pure Pt examples, it is no longer possible to use the integration of the three fitted peaks to estimate coverage of sites on the Pt surface. The peak profile is likely to be a convolution of metal oxide coverage effects, creation of new bifunctional sites, and electronic perturbation of Pt terrace sites.

To deconvolute these effects, we also performed steady state CO oxidation on a subset of Pt-metal oxide composite materials using a rotating disk electrode setup. Samples that exhibited the negatively shifted CO stripping feature between 463 and 481 mV (Mn, Ni, In) showed significantly lower onset and half-wave potentials ($E_{1/2}$) compared to pure Pt (**Figure 1.8**, **1.9**). The most active sample, Pt-In oxide, exhibited a ~150 mV reduction in the potential required to achieve 1 mA/cm^2 of steady state CO oxidation at 1600 rpm. In contrast, samples that did not exhibit significant shifts in the low overpotential CO stripping feature, e.g. Pt-Cr oxide, showed CO oxidation activity very similar to pure Pt nanoparticles. Using the H_{upd} region to determine Pt ECSA, we obtained the kinetic current density per Pt area ($j_{k\text{-}Pt}$) for CO oxidation at 0.42 V and 0.48 V vs. RHE.[41] The $j_{k\text{-}Pt}$ value for each catalyst is correlated to the peak potential of the low overpotential feature in CO stripping (**Figure 1.8f**), indicating that the surface sites represented by peak 1 are implicated in CO oxidation catalysis at these potentials. This further suggests that the shift in peak potential in the CO stripping profile is representative of bifunctional active sites between Pt and the metal oxide shell.

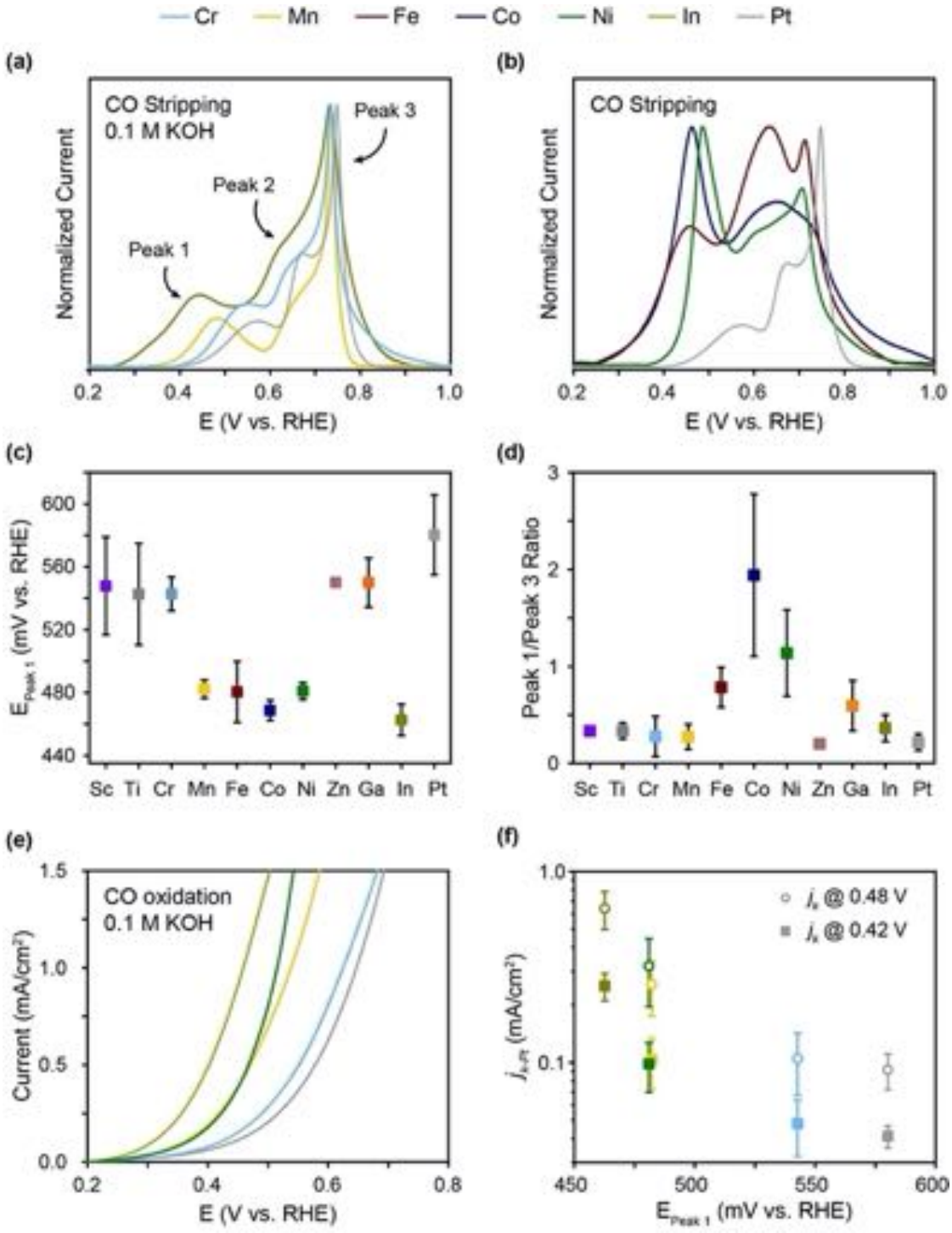

Figure 1.8. (**a**) Normalized CO stripping profiles for pure Pt and Pt-MO_x nanoparticles where M = Cr, Mn, In and (**b**) where M = Fe, Co, Ni. (**c**) Peak potential of Peak 1 in the CO stripping profile vs. M and (**d**) ratio of peak heights for Peak 1/Peak 3 in the CO stripping profile vs. M. (**e**) Linear scan voltammetry in CO-saturated electrolyte for pure Pt and Pt-M where M = Cr, Mn, Ni, In and (**f**) kinetic current density for CO oxidation normalized to Pt surface area ($j_{k\text{-Pt}}$) vs. the peak potential of Peak 1 in the CO stripping profile.

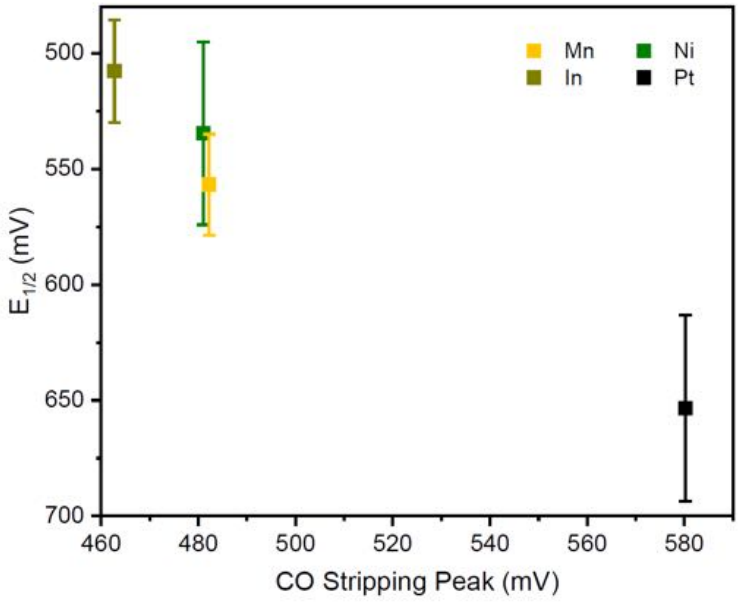

Figure 1.9. $E_{1/2}$ vs CO Stripping Peak 1 Potential on Pt-MnO_x, Pt-NiO_x, Pt-InO_x and Pure Pt.

Previous work from the Markovic group postulated that the ability to transfer hydroxide from the surface metal hydroxide with concurrent reduction of the metal center ($M^{n+}(OH)_x$ + Pt-CO → $M^{(n-1)+}(OH)_{x-1}$ + Pt-COOH) is critical towards activating the bifunctional CO oxidation mechanism.[17] In particular, the activity descriptor of import is the binding strength of OH_{ad} to the metal, which is experimentally represented by the amount of OH formed during electrochemical oxidation (θ_{OHad}). In our samples, we not only see improved CO oxidation reactivity on the first-row transition metals with accessible II/III redox couples (Mn and Ni) as observed in previous reports, we also see strong enhancement in $j_{k\text{-}Pt}$ for In, which should not undergo thermodynamically favorable reduction within the CO oxidation potential window. We hypothesize that post-transition metal hydroxide species proximal to Pt-CO may undergo a bifunctional reaction through a kinetically accessible state as long as the M-OH bond is sufficiently weak, an effect that has also been observed on PtSn alloys. The ability to oxidize steady state CO at 1 mA/cm^2 with potentials as low 0.46 V vs. RHE should confer significant poisoning resistance to Pt electrodes for both the anode and cathode reactions in hydrogen and alcohol fuel cells.[30, 42, 43] The submonolayer core-shell structure described herein, in comparison to alloys, may be particularly advantageous for CO-resistant catalysis insofar as the activity of the underlying Pt nanoparticle for reactions such as oxygen reduction and hydrogen evolution are unperturbed by the shell metal oxide (**Figure 1.10, 1.11, Table 1.3**).

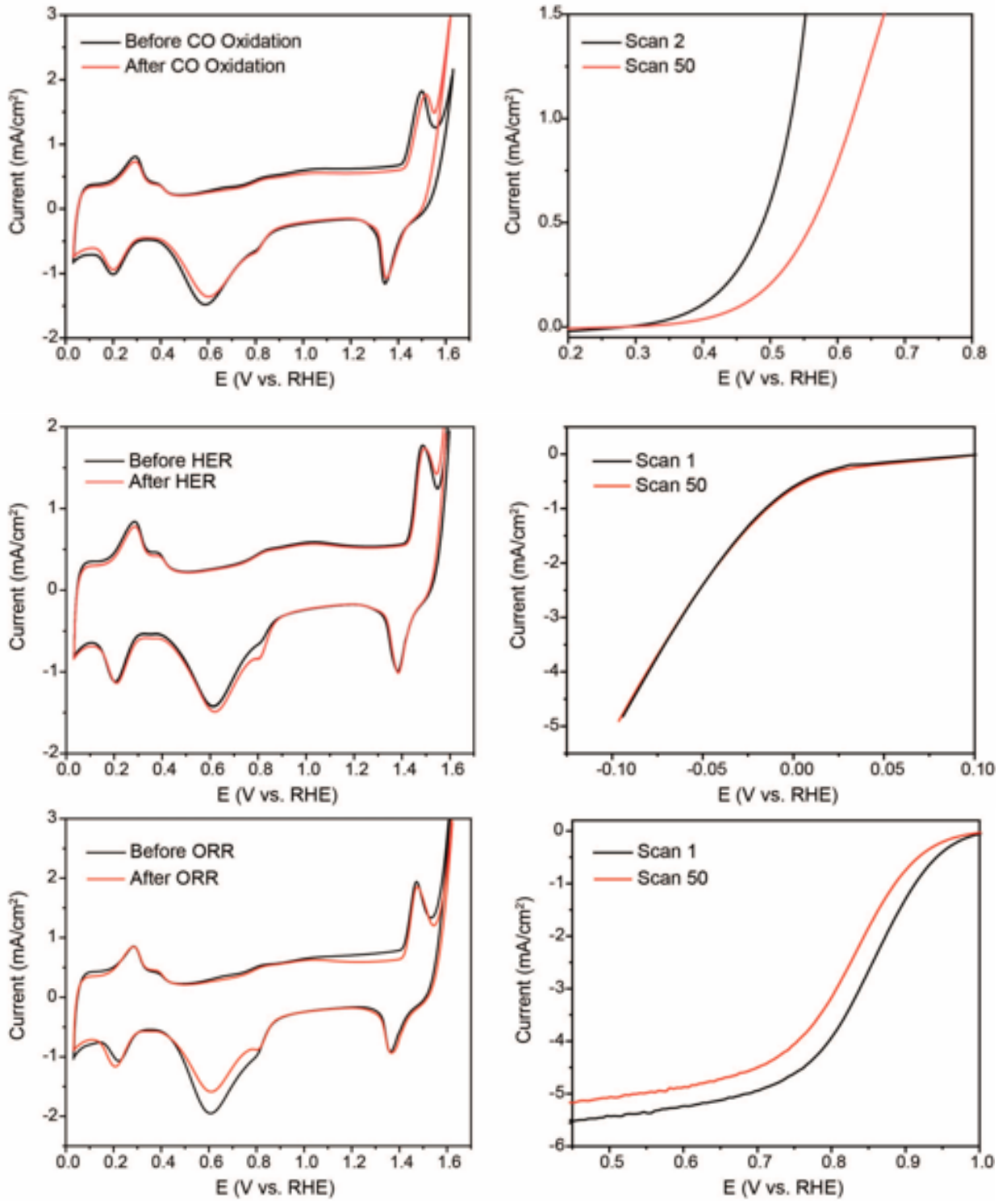

Figure 1.10. Electrochemical stability studies for Pt-NiO_x under CO oxidation, hydrogen evolution, and oxygen reduction conditions.

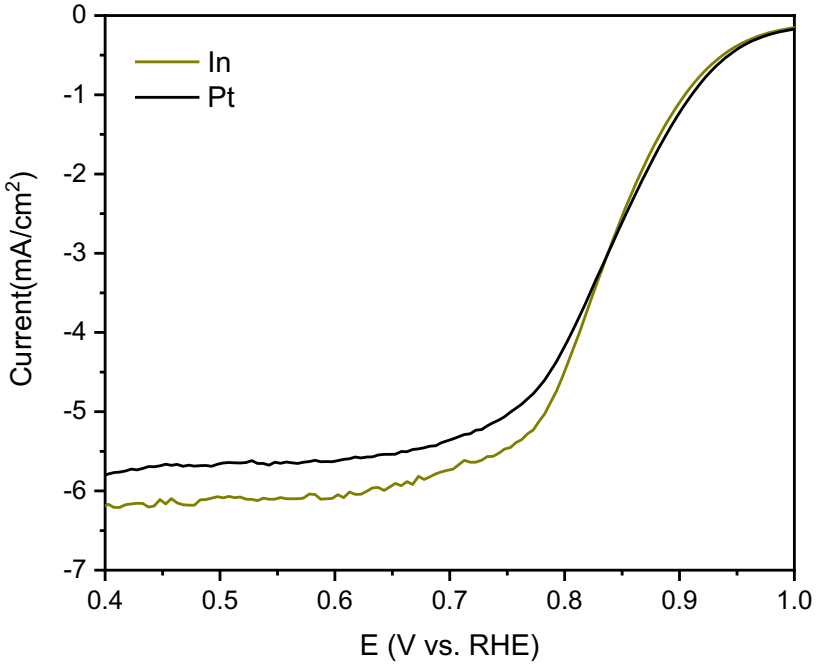

Figure 1.11. Electrochemical ORR on Pure Pt and Pt-InO_x.

Table 1.3. ORR kinetic current density and half-wave potentials and for Pt and Pt-InO_x. Data was collected using rotating disc electrodes at 1600 rpm in 0.1 M KOH saturated with O_2.

Sample	j_k **@ 0.86 V** (mA/cm^2)	$E_{1/2}$ (mV vs. RHE)
Pt	4.3	843
In	3.9	838

1.4 Conclusion

In conclusion, we have demonstrated a versatile synthetic method using colloidal surface adsorption reactions to generate ultra-thin layers of metal oxides and hydroxides on Pt core nanoparticles. Using these composite materials, we show that the activity for oxidative desorption of CO at Pt surface sites is strongly dependent on the identity of the metal oxide via both stripping of surface-adsorbed CO and steady state CO oxidation. We hypothesize that bifunctional participation of the metal oxide enables oxidative removal of CO at ~200 mV lower overpotential than Pt/C, particularly in the cases of In, Ni, and Mn oxides. This synthetic method provides a versatile solution-phase route toward CO-resistant Pt nanoparticle catalysts for potential use in fuel cell devices.

1.5 Materials

Indium chloride (98%), sodium hydroxide (97%), chromium (III) nitrate nonahydrate (99.99%), tetrabutylammonium chloride (97%), and potassium hydroxide (semiconductor grade, 99.99%) were purchased from Sigma Aldrich. Hydrogen hexachloroplatinate(IV) hexahydrate (38.0-40.0% Pt), zinc(II) chloride (99.99%), manganese(II) chloride tetrahydrate (99+%), and iron(II) chloride tetrahydrate (99%) were purchased from Acros Organics. Nickel(II) chloride hexahydrate (99.3%), cobalt(II) chloride hexahydrate (98%), scandium(III) chloride hexahydrate (99.9%), gallium(III) chloride (99.999%), titanium(IV) chloride (99.99)%, and N,N-dimethylformamide (99.8%) were purchased from Alfa Aesar. Nitric acid (68.0-70.0%), acetone (99.5 %), and formamide (99.5%) were purchased from Fisher Scientific. Ethylene glycol (99.0%) was purchased from VWR International. Tetrafluoroboric acid diethyl ether complex (50 - 55%) was purchased from BeanTown Chemical. Vulcan XC 72R carbon powder was purchased from the Fuel Cell Store. Carbon monoxide (99.99%) and nitrogen (99.99%) were purchased from Indiana Oxygen. All chemicals were used without further purification. Electrolyte solutions were prepared from Nanopure water (ASTM Type I, 18.2 MΩ), purified using a Thermo Scientific Barnstead Ultrapure Water System.

1.6 Synthetic Methods

1.6.1 "Unprotected" Pt: Synthesis of 1-2 nm Pt nanoparticles

$H_2PtCl_6 \cdot 6H_2O$ (499 mg, 0.965 mmol) was suspended in a 25 mL solution of 0.5 M NaOH in ethylene glycol. The suspension was sonicated until the $H_2PtCl_6 \cdot 6 H_2O$ fully dissolved to form a translucent yellow-orange solution. The solution was then stirred and heated to 160 °C for 3 hours, during which the color of the reaction mixture proceeded from yellow-orange to dark brown. The resulting dark brown solution was cooled to room temperature and transferred to a centrifuge tube. The nanoparticles were precipitated out of the ethylene glycol solution using 6 equiv. HBF_4 with respect to Pt and an equal volume of water with respect to ethylene glycol. The solution was centrifuged at 8500 rpm for 10 min. After centrifugation, the yellow liquid was decanted and the solid was redispersed in DMF containing 1 equiv. of NBu_4Cl with respect to Pt. 100 mL of toluene were then added to precipitate the nanoparticles a second time. After centrifuging at 8500 rpm for

10 min, the liquid was decanted, and 9.65 mL of DMF containing 1 equiv. of NBu_4Cl with respect to Pt were added to obtain a 0.1 M solution by Pt mol%.

1.6.2 Pt-MX_n: Adsorption of 1st row TM precursors on "unprotected" Pt NPs

Prior to each Pt-MX_n adsorption reaction, fresh stock solutions of the metal salts were prepared. In ambient atmosphere, $NiCl_2$•6 H_2O, $CoCl_2$•6 H_2O, $MnCl_2$•4 H_2O, $Cr(NO_3)_3$•9 H_2O and $InCl_3$ (0.2 M) were dissolved in DMF, and $ScCl_3$•6 H_2O, $GaCl_3$, $ZnCl_2$ (0.2 M) were dissolved in formamide. Under N_2 atmosphere, $FeCl_2$•4 H_2O and $TiCl_4$ (0.2 M) were dissolved in DMF. All reagents for subsequent reactions are taken from these stock solutions.

To introduce the second metal, the "unprotected" Pt NPs (0.01 mmol, 100 μL of 0.1 M) were combined with metal precursor (0.05 mmol, 250 μL of 0.2 M) and diluted to a total volume of 500 μL in DMF. The solution was carefully stirred for 12 hrs. The nanoparticles were precipitated using acetone, centrifuged, and the liquid was decanted. The nanoparticles were suspended in 200 μL of acetone and the precipitation and centrifugation steps were repeated three times. The nanoparticles were redispersed in 1 mL of DMF to obtain a 0.01 M nominal concentration based on Pt atom%. Exact concentration is determined by ICP-MS.

Pt-M (M = Ni, Co, Mn, Cr, In, Sc, Ga, Zn) were prepared in air. Pt-Fe and Pt-Ti were prepared in the glovebox under N_2.

In the cleaning procedure for Pt-$ScCl_3$, $GaCl_3$, and $ZnCl_2$, formamide was used instead of acetone to clean away residual metal halide precursor. In the cleaning procedure for Pt-$FeCl_2$, dimethylformamide was used instead of acetone to clean away residual $FeCl_2$ precursor.

1.7 References

(1) W.T. Yu, M.D. Porosoff, J.G.G. Chen, *Chem. Rev.*, **2012**, *112*, 5780.

(2) H.S. Liu, C.J. Song, L. Zhang, J.J. Zhang, H.J. Wang, D.P. Wilkinson, *J. Power Sources*, **2006**, *155*, 95.

(3) Y.G. Guo, J.S. Hu, L.J. Wan, *Adv. Mater.*, **2008**, *20*, 2878.

(4) R.R. Davda, J.W. Shabaker, G.W. Huber, R.D. Cortright, J.A. Dumesic, *Appl. Catal. B*, **2005**, *56*, 171.

(5) D.M. Alonso, S.G. Wettstein, J.A. Dumesic, *Chem. Soc. Rev.*, **2012**, *41*, 8075.

(6) M.B. Gawande, P.S. Branco, R.S. Varma, *Chem. Soc. Rev.*, **2013**, *42* 3371.

(7) A. Bruix, J.A. Rodriguez, P.J. Ramirez, S.D. Senanayake, J. Evans, J.B. Park, D. Stacchiola, P. Liu, J. Hrbek, F. Illas, *J. Am. Chem. Soc.*, **2012**, *134*, 8968.

(8) M. Cargnello, V.V.T. Doan-Nguyen, T.R. Gordon, R.E. Diaz, E.A. Stach, R.J. Gorte, P. Fornasiero, C.B. Murray, *Science*, **2013**, *341*, 771.

(9) O. Dulub, W. Hebenstreit, U. Diebold, *Phys. Rev. Lett.*, **2000**, *84*, 3646.

(10) M. Englisch, A. Jentys, J.A. Lercher, *J. Catal.*, **1997**, *166*, 25.

(11) Q. Fu, H. Saltsburg, M. Flytzani-Stephanopoulos, *Science*, **2003**, *301*, 935.

(12) M. Moses-DeBusk, M. Yoon, L.F. Allard, D.R. Mullins, Z.L. Wu, X.F. Yang, G. Veith, G.M. Stocks, C.K. Narula, *J. Am. Chem. Soc.,* **2013**, *135*, 12634.

(13) G.N. Vayssilov, Y. Lykhach, A. Migani, T. Staudt, G.P. Petrova, N. Tsud, T. Skala, A. Bruix, F. Illas, K.C. Prince, V. Matolin, K.M. Neyman, J. Libuda, *Nat. Mater.,* **2011**, *10*, 310.

(14) J.S. Spendelow, J.D. Goodpaster, P.J.A. Kenis, A. Wieckowski, *J. Phys. Chem. B,* **2016***, 110*, 9545.

(15) R. Subbaraman, D. Tripkovic, D. Strmcnik, K.-C. Chang, M. Uchimura, A.P. Paulikas, V. Stamenkovic, N.M. Markovic, *Science,* **2011**, *334*, 1256.

(16) N. Danilovic, R. Subbaraman, D. Strmcnik, K.C. Chang, A.P. Paulikas, V.R. Stamenkovic, N.M. Markovic, *Angew. Chem., Int. Ed.,* **2012**, *51*, 12495.

(17) R. Subbaraman, D. Tripkovic, K.-C. Chang, D. Strmcnik, A.P. Paulikas, P. Hirunsit, M. Chan, J. Greeley, V. Stamenkovic, N.M. Markovic, *Nat. Mater.*, **2012**, *11*, 550.

(18) Y. Wang, J. Ren, K. Deng, L. Gui, Y. Tang, *Chem. Mater.,* **2000**, *12*, 1622.

(19) H. Zhang, J. Jang, W.Y. Liu, D.V. Talapin, *ACS Nano,* **2014**, *8*, 7359.

(20) D.N. Dirin, S. Dreyfuss, M.I. Bodnarchuk, G. Nedelcu, P. Papagiorgis, G. Itskos, M.V. Kovalenko, *J. Am. Chem. Soc.,* **2014**, *136*, 6550.

(21) X. Huang, A.J. Shumski, X. Zhang, C.W. Li, *J. Am. Chem. Soc.,* **2018**, *140*, 8918.

(22) J. Huang, W.Y. Liu, D.S. Dolzhnikov, L. Protesescu, M.V. Kovalenko, B. Koo, S. Chattopadhyay, E.V. Shenchenko, D.V. Talapin, *ACS Nano,* **2014**, *8*, 9388.

(23) M.C. Biesinger, B.P. Payne, A.P. Grosvenor, L.W.M. Lau, A.R. Gerson, R.S.C. Smart, *Appl. Surf. Sci.,* **2011**, *257*, 2717.

(24) M.C. Biesinger, L.W.M. Lau, A.R. Gerson, R.S.C. Smart, *Appl. Surf. Sci.,* **2010**, *257*, 887.

(25) C. Donley, D. Dunphy, D. Paine, C. Carter, K. Nebesny, P. Lee, D. Alloway, N.R. Armstrong, *Langmuir,* **2002**, *18*, 450.

(26) C.V. Ramana, E.J. Rubio, C.D. Barraza, A. Miranda Gallardo, S. McPeak, S. Kotru, J.T. Grant, *J. Appl. Phys.,* **2014**, *115,* 043508.

(27) D.F. van der Vliet, M.T.M. Koper, *Surf. Sci.,* **2010**, *604*, 1912.

(28) N.M. Markovic, S.T. Sarraf, H.A. Gasteiger, P.N. Ross, *J. Chem. Soc., Faraday Trans.,* **1996**, *92*, 3719.

(29) N.M. Markovic, H.A. Gasteiger, N. Philip, *J. Phys. Chem.,* **1996**, *100*, 6715.

(30) S. Mukerjee, R.C. Urian, *Electrochim. Acta,* **2002**, *47*, 3219.

(31) B.E. Hayden, M.E. Rendall, O. South, *J. Am. Chem. Soc.,* **2003**, *125*, 7738.

(32) A.V. Tripkovic, K.D. Popovic, B.N. Grgur, B. Blizanac, P.N. Ross, N.M. Markovic, *Electrochim. Acta,* **2002**, *47*, 3707.

(33) W.X. Du, G.X. Yang, E. Wong, N.A. Deskins, A.I. Frenkel, D. Su, X.W. Teng, *J. Am. Chem. Soc.,* **2014**, *136*, 10862.

(34) Y. Wang, G.W. Wang, G.W. Li, B. Huang, J. Pan, Q. Liu, J.J. Han, L. Xiao, J.T. Lu, L. Zhuang, *Energy Environ. Sci.,* **2015**, *8*, 177.

(35) W.J. Huang, H.T. Wang, J.G. Zhou, J. Wang, P.N. Duchesne, D. Muir, P. Zhang, N. Han, F.P. Zhao, M. Zeng, J. Zhong, C.H. Jin, Y.G. Li, S.T. Lee, H.J. Dai, *Nat. Commun*., **2015**, *6*, 10035.

(36) G. Garcia, M.T.M. Koper, *ChemPhysChem*, **2011**, *12* , 2064.

(37) G. García, M.T.M. Koper, *J. Am. Chem. Soc*., **2009**, *131*, 5384.

(38) R. Gisbert, G. Garcia, M.T.M. Koper, *Electrochim. Acta*., **2011**, *56*, 2443.

(39) G. Garcia, M.T.M. Koper, *PCCP*, **2008**, *10*, 3802.

(40) F. Maillard, E.R. Savinova, U. Stimming, *J. Electroanal. Chem.,* **2007***, 599*, 221.

(41) T. Biegler, D.A.J. Rand, R. Woods, *J. Electroanal. Chem*., **1971**, *29*, 269.

(42) S. Mukerjee, S.J. Lee, E.A. Ticianelli, J. McBreen, B.N. Grgur, N.M. Markovic, P.N. Ross, J.R. Giallombardo, E.S. De Castro, Electrochem. *Solid-State Lett.*, **1999**, *2*, 12.

(43) Z.F. Liu, G.S. Jackson, B.W. Eichhorn, *Angew. Chem., Int. Ed*., **2010**, *49*, 3173.

CHAPTER 2. REVERSIBLE ELECTRON DOPING OF LAYERED NICKEL HYDROXIDE AND COBALT HYDROXIDE NANOPLATES USING N-BUTYLLITHIUM

Adapted with permission from Martinez, E. Y.; Zhu, K.; Li, C. W. *Nano Letters,* **2020,** *20*, 7580−7587. (DOI: 10.1021/acs.nanolett.0c03092)

2.1 Abstract

Ambipolar doping of metal oxides is critical toward broadening the functionality of semiconducting oxides in electronic devices. Most metal oxides, however, show a strong preference for a single doping polarity due to the intrinsic stability of particular defects in an oxide lattice. In this work, we demonstrate that layered metal hydroxide nanomaterials of Co and Ni, which are intrinsically p-doped in their anhydrous rock salt form, can be n-doped using n-BuLi as a strong electron donor. A combination of X-ray characterization techniques reveal that hydroxide vacancy formation, Li^+ adsorption, and varying degrees of electron delocalization are responsible for the stability of injected electrons. The doped electrons induce conductivity increases of 4−6 orders of magnitude relative to the undoped $M(OH)_2$. We anticipate that chemical electron doping of layered metal hydroxides may be a general strategy to increase carrier concentration and stability for n-doping of intrinsically p-type metal oxides.

2.2 Introduction

Transition metal oxides are currently used in electronic devices as transparent, flexible conductors and carrier transport layers.[1-10] However, the incorporation of metal oxides into more complex electronic devices such as light emitting diodes requires that a single oxide composition exhibit both p- and n-type doping, which has been difficult to achieve due to the inherent asymmetry in dopability for any given oxide structure.[11-17] This asymmetry arises from the fact that p- and n-type oxides exhibit very different formation energies for the intrinsic defects that dictate the type of free carriers that can form in the material. Late transition metal oxides such as NiO and CoO are intrinsically p-doped due to the stability of M^{3+} ions paired with M-vacancies or O interstitials in the lattice.[18-20] It is correspondingly difficult to electron dope NiO and CoO because the O-vacant structure formed upon electron injection collapses through over-reduction or

disproportionation to M^0 and undoped oxide.[21-23] Studies of NiO and CoO as anodes for Li-ion batteries have shown that electrochemical reduction proceeds directly from metal oxide to metal with no evidence of an intermediate n-doped phase.[24-33]

We hypothesize that hydrated forms of NiO and CoO with the layered metal hydroxide crystal structure would be more capable of supporting n-type doping because charge compensation and stabilization of vacancy defects could be provided by intercalation of ions and small molecules in between the two-dimensional layers. Indeed, both $Ni(OH)_2$ and $Co(OH)_2$ are known to form structures containing stable OH-vacancies when synthesized in the presence of anionic intercalants.[34-38] A few examples in the literature have shown in-situ formation of an n-doped $Ni(OH)_x$ state during electrochemical cycling, but structural characterization of the n-doped material was difficult to obtain due to the transient nature of the electrochemically-generated species.[39,40] In this work, we develop a chemical method to reversibly n-dope metal hydroxide nanoplates (M = Ni, Co) using n-BuLi as an electron donor and carefully characterize the structural and electronic changes that occur upon electron injection.

We drew synthetic inspiration from reversible electron doping methods developed for chalcogenide quantum dots and metal oxide nanocrystals as well as methods for the chemical exfoliation of 2D transition metal dichalcogenides and oxides.[41-52] In particular, n-BuLi treatment of layered structures such as MoS_2 and WO_3 induced electron injection, Li intercalation, stable defect formation, and eventual exfoliation to monolayers.[52-62] No examples of the n-BuLi treatment exist for layered metal hydroxides, but we anticipate that many of the same elementary processes would apply (**Figure 2.1**).

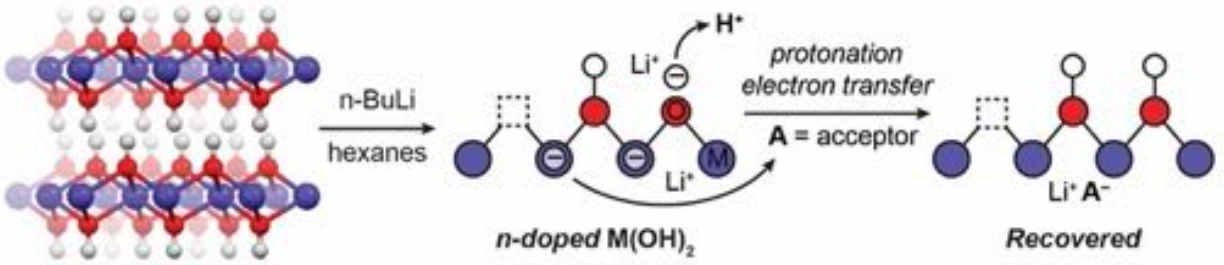

Figure 2.1. Schematic of reversible *n*-BuLi electron injection into layered metal hydroxides.

2.3 Results and Discussion

2.3.1 Synthesis and Characterization

We synthesize β-phase $Co(OH)_2$ hexagonal nanoplatelets of 200 nm width and 3 nm thickness using hydrothermal growth at 70 °C (**Figure B.1**).[63] To electron-dope the nanosheets, 50 mg of the $Co(OH)_2$ powder is suspended in hexanes, treated with 0.05 – 0.5 equiv. of n-BuLi with respect to Co, and stirred vigorously for 3 hours under inert atmosphere. At the end of the reaction, the $Co(OH)_2$ powder exhibits a color change from pale pink to dark brown (**Figure 2.2a, B.2a**). The same process on β-phase $Ni(OH)_2$ hexagonal nanoplatelets results in a color change from pale green to black (**Figure 2.2b, B.2b**). Upon exposure to a proton source and mild electron acceptor, MeOH and decamethylferrocenium tetrafluoroborate ($*Fc^+$), both powders revert to their original hues based on diffuse-reflectance UV-Vis (DRUV-Vis), suggesting that the injected electrons can be reversibly extracted (**Figure 2.1b-c, Recovered, Figure B.3**). At large quantities of n-BuLi (≥0.75 equiv), the color of the material does not recover after protonation and oxidation, indicating irreversible decomposition of the layered hydroxide sheets (**Figure B.4**). As a result, we focus the remainder of our studies on n-BuLi treatments ≤0.5 equiv.

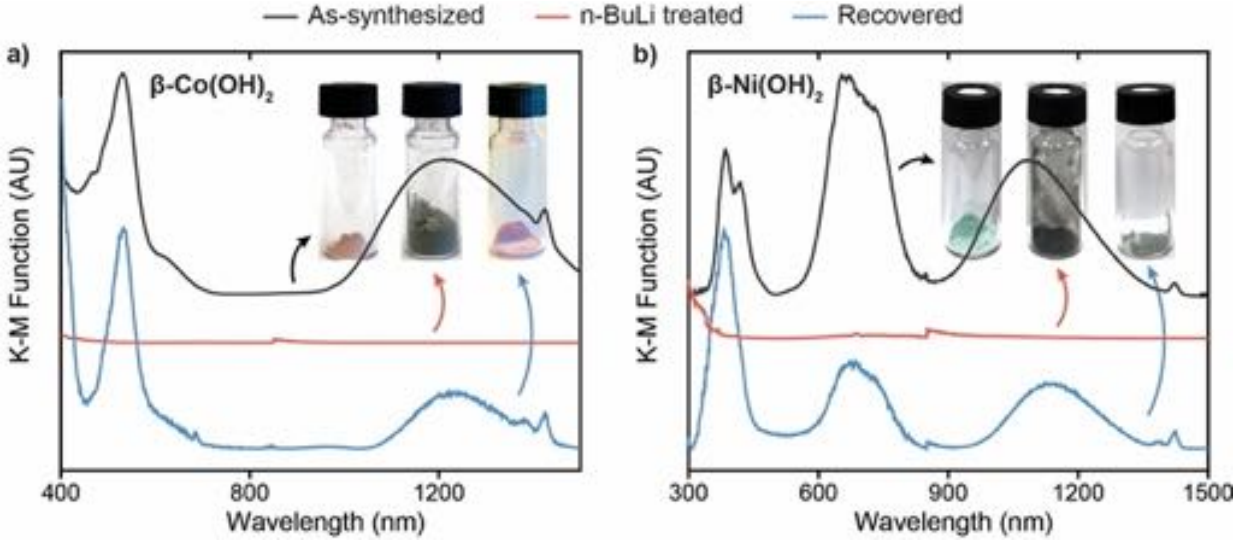

Figure 2.2. DRUV−vis and photographs of as-synthesized, 0.5 equiv *n*-BuLi treated, and recovered (**a**) β-$Co(OH)_2$ and (**b**) β-$Ni(OH)_2$ nanopowders.

Because NiO_x is a well-known electrochromic oxide that exhibits a bleached state in the stoichiometric form and colored states upon both oxidation (hole-doping) and reduction (electron-doping), we postulate that similar electronic mechanisms, including metal-centered reduction, Li incorporation, and oxygen vacancy formation, are responsible for the reversible color changes in n-BuLi treated metal hydroxides.[40,64,65] To understand the structural changes upon n-BuLi treatment and determine where the injected electrons reside in the $M(OH)_2$ structure, we perform structural characterization, electron titration, and conductivity measurements.

Transmission electron microscopy (TEM) images of the Co and Ni hydroxides after 0.5 equiv n-BuLi treatment look identical to the untreated samples with good maintenance of the hexagonal platelet morphology (**Figure 2.3**).

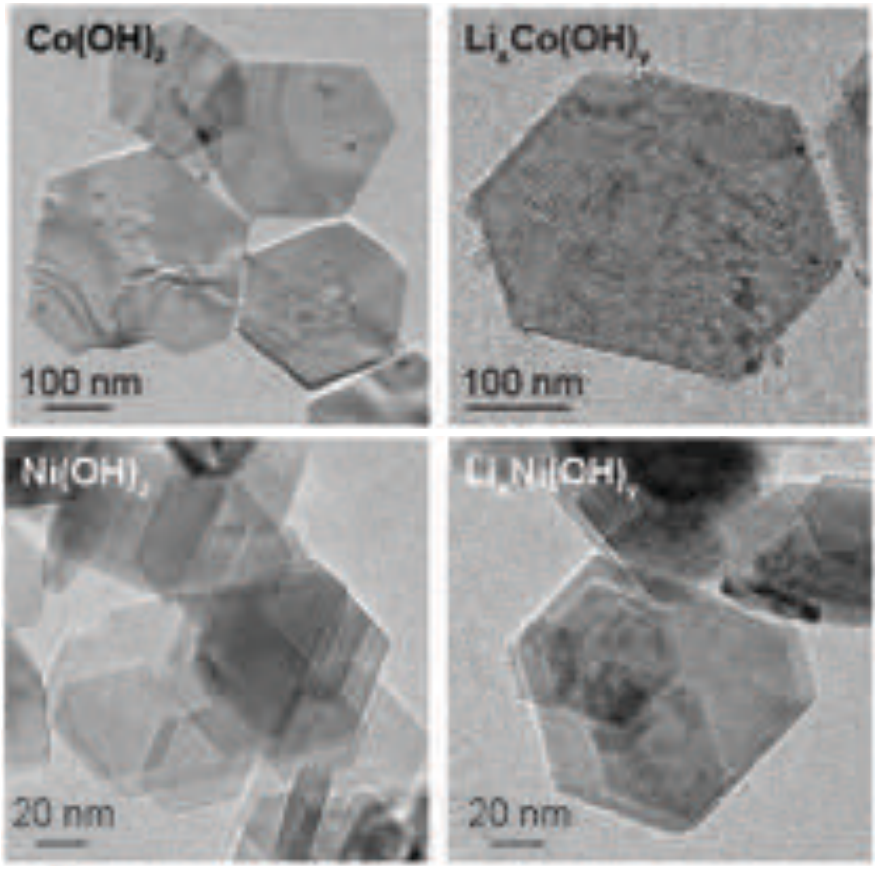

Figure 2.3. TEM images for as-synthesized and 0.5 equiv *n*-BuLi treated $Co(OH)_2$ and $Ni(OH)_2$ nanoplatelets.

The selected-area diffraction pattern (SAED) of an individual nanoplatelet remains single-crystalline after n-BuLi treatment, and the X-ray diffraction (XRD) patterns show that the brucite β-$M(OH)_2$ phase of the as-synthesized nanoplatelets is retained (**Figure 2.4, 2.5**). Importantly, in both the SAED and XRD patterns, no metallic Ni or Co phases are observed that would indicate reductive decomposition of the layered $M(OH)_2$ structure after 0.5 equiv n-BuLi treatment. While the $Ni(OH)_2$ XRD peak positions are exactly maintained, all peaks in the n-BuLi treated $Co(OH)_2$ shift to lower angle, indicating an overall expansion in the crystal structure (**Figure 2.2b**, **Table 2.1**). While we initially hypothesized that Li intercalation into the interlayer galleries might be a mechanism for charge compensation in these materials, the (00n) peak at 18.8° (**inset**) shifts the same amount as all other peaks in the pattern. The uniform crystal structure deformation may instead be attributed to defect formation or the presence of delocalized electrons.

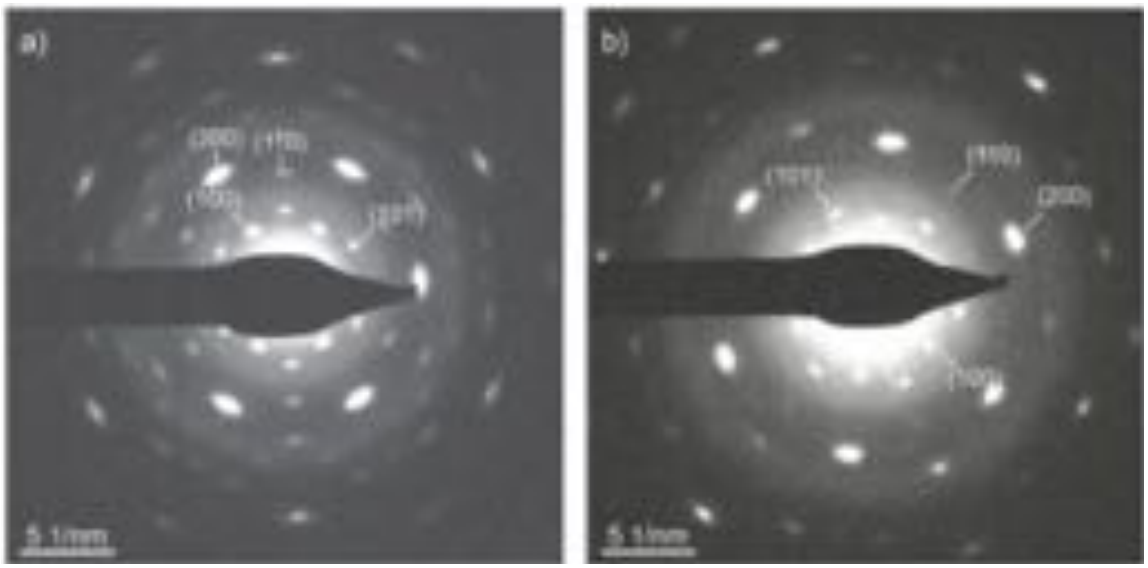

Figure 2.4. Selected area electron diffraction (SAED) pattern of a single nanoplatelet of (**a**) $Co(OH)_2$ and (**b**) 0.5 equiv. n-BuLi $Co(OH)_2$.

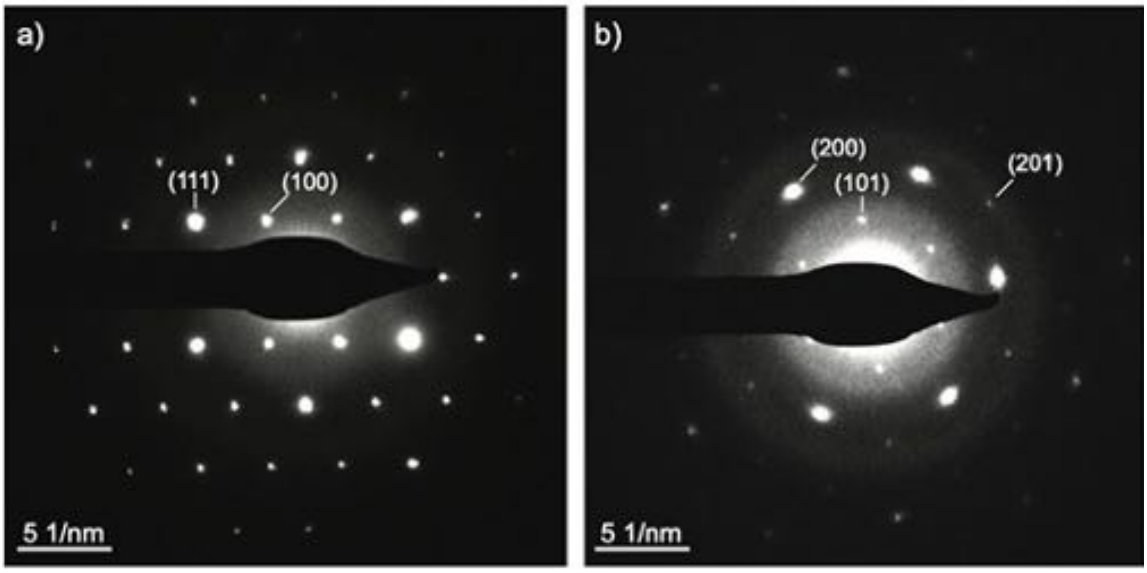

Figure 2.5. SAED pattern of a single nanoplatelet for (**a**) $Ni(OH)_2$ and (**b**) 0.5 equiv. n-BuLi $Ni(OH)_2$.

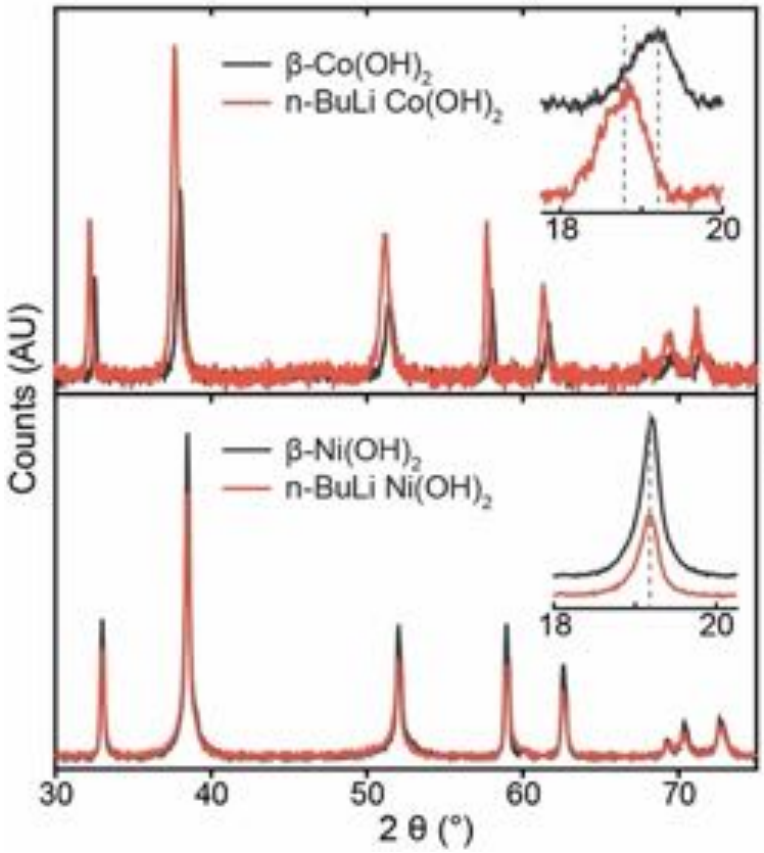

Figure 2.6. Powder XRD patterns for as-synthesized and 0.5 equiv *n*-BuLi treated $Co(OH)_2$ and $Ni(OH)_2$ nanoplatelets.

Table 2.1. Powder XRD peak positions and peak widths for $Co(OH)_2$ nanoplates before and after 0.5 equiv. n-BuLi treatment.

	h k l	**2 θ (°)**	**d-spacing (Å)**	**FWHM (°)**
$Co(OH)_2$	0 0 1	19.1	4.64	0.7
	1 0 0	32.5	2.75	0.2
	1 0 1	38.0	2.37	0.5
	1 0 2	51.5	1.78	0.7
	1 1 0	58.0	1.59	0.3
	1 1 1	61.7	1.50	0.5
	2 0 0	68.1	1.38	0.6
	1 0 3	69.7	1.35	1.1
	2 0 1	71.5	1.32	0.9

	h k l	**2 θ (°)**	**d-spacing (Å)**	**FWHM (°)**
0.5 equiv. n-BuLi $Co(OH)_2$	0 0 1	18.8	4.73	0.7
	1 0 0	32.2	2.78	0.2
	1 0 1	37.7	2.39	0.5
	1 0 2	51.2	1.78	0.7
	1 1 0	57.7	1.60	0.3
	1 1 1	61.4	1.51	0.5
	2 0 0	67.8	1.38	0.4
	1 0 3	69.3	1.35	1.0
	2 0 1	71.2	1.32	0.7

Table 2.2. Powder XRD peak positions and peak widths for $Ni(OH)_2$ nanoplates before and after 0.5 equiv. n-BuLi treatment.

	h k l	**2 θ (°)**	**d-spacing (Å)**	**FWHM (°)**
$Ni(OH)_2$	0 0 1	19.2	4.62	0.3
	1 0 0	33.0	2.71	0.2
	1 0 1	38.5	2.34	0.3
	1 0 2	52.1	1.76	0.4
	1 1 0	59.0	1.57	0.3
	1 1 1	62.6	1.48	0.4
	2 0 0	69.3	1.35	0.5
	1 0 3	70.4	1.34	0.5
	2 0 1	72.8	1.30	0.6

	h k l	**2 θ (°)**	**d-spacing (Å)**	**FWHM (°)**
0.5 equiv. n-BuLi $Ni(OH)_2$	0 0 1	19.2	4.63	0.3
	1 0 0	33.0	2.71	0.2
	1 0 1	38.5	2.34	0.4
	1 0 2	52.0	1.76	0.4
	1 1 0	59.0	1.56	0.4
	1 1 1	62.7	1.48	0.4
	2 0 0	69.4	1.35	0.6
	1 0 3	70.4	1.34	0.7
	2 0 1	72.8	1.30	0.8

To more clearly probe the defect structure of the n-doped materials, we also collect Co and Ni K-edge X-ray absorption spectroscopy (XAS). In the Co K-edge X-ray absorption fine structure (EXAFS), the 0.5 equiv n-BuLi treated sample clearly shows the first-shell Co–O and second-shell Co–O–Co scattering pathways at the same radial distances as pristine β-$Co(OH)_2$ with no new intensity at the metallic Co–Co distance that would be expected for Co^0 nanoclusters (**Figure 2.7**). However, the EXAFS scattering intensity drops significantly after n-BuLi treatment, which can be fit to a reduction in the coordination number (CN) for both pathways but also an increase in the Debye-Waller factor (σ^2) (**Table 2.3, Figure B.5**). The Co–O CN, which has a value of ~6 in the as-synthesized $Co(OH)_2$ crystal structure, drops to 4.7 after n-BuLi treatment, suggesting that significant hydroxide vacancies are formed to compensate for electron injection. Additionally, an increase in Debye-Waller factor indicates an increase in disorder in the crystal structure, which combined with the crystal structure expansion observed in the powder XRD, points to the formation of vacancies and other structural defects.

In contrast, the n-BuLi treated $Ni(OH)_2$ nanoplatelets show almost no change in EXAFS scattering relative to the as-synthesized $Ni(OH)_2$ (**Figure 2.7**). The Ni–O and Ni–O–Ni scattering pathways retain coordination numbers and bond distances similar to the as-synthesized sample, and no new intensity due to metallic Ni–Ni scattering is observed. The XANES data in both cases show little change in edge energy relative to as-synthesized $M(OH)_2$ (**Figure 2.8**).

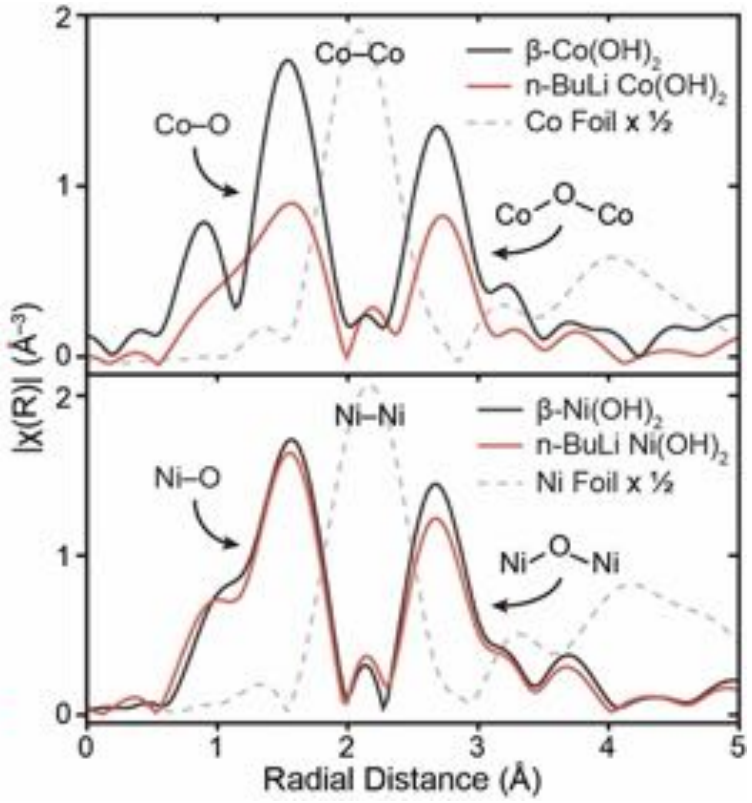

Figure 2.7. Co and Ni K-edge EXAFS of as-synthesized and 0.5 equiv *n*-BuLi treated $Co(OH)_2$ and $Ni(OH)_2$ nanoplatelets.

Table 2.3. Co and Ni K-Edge XAS fitting parameters for as-synthesized and 0.5 equiv *n*-BuLi treated $Co(OH)_2$ and $Ni(OH)_2$ as well as Co and Ni foil references.

Sample	Edge	Edge Energy (eV)	Scattering Pair	CN	R (Å)	σ^2 (Å^2)	E^0 (eV)
Co Foil	Co	7708.7	Co–Co	12	2.50	0.007	–0.09
β-$Co(OH)_2$	Co	7722.3	Co–O	6.2	2.09	0.004	–4.2
			Co–Co	5.6	3.18	0.004	–1.4
n-BuLi $Co(OH)_2$	Co	7722.0	Co–O	4.7	2.04	0.008	4.4
			Co–Co	5.0	3.22	0.008	3.3
Ni Foil	Ni	8333.0	Ni–Ni	12	2.49	0.006	8.4
β-$Ni(OH)_2$	Ni	8347.0	Ni–O	6.6	2.06	0.005	–3.6
			Ni–Ni	5.5	3.13	0.005	–0.96
n-BuLi $Ni(OH)_2$	Ni	8347.4	Ni–O	6.4	2.05	0.005	–5.1
			Ni–Ni	5.3	3.14	0.005	–0.53

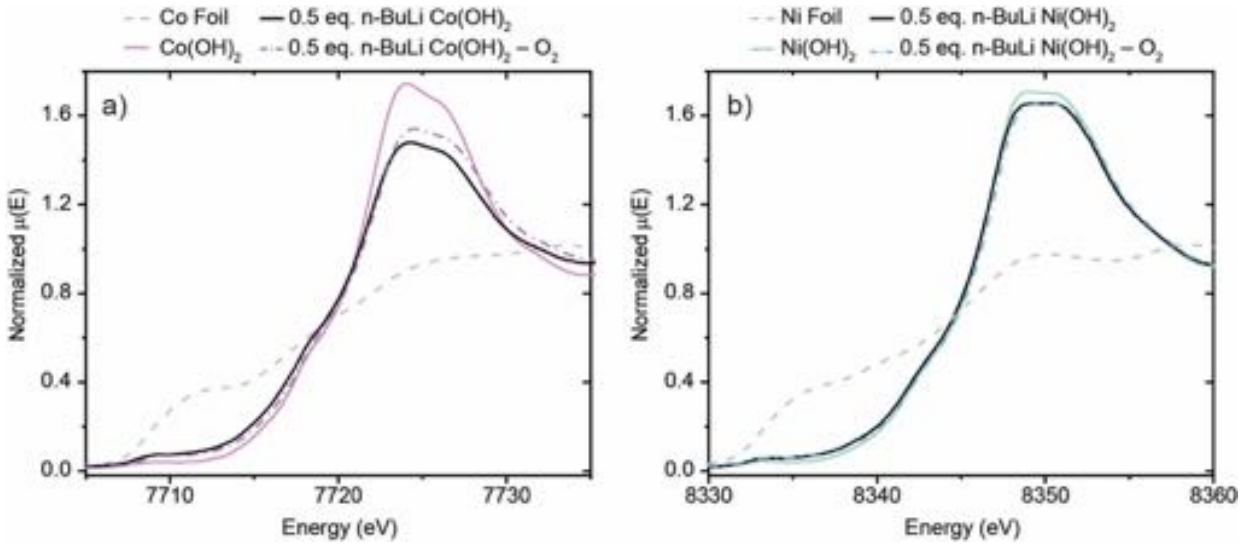

Figure 2.8. X-ray absorption near edge (XANES) region for the metal foil, as-synthesized $M(OH)_2$, n-BuLi treated $M(OH)_2$, and after in-situ exposure to O_2 for both (**a**) Co and (**b**) Ni.

X-ray photoelectron spectroscopy (XPS) of the metal, oxygen, and valence band regions provide insight into the electronic changes incurred during n-BuLi treatment. As-synthesized $Co(OH)_2$ has an asymmetric Co $2p_{3/2}$ peak centered at 780 eV, which after 0.5 equiv n-BuLi treatment, looks identical with only a slight broadening of the Co^{2+} feature (**Figure 2.9a**). In the valence band (VB) region, as-synthesized $Co(OH)_2$ shows a first maximum at 2.5 eV below the Fermi level corresponding to the Co 3d electrons, which broadens slightly toward the Fermi level after n-BuLi treatment (**Figure 2.9b**). Notably, the lack of any reduced Co oxidation states in the Co $2p_{3/2}$ or VB spectra indicates that the injected electrons are not localized onto Co centers but may instead be delocalized in the material or trapped on non-metal sites. In contrast, the Ni $2p_{3/2}$ region exhibits a clear peak at lower binding energy after n-BuLi treatment corresponding to a reduced Ni species, suggesting that injected electrons localize to a significant degree on the Ni atom (**Figure 2.9d**). In the valence band region, a strong shoulder feature at lower binding energy and a broadening of the Ni valence band electrons toward the Fermi level become clearly evident, again indicating that the Ni center has been partially reduced (**Figure 2.9e**). These observations are consistent with XPS and UPS measurements of vacuum-annealed and electrochemically-reduced NiO films in the literature that similarly show the localization of the electron onto the metal center with n-doping.[21,40,66]

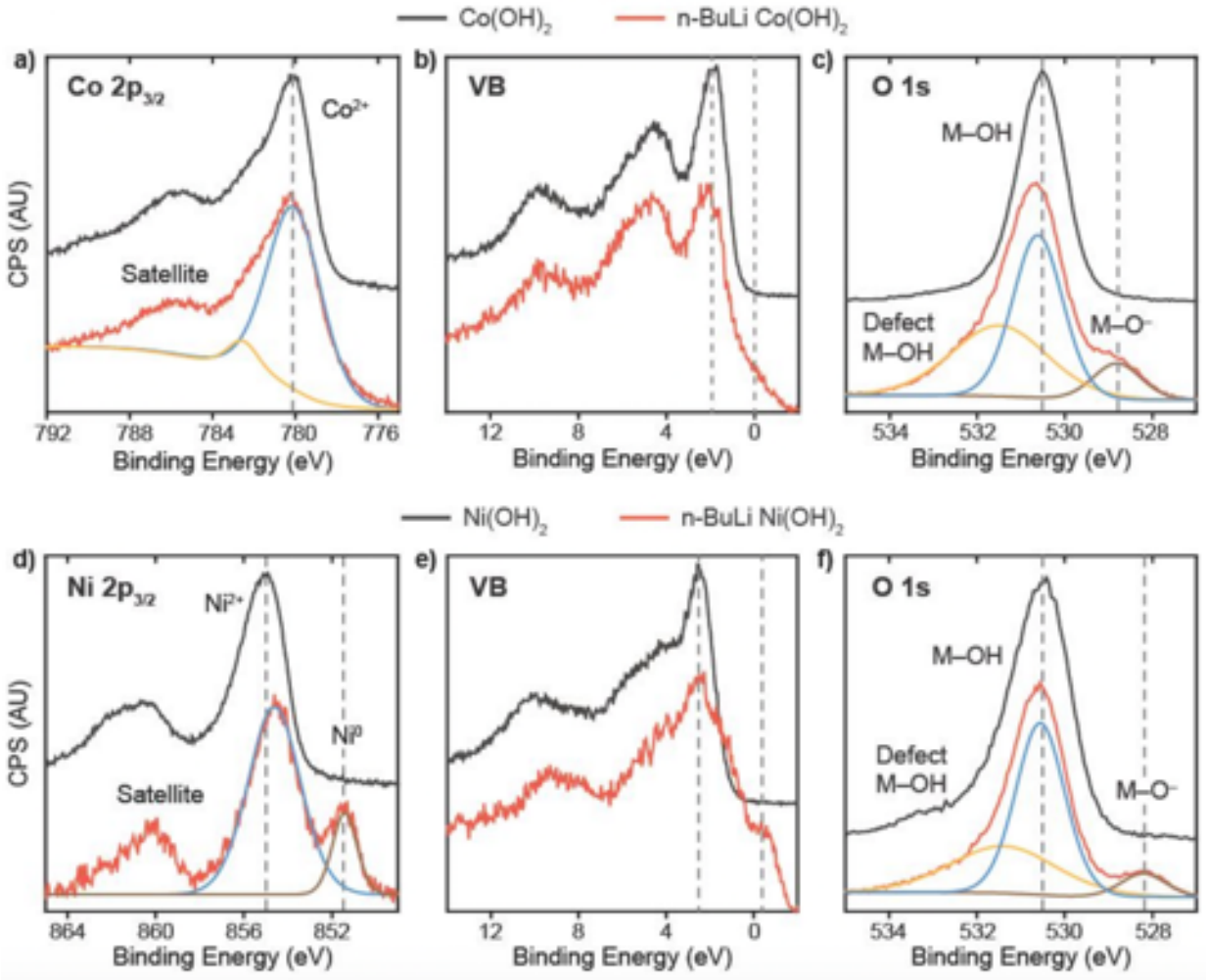

Figure 2.9. High-resolution XPS data for the M $2p_{3/2}$ valence band and O 1s regions for as-synthesized and 0.5 equiv *n*-BuLi treated (a−c) $Co(OH)_2$ and (d−f) $Ni(OH)_2$.

Lithium is observed in both materials with a larger ratio of Li:M in the n-doped $Ni(OH)_2$ though the poor sensitivity of XPS towards Li precludes absolute quantification (**Figure 2.10**, **Table 2.4**).

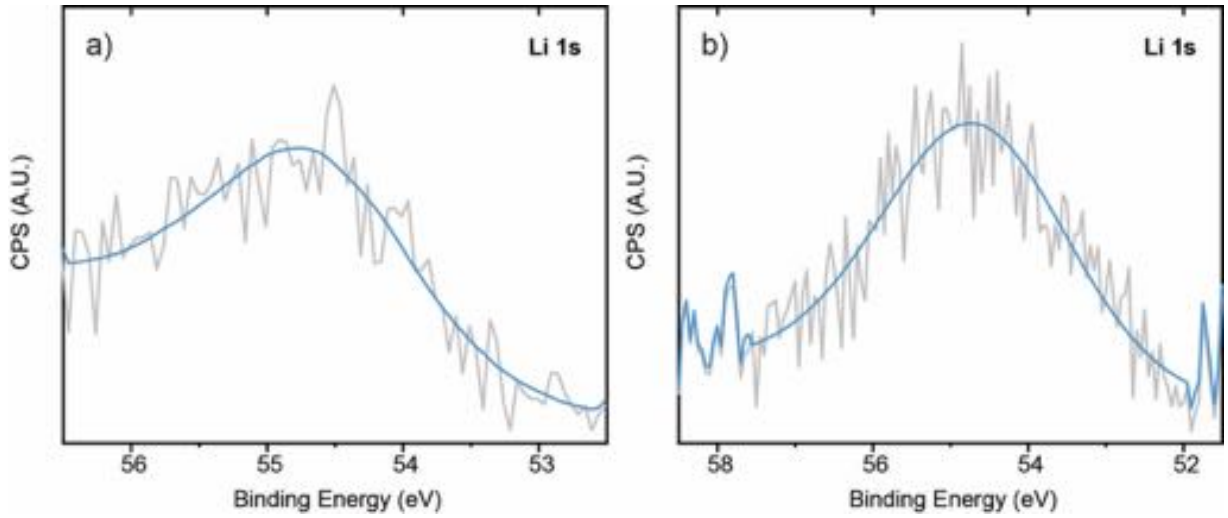

Figure 2.10. High resolution XPS of Li 1s region for (**a**) 0.5 equiv. n-BuLi treated $Co(OH)_2$ and (**b**) 0.5 equiv. n-BuLi treated $Ni(OH)_2$.

Taken together, the structural data suggest that Ni and Co exhibit different charge compensating mechanisms upon electron doping with OH-vacancies and structural distortions dominating in $Co(OH)_2$ due to the lower reducibility of the metal center and Ni^{2+} reduction coupled to Li^+ adsorption predominant in $Ni(OH)_2$.

The O 1s region in both the 0.5 equiv n-BuLi $Co(OH)_2$ and $Ni(OH)_2$ materials show significant changes from the undoped sample, most notably in the appearance of an O feature at 528.5 eV (**Figure 2.9c, f**). This lower energy O peak has been attributed to oxidic M–O–M moieties, which can be generated through deprotonation of M–OH to form $M–O^-$ since n-BuLi has high basicity in addition to strong reducing ability.[67,68] To ensure that the deprotonation of surface hydroxyls is not responsible for the other observed changes in the electronic structure, we treat the metal hydroxide nanoplatelets with a strong base that has no reducing ability, lithium diispropylamide (LDA) (**Figure 2.11**).

In this case, no electronic changes are observed in the Co and Ni 2p regions of the XPS, but the $M–O^-$ features are still formed (**Table 2.4, Figure B.6**). Deprotonation of the $M(OH)_2$ materials induces changes in the DRUV-Vis spectra that are very different from the n-BuLi treated samples, and both the color change and $M–O^-$ feature in the XPS are completely reversible upon protonation with MeOH (**Figure 2.12, B.7**). As a result, we feel confident that the electronic and structural changes observed upon n-BuLi treatment are primarily due to electron injection rather than deprotonation.

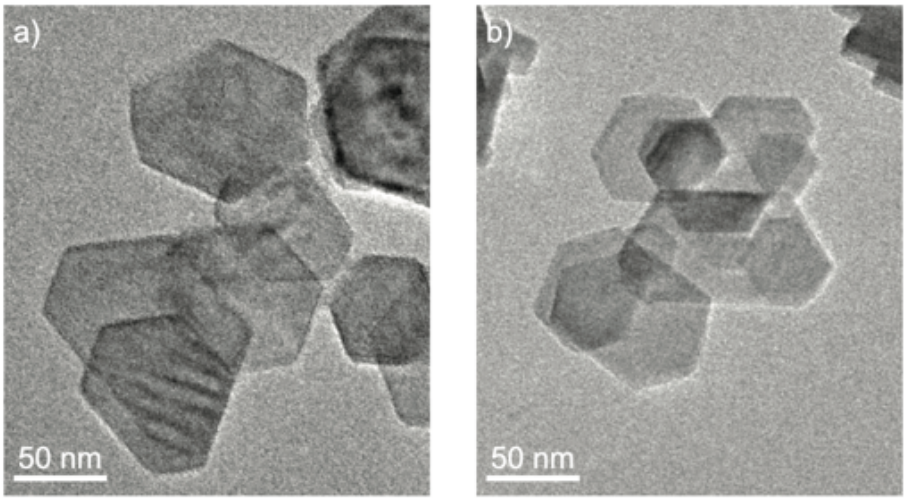

Figure 2.11. TEM images of (**a**) LDA treated $Co(OH)_2$ and (**b**) LDA treated $Ni(OH)_2$ with no change to nanoplate shape and size relative to the as-synthesized $M(OH)_2$.

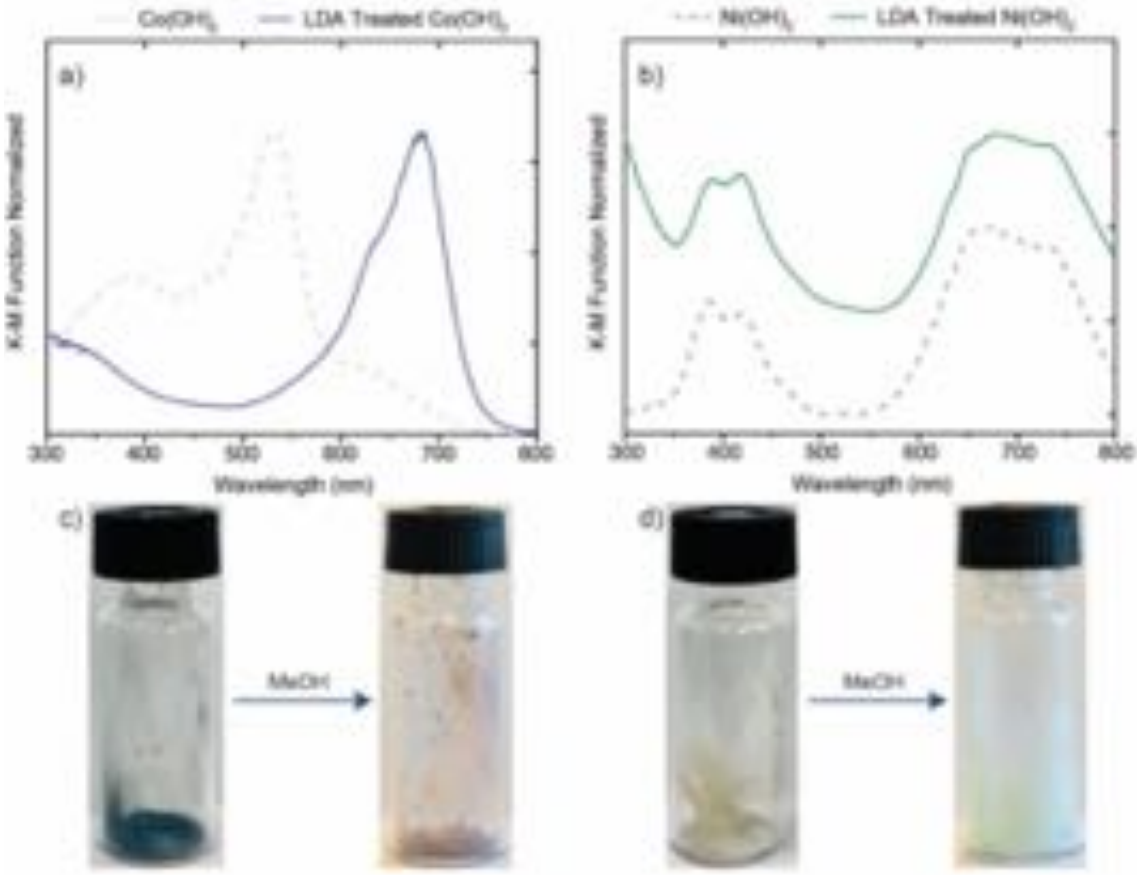

Figure 2.12. DRUV-Vis of LDA treated (**a**) $Co(OH)_2$ and (**b**) $Ni(OH)_2$. Photographs of LDA-treated and MeOH-reprotonated (**c**) $Co(OH)_2$ and (**d**) $Ni(OH)_2$ powders.

Table 2.4. Analysis of the high-resolution XPS features in the O 1s and M 2p regions for LDA treated, n-BuLi treated, and recovered $M(OH)_2$ samples.

Sample	O 1s		M 2p	
	M-O⁻ ~528.5 eV	**M-OH ~530.6 eV**	**$M^{0,+1}$ 851.4 eV**	**M^{2+} ~855 eV**
LDA treated $Ni(OH)_2$	8%	92%	0%	100%
LDA treated $Ni(OH)_2$ + MeOH	0%	100%	0%	100%
0.5 equiv. n-BuLi $Ni(OH)_2$	5%	95%	18%	82%
0.5 eq n-BuLi $Ni(OH)_2$ + MeOH + $*Fc^+$	0%	100%	0%	100%
1 equiv. n-BuLi $Ni(OH)_2$	26%	74%	38%	62%

Sample	O 1s		M 2p	
	M-O⁻ ~528.5 eV	**M-OH ~530.6 eV**	**$M^{0,+1}$ ~777 eV**	**M^{2+} ~ 780.1 eV**
LDA treated $Co(OH)_2$	22%	78%	0%	100%
LDA treated $Co(OH)_2$ + MeOH	14%	86%	0%	100%
0.5 eq n-BuLi $Co(OH)_2$	11%	90%	0%	100%
0.5 eq n-BuLi $Co(OH)_2$ + MeOH + $*Fc^+$	0%	100%	0%	100%
1 equiv. n-BuLi $Co(OH)_2$	18%	82%	16%	85%

Table 2.5. Atomic ratios obtained using XPS for n-BuLi treated and recovered $M(OH)_2$ samples.

Sample	Atomic Fraction wrt M			
	M 2p	**Li 1s[a]**	**O 1s**	**F 1s**
0.5 equiv. n-BuLi $Ni(OH)_2$	1	1.6	2.8	0
0.5 equiv. n-BuLi $Ni(OH)_2$ + MeOH + $*Fc^+$	1	0	6.3	0.9
1 equiv. n-BuLi $Ni(OH)_2$	1	17	13	0
0.5 equiv. n-BuLi $Co(OH)_2$	1	0.8	3.4	0
0.5 equiv. n-BuLi $Co(OH)_2$ + MeOH + $*Fc^+$	1	0	5.6	1.1
1 equiv. n-BuLi $Co(OH)_2$	1	9.7	7.6	0

[a]*Li sensitivity is extremely low in XPS, and ratios given are only a rough estimate.*

After protonation and electron extraction, both Co and Ni samples recover electronically to the as-synthesized metal hydroxide. The reduced Ni features in the valence band and Ni $2p_{3/2}$ XPS regions disappear in $Ni(OH)_2$ while the d–d transitions in the UV-Vis spectrum return in both metal hydroxides (**Figure 2.2, 2.13-14, B.3**).

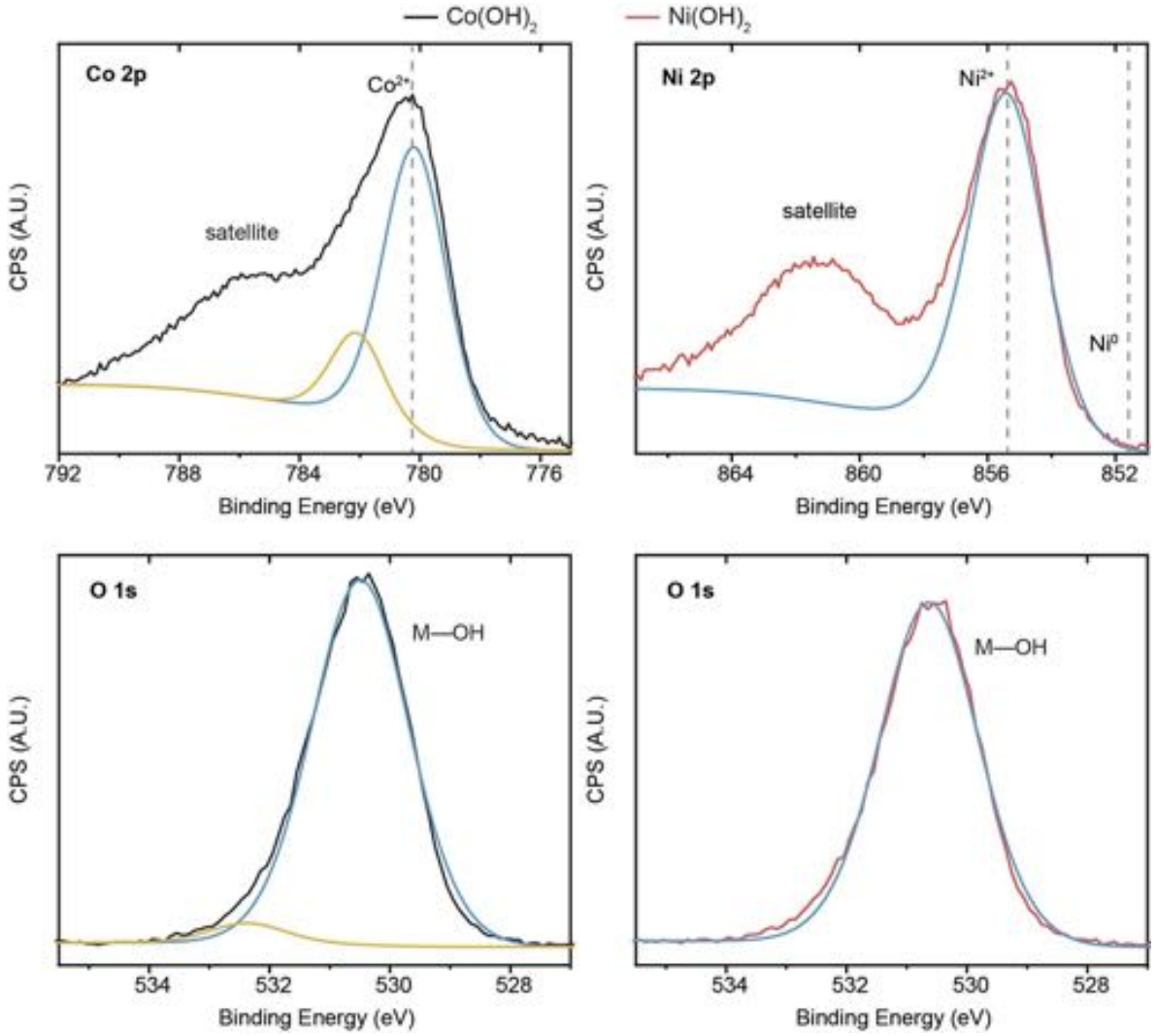

Figure 2.13. High-resolution XPS of M 2p and O 1s regions of the 0.5 equiv. n-BuLi $M(OH)_2$ after full recovery, i.e. protonation and electron extraction (MeOH + $*Fc^+$).

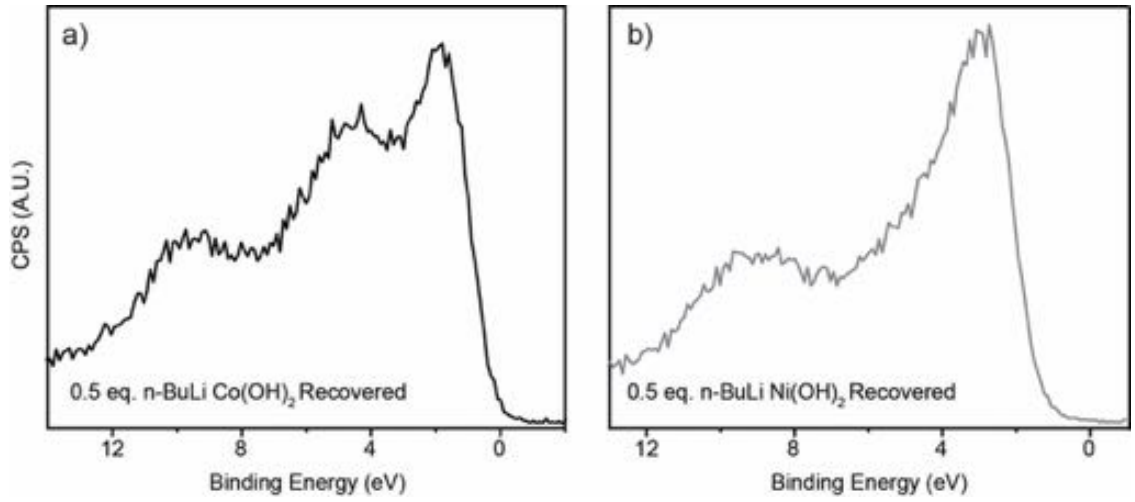

Figure 2.14. Valence band region of (**a**) 0.5 equiv. n-BuLi $Co(OH)_2$ and (**b**) 0.5 equiv. n-BuLi $Ni(OH)_2$ after full recovery, i.e. protonation and electron extraction (MeOH + $*Fc^+$).

The small lattice expansion observed in the XRD pattern for $Co(OH)_2$ reverts to the as-synthesized structure (**Figure 2.15, Table 2.6**). However, XAS data collected after in-situ O_2 exposure of the n-doped samples show that undercoordinated Co atoms with large Debye-Waller factor persist (**Figure 2.16, Table 2.7**). While O_2 exposure behaves somewhat differently than the MeOH + $*Fc^+$ recovery, the data nonetheless suggest that vacancies persist in the structure after electrons are removed. In both materials, 0.2-0.3 mol of BF_4^- per mol of metal is now associated with the nanosheet to charge-balance hydroxide vacancies formed during the n-BuLi treatment (**Table 2.5**).

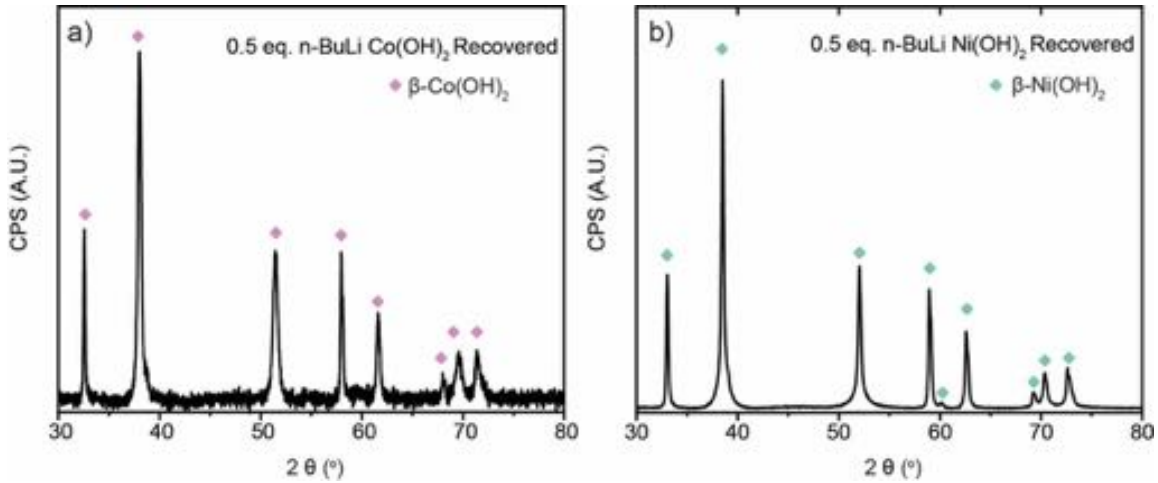

Figure 2.15. Powder XRD patterns for 0.5 equiv. n-BuLi (**a**) $Co(OH)_2$ and (**b**) $Ni(OH)_2$ after full recovery, i.e. protonation and electron extraction (MeOH + $*Fc^+$).

Table 2.6. Powder XRD peak positions and peak widths for 0.5 equiv. n-BuLi $Co(OH)_2$ and $Ni(OH)_2$ after full recovery, i.e. protonation and electron extraction (MeOH + $*Fc^+$).

	h k l	**2 θ (º)**	**d-spacing (Å)**	**FWHM (º)**
0.5 equiv. n-BuLi $Co(OH)_2$ + MeOH + $*Fc^+$	0 0 1	19.1	4.64	0.6
	1 0 0	32.5	2.75	0.2
	1 0 1	38.0	2.37	0.3
	1 0 2	51.5	1.78	0.6
	1 1 0	58.0	1.59	0.3
	1 1 1	61.6	1.50	0.4
	2 0 0	68.1	1.38	0.5
	1 0 3	69.6	1.35	0.9
	2 0 1	71.6	1.32	0.8

	h k l	**2 θ (º)**	**d-spacing (Å)**	**FWHM (º)**
0.5 equiv. n-BuLi $Ni(OH)_2$ + MeOH + $*Fc^+$	0 0 1	19.2	4.62	0.2
	1 0 0	33.0	2.71	0.2
	1 0 1	38.5	2.34	0.3
	1 0 2	52.1	1.76	0.4
	1 1 0	59.0	1.56	0.3
	1 1 1	62.7	1.48	0.3
	2 0 0	69.3	1.35	0.4
	1 0 3	70.4	1.34	0.5
	2 0 1	72.8	1.30	0.6

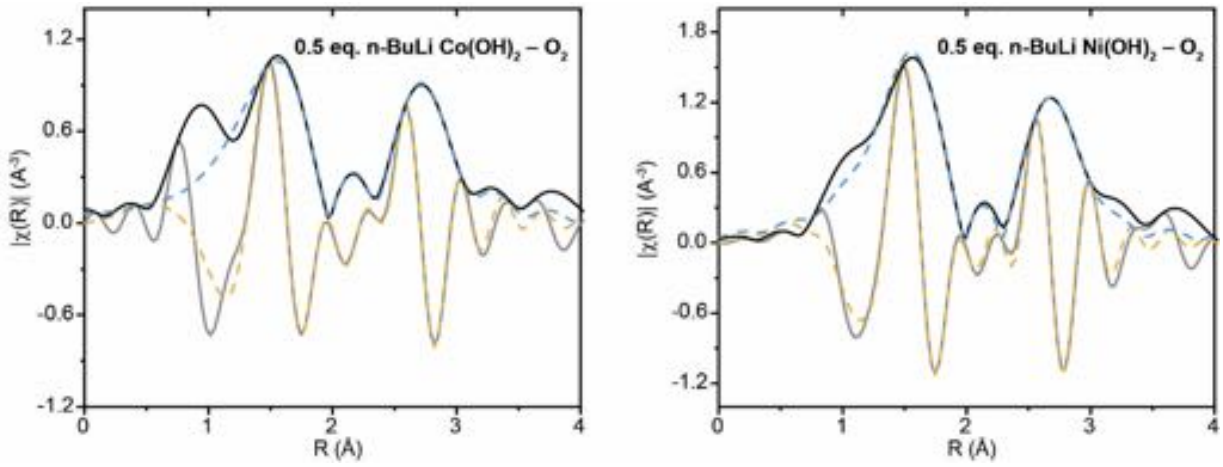

Figure 2.16. Co and Ni K-edge EXAFS fitting results for 0.5 n-BuLi $Co(OH)_2$ and $Ni(OH)_2$ samples after in-situ O_2 exposure. The black solid line is the FT magnitude, the dotted blue line is the fit to the FT magnitude, the solid gray line is the FT real part, and the dotted yellow line is the fit to the FT real part.

Table 2.7. Co and Ni K-edge fitting parameters for n-doped $M(OH)_2$ samples after in-situ O_2 exposure.

Sample	Edge	Edge Energy (eV)	Scattering pair	CN	R (Å)	σ^2 (Å^2)	E^0 (eV)
n-BuLi $Co(OH)_2$ + O_2	Co	7722.0	Co–O	5.0	2.12	0.008	–3.5
			Co–Co	5.5	3.18	0.008	0.68
n-BuLi $Ni(OH)_2$ + O_2	Ni	8347.4	Ni–O	6.4	2.06	0.005	–5.2
			Ni–Ni	5.5	3.13	0.005	0.20

In contrast the 0.5 equiv n-BuLi sample characterized in detail above, partial decomposition of the layered metal hydroxide is observed after 1 equiv n-BuLi treatment. Broad peaks appear in the XRD that indicate formation of metallic nanoparticles, and XPS of the M 2p regions show that 38% Ni^0 and 16% Co^0 are formed from the M^{2+} starting material (**Figure 2.17, Table 2.4**). We restrict the amount of n-BuLi used in the doping step to ≤0.5 equiv to ensure that no metal nanoparticles or other decomposition products interfere with electron counting and conductivity measurements.

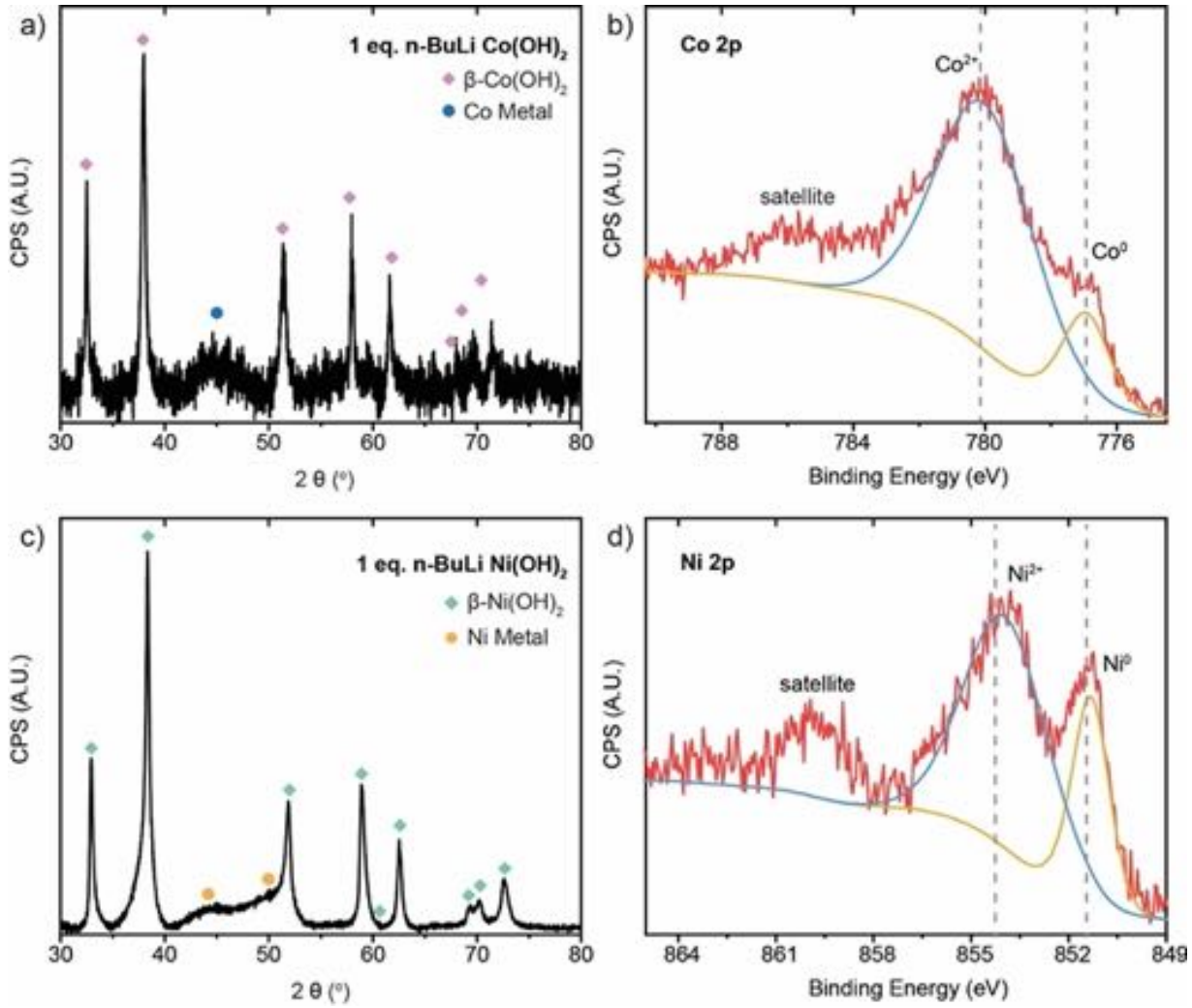

Figure 2.17. Powder XRD patterns and high-resolution XPS of the M 2p region for 1 equiv. n-BuLi treated (**a, b**) $Co(OH)_2$ and (**d, e**) $Ni(OH)_2$ showing Co^0 and Ni^0 metallic phase formation.

2.3.2 Electron Counting and Conductivity

To determine the number of electrons injected in the $M(OH)_2$ nanoplatelets during the n-BuLi treatment, we titrate stored electrons using $*Fc^+$ (**Figure 2.18**).[69,70] To ensure that $*Fc^+$ consumption reflects only the number of doped electrons, we perform several control experiments using undoped and LDA-deprotonated $M(OH)_2$ nanoplates (**Table 2.8**). As expected, the undoped $M(OH)_2$ nanoplates do not react with $*Fc^+$ under any circumstances (**Figure 2.19**). The LDA-deprotonated $M(OH)_2$ samples, however, do consume $*Fc^+$ due to the accelerated oxidation of M^{2+} to M^{3+} under strongly alkaline conditions, a process that is particularly pronounced on the more oxidizable $Co(OH)_2$ (**Figure 2.19, B.8**).[71,72] If methanol is added to protonate basic sites on the

surface prior to electron counting, the reaction between LDA $M(OH)_2$ and $*Fc^+$ is completely inhibited. Similar behavior with and without MeOH is observed on the n-BuLi treated $M(OH)_2$ nanoplates, and all electron counts henceforth will include a MeOH protonation step prior to $*Fc^+$ exposure to avoid "overcounting" due to oxidation (**Figure B.10**). Using this method, the $M(OH)_2$ nanoplates n-doped with 0.5 equiv n-BuLi store 0.28 mols of electrons per mol of Co and 0.14 mols of electrons per mol of Ni.

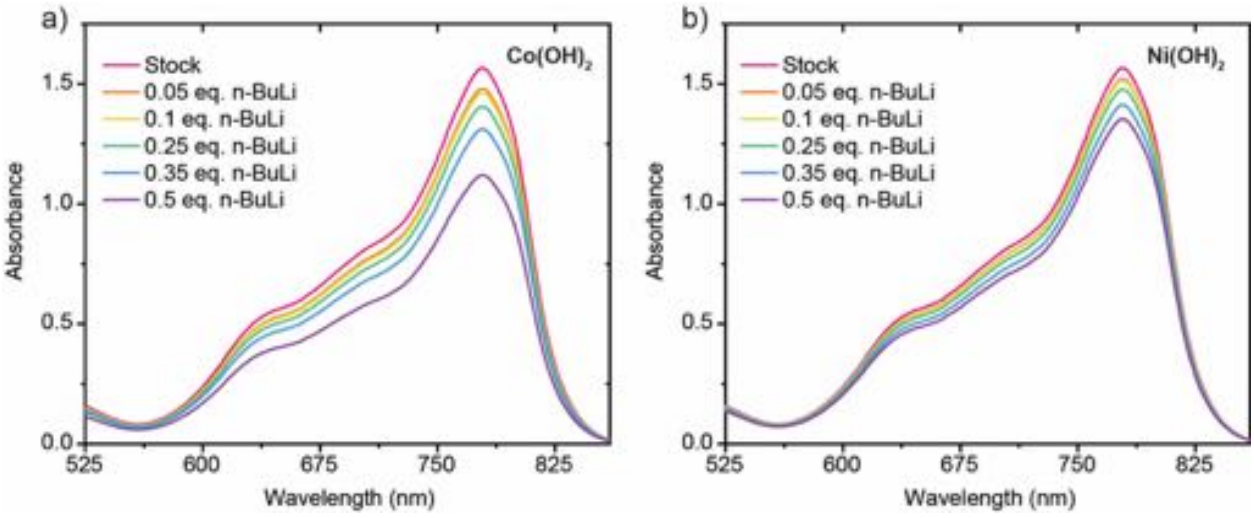

Figure 2.18. UV-Vis of the $*Fc^+$ absorption feature after reaction with n-doped (**a**) $Co(OH)_2$ and (**b**) $Ni(OH)_2$ treated with different equivalents of n-BuLi. All samples were reprotonated with MeOH prior to $*Fc^+$ addition.

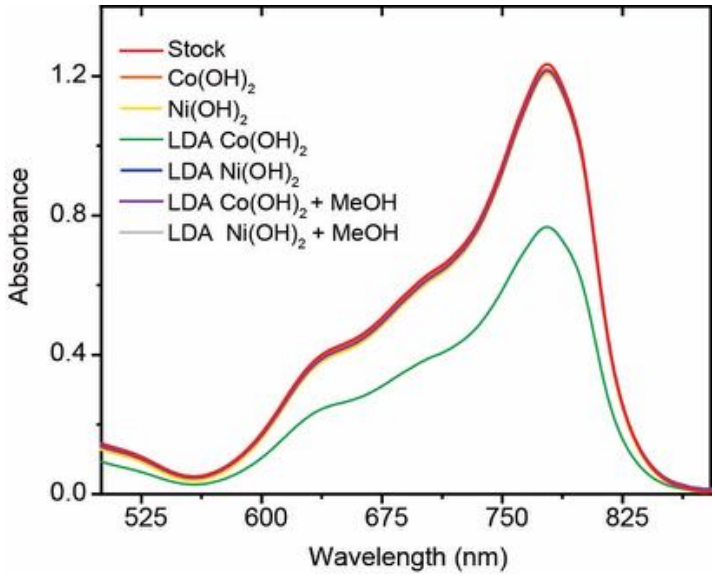

Figure 2.19. Electron counting controls. UV-Vis of $*Fc^+$ absorption feature after reaction with undoped $M(OH)_2$, LDA-treated $M(OH)_2$, and LDA-treated and reprotonated $M(OH)_2$.

Table 2.8. Equivalents of $*Fc^+$ consumed for electron counting controls.

Sample	$*Fc^+$ Consumed (Equiv. wrt M)
$Co(OH)_2$	0.0063
$Ni(OH)_2$	0.0084
LDA $Co(OH)_2$	0.51
LDA $Ni(OH)_2$	0.043
LDA $Co(OH)_2$ + MeOH	0.0085
LDA $Ni(OH)_2$ + MeOH	0.0079

The number of electrons stored per M atom in the $M(OH)_2$ structure can be tuned by modifying the amount of n-BuLi added during the electron injection step. Up to 0.5 equiv n-BuLi, the number of electrons injected into the metal hydroxide structure increases linearly with the amount of reductant (**Figure 2.21a**). For the same equivalents of n-BuLi, $Co(OH)_2$ stores a slightly higher number of electrons per metal atom than $Ni(OH)_2$, likely due to the smaller band gap of $Co(OH)_2$. The number of electrons injected into the sample correspond to carrier concentrations ranging from $6.8 \bullet 10^{20}$ to $6.6 \bullet 10^{21}$ electrons/cm^3, which are in a similar range to photodoped colloidal ZnO and TiO_2 nanocrystals with a variety of chemical reductants.[49,69,73]

To ascertain whether the injected electrons are mobile in the material, we carry out two-point conductivity measurements on pressed pellets of the n-BuLi treated metal hydroxides (**Figure 2.20**).[74]

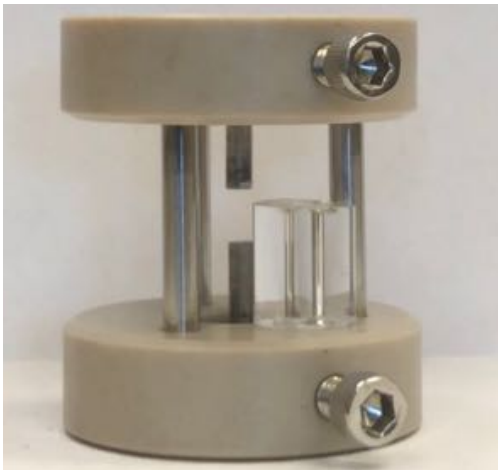

Figure 2.20. Home-built apparatus for two-point conductivity measurement.

I-V curves are collected for each sample on at least four different pellet thicknesses to obtain the average conductivity of the sample (**Figure B.11-B.14**). While measurements made in this manner include significant contributions due to grain boundary resistance, we nonetheless see large changes in conductivity upon n-doping using n-BuLi. Undoped $Co(OH)_2$ and $Ni(OH)_2$ exhibit negligible conductivity of ~10^{-12} S/cm. The conductivity increases significantly even at the lowest equivalents of n-BuLi (0.25 equiv) with 2-3 orders of magnitude increases for $Co(OH)_2$ and $Ni(OH)_2$ at <0.1 electrons stored per metal atom (**Figure 2.21b**). The conductivity values continue to increase steadily with increasing equivalents of n-BuLi. At maximum doping levels prior to material breakdown, we observe conductivity values of $4 \bullet 10^{-8}$ S/cm for $Ni(OH)_2$ and $3 \bullet 10^{-6}$ S/cm for $Co(OH)_2$ at 0.5 equiv n-BuLi. Importantly, the conductivity drops back down to 10^{-12} S/cm after removal of the injected electrons, clearly indicating that the doped carriers are the electronically mobile species in the sample. The trends in conductivity as a function of the electron number are similar between $Co(OH)_2$ and $Ni(OH)_2$, suggesting a similar electron mobility between these two compositions despite their differences in oxidation state and structural disorder upon electron injection (**Figure 2.22**).

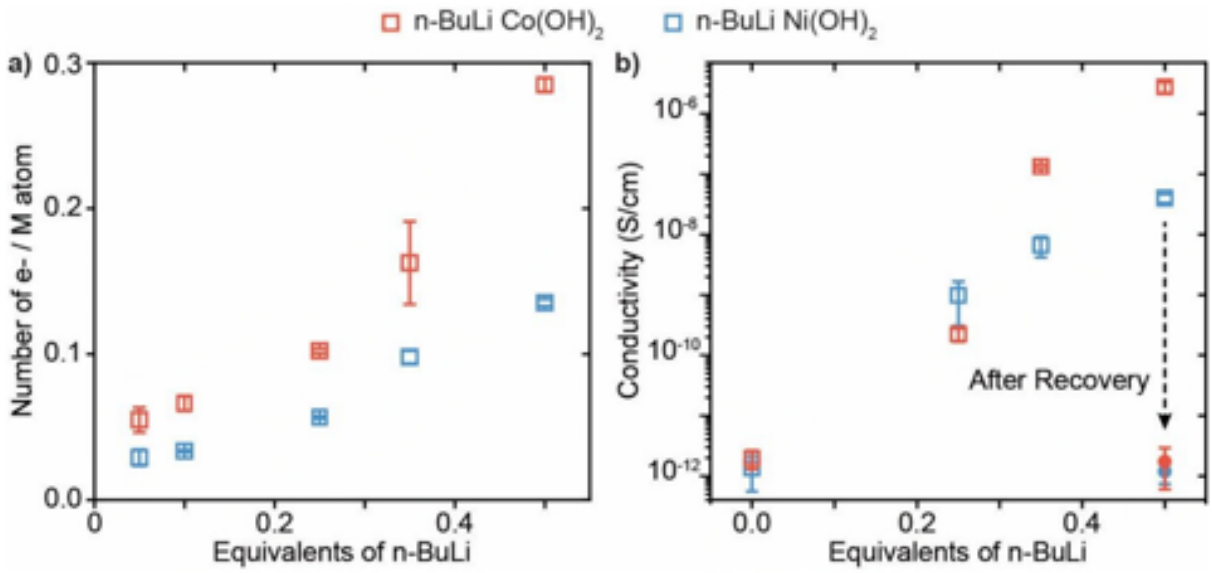

Figure 2.21. (**a**) Electron count obtained from $*Fc^+$ titration and (**b**) two-point conductivity values for n-doped $Co(OH)_2$ and $Ni(OH)_2$ at varying equivalents of *n*-BuLi.

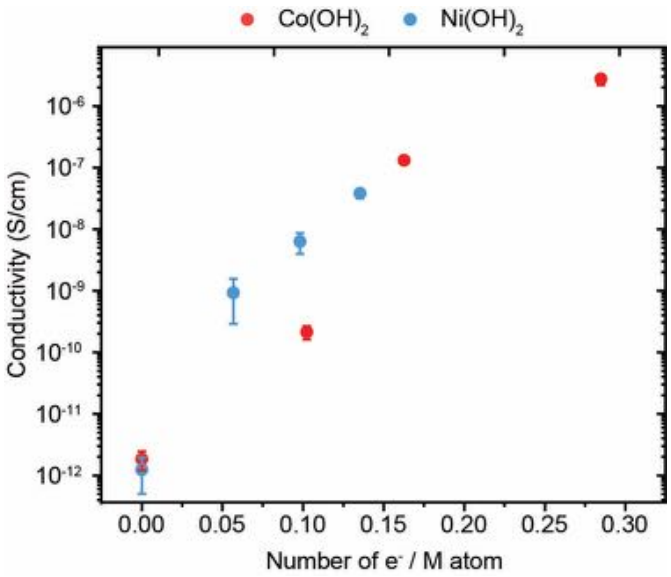

Figure 2.22. Conductivity as a function of the number of electrons stored in n-BuLi treated $Co(OH)_2$ and $Ni(OH)_2$.

We also measure the pellet conductivity for several control samples to ensure that none of the phases formed through deprotonation or decomposition are responsible for the observed conductivity (**Table 2.9**).

Table 2.9. Measured conductivity values for all control $M(OH)_2$ treatments.

Sample	Avg. Conductivity (S/cm)
LDA treated $Co(OH)_2$	$8 \pm 4 \times 10^{-12}$
LDA treated $Ni(OH)_2$	$6 \pm 4 \times 10^{-13}$
LDA treated $Co(OH)_2$ + $*Fc^+$	$3 \pm 1 \times 10^{-10}$
LDA treated $Ni(OH)_2$ + $*Fc^+$	$6 \pm 1 \times 10^{-13}$
0.1 eq n-BuLi $Co(OH)_2$ + MeOH	$1 \pm 1 \times 10^{-12}$
0.5 eq n-BuLi $Co(OH)_2$ + MeOH	$1 \pm 0.5 \times 10^{-12}$
0.5 eq n-BuLi $Ni(OH)_2$ + MeOH	$3 \pm 4 \times 10^{-12}$
1 equiv. n-BuLi $Co(OH)_2$	$2 \pm 0.4 \times 10^{-4}$
1 equiv. n-BuLi $Ni(OH)_2$	$1 \pm 0.5 \times 10^{-4}$
1 equiv. n-BuLi $Co(OH)_2$ + $*Fc^{+a}$	$2 \pm 1 \times 10^{-12}$
1 equiv. n-BuLi $Ni(OH)_2$ + $*Fc^{+a}$	$1 \pm 0.8 \times 10^{-12}$
1 equiv. n-BuLi $Co(OH)_2$ + CSA[b]	$9 \pm 6 \times 10^{-11}$
1 equiv. n-BuLi $Ni(OH)_2$ + CSA[b]	$9 \pm 0.8 \times 10^{-13}$
0.5 eq n-BuLi $Ni(OH)_2$ + CSA[b]	$1 \pm 0.9 \times 10^{-12}$
0.5 eq n-BuLi $Co(OH)_2$ + CSA[b]	$1 \pm 0.7 \times 10^{-12}$

[a]*Direct $*Fc^+$ treatment of 1 equiv. n-BuLi $M(OH)_2$ oxidizes M^0 species to rock salt MO species and cannot be used to assess the residual conductivity of the metallic nanoparticles (**Figure B.15**).*

[b]*A strong acid, camphorsulfonic acid (CSA), is used to intentionally passivate the electrons stored in the material without oxidizing any M^0 species that may be formed during n-doping.*

Materials deprotonated using LDA show no changes in conductivity relative to the as-synthesized material. When LDA samples are intentionally oxidized using $*Fc^+$, we see a small increase in conductivity for Co ($3 \bullet 10^{-10}$ S/cm) and no change for Ni ($6 \bullet 10^{-13}$ S/cm). In samples treated with 1 equiv n-BuLi that partially decompose to metallic nanoparticles, both materials remain insulating after passivation of n-doped electrons ($9 \bullet 10^{-11}$ S/cm on Co, $9 \bullet 10^{-13}$ S/cm on Ni) despite the persistence of M^0 species in the sample (**Figure 2.23**).

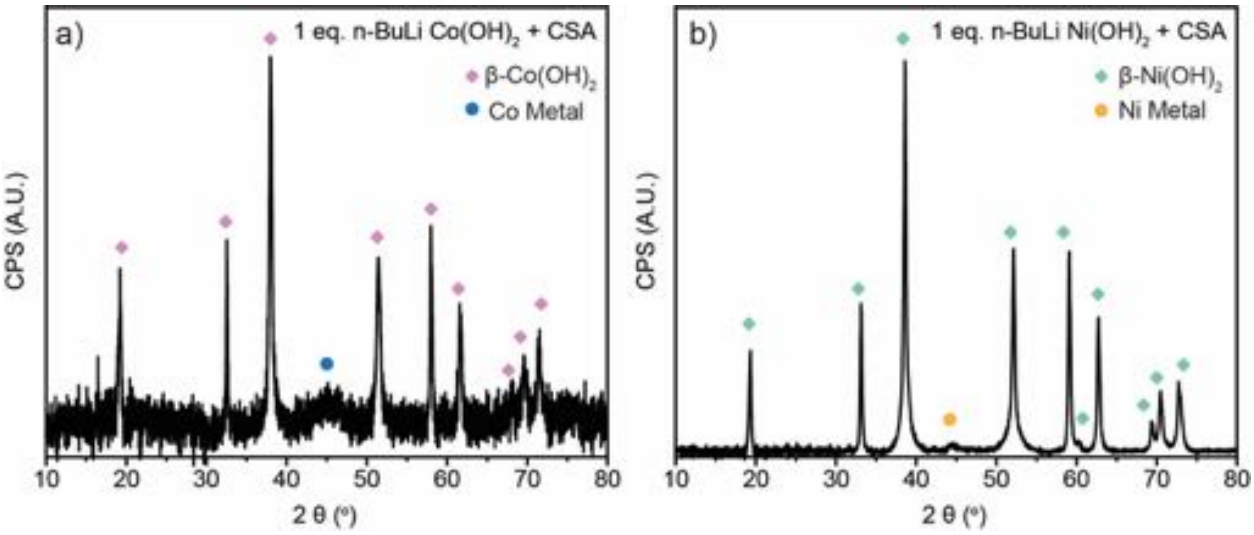

Figure 2.23. Powder XRD patterns for 1 equiv. n-BuLi (**a**) $Co(OH)_2$ and (**b**) $Ni(OH)_2$ powders after protonation and passivation of electrons using CSA. Crystalline M^0 phases are observed.

Given these controls, we believe that n-BuLi must introduce delocalized or shallowly-trapped n-type carriers in order to enable mobility throughout the entire pellet. It is likely, however, that a significant degree of electron trapping still occurs in both compositions given the large electron counts. In addition, the MeOH protonation step used to inhibit over-oxidation during electron counting induces a loss in conductivity, the origin of which is not yet understood and will be investigated in future studies.

2.4 Conclusion

In conclusion, we show that n-doping of late transition metal layered hydroxide structures is possible using the strong alkali metal reductant n-BuLi. By tuning the reductant concentration, a range of electron numbers up to 0.28 electrons per Co and 0.14 electrons per Ni can be injected into the two-dimensional layers without structural collapse. The two-dimensional structure is critical to enabling the large carrier densities because of its ability to support hydroxide vacancy formation and Li^+ adsorption for charge compensation. The injected electrons dramatically increase the conductivity of the metal hydroxide layer by 4-6 orders of magnitude relative to the undoped material. Numerous questions remain about the role of electron trapping and sample deprotonation, and future work will probe whether different populations of shallowly and deeply trapped electrons exist in the system. Based on this work, we postulate that chemical electron

doping of layered metal hydroxides instead of their corresponding three-dimensional metal oxides could be a general strategy to increase the carrier concentration and stability for n-doping of intrinsically p-type compositions.

2.5 Materials

Cobalt(II) nitrate hexahydrate (99%), n-butyllithium in hexanes (1.6 M, 98%) and diisopropylamine (99%) were purchased from Acros Organics. Sodium hydroxide (97%), bis(pentamethylcyclopentadienyl)iron(II) (97%), camphorsulfonic acid (CSA) (99%), and p-benzoquinone (98%) were purchased from Sigma Aldrich. Anhydrous methanol (99.8%) was purchased from Millipore Sigma. Nickel(II) nitrate hexahydrate (98%), anhydrous tetrahydrofuran (99.8%), anhydrous acetonitrile (99.8%) and anhydrous hexane were purchased from Alfa Aesar. Potassium hydroxide (≥85.0%) was purchased from Fisher Scientific. Tetrafluoroboric acid diethyl ether complex (50-55%) was purchased from BeanTown Chemical. Diisopropylamine was distilled from potassium hydroxide before use. Solvents were degassed and stored over activated 3 Å molecular sieves before use. All other chemicals were used without further purification. Nanopure water (ASTM Type I, 18.2 MΩ) was purified using a Thermo Scientific Barnstead Ultrapure Water System. Decamethylferrocenium tetrafluoroborate (*Fc^+) was prepared by a previously reported procedure.[1]

2.6 Synthetic Methods

2.6.1 β-Cobalt Hydroxides: Synthesis of hexagonal cobalt hydroxide nanoplatelets

The synthesis of β-cobalt hydroxide nanoplatelets is based on a literature procedure.[2] Cobalt(II) nitrate hexahydrate (2.91 g, 10.0 mmol) was dissolved in 40 mL of Nanopure water and degassed at 70 °C for 30 min. Then, 10 mL of 2 mM NaOH was added and the solution was aged for 1 hour at 70 °C. After cooling to room temperature, the pink suspension was centrifuged at 8500 rpm for 10 minutes. The supernatant was decanted and the remaining solid was rinsed thrice using 10 mL of H_2O and once with 10 mL of EtOH. After decanting the solvent, the pink solid was dried under vacuum at 60 °C for 18 hours.

2.6.2 β-Nickel Hydroxides: Synthesis of hexagonal nickel hydroxide nanoplatelets

The synthesis of β-nickel hydroxide nanoplatelets is based on a literature procedure.[3] Nickel(II) nitrate hexahydrate (2.91 g, 15.9 mmol) was dissolved in 40 mL of 2 M NaOH solution and stirred for 10 minutes at room temperature. The reaction solution was then transferred to a Teflon-lined hydrothermal reactor and heated at 160 °C for 24 hours. After cooling the reaction vessel to room temperature, the reaction medium was centrifuged at 8500 rpm for 10 minutes, the supernatant was decanted, and the remaining solid was rinsed thrice using 10 mL of H_2O and once with 10 mL of EtOH. The solid was dried under vacuum at 60 °C for 18 hours.

2.6.3 Electron doping of metal-hydroxide sheets with n-BuLi

To a suspension of $Co(OH)_2$ or $Ni(OH)_2$ (50 mg, 0.54 mmol) in hexanes (27 mL) was added 168 µL of n-BuLi (0.01 M in hexanes, 0.5 equiv. wrt to $M(OH)_2$). The final concentration of n-BuLi in hexanes should be kept at ≤0.01 M to avoid material decomposition. An immediate color change in the suspension is observed from pale green ($Ni(OH)_2$) or pink ($Co(OH)_2$) to black. After stirring at room temperature for 3 hours, the reaction medium was centrifuged and the supernatant was decanted. The resulting solid was rinsed once with 5 mL of hexanes and dried under vacuum.

2.6.4 Deprotonation of metal-hydroxide sheets

To prepare lithium diisopropylamide (LDA), diisopropylamine (170 µL, 1.2 mmol) in 3 mL of THF was cooled to –32 °C. 0.92 equiv. of n-BuLi (1.6 M in hexanes, 690 µL, 1.1 mmol) was added and the solution was stirred at –32 °C for 15 minutes. Separately, $Co(OH)_2$ (102.2 mg, 1.1 mmol) or $Ni(OH)_2$ (102.0 mg, 1.1 mmol) powder was suspended in THF (40 mL) and cooled to –32 °C. The solution of freshly-prepared LDA (1 equiv. wrt $M(OH)_2$) was added at –32 °C, and the reaction was stirred and warmed to room temperature over 3 h. The reaction medium was then centrifuged and the supernatant decanted. To remove excess LDA, the solids were resuspended in 5 mL of THF, sonicated for a few seconds, and collected by centrifugation. This cleaning step was repeated once more using THF and then three additional times using hexanes. The resulting powder was dried under vacuum.

2.6.5 Protonation of electron-doped metal hydroxide sheets

Electron-doped $M(OH)_2$ powder (4.0 mg, 0.043 mmol) was suspended in 1 mL of methanol and stirred for 1 hour. The reaction medium was centrifuged and the supernatant was decanted. The resulting solid was dried under vacuum.

Electron-doped $M(OH)_2$ powder (4.0 mg, 0.043 mmol) was suspended in 1 mL of THF with CSA (1 equiv. wrt $M(OH)_2$, 0.043 mmol, 10.0 mg) and stirred for 1 hour. The reaction medium was centrifuged and the supernatant was decanted. The resulting solid was rinsed with 1 mL of THF and dried under vacuum.

2.6.6 Electron Counting

The electron counting method using decamethylferrocenium tetrafluoroborate ($*Fc^+$) is based on a modified literature procedure.[9-10] A suspension of $Co(OH)_2$ and $Ni(OH)_2$ in hexanes was obtained through n-BuLi treatment as described in the synthetic methods. Prior to electron counting, the samples were soaked in MeOH to reprotonate basic sites. A stock solution of $*Fc^+$ in MeCN or MeOH (3.96 mM, 10 mL) was then added to each sample and stirred under inert atmosphere for 36 hours. The suspension was centrifuged to remove the solids, and the supernatant containing a mixture of $*Fc^+$ and *Fc was collected. The concentration of reacted $*Fc^+$ is determined based on the UV-Vis absorbance of the supernatant at 778 nm assuming an extinction coefficient for $*Fc^+$ (ε_{778}) of 492.90 $M^{-1} \times cm^{-1}$ in MeCN and 462.53 $M^{-1} \times cm^{-1}$ in MeOH. The electron counting experiment was performed on two separate samples at each n-BuLi loading to obtain an average electron count and error bar.

2.7 References

(1) Ginley, D. S.; Bright, C., *MRS Bull.*, **2000**, *25*, 15-18.

(2) Minami, T., *Semicond. Sci. Tech.*, **2005**, *20*, S35-S44.

(3) Fortunato, E.; Ginley, D.; Hosono, H.; Paine, D. C., *MRS Bull.,* **2007**, *32*, 242-247.

(4) You, J. B.; Meng, L.; Song, T. B.; Guo, T. F.; Yang, Y.; Chang, W. H.; Hong, Z. R.; Chen, H. J.; Zhou, H. P.; Chen, Q.; Liu, Y. S.; De Marco, N.; Yang, Y., *Nat. Nanotechnol.*, **2016**, *11*, 75-81.

(5) You, J. B.; Chen, C. C.; Dou, L. T.; Murase, S.; Duan, H. S.; Hawks, S. A.; Xu, T.; Son, H. J.; Yu, L. P.; Li, G.; Yang, Y., *Adv. Mater.*, **2012**, *24*, 5267-5272.

(6) Zhu, Z. L.; Bai, Y.; Zhang, T.; Liu, Z. K.; Long, X.; Wei, Z. H.; Wang, Z. L.; Zhang, L. X.; Wang, J. N.; Yan, F.; Yang, S. H., *Angew. Chem. Int. Ed.,* **2014**, *53*, 12571-12575.

(7) Manders, J. R.; Tsang, S. W.; Hartel, M. J.; Lai, T. H.; Chen, S.; Amb, C. M.; Reynolds, J. R.; So, F., *Adv. Funct. Mater.,* **2013**, *23*, 2993-3001.

(8) Nomura, K.; Ohta, H.; Takagi, A.; Kamiya, T.; Hirano, M.; Hosono, H., *Nature*, **2004**, *432*, 488-492.

(9) Fortunato, E.; Barquinha, P.; Martins, R., *Adv. Mater.,* **2012**, *24*, 2945-2986.

(10) Petti, L.; Munzenrieder, N.; Vogt, C.; Faber, H.; Buthe, L.; Cantarella, G.; Bottacchi, F.; Anthopoulos, T. D.; Troster, G., *Appl. Phys. Rev.,* **2016**, *3*.

(11) Park, J. S.; Maeng, W. J.; Kim, H. S.; Park, J. S., *Thin Solid Films*, **2012**, *520*, 1679-1693.

(12) Ruhle, S.; Anderson, A. Y.; Barad, H. N.; Kupfer, B.; Bouhadana, Y.; Rosh-Hodesh, E.; Zaban, A., *J. Phys. Chem. Lett.,* **2012**, *3*, 3755-3764.

(13) Lany, S.; Osorio-Guillen, J.; Zunger, A., *Phys. Rev. B*, **2007**, *75*.

(14) Greiner, M. T.; Chai, L.; Helander, M. G.; Tang, W. M.; Lu, Z. H., *Adv. Funct. Mater.,* **2012**, *22*, 4557-4568.

(15) Zhang, S. B.; Wei, S. H.; Zunger, A., *Phys. Rev. B*, **2001**, *63*.

(16) Look, D. C.; Claftin, B., *Phys. Status Solidi B*, **2004**, *241*, 624-630.

(17) Goyal, A.; Gorai, P.; Anand, S.; Toberer, E. S.; Snyder, G. J.; Stevanović, V., *Chem. Mater.,* **2020**, *32*, 4467-4480.

(18) Bosman, A. J.; Crevecoeur, C., *Phys. Rev.,* **1966**, *144*, 763-770.

(19) Wu, J. B.; Nan, C. W.; Lin, Y. H.; Deng, Y., *Phys. Rev. Lett.,* **2002**, *89*.

(20) Osorio-Guillen, J.; Lany, S.; Zunger, A., *AIP Conf. Proc.,* **2010**, *1199*, 128-129.

(21) Reinert, F.; Steiner, P.; Hufner, S.; Schmitt, H.; Fink, J.; Knupfer, M.; Sandl, P.; Bertel, E., *Z. Phys. B*, **1995**, *97*, 83-93.

(22) Khowash, P. K.; Ellis, D. E., *Phys. Rev. B*, **1987**, *36*, 3394-3399.

(23) Park, S.; Ahn, H. S.; Lee, C. K.; Kim, H.; Jin, H.; Lee, H. S.; Seo, S.; Yu, J.; Han, S., *Phys. Rev. B*, **2008**, *77*.

(24) Poizot, P.; Laruelle, S.; Grugeon, S.; Dupont, L.; Beaudoin, B.; Tarascon, J. M., *C. R. Acad. Sci*., **2000**, **3**, 681-691.

(25) Poizot, P.; Laruelle, S.; Grugeon, S.; Dupont, L.; Tarascon, J. M., *Nature*, **2000**, *407*, 496-499.

(26) Poizot, P.; Laruelle, S.; Grugeon, S.; Tarascon, J. M., *J. Electrochem. Soc*., **2002**, *149*, A1212-A1217.

(27) Chae, B. M.; Oh, E. S.; Lee, Y. K., *J. Power Sources*, **2015**, *274*, 748-754.

(28) Kim, H.; Choi, W. I.; Jang, Y.; Balasubramanian, M.; Lee, W.; Park, G. O.; Park, S. B.; Yoo, J.; Hong, J. S.; Choi, Y. S.; Lee, H. S.; Bae, I. T.; Kim, J. M.; Yoon, W. S., *ACS Nano*, **2018**, *12*, 2909-2921.

(29) Varghese, B.; Reddy, M. V.; Yanwu, Z.; Lit, C. S.; Hoong, T. C.; Rao, G. V. S.; Chowdari, B. V. R.; Wee, A. T. S.; Lim, C. T.; Sow, C. H., *Chem. Mater.,* **2008**, *20*, 3360-3367.

(30) Choi, H. C.; Lee, S. Y.; Kim, S. B.; Kim, M. G.; Lee, M. K.; Shin, H. J.; Lee, J. S., *J. Phys. Chem. B*, **2002**, *106*, 9252-9260.

(31) Boesenberg, U.; Marcus, M. A.; Shukla, A. K.; Yi, T. H.; McDermott, E.; Teh, P. F.; Srinivasan, M.; Moewes, A.; Cabana, J., *Sci. Rep.,* **2014**, *4*.

(32) Wang, Y.; Qin, Q. Z., *J. Electrochem. Soc.,* **2002**, *149*, A873-A878.

(33) Obrovac, M. N.; Dunlap, R. A.; Sanderson, R. J.; Dahn, J. R., *J. Electrochem. Soc.,* **2001**, *148*, A576-A588.

(34) Ma, R. Z.; Liu, Z. P.; Takada, K.; Fukuda, K.; Ebina, Y.; Bando, Y.; Sasaki, T., *Inorg. Chem.*, **2006**, *45*, 3964-3969.

(35) Liu, Z. P.; Ma, R. Z.; Osada, M.; Takada, K.; Sasaki, T., *J. Am. Chem. Soc.,* **2005**, *127,* 13869-13874.

(36) Yarger, M. S.; Steinmiller, E. M. P.; Choi, K. S., *Chem. Commun.,* **2007**, 159-161.

(37) Ida, S.; Shiga, D.; Koinuma, M.; Matsumoto, Y., *J. Am. Chem. Soc.,* **2008**, *130*, 14038-14039.

(38) Lee, J. W.; Ko, J. M.; Kim, J. D., *J. Phys. Chem. C*, **2011**, *115*, 19445-19454.

(39) Passerini, S.; Scrosati, B., *J. Electrochem. Soc.,* **1994**, *141*, 889-895.

(40) Wang, Q.; Puntambekar, A.; Chakrapani, V., *Nano Lett*., **2016**, *16*, 7067-7077.

(41) Schimpf, A. M.; Knowles, K. E.; Carroll, G. M.; Gamelin, D. R., *Acc. Chem. Res.,* **2015**, *48*, 1929-1937.

(42) Shim, M.; Guyot-Sionnest, P., *Nature*, **2000**, *407*, 981-983.

(43) Wang, C. J.; Shim, M.; Guyot-Sionnest, P., *Science*, **2001**, *291*, 2390-2392.

(44) Yu, D.; Wang, C. J.; Guyot-Sionnest, P., *Science*, **2003**, *300*, 1277-1280.

(45) Shim, M.; Guyot-Sionnest, P., *J. Am. Chem. Soc*., **2001**, *123*, 11651-11654.

(46) Liu, W. K.; Whitaker, K. M.; Kittilstved, K. R.; Gamelin, D. R., *J. Am. Chem. Soc.,* **2006**, *128*, 3910-3911.

(47) Valdez, C. N.; Braten, M.; Soria, A.; Gamelin, D. R.; Mayer, J. M., *J. Am. Chem. Soc.*, **2013**, *135*, 8492-8495.

(48) Koh, W. K.; Koposov, A. Y.; Stewart, J. T.; Pal, B. N.; Robel, I.; Pietryga, J. M.; Klimov, V. I., *Sci. Rep.,* **2013**, *3*.

(49) Schimpf, A. M.; Gunthardt, C. E.; Rinehart, J. D.; Mayer, J. M.; Gamelin, D. R., *J. Am. Chem. Soc.,* **2013**, *135*, 16569-16577.

(50) Rinehart, J. D.; Schimpf, A. M.; Weaver, A. L.; Cohn, A. W.; Gamelin, D. R., *J. Am. Chem. Soc.,* **2013**, *135*, 18782-18785.

(51) Schimpf, A. M.; Lounis, S. D.; Runnerstrom, E. L.; Milliron, D. J.; Gamelin, D. R., *J. Am. Chem. Soc.,* **2015**, *137*, 518-524.

(52) Voiry, D.; Goswami, A.; Kappera, R.; Silva, C. D. C. E.; Kaplan, D.; Fujita, T.; Chen, M. W.; Asefa, T.; Chhowalla, M., *Nat. Chem.,* **2015**, *7*, 45-49.

(53) Chen, X.; McDonald, A. R., *Adv. Mater.,* **2016**, *28*, 5738-5746.

(54) Paredes, J. I.; Munuera, J. M.; Villar-Rodil, S.; Guardia, L.; Ayan-Varela, M.; Pagan, A.; Aznar-Cervantes, S. D.; Cenis, J. L.; Martinez-Alonso, A.; Tascon, J. M. D., *ACS Appl. Mater. Interfaces*, **2016**, *8*, 27974-27986.

(55) Backes, C.; Berner, N. C.; Chen, X.; Lafargue, P.; LaPlace, P.; Freeley, M.; Duesberg, G. S.; Coleman, J. N.; McDonald, A. R., *Angew. Chem. Int. Ed.*, **2015**, *54*, 2638-2642.

(56) Chhowalla, M.; Shin, H. S.; Eda, G.; Li, L. J.; Loh, K. P.; Zhang, H., *Nat. Chem.,* **2013**, *5*, 263-275.

(57) Golden, J. H.; Disalvo, F. J.; Frechet, J. M. J., *Chem. Mater.,* **1994**, *6*, 844-849.

(58) Vera-Hidalgo, M.; Giovanelli, E.; Navio, C.; Perez, E. M., *J. Am. Chem. Soc.,* **2019**, *141*, 3767-3771.

(59) Cheng, K. H.; Jacobson, A. J.; Whittingham, M. S., *Solid State Ionics*, **1981**, *5*, 355-358.

(60) Yu, M.; Shao, H.; Wang, G.; Yang, F.; Liang, C.; Rozier, P.; Wang, C.-Z.; Lu, X.; Simon, P.; Feng, X., *Nat. Commun.,* **2020**, *11*, 1348.

(61) Yamada, H.; Hibino, M.; Kudo, T., *Solid State Ionics*, **2001**, *140*, 249-255.

(62) West, K.; Zachauchristiansen, B.; Jacobsen, T., *Electrochim. Acta*, **1983**, *28*, 1829-1833.

(63) Wang, B. X.; Lin, H.; Yin, Z. G., *Mater. Lett.,* **2011**, *65*, 41-43.

(64) Wen, R. T.; Granqvist, C. G.; Niklasson, G. A., *Adv. Funct. Mater.,* **2015**, *25*, 3359-3370.

(65) Granqvist, C. G., *Solid State Ionics*, **1994**, *70*, 678-685.

(66) Gupta, P.; Dutta, T.; Mal, S.; Narayan, J., *J. Appl. Phys.,* **2012**, *111*.

(67) Dupin, J. C.; Gonbeau, D.; Vinatier, P.; Levasseur, A., *Phys. Chem. Chem. Phys.,* **2000**, *2*, 1319-1324.

(68) Weidler, N.; Schuch, J.; Knaus, F.; Stenner, P.; Hoch, S.; Maljusch, A.; Schafer, R.; Kaiser, B.; Jaegermann, W., *J Phys. Chem. C*, **2017**, *121*, 6455-6463.

(69) Schrauben, J. N.; Hayoun, R.; Valdez, C. N.; Braten, M.; Fridley, L.; Mayer, J. M., *Science*, **2012**, *336*, 1298-1301.

(70) Schimpf, A. M.; Ochsenbein, S. T.; Buonsanti, R.; Milliron, D. J.; Gamelin, D. R., *Chem. Commun.,* **2012**, *48*, 9352-9354.

(71) Pralong, V.; Delahaye-Vidal, A.; Beaudoin, B.; Gerand, B.; Tarascon, J. M., *J. Mater. Chem.*, **1999**, *9*, 955-960.

(72) Ramesh, T. N., *Ind. Eng. Chem. Res.,* **2010**, *49*, 1530-1533.

(73) Carroll, G. M.; Schimpf, A. M.; Tsui, E. Y.; Gamelin, D. R., *J. Am. Chem. Soc.,* **2015**, *137*, 11163-11169.

(74) Sun, L.; Park, S. S.; Sheberla, D.; Dinca, M., *J. Am. Chem. Soc.,* **2016**, *138*, 14772-14782.

CHAPTER 3. INFLUENCE OF DEFECT STABILITY ON N-TYPE CONDUCTIVITY IN ELECTRON-DOPED ALPHA AND BETA COBALT(II) HYDROXIDE NANOSHEETS

Adapted with permission from Martinez, E. Y.; Zhu, K.; Li, C. W. *Inorg. Chem.,* **2021** (DOI: 10.1021/acs.inorgchem.1c00455)

3.1 Abstract

Electronic doping of transition metal oxides (TMOs) is typically accomplished through the synthesis of nonstoichiometric oxide compositions and the subsequent ionization of intrinsic lattice defects. As a result, ambipolar doping of wide band gap TMOs is difficult to achieve because the formation energies and stabilities of vacancy and interstitial defects vary widely as a function of oxide composition and crystal structure. Facile formation of lattice defects for one carrier type is frequently paired with high energy and unstable generation of the defects required for the opposite carrier polarity. Previous work from our group showed that the brucite layered metal hydroxides of Co and Ni, intrinsically p-type materials in their anhydrous three-dimensional forms, could be n-doped using a strong chemical reductant. In this work, we extend the electron-doping study to the α polymorph of $Co(OH)_2$ and elucidate the defects responsible for n-type doping in these two-dimensional materials. Through structural and electronic comparisons between the β, α, and rock salt structures within the cobalt (hydr)oxide family of materials, we show that both layered structures exhibit facile formation of anion vacancies, the necessary defect for n-type doping, that are not accessible in the cubic CoO structure. However, the brucite polymorph is much more stable to reductive decomposition in the presence of doped electrons due to its tighter layer-to-layer stacking and octahedral coordination geometry, which results in a maximum conductivity of 10^{-4} S/cm, three orders of magnitude higher than the maximum value attainable on the hydrotalcite $Co(OH)_2$ structure.

3.2 Introduction

Transition metal oxides (TMOs) have been incorporated into electronic devices as carrier transport layers, transparent conductors, and thin-film transistors, particularly for low-cost or flexible applications.[1-7] However, unlike Group IV or III-V semiconductors, the application of

TMOs in semiconductor devices has been limited by their inability to achieve both n-type and p-type conductivity through doping. This limitation arises in part because electronic-doping of TMOs typically occurs via intrinsic lattice defects and compositional nonstoichiometry.[8-12] Depending on the formation energies of the various structural defects within the crystal lattice (i.e. vacancies and interstitials of either the metal cation or oxygen), any given oxide composition will show a marked preference for either n-type or p-type doping.

Late first-row transition metal oxides such as Co, Ni, and Cu oxide exhibit low formation energies and good stabilities for metal cation vacancies (V_M), and the substoichiometric forms of these oxides, $M_{1-x}O$, are p-type semiconductors (**Figure 3.1a**).[13-20] In contrast, oxides such as TiO_2 and ZnO readily form oxygen vacancies (V_O) and show n-type conductivity when substoichiometric in oxygen (**Figure 3.1b**).[21-29] In both cases, it is difficult to form mobile carriers of the opposite polarity because the relevant structural defect is either energetically inaccessible or highly unstable.[30-33] It is critical, therefore, to understand the structural factors that dictate defect formation energy and stability in TMOs in order to achieve ambipolar doping.

CoO and NiO have garnered widespread interest as p-type semiconductors due to the tunability and stability of metal cation vacancies in their cubic rock salt lattice (**Figure 3.1c**). Using a strong chemical reductant, our group showed in a previous report that it was possible to achieve n-type doping of cobalt oxide materials by moving from the cubic structure to the brucite layered metal hydroxide structure (β-$M(OH)_2$).[34] We postulated that the stability of n-type carriers could stem from a variety of factors unique to the two-dimensional structure, including lower formation energies for oxygen vacancies, intercalation of ions and small molecules to stabilize defects, and retention of reduced metal centers in the two-dimensional layer (**Figure 3.1d**).

In this work, we perform chemical electron-doping and structural characterization studies on several members of the cobalt (hydr)oxide family of materials in order to more definitively elucidate the structural features necessary to support mobile n-type carriers. Specifically, we turn to an alternate polymorph of layered cobalt hydroxide, hydrozincite-like α-$Co(OH)_2$, which has a smaller band gap, wider interlayer spacing, and mixed Co coordination geometry relative to β-$Co(OH)_2$ (**Figure 3.1e**). By pairing conductivity measurements and detailed X-ray spectroscopy for n-BuLi-treated α-$Co(OH)_2$ compared to β-$Co(OH)_2$ and rock-salt CoO, we are able to illuminate the complex interplay between crystal structure, Co coordination environment, vacancy stability, and n-type conductivity in cobalt hydroxide nanomaterials.

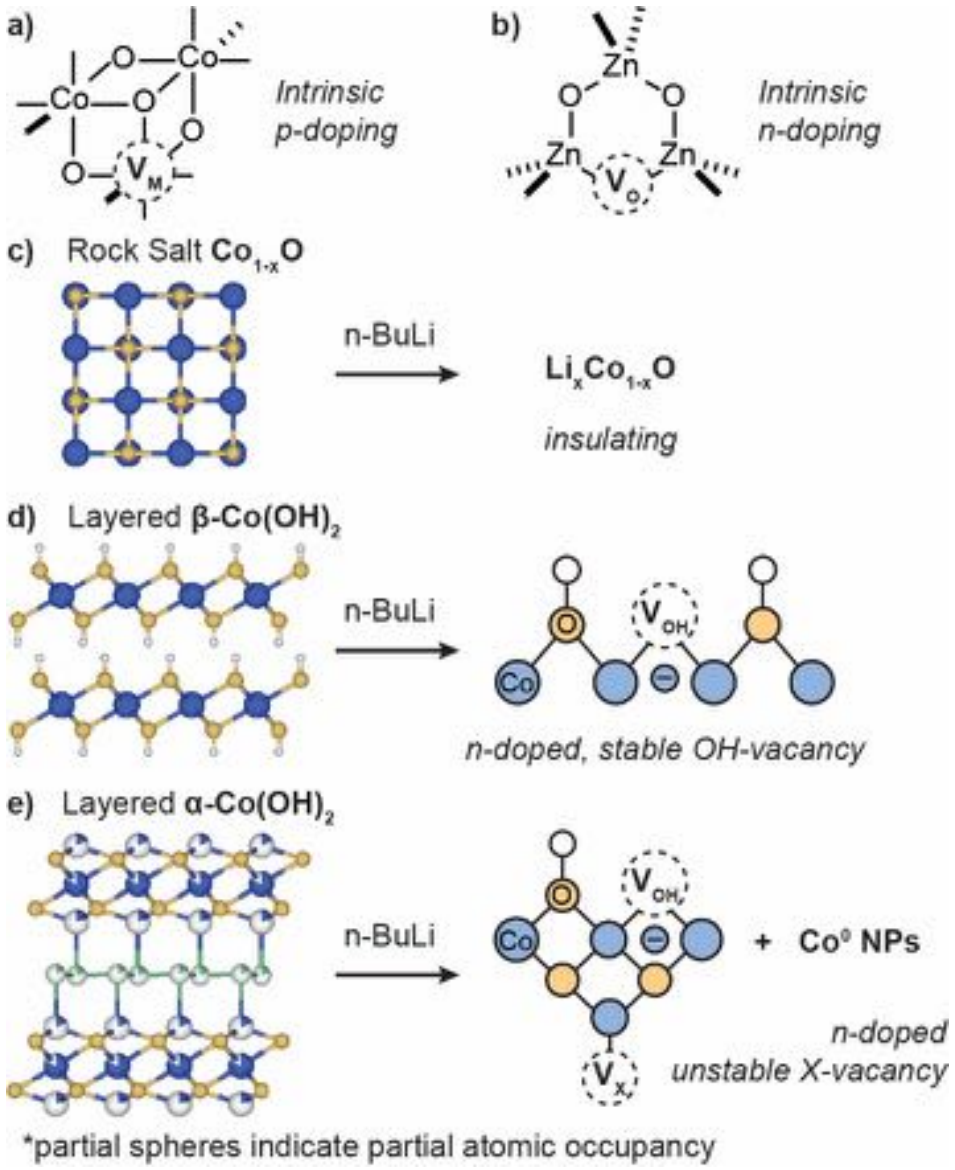

Figure 3.1. (**a, b**) Prototypical transition metal oxides exhibiting intrinsic p-doping and n-doping due to the formation of stable metal (V_M) or oxygen (V_O) vacancies. (**c-e**) Structural changes upon n-BuLi doping for three different cobalt (hydr)oxide polymorphs.

3.3 Results and Discussion

3.3.1 Synthesis

We synthesized hexagonal nanoplatelets of α-$Co(OH)_2$ and β-$Co(OH)_2$ using literature methods (**Figure 3.2**).[35,36] α-$Co(OH)_2$ intercalated with Cl^- anions (α-$Co(OH)_2$-Cl) has a hydrozincite-like crystal structure with interlayer spacing of 7.95 Å (**Table 3.1**). The two-dimensional layers comprise a mixture of octahedral and tetrahedral sites, and the tetrahedral sites are coordinated to the interlayer anion, in this case Cl^-, that stabilize the layered structure.[37] β-$Co(OH)_2$ has a brucite crystal structure, in which the layers are composed of pure octahedral sites with no anionic intercalants and much narrower interlayer spacing of 4.62 Å (**Table 3.1**).

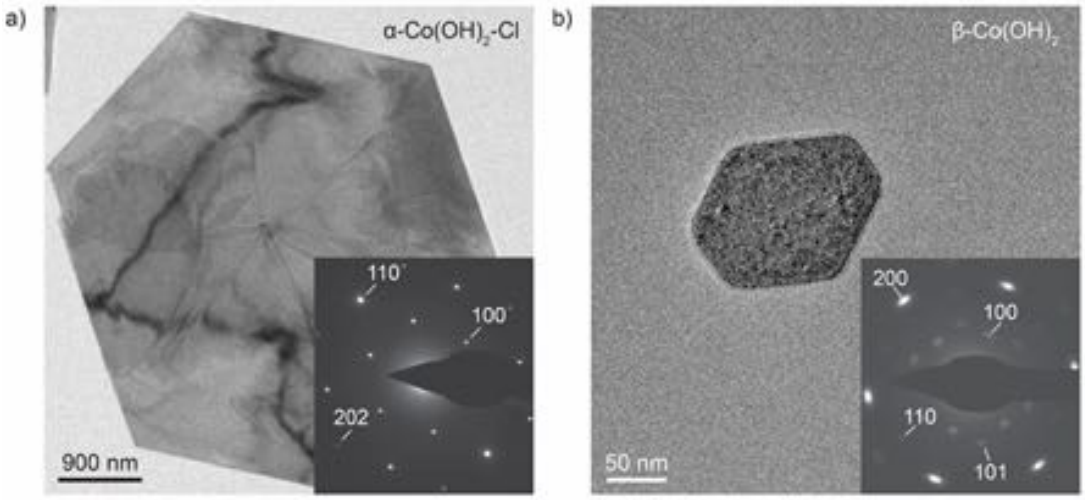

Figure 3.2. TEM images and SAED patterns of as-synthesized (**a**) α-$Co(OH)_2$-Cl and (**b**) β-$Co(OH)_2$.

Table 3.1. Powder XRD peak positions and calculated d-spacings for as-synthesized α-$Co(OH)_2$-Cl and β-$Co(OH)_2$.

Sample	*h k l*	2 θ (°)	d-spacing (Å)
β-$Co(OH)_2$	0 0 1	19.2	4.62
	1 0 0	32.5	2.75
	1 0 1	37.9	2.37
	1 0 2	51.4	1.78
	1 1 0	57.9	1.59
	1 1 1	61.7	1.50
	2 0 0	68.0	1.38
	1 0 3	69.7	1.35
	2 0 1	71.4	1.32
α-$Co(OH)_2$-Cl	0 0 3	11.1	7.95
	0 0 6	22.3	3.99
	1 0 1	33.1	2.70
	0 1 2	33.8	2.65
	0 1 5	38.0	2.37
	0 1 8	44.9	2.02
	0 0 $\underline{12}$	45.3	2.00
	1 0 $\underline{10}$	50.7	1.80
	0 1 $\underline{11}$	53.8	1.70
	1 1 0	58.7	1.57
	1 1 3	59.9	1.54

The diverging Co coordination geometries between α- and β-$Co(OH)_2$ give rise to different electronic absorption properties and their respective colors of green and pink. The diffuse reflectance UV-Vis of α-$Co(OH)_2$ reflects the mixed coordination geometry with two lower energy absorption peaks (626, 667 nm) stemming from tetrahedral Co sites and one higher energy absorption at 466 nm due to the octahedral sites (**Figure 3.3**).[37]

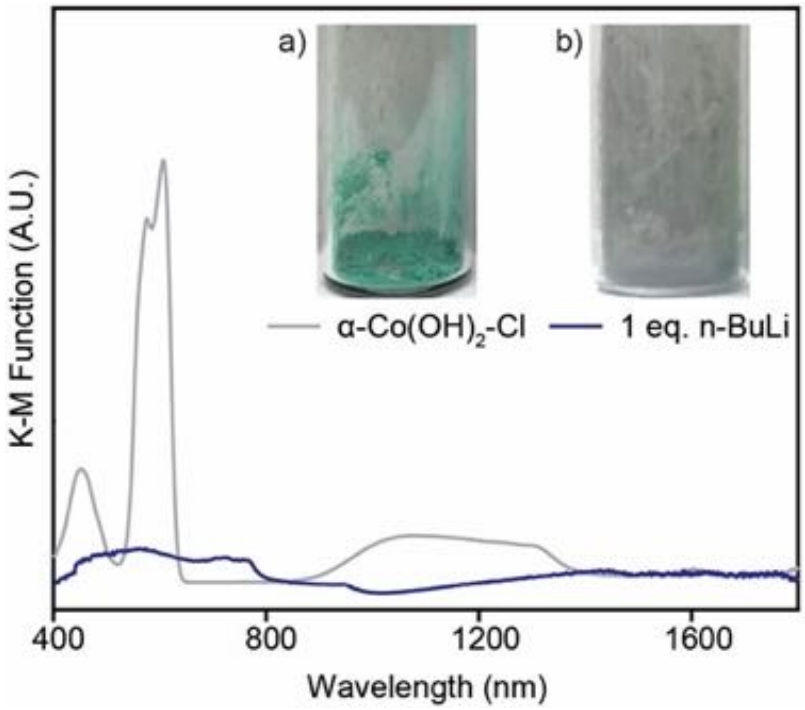

Figure 3.3. DRUV-Vis and photographs of (**a**) as-synthesized α-$Co(OH)_2$-Cl and (**b**) after treatment with 1 equiv. n-BuLi.

3.3.2 Conductivity

Using the method from our previous report, electron doping on α-$Co(OH)_2$-Cl was carried out with a chemical reductant, n-butyllithium (n-BuLi) by varying the amount of n-BuLi from 0.25 to 1.0 equiv. with respect to Co. The α-$Co(OH)_2$-Cl nanoplatelets turn from green to black upon n-BuLi treatment, indicating electron injection into the material (**Figure 3.3**). We then carried out two-point conductivity measurements on the electron-doped α-$Co(OH)_2$ and compared them to our previous measurements on β-$Co(OH)_2$ (**Figure 3.4**).

The as-synthesized α- and β-$Co(OH)_2$ are both completely insulating (10^{-13} S/cm for α, 10^{-11} S/cm for β). On β-$Co(OH)_2$, the increase in conductivity upon n-BuLi doping occurs non-linearly with a significant leap from 10^{-11} S/cm to 10^{-6} S/cm with the first 0.25 equiv. of n-BuLi and a slower increase up to the plateau value of 10^{-4} S/cm thereafter. Beyond 1.5 equiv. n-BuLi, the conductivity decays slightly back to 10^{-6} S/cm. Conversely, α-$Co(OH)_2$-Cl increases fairly linearly in conductivity as a function of the n-BuLi loading up to 1.0 equiv. and plateaus at an electrical conductivity of 10^{-6} S/cm even in the presence of large excesses of n-BuLi. The maximum conductivity on n-doped α-$Co(OH)_2$ (10^{-6} S/cm) is substantially lower than that attainable on β-

$Co(OH)_2$ (10^{-4} S/cm) despite its smaller bandgap. To understand the structural origins of these conductivity differences, we utilized a full suite of characterization strategies including X-ray absorption and photoelectron spectroscopies, electron microscopy, elemental analysis, and diffraction. As a note, the β-$Co(OH)_2$ material treated with 0.5 equiv. n-BuLi was characterized in detail in our previous work but is included here with the samples at other equivalents in order to elucidate the structural trends as a function of n-BuLi loading.

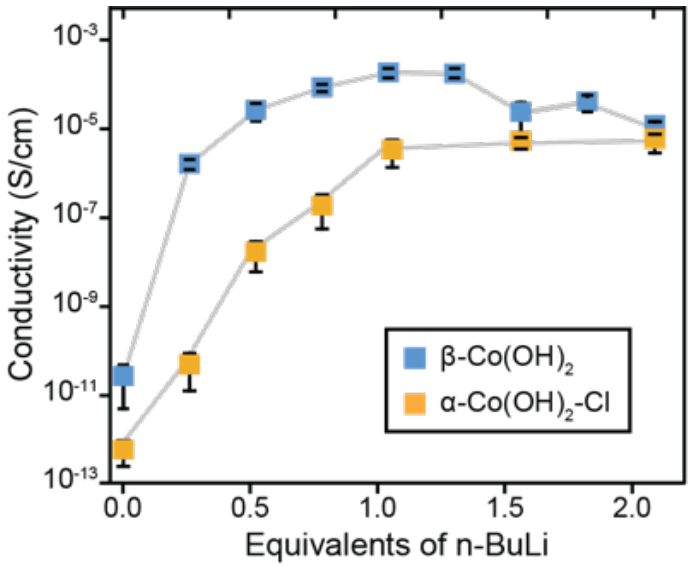

Figure 3.4. Two-point conductivity values as a function of n-BuLi loading for electron-doped β-$Co(OH)_2$ and α-$Co(OH)_2$-Cl.

3.3.3 Electronic Characterization

Co K-edge X-ray absorption near-edge spectroscopy (XANES) and X-ray photoelectron spectroscopy (XPS) are utilized to examine the average oxidation state of Co atoms after n-BuLi treatment. On β-$Co(OH)_2$, the XANES white line intensity remains essentially identical to the as-synthesized sample when treated with 0.25–0.75 equiv. of n-BuLi, indicating no change in Co^{2+} oxidation state during the n-BuLi treatment (**Figure 3.5a**). At 1 equiv. n-BuLi, a small drop in white line intensity is observed, likely due to a small amount of Co^{2+} reduction. In contrast, the white-line intensity of α-$Co(OH)_2$-Cl drops systematically with the addition of n-BuLi, indicating that n-BuLi electron injection is always accompanied by Co^{2+} reduction (**Figure 3.5b**). After treatment with 3 equiv. of n-BuLi, the XANES feature approaches the shape and intensity of a

metallic Co foil. These data clearly show that the α-$Co(OH)_2$ structure is more prone to metal-centered reduction than β-$Co(OH)_2$ during the n-doping process.

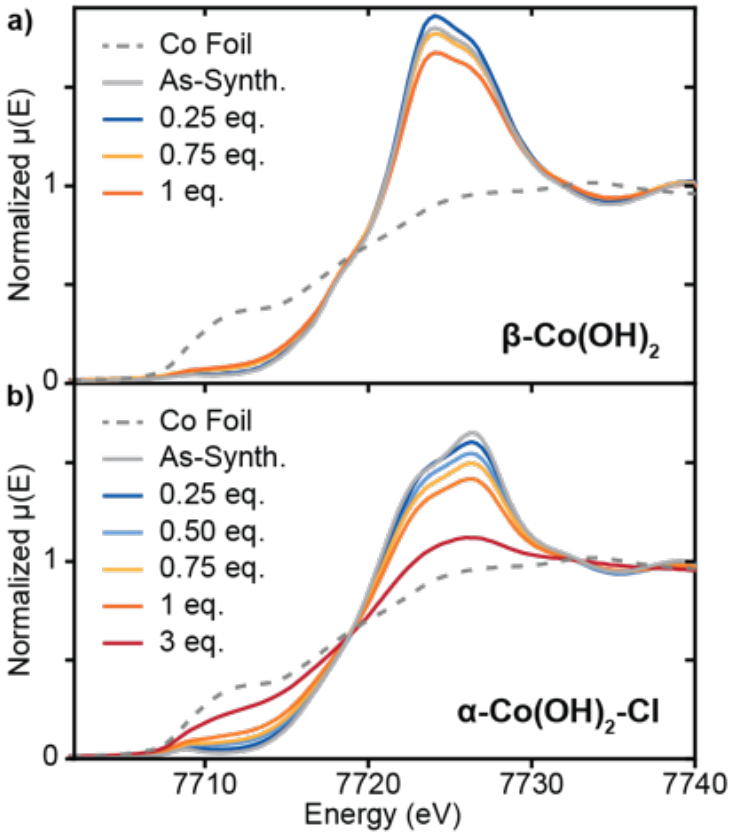

Figure 3.5. Co K-edge XANES spectra of (**a**) β-$Co(OH)_2$ and (**b**) α-$Co(OH)_2$-Cl at varying loadings of n-BuLi.

In order to quantify the reduced Co species observed in the XANES, we obtained XPS of the Co $2p_{3/2}$ region, which is highly sensitive to the oxidation state of Co.[38,39] As expected, the β-$Co(OH)_2$ sample shows no change in the XPS spectrum from the as-synthesized sample up to 0.75 equiv. of n-BuLi (**Figure 3.6a**). These spectra are dominated by a peak at 780 eV, which is the typical binding energy for the Co^{2+} oxidation state in $Co(OH)_2$. After the addition of 1 equiv. n-BuLi, the Co $2p_{3/2}$ peak exhibits a significant shoulder centered at 777 eV, representing 15% of total Co atoms that have been reduced to Co^0 (**Figure 3.6c, Table 3.2**). Interestingly, α-$Co(OH)_2$-Cl begins to show the Co^0 shoulder even at low loadings of n-BuLi (**Figure 3.6b**). From 0.25 equiv. to 1.0 equiv. of n-BuLi, the proportion of Co^0 atoms in the sample increases steadily from 3% to 13% (**Figure 3.6d**). These data are consistent with the XANES data presented above, clearly

showing that metal-centered reduction dominates on the α-$Co(OH)_2$-Cl at any concentration of injected electrons while β-$Co(OH)_2$ is capable of stabilizing the n-doped electrons through other mechanisms up until 1.0 equiv. of n-BuLi.

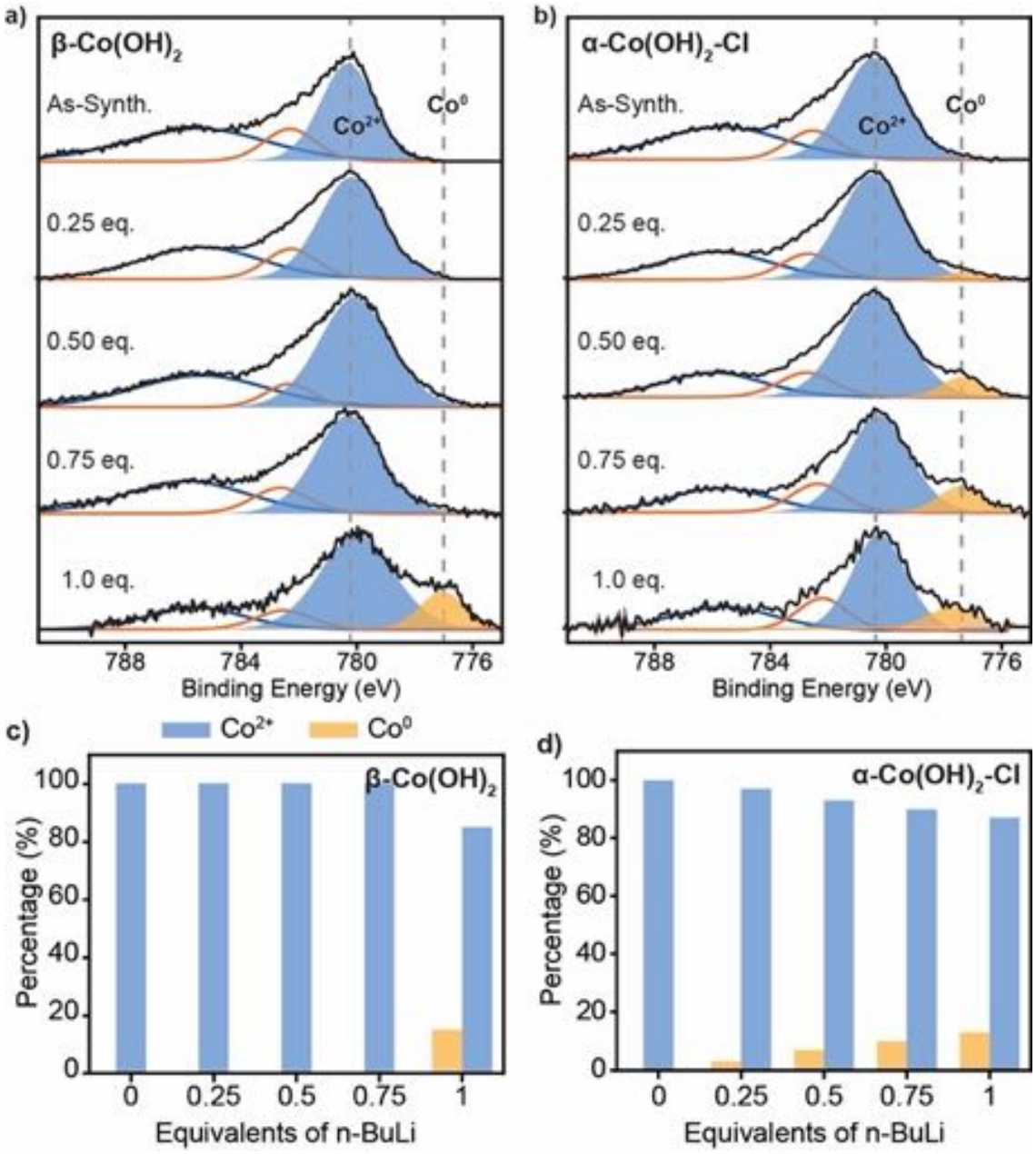

Figure 3.6. High resolution XPS data of the Co $2p_{3/2}$ region for (**a**) β-$Co(OH)_2$ and (**b**) α-$Co(OH)_2$-Cl at varying loadings of n-BuLi. (**c, d**) Quantification of relative Co^{2+} and Co^0 percentages as a function of n-BuLi loading.

Table 3.2. Analysis of the high-resolution XPS features in the Co $2p_{3/2}$ regions for n-BuLi treated α- and β-$Co(OH)_2$ samples.

Sample	**Co 2p**	
α-$Co(OH)_2$-Cl	**Co^0 ~777.5 eV**	**Co^{2+} ~780.3 eV**
As-Synthesized	0%	100%
0.25 equiv. n-BuLi	3%	97%
0.5 equiv. n-BuLi	7%	93%
0.75 equiv. n-BuLi	10%	90%
1 equiv. n-BuLi	13%	88%

Sample	**Co 2p**	
β-$Co(OH)_2$	**Co^0 ~777.2 eV**	**Co^{2+} ~ 780.2 eV**
As-Synthesized	0%	100%
0.25 equiv. n-BuLi	0%	100%
0.5 equiv. n-BuLi	0%	100%
0.75 equiv. n-BuLi	0%	100%
1 equiv. n-BuLi	15%	85%

3.3.4 Structural Characterization

In light of the differences in Co oxidation state in the α- and β-structures, we sought to understand how Co coordination geometry was impacted by electron-doping through Co K-edge X-ray absorption fine structure (EXAFS) data. We performed k^2-weighted fitting of the Fourier-transformed data to obtain the coordination number (CN) and bond distance (R) for all first and second shell scattering atoms (**Table 3.3, Table C.1, Figure C.7-C.8**). We denote the first and second coordination shells of $Co(OH)_2$ as Co–O (~2.08 Å) and Co–Co (~3.15 Å) and the first shell of metallic Co as $Co–Co^M$ (~2.51 Å). In our previous report on β-$Co(OH)_2$, we observed that the first-shell Co–O CN dropped from 6.1 to 4.7 after 0.5 equiv. n-BuLi treatment with no obvious crystal structure degradation, which suggested that hydroxide vacancies played a significant role in stabilizing n-doped electrons in the brucite crystal structure.

We have now obtained EXAFS data for β-$Co(OH)_2$ over the full range of n-BuLi loadings, which shows that the majority of the OH-vacancy formation occurs in the first 0.25 equiv. of n-

BuLi doping (**Figure 3.7a**). The Co–O CN drops from 6.1 in the as-synthesized sample to 5.1 after 0.25 equiv. n-BuLi, consistent with the large change in conductivity in the same n-BuLi loading regime (**Figure 3.8**). Beyond 0.5 equiv. n-BuLi, the Co–O CN stays relatively constant at ~4.7. At 1 equiv. n-BuLi, where the XANES and XPS show Co^{2+} reduction, we begin to observe a Co–Co^{M} scattering pathway in between the first and second shells of $Co(OH)_2$, which indicates a small amount of metallic nanoparticle formation. The observed plateau in Co–O CN at higher n-BuLi loading trends qualitatively with the plateau behavior in β-$Co(OH)_2$ conductivity, supporting the hypothesis that hydroxide vacancies are an essential defect toward n-type carrier generation.

On α-$Co(OH)_2$-Cl, the EXAFS data shows that the material has poor stability to anion vacancy formation and decomposes steadily to metallic Co nanoparticles during n-BuLi treatment (**Figure 3.7b**). In as-synthesized α-$Co(OH)_2$-Cl, the Co–O CN is 5.2 due to the combination of octahedral and tetrahedral sites in the structure (**Figure 3.7b**). Treatment with 0.25 equiv. n-BuLi results in a slight drop in Co–O CN from 5.2 to 4.8. As the n-BuLi concentration is further increased, the $Co(OH)_2$ scattering peaks continue to drop in intensity, but this drop is coupled to a significant growth in metallic Co–Co^{M} scattering. At 1.0 equiv. n-BuLi, the Co–O CN has dropped to 3.5 while the Co–Co^{M} CN has grown to 2.4.

These data indicate that α-$Co(OH)_2$-Cl after n-BuLi doping comprises a heterogeneous mixture of doped $Co(OH)_2$ nanosheets and decomposed Co^0 nanoparticles. While some hydroxide vacancies are likely present in the doped nanosheets, the heterogeneity of the sample makes it difficult to accurately quantify the number of vacancies using EXAFS coordination numbers. Based on these data, we postulate that the hydrozincite-like crystal structure supports a limited number of hydroxide vacancies before structural collapse to Co^0 nanoparticles begins to occur. This limited hydroxide vacancy concentration likely contributes to the lower average conductivities attainable by α-$Co(OH)_2$-Cl relative to the more stable β-$Co(OH)_2$.

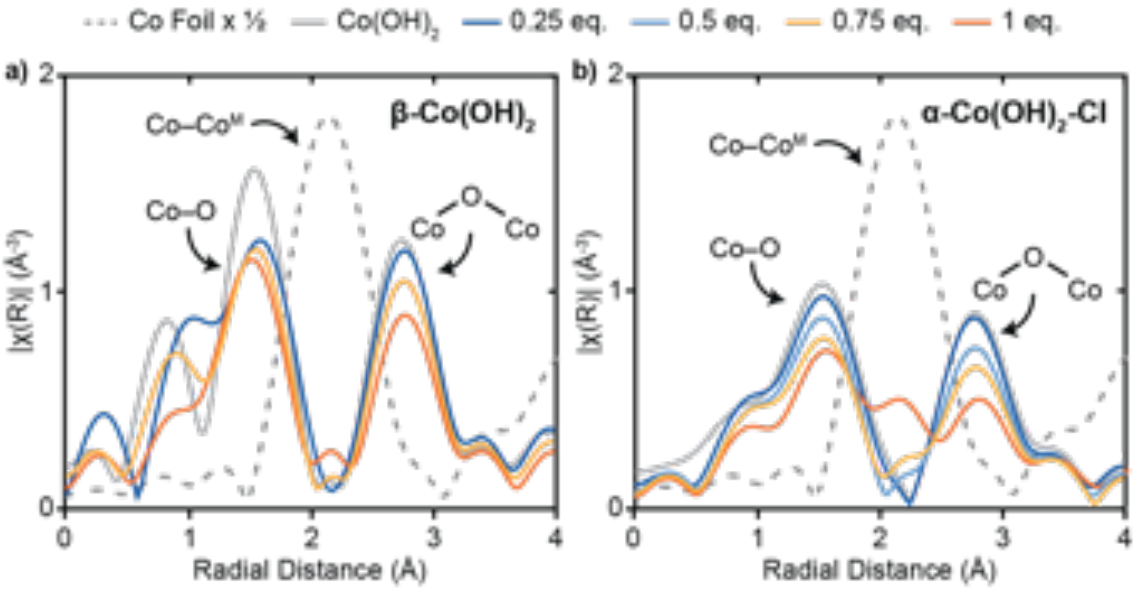

Figure 3.7. Co K-edge EXAFS spectra of (**a**) β-$Co(OH)_2$ and (**b**) α-$Co(OH)_2$-Cl at varying loadings of n-BuLi.

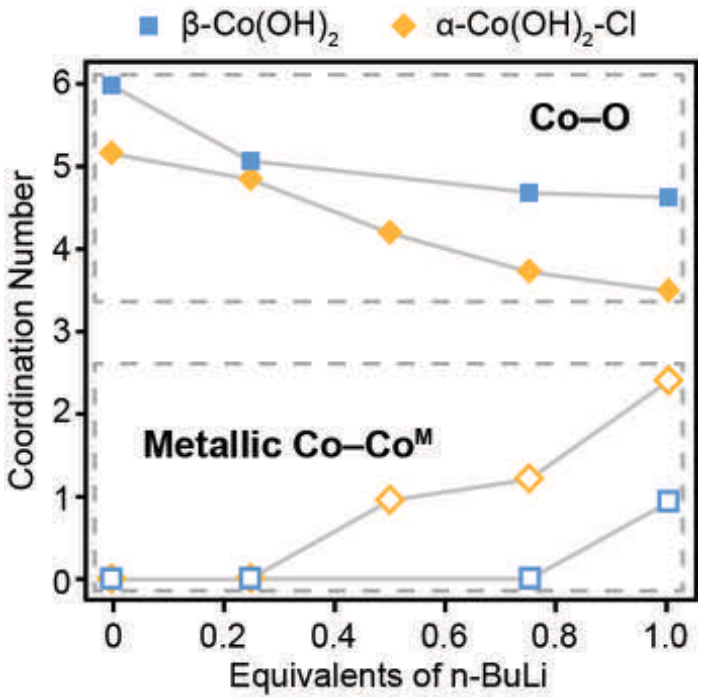

Figure 3.8. Coordination numbers for Co–O and metallic Co–Co^M in both samples as a function of n-BuLi loading.

Table 3.3. Co K-Edge EXAFS fitting parameters for β-$Co(OH)_2$ and α-$Co(OH)_2$-Cl at varying loadings of n-BuLi.

Sample	Edge Energy (eV)	Scattering Pair	CN[a]	R (Å)[a]	σ^2 (Å^2)	E^0 (eV)
Co Foil[b]	7708.8	Co–Co^M	12	2.50	0.008	---
β-$Co(OH)_2$ As-Synth.	7722.3	Co–O	6.1	2.09	0.005	–3.4
		Co–Co	5.7	3.16	0.005	–3.4
β-$Co(OH)_2$ 0.25 equiv. n-BuLi	7722.1	Co–O	5.1	2.11	0.005	–1.4
		Co–Co	5.4	3.18	0.005	–1.4
β-$Co(OH)_2$ 0.75 equiv. n-BuLi	7722.2	Co–O	4.7	2.09	0.005	–2.5
		Co–Co	4.6	3.16	0.005	–2.5
β-$Co(OH)_2$ 1 equiv. n-BuLi	7722.1	Co–O	4.7	2.08	0.005	–3.7
		Co–Co^M	1.0	2.51	0.005	–3.7
		Co–Co	4.2	3.15	0.005	–3.7
α-$Co(OH)_2$ As-Synth.	7722.8	Co–O	5.2	2.08	0.009	–2.0
		Co–Co	5.6	3.14	0.009	–2.0
α-$Co(OH)_2$ 0.25 equiv. n-BuLi	7721.1	Co–O	4.8	2.08	0.009	–2.1
		Co–Co	5.6	3.15	0.009	–2.1
α-$Co(OH)_2$ 0.5 equiv. n-BuLi	7721.2	Co–O	4.2	2.08	0.009	–1.7
		Co–Co^M	1.0	2.52	0.009	–1.7
		Co–Co	4.9	3.15	0.009	–1.7
α-$Co(OH)_2$ 0.75 equiv. n-BuLi	7721.1	Co–O	3.8	2.08	0.009	–1.5
		Co–Co^M	1.2	2.52	0.009	–1.5
		Co–Co	4.3	3.15	0.009	–1.5
α-$Co(OH)_2$ 1 equiv. n-BuLi	7721.5	Co–O	3.5	2.07	0.009	–2.7
		Co–Co^M	2.4	2.50	0.009	–2.7
		Co–Co	3.5	3.15	0.009	–2.7

[a]*Error bars for EXAFS fitting data provided in Table S3.* [b]*Reference sample used to obtain amplitude reduction factor.*

On both polymorphs, EXAFS characterization of samples treated with >1 equiv. n-BuLi provides clear evidence that Co^0 species do not contribute significantly to sample conductivity. After treatment with 1.5 equiv n-BuLi on β-$Co(OH)_2$ or 3 equiv. n-BuLi on α-$Co(OH)_2$-Cl, the EXAFS spectra are dominated by metallic Co–Co^M scattering (**Figure 3.9, Table C.1**). These samples, however, show lower conductivities relative to their counterparts treated with 1.0 equiv. n-BuLi, suggesting that the decomposed Co^0 nanoparticles embedded in $Co(OH)_2$ nanosheets are not responsible for the measured conductivity.

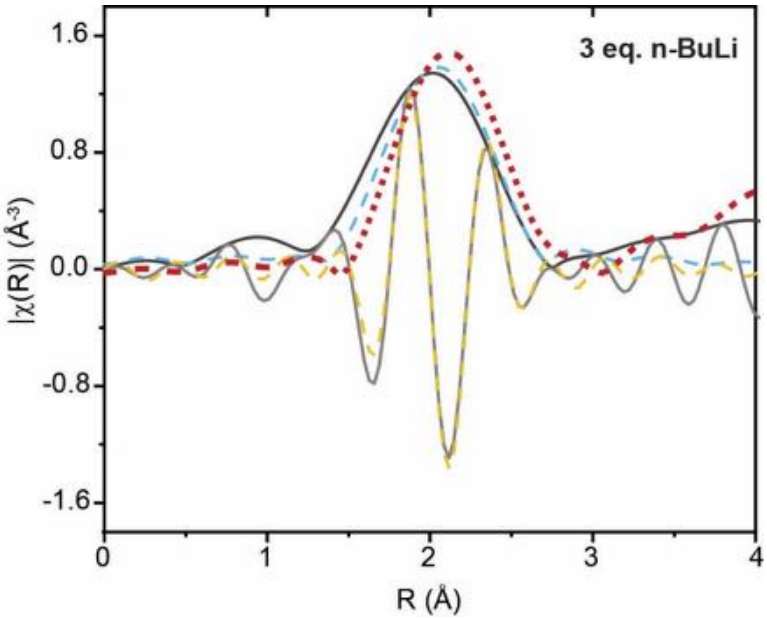

Figure 3.9. Co K-edge EXAFS fitting data for α-$Co(OH)_2$-Cl treated with 3 equivalents of n-BuLi. The black solid line is the FT magnitude, the dotted blue line is the fit to the FT magnitude, the solid gray line is the FT real part, and the dotted yellow line is the fit to the FT real part. Co foil is shown in the dashed red line as a comparison.

The decomposition of the α-$Co(OH)_2$-Cl structure observed by EXAFS is corroborated by transmission electron microscopy (TEM), selected area electron diffraction (SAED), and powder X-ray diffraction (XRD). TEM images of n-BuLi treated samples show that while some 1-5 μm hexagonal nanoplatelets remain in the sample, decomposition to smaller disordered sheets is also observed (**Figure 3.10**).

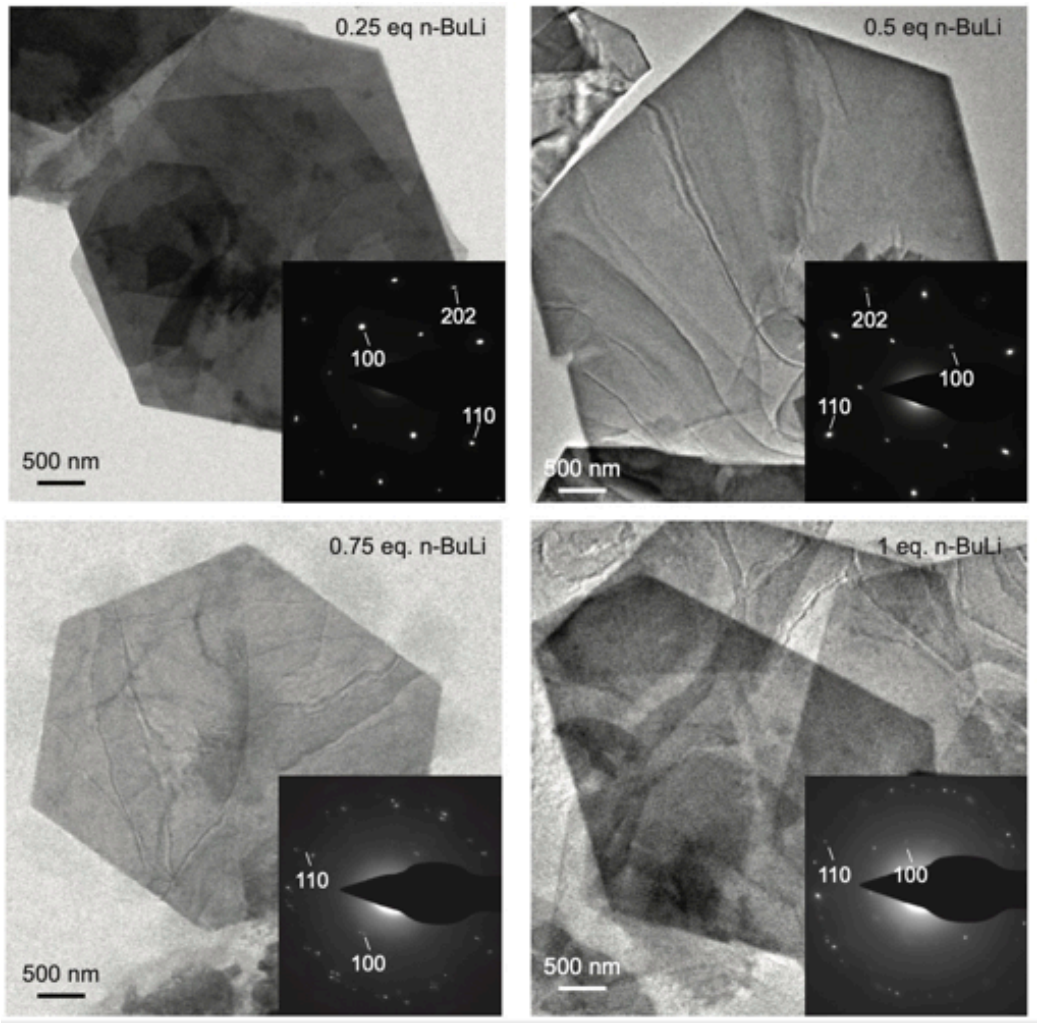

Figure 3.10. TEM images and SAED patterns of α-$Co(OH)_2$-Cl treated with varying equivalents of n-BuLi.

More tellingly, the crystallinity of the hydrozincite-like structure decays steadily with increasing n-BuLi as assessed by the intensity of SAED diffraction spots and powder XRD peaks, consistent with crystal structure collapse as Co^0 species are formed (**Figure 3.10, 3.12**). After treatment with 3 equiv. n-BuLi, broad features associated with small, crystalline Co^0 nanoparticles are observed (**Figure 3.12, C.9**). The brucite β-$Co(OH)_2$ hexagonal nanoplatelets in comparison show excellent retention of crystal structure and morphology up to 1 equiv. n-BuLi (**Figure 3.11, 3.13**).

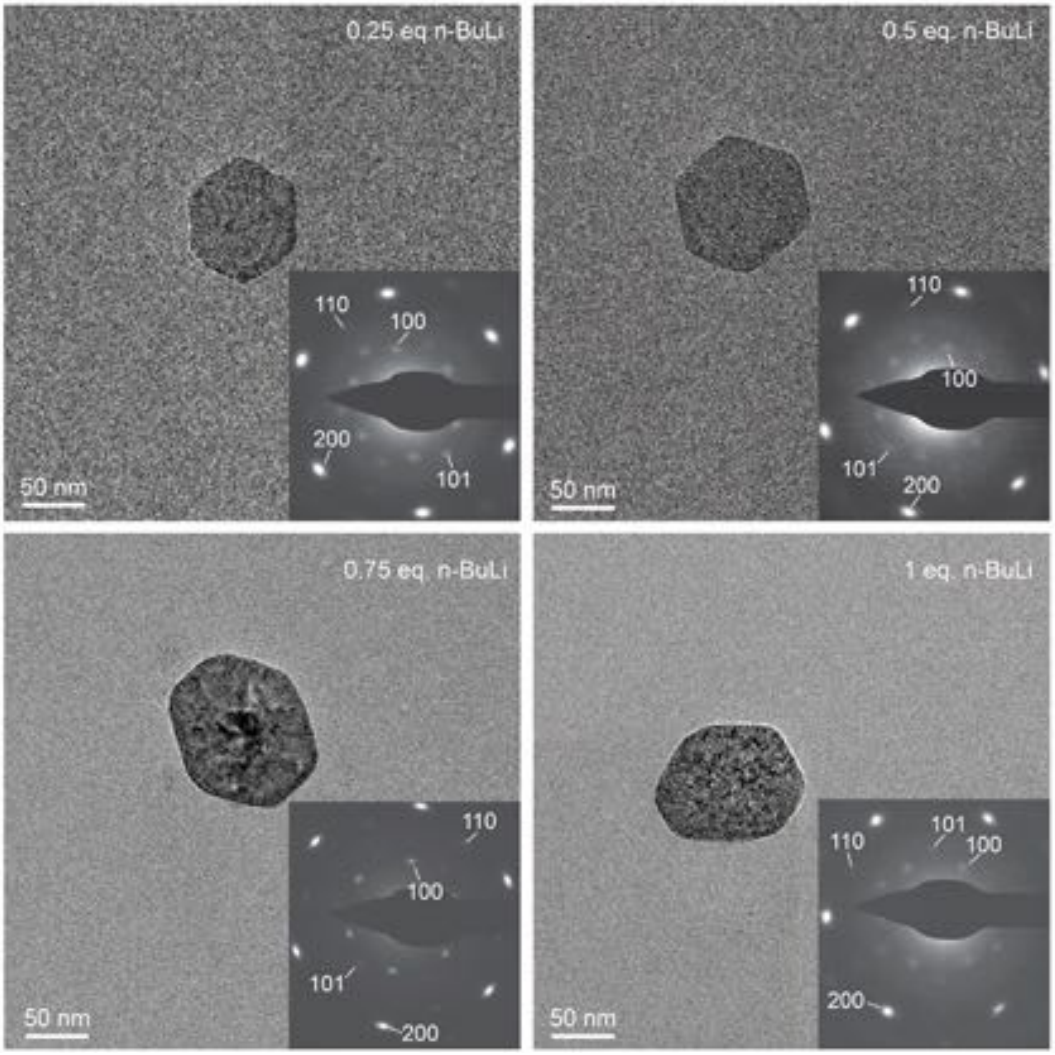

Figure 3.11. TEM images and SAED patterns of β-$Co(OH)_2$ treated with varying equivalents of n-BuLi.

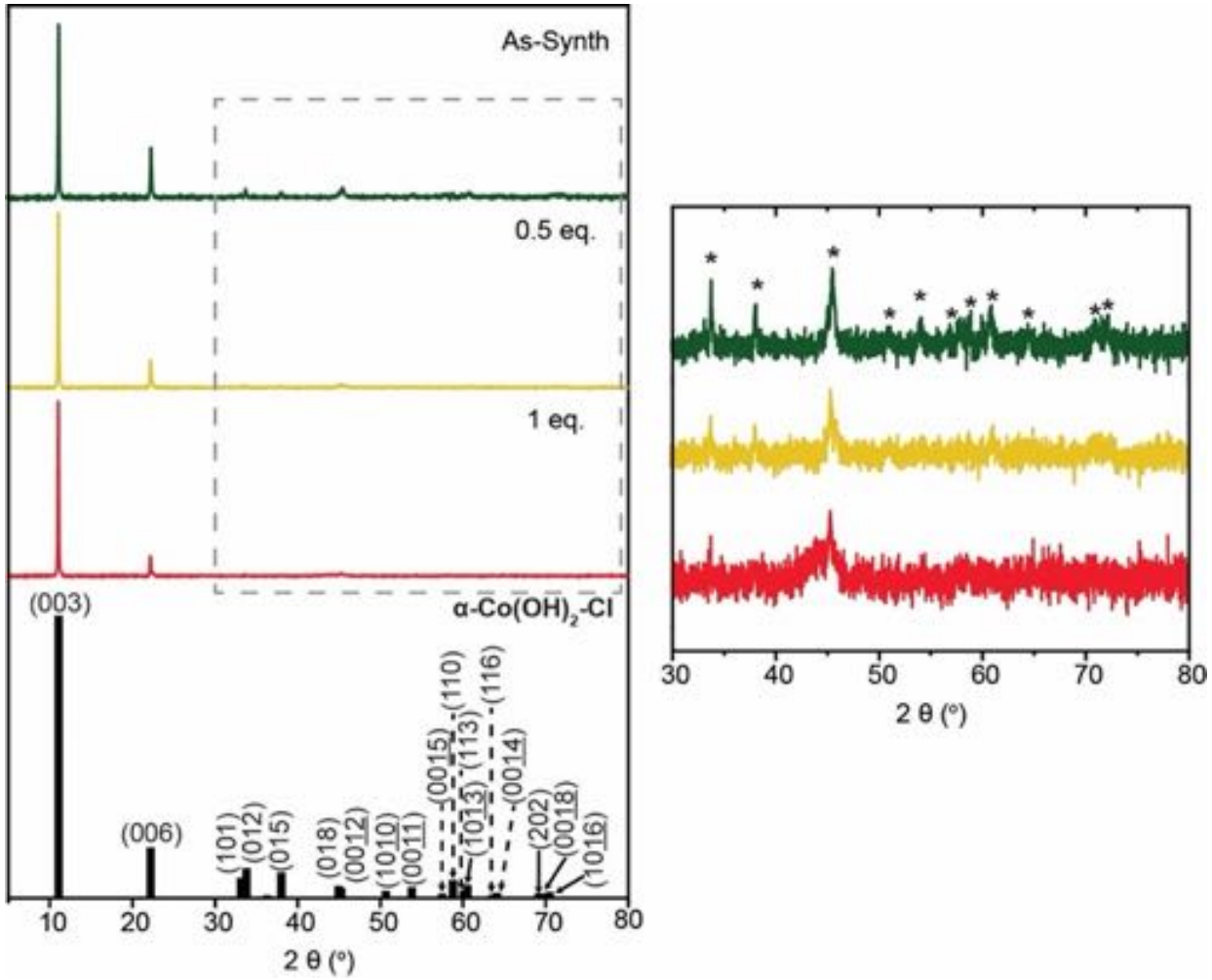

Figure 3.12. XRD characterization of α-$Co(OH)_2$-Cl treated with varying equivalents of n-BuLi and reference pattern for α-$Co(OH)_2$-Cl (JCPDS card No. 00-046-0605).

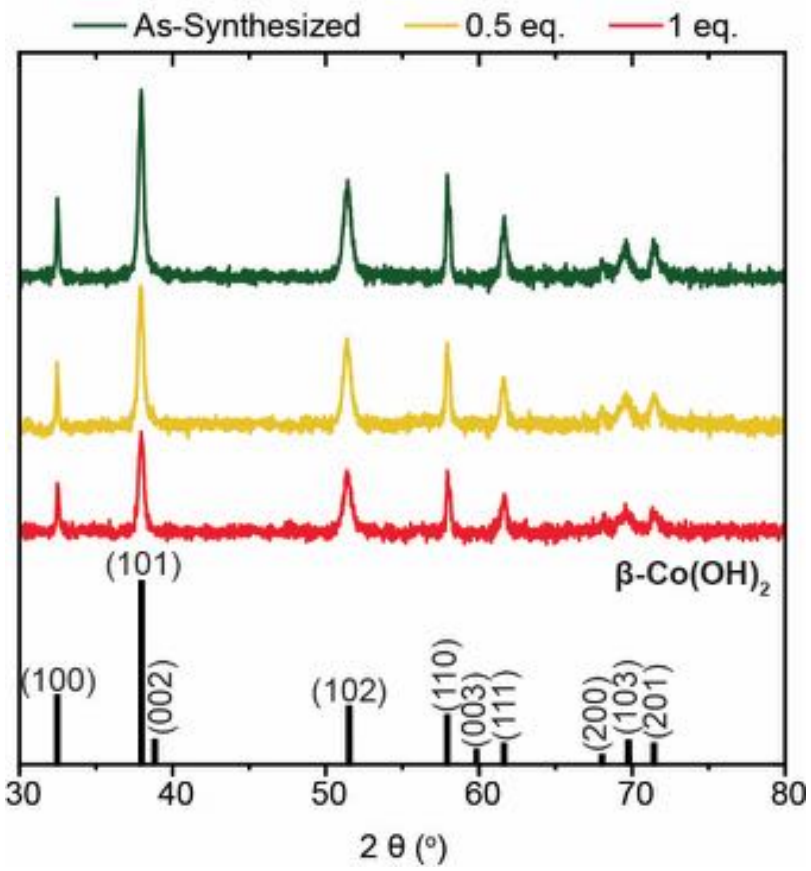

Figure 3.13. XRD characterization of β-$Co(OH)_2$ treated with varying equivalents of n-BuLi and reference pattern for β-$Co(OH)_2$ (JCPDS card No. 00-030-0443).

The poor structural stability of α-$Co(OH)_2$-Cl may be due in part to the loss of intercalated Cl^- ions during the n-BuLi doping process. When the nanoplatelets are rinsed with THF after n-BuLi treatment, a significant drop in Cl^- ion concentration is observed from 26 at% in the as-synthesized sample to 12 at% at 1 equiv. n-BuLi (**Figure 3.14**).

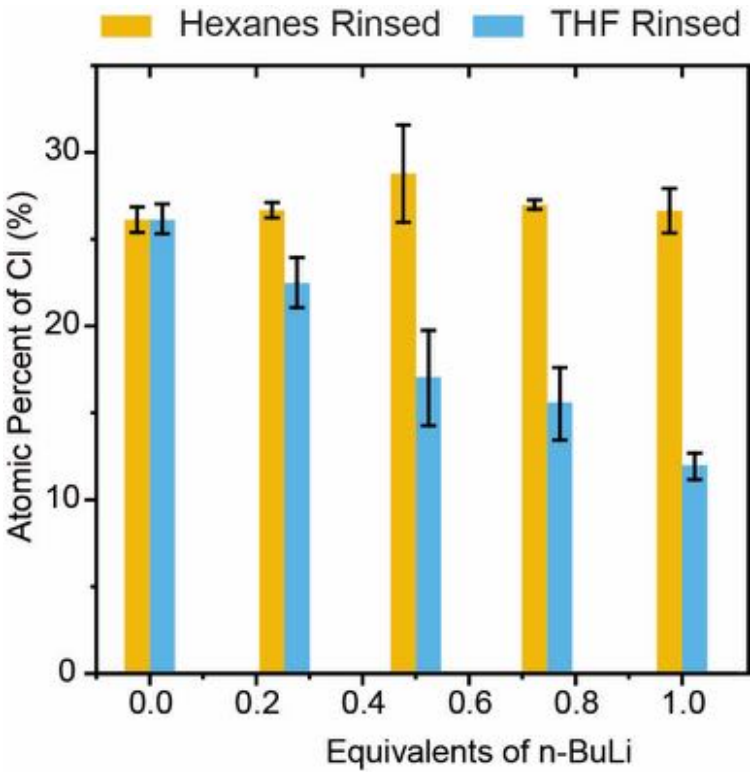

Figure 3.14. Atomic percent Cl relative to Co (assuming Co = 100%) obtained by TEM-EDS for α-$Co(OH)_2$-Cl treated with varying equivalents of n-BuLi and rinsed with either hexanes or THF prior to analysis.

We hypothesize that deintercalation of Cl^- ions serves as an alternative to OH-vacancy formation in the hydrozincite-like structure to compensate n-doped electrons, and the tetrahedral Co atoms coordinated to interlayer Cl^- may be preferentially reduced due to their greater exposure to the reaction medium. Loss of interlayer anions coupled to the metal-centered reduction process results in rapid collapse of the α-$Co(OH)_2$ structure with increasing n-BuLi concentration.

Together, these data suggest that stable anion vacancy defects are essential toward generating mobile n-type carriers in layered cobalt hydroxide materials during n-BuLi electron doping. In the β-$Co(OH)_2$ series, we observe a direct correlation between sample conductivity and hydroxide vacancy content based on the drop in Co-O coordination number in the EXAFS fitting. The brucite structure remains stable in the presence of hydroxide vacancies until 1.0 equiv. n-BuLi with respect to Co, which results in large carrier concentrations and high sample conductivities. While the α-$Co(OH)_2$ sample forms anion vacancies in an equally facile manner, the defective α-structure begins to decompose to Co^0 nanoparticles even at low vacancy concentrations. Because

Co^0 species are a trap state that do not contribute to conductivity, α-$Co(OH)_2$-Cl exhibits significantly lower conductivity values across the entire n-BuLi doping series.

To determine whether the instability of α-$Co(OH)_2$-Cl is applicable in general to the α polymorph, we also performed the n-BuLi electron doping on an α-$Co(OH)_2$ sample intercalated with sodium dodecyl sulfate (α-$Co(OH)_2$-SDS). The α-$Co(OH)_2$-SDS sample is prepared based on literature methods and has a significantly wider interlayer spacing than α-$Co(OH)_2$-Cl at 28.48 Å (**Figure 3.15, 3.16, Table 3.4**).[40] The conductivity of α-$Co(OH)_2$-SDS increases linearly from 10^{-12} to 10^{-6} S/cm with increasing n-BuLi in a similar fashion to α-$Co(OH)_2$-Cl (**Figure 3.17**).

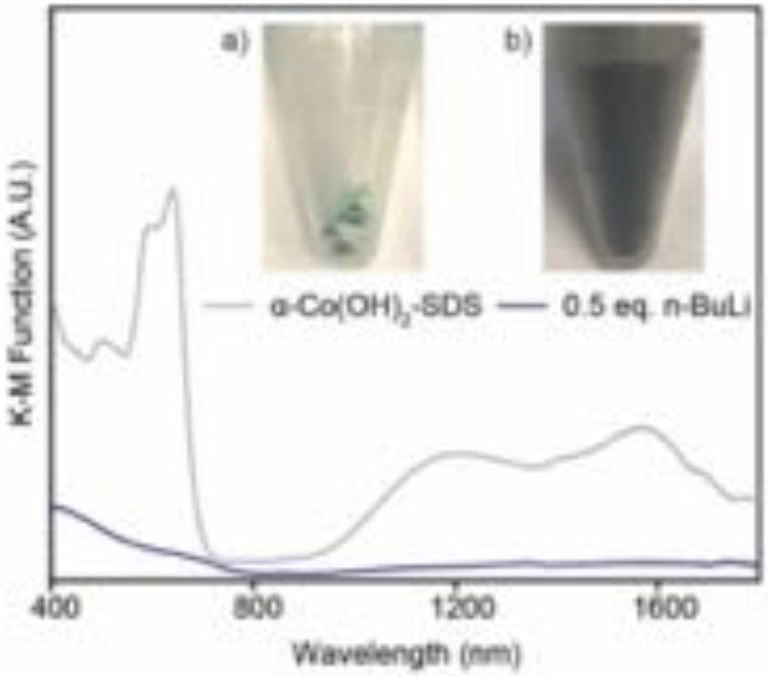

Figure 3.15. DRUV-Vis and photographs of (**a**) as-synthesized α-$Co(OH)_2$ SDS and (**b**) after treatment with 1 equiv. n-BuLi.

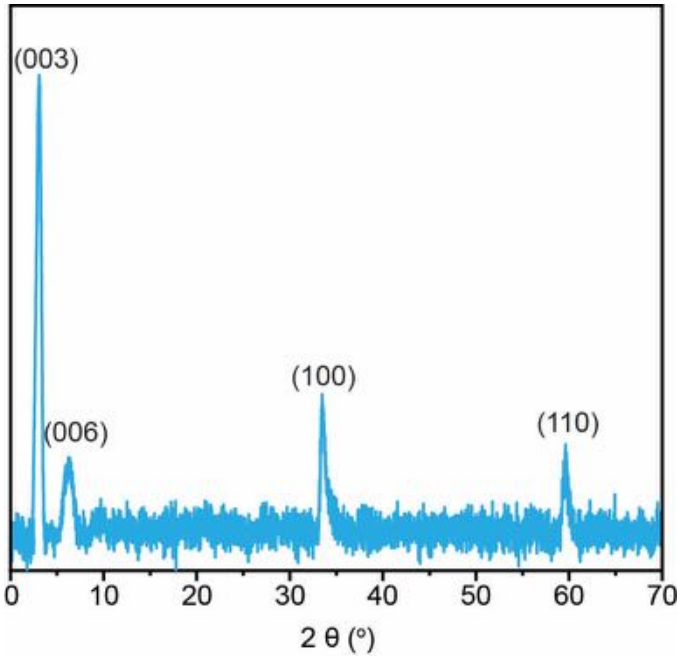

Figure 3.16. XRD characterization of α-$Co(OH)_2$-SDS.

Table 3.4. Powder XRD peak positions and calculated d-spacings for α-$Co(OH)_2$-SDS.

Sample	*h k l*	2 θ (°)	d-spacing (Å)
α-$Co(OH)_2$-SDS	0 0 3	3.1	28.48
	0 0 6	6.2	14.20
	1 0 0	33.5	2.67
	1 1 0	59.6	1.55

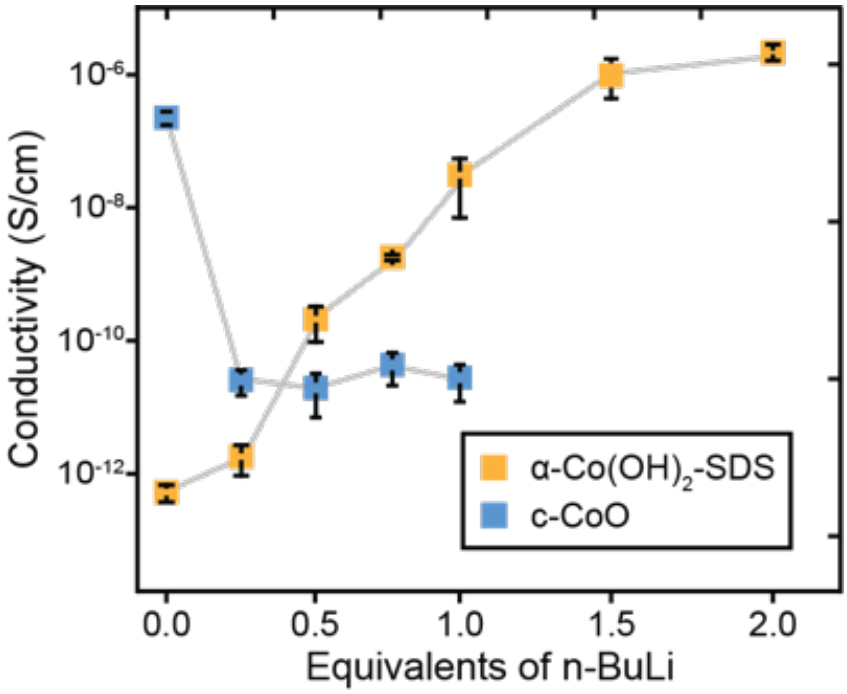

Figure 3.17. Two-point conductivity values as a function of n-BuLi loading for electron-doped α-$Co(OH)_2$-SDS and c-CoO.

By TEM and SAED, we observe a similar loss in crystallinity and formation of Co^0 nanoparticles during n-BuLi doping (**Figure C.13, C.14**). The quantity of Co^0 based on the Co $2p_{3/2}$ region of the XPS is also quite comparable with 4% Co^0 at 0.5 equiv. and a linear increase up to 9% at 1 equiv. n-BuLi (**Figure 3.18a, Table 3.5**). Surprisingly, the Co^0 species can be removed if the sample is rinsed with THF after n-BuLi treatment, likely due to improved solvent penetration into the wider interlayer galleries (**Figure 3.18b**). In the rinsed samples, the conductivity values and trends are identical to α-$Co(OH)_2$-SDS samples that were not washed with THF, further supporting the conclusion that Co^0 species do not contribute to n-type conductivity (**Figure 3.19**). In addition, XPS of the S 2p region show a reduced sulfur feature at 166 eV, indicating that n-BuLi partially reduces the SDS anion in addition to the cobalt hydroxide layer (**Figure 3.20, 3.21, C.15**).[41] This side reaction likely contributes to the lower conductivity of α-$Co(OH)_2$-SDS relative to α-$Co(OH)_2$-Cl as a function of n-BuLi loading. Based on these data, we conclude that the hydrozincite-like crystal structure is poorly positioned to stabilize hydroxide vacancies regardless of the intercalated anion, and n-type conductivity in α-$Co(OH)_2$ is inherently limited due to structural degradation of the 2D sheets to metallic Co nanoclusters.

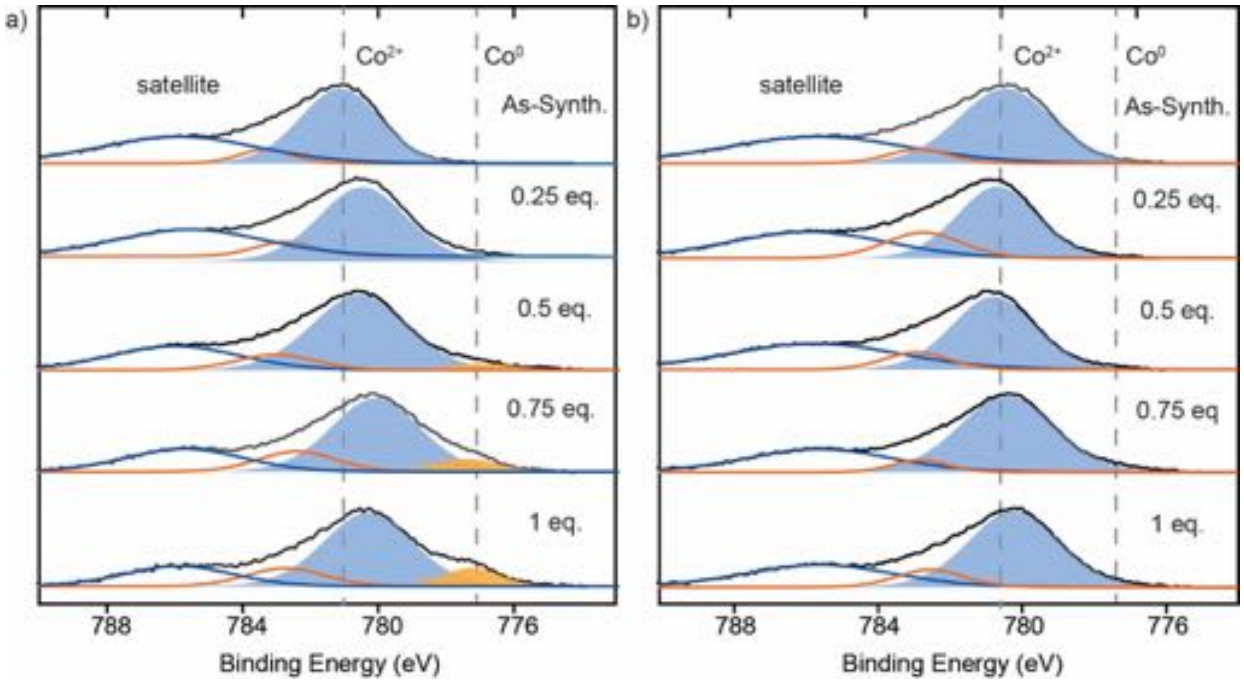

Figure 3.18. High resolution XPS for the Co $2p_{3/2}$ region of α-$Co(OH)_2$-SDS treated with varying equivalents of n-BuLi and rinsed with (**a**) hexanes and (**b**) THF.

Table 3.5. Analysis of the high-resolution XPS features in the Co 2p regions for n-BuLi treated α-$Co(OH)_2$-SDS samples (rinsed with hexanes).

Sample	**Co 2p**	
α-$Co(OH)_2$-SDS	**Co^0 ~ 777.1 eV**	**Co^{2+} ~780.5 eV**
As-Synthesized	0%	100%
0.25 equiv. n-BuLi	0%	100%
0.50 equiv. n-BuLi	4%	96%
0.75 equiv. n-BuLi	7%	93%
1.0 equiv. n-BuLi	9%	91%

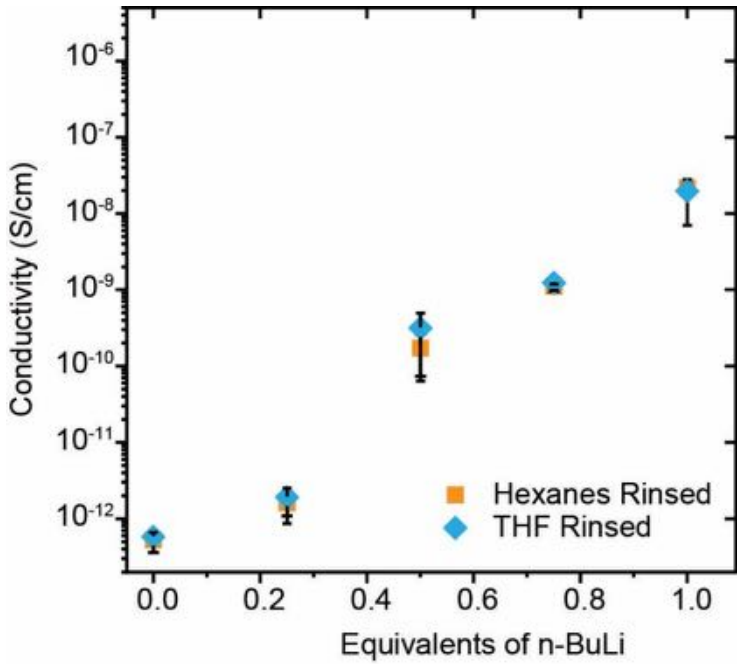

Figure 3.19. Conductivity of α-$Co(OH)_2$-SDS treated with varying equivalents of n-BuLi after rinsing with either hexanes or THF.

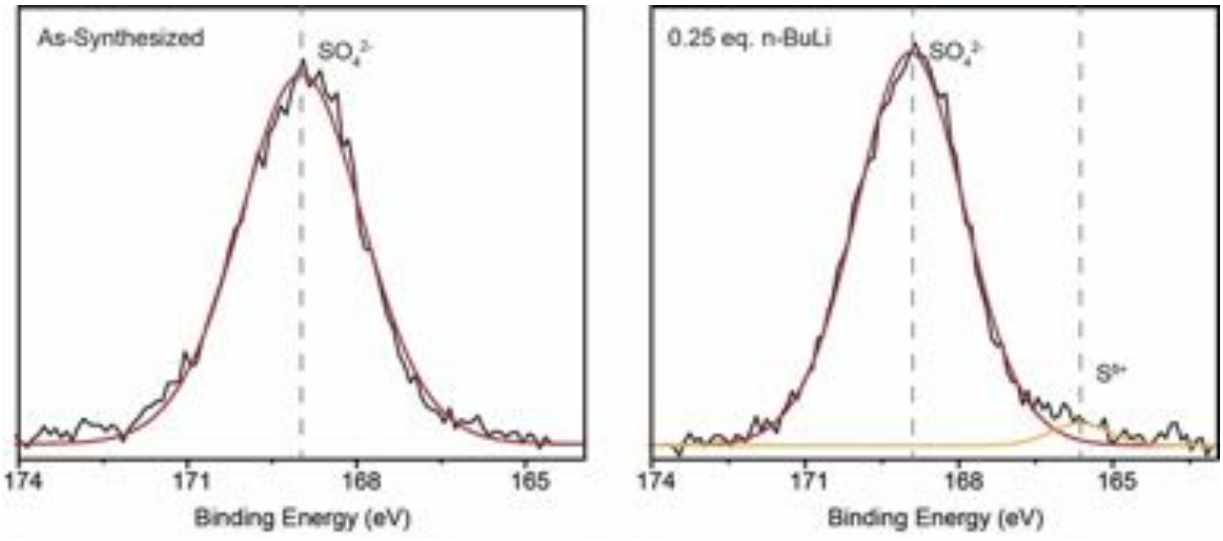

Figure 3.20. High resolution XPS for the S 2p region of α-$Co(OH)_2$-SDS treated 0.25 equivalents of n-BuLi.

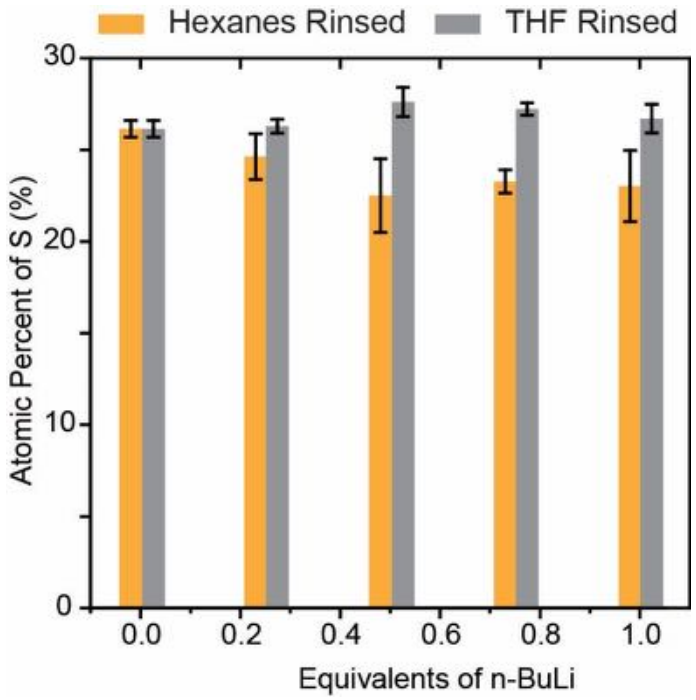

Figure 3.21. Atomic percent S relative to Co (assuming Co = 100%) obtained by TEM-EDS for α-$Co(OH)_2$-SDS treated with varying equivalents of n-BuLi and rinsed with either hexanes or THF prior to analysis.

Finally, we prepared a rock-salt cobalt oxide material as a comparison to our α- and β-$Co(OH)_2$ samples to ascertain whether the 2D layered structures show more stable oxygen vacancy defects compared to a cubic crystalline material.[42] Cubic cobalt oxide (c-CoO) is a well-known p-type semiconductor in which the intrinsic form, with formula $Co_{1-x}O$, encompasses a small quantity of cobalt vacancies (V_{Co}) that act as hole defects.[15,43-45] Cobalt(III) acetylacetonate was thermally decomposed in benzylamine to generate ~50 nm quasi-nanocubes of c-CoO, which indeed show p-type conductivity of 10^{-7} S/cm (**Figure 3.17, Figure C.16**). Upon n-BuLi treatment from 0.25-1.0 equiv., the conductivity of c-CoO decreases to 10^{-11} S/cm and remains completely insulating even at high n-BuLi loadings. These data show that the electrons injected by n-BuLi are capable of compensating the p-type carriers in the intrinsic material but are incapable of generating new O-vacancies to create n-type carriers.

The Co $2p_{3/2}$ XPS data show only the primary Co^{2+} peak centered at 780 eV, which remain unchanged after all n-BuLi treatments (**Figure C.19**). Powder XRD patterns also exhibit the crystalline peaks of cubic CoO at all loadings of n-BuLi with no changes in peak intensity (**Figure 3.20b**). A small upward shift in peak position is indicative of a lattice contraction, which has

previously been observed in the literature when p-type $Co_{1-x}O$ is quenched by lithium radicals to form $Li_xCo_{1-x}O$.[46,47] Our inability to generate an n-type form of CoO using n-BuLi electron doping is consistent with theoretical calculations from the literature, which show an extremely high formation energy for the necessary oxygen vacancy defects in c-CoO.[48,49]

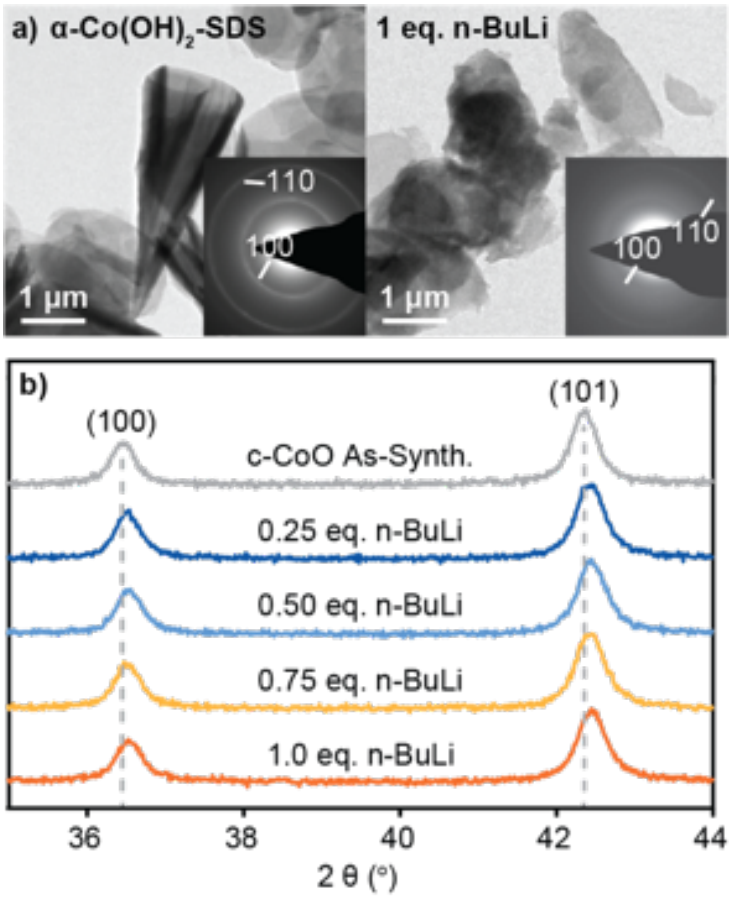

Figure 3.22. (**a**) TEM images of α-$Co(OH)_2$-SDS before and after 1 equiv. n-BuLi treatment. (**b**) Powder XRD patterns of c-CoO at varying n-BuLi loadings.

3.4 Conclusion

In conclusion, we show that both the α and β polymorphs of layered cobalt hydroxide structures can be electron-doped using n-BuLi as a strong electron donor. The conductivity of doped samples is strongly correlated to the ability of the layered crystal structure to stabilize hydroxide vacancies without decomposing to Co^0 nanoparticles (**Figure 3.1**). In the brucite β-$Co(OH)_2$ structure, the octahedral Co coordination and tight interlayer spacing lends itself to stable hydroxide vacancy formation and is thus able to support n-type conductivities up to 10^{-4} S/cm. In

contrast, the hydrozincite-like α-$Co(OH)_2$ intercalated with either Cl or SDS anions begins to form unproductive Co^0 defects even at low loadings of n-BuLi and as a result, achieves a maximum conductivity of 10^{-6} S/cm, two orders of magnitude lower than the brucite structure. In both cases, the formation energy for hydroxide vacancy defects in the layered structure is substantially lower than that of oxide vacancy defects in the cubic cobalt oxide crystal structure. The three-dimensional rock salt CoO is completely incapable of forming the requisite O-vacancies to achieve n-type doping even in the presence of large excesses of n-BuLi. Based on this work, it is clear that moving from an anhydrous 3D oxide structure to its corresponding 2D layered metal hydroxide dramatically changes the energy landscape for carrier defect formation and may serve as a general strategy to achieve ambipolar doping of TMOs.

3.5 Materials

Cobalt(II) nitrate hexahydrate (99%) and n-butyllithium in hexanes (1.6 M, 98%) were purchased from Acros Organics. Sodium hydroxide (97%), sodium chloride (≥99%), cobalt(III) acetylacetonate (98%), benzylamine (≥99%), and sodium dodecyl sulfate (+99%) were purchased from Sigma Aldrich. Anhydrous tetrahydrofuran (99.8%), cobalt(II) chloride hexahydrate (98%), and hexamethylenetetramine (+99%) were purchased from Alfa Aesar. Potassium hydroxide (≥85.0%), ethanol (99.5%), and hexanes (≥98.5%) were purchased from Fisher Scientific. Solvents were degassed and stored over activated 3 Å molecular sieves before use. All other chemicals were used without further purification. Nanopure water (ASTM Type I, 18.2 MΩ) was purified using a Thermo Scientific Barnstead Ultrapure Water System.

3.6 Synthetic Methods

3.6.1 Synthesis of α-$Co(OH)_2$-Cl

The synthesis of α-$Co(OH)_2$-Cl nanoplatelets is based on a literature procedure.[1] Cobalt(II) chloride hexahydrate (476 mg, 2 mmol), sodium chloride (584 mg, 10 mmol) and hexamethylenetetramine (1.682 g, 12 mmol) were dissolved in 200 mL of Nanopure water and degassed for 30 min. The resulting solution was heated to 90 °C and aged for 1 hr, during which the reaction medium changed from pink to blue-green. After cooling to room temperature, the

blue-green suspension was collected and centrifuged at 8500 rpm for 10 min. The supernatant was decanted and the remaining solid was rinsed thrice using 40 mL of H_2O and EtOH (1:1). After decanting the solvent, the blue-green solid was dried under vacuum for 18 hrs.

3.6.2 Synthesis of α-$Co(OH)_2$-SDS

The synthesis of α-$Co(OH)_2$-SDS nanoplatelets is based on a literature procedure with modifications.[2] Cobalt(II) nitrate hexahydrate (582 mg, 4 mmol), sodium dodecyl sulfate (5.767 g, 20 mmol) and hexamethylenetetramine (3.365 g, 24 mmol) were dissolved in 400 mL of Nanopure water and degassed for 30 min. The solution was heated to 70 °C and aged for 3 hrs. After cooling to room temperature, the suspension was centrifuged and the supernatant was decanted. The remaining solid was rinsed thrice using 40 mL of H_2O and EtOH (1:1). After decanting the solvent, the blue-green solid was dried under vacuum for 18 hrs.

3.6.3 Synthesis of c-CoO

The synthesis of cubic CoO nanoparticles is based on a literature procedure.[4] A green suspension of cobalt(III) acetylacetonate (0.400 g, 1.12 mmol) in benzylamine (6.14 mL, 56.1 mmol) was degassed for 30 min. Next, the suspension was heated to 120 °C and aged for 12 hrs, during which the solution changed from green to brown. The suspension was quickly heated to 175 °C and aged for an additional 2 hrs. After cooling to room temperature, the dark brown suspension was centrifuged at 8500 rpm and the supernatant was decanted. The solid was rinsed twice with 30 mL of EtOH. After decanting the solvent, the dark-brown solid was dried under vacuum for 18 hours.

3.6.4 Electron doping of $Co(OH)_2$ and CoO with n-BuLi

A representative procedure for 0.5 equiv. n-BuLi doping of $Co(OH)_2$ is provided. To a suspension of $Co(OH)_2$ (0.54 mmol) in hexanes (27 mL), 168 µL of n-BuLi (0.01 M in hexanes, 0.5 equiv. wrt to $Co(OH)_2$) was added and stirred at room temperature for 3 hrs. The final concentration of n-BuLi in hexanes should be kept at ≤0.01 M to avoid material decomposition. An immediate color change in the suspension is observed from blue-green (α-$Co(OH)_2$) or pink

(β-$Co(OH)_2$) to black (**Figure C.3, C.15**). The reaction medium was centrifuged and the supernatant was decanted. The resulting solid was rinsed once with 5 mL of hexanes and dried under vacuum prior to conductivity measurements and/or further characterization. In α-$Co(OH)_2$, when removal of de-intercalated or decomposed species was desired after n-BuLi doping, samples were instead rinsed with THF (**Figure 3.14, 3.18, 3.21**). The cleaning solvent had no impact on sample conductivity (**Figure 3.19, C.10**).

3.7 References

(1) Minami, T., *Semicond. Sci. Technol.,* **2005**, *20*, S35.

(2) Fortunato, E.; Ginley, D.; Hosono, H.; Paine, D. C., *MRS Bull.,* **2007**, *32*, 242-247.

(3) Ginley, D. S.; Bright, C., *MRS Bull.,* **2000**, *25*, 15-18.

(4) You, J.; Chen, C. C.; Dou, L.; Murase, S.; Duan, H. S.; Hawks, S. A.; Xu, T.; Son, H. J.; Yu, L.; Li, G., *Adv. Mater.,* **2012**, *24*, 5267-5272.

(5) Petti, L.; Münzenrieder, N.; Vogt, C.; Faber, H.; Büthe, L.; Cantarella, G.; Bottacchi, F.; Anthopoulos, T. D.; Tröster, G., *Appl. Phys. Rev.,* **2016**, *3*, 021303.

(6) Fortunato, E.; Barquinha, P.; Martins, R., *Adv. Mater.,* **2012**, *24*, 2945-2986.

(7) Nomura, K.; Ohta, H.; Takagi, A.; Kamiya, T.; Hirano, M.; Hosono, H., *Nature,* **2004**, *432*, 488-492.

(8) Goyal, A.; Gorai, P.; Anand, S.; Toberer, E. S.; Snyder, G. J.; Stevanovic, V., *Chem. Mater.,* **2020**, *32*, 4467-4480.

(9) Kumar, A.; Islam, R.; Pramanik, D.; Saraswat, K., *J. Vac. Sci. Technol. A,* **2019**, *37*.

(10) Lany, S.; Osorio-Guillen, J.; Zunger, A., *Phys. Rev. B,* **2007**, *75*.

(11) Zhang, S.; Wei, S.-H.; Zunger, A., *Adv. Mater.,* **2001**, *63*, 075205.

(12) Greiner, M. T.; Chai, L.; Helander, M. G.; Tang, W. M.; Lu, Z. H., *Adv. Funct. Mater.,* **2012**, *22*, 4557-4568.

(13) Bransky, I.; Wimmer, J. M., *J. Phys. Chem. Solids,* **1972**, *33*, 801-812.

(14) Fryt, E., *Oxid. Met.,* **1976**, *10*, 311-327.

(15) Li, B.; Rui, Y. C.; Xu, J. L.; Wang, Y. Q.; Yang, J. X.; Zhang, Q. H.; Muller-Buschbaum, P., *J. Colloid Interface Sci.,* **2020**, *573*, 78-86.

(16) Jang, W. L.; Lu, Y. M.; Hwang, W. S.; Hsiung, T. L.; Wang, H. P., *Appl. Phys. Lett.,* **2009**, *94*.

(17) Sato, H.; Minami, T.; Takata, S.; Yamada, T., *Thin Solid Films,* **1993**, *236*, 27-31.

(18) Yang, J. L.; Lai, Y. S.; Chen, J. S., *Thin Solid Films,* **2005**, *488*, 242-246.

(19) Jeong, Y. K.; Choi, G. M., *J. Phys. Chem. Solids,* **1996**, *57*, 81-84.

(20) Zivkovic, A.; de Leeuw, N. H, *Phys. Rev. Materials.,* **2020**, *4*.

(21) Blumenthal, R. N.; Baukus, J.; Hirthe, W. M., *J. Electrochem. Soc.,* **1967**, *114*, 172.

(22) Forro, L.; Chauvet, O.; Emin, D.; Zuppiroli, L.; Berger, H.; Levy, F., *J. Appl. Phys.,* **1994**, *75*, 633-635.

(23) Nowotny, M. K.; Bak, T.; Nowotny, J., *J. Phys. Chem. B,* **2006**, *110*, 16270-16282.

(24) Panayotov, D. A.; Yates, J. T., *Chem. Phys. Lett.,* **2007**, *436*, 204-208.

(25) Di Valentin, C.; Pacchioni, G.; Selloni, A., *J. Phys. Chem. C,* **2009**, *113*, 20543-20552.

(26) Ozgur, U.; Alivov, Y. I.; Liu, C.; Teke, A.; Reshchikov, M. A.; Dogan, S.; Avrutin, V.; Cho, S. J.; Morkoc, H., *J. Appl. Phys.,* **2005**, *98*.

(27) Kim, Y. S.; Park, C. H., *Phys. Rev. Lett.,* **2009**, *102*.

(28) Liu, L.; Mei, Z.; Tang, A.; Azarov, A.; Kuznetsov, A.; Xue, Q.-K.; Du, X. J. P. R. B., *Phys. Rev. B,* **2016**, *93*, 235305.

(29) Selim, F. A.; Weber, M. H.; Solodovnikov, D.; Lynn, K. G., *Phys. Rev. Lett.,* **2007**, *99*.

(30) Gupta, P.; Dutta, T.; Mal, S.; Narayan, J., *J. Appl. Phys.,* **2012**, *111*, 013706.

(31) Wang, Q.; Puntambekar, A.; Chakrapani, V., *Nano Lett.,* **2016**, *16*, 7067-7077.

(32) Reinert, F.; Steiner, P.; Hufner, S.; Schmitt, H.; Fink, J.; Knupfer, M.; Sandl, P.; Bertel, E. *Z. Phys. B,* **1995**, *97*, 83-93.

(33) Fan, J. C.; Sreekanth, K. M.; Xie, Z.; Chang, S. L.; Rao, K. V., *Prog. Mater. Sci.,* **2013**, *58*, 874-985.

(34) Martinez, E. Y.; Zhu, K.; Li, C. W., *Nano Lett.,* **2020**, *20*, 7580-7587.

(35) Liu, Z.; Ma, R.; Osada, M.; Takada, K.; Sasaki, T., *J. Am. Chem. Soc.,* **2005**, *127*, 13869-13874.

(36) Cheng, J.; Chen, X.; Wu, J.-S.; Liu, F.; Zhang, X.; Dravid, V. P., *CrystEngComm,* **2012**, *14*, 6702-6709.

(37) Ma, R.; Liu, Z.; Takada, K.; Fukuda, K.; Ebina, Y.; Bando, Y.; Sasaki, T., *Inorg. Chem.,* **2006**, *45*, 3964-3969.

(38) Yang, J.; Liu, H.; Martens, W. N.; Frost, R. L., *J. Phys. Chem. C,* **2010**, *114*, 111-119.

(39) Biesinger, M. C.; Payne, B. P.; Grosvenor, A. P.; Lau, L. W. M.; Gerson, A. R.; Smart, R. S., *Appl. Surf. Sci.,* **2011**, *257*, 2717-2730.

(40) Liu, X.; Ma, R.; Bando, Y.; Sasaki, T., *Angew. Chem.,* **2010**, *122*, 8429-8432.

(41) Fantauzzi, M.; Elsener, B.; Atzei, D.; Rigoldi, A.; Rossi, A., *RSC Adv.,* **2015**, *5*, 75953-75963.

(42) Seo, W. S.; Shim, J. H.; Oh, S. J.; Lee, E. K.; Hur, N. H.; Park, J. T., *J. Am. Chem. Soc.,* **2005**, *127*, 6188-6189.

(43) Constant, K. P.; Mason, T. O.; Rothman, S. J.; Routbort, J. L., *J. Phys. Chem. Solids,* **1992**, *53*, 405-411.

(44) Constant, K. P.; Mason, T. O.; Routbort, J. L., *J. Phys. Chem. Solids,* **1992**, *53*, 413-418.

(45) Joshi, G.; Pai, M.; Harrison, H.; Sandberg, C.; Aragón, R.; Honig, J., *MRS Bull.,* **1980**, *15*, 1575-1579.

(46) Iguchi, E.; Hashimoto, T.; Yokoyama, S., *J. Phys. Soc. Jpn.,* **1996**, *65*, 221-229.

(47) Wu, Y.; Pasero, D.; McCabe, E.; Matsushima, Y.; West, A., *J. Mater. Chem.,* **2009**, *19*, 1443-1448.

(48) Koel, G.; Gellings, P., *Oxid. Met.,* **1972**, *5*, 185-203.

(49) Wu, J. M.; Chen, L. J.; Yang, X. B.; Zhao, Y. J., *Phys. Lett. A,* **2014**, *378*, 2635-2639.

APPENDIX A. SUPPORTING INFORMATION FOR CHAPTER 1

1. Physical Characterization Methods

Transmission electron microscopy (TEM) images and Energy-dispersive X-ray spectra (EDS) were acquired using an FEI Tecnai G20 TEM equipped with a 200 kV LaB_6 filament and an Oxford Instruments X-MAX SDD EDS detector. High-resolution scanning transmission electron microscopy (STEM) and EDS mapping were obtained on an FEI Talos F200X S/TEM with a 200 kV X-FEG field-emission source and a super X-EDS system. X-ray photoelectron (XPS) spectra were obtained with a Kratos AXIS Ultra Delay-Line Detector Imaging X-ray Photoelectron Spectrometer. XPS binding energies were fingerprinted against reference data from literature.[1-5] Inductively-coupled plasma ionization mass spectrometry (ICP-MS) data was collected using a Thermo Fisher ELEMENT 2.

Samples for TEM were prepared by drop-drying 1 μL of a nominally 10 mM colloidal nanoparticle solution onto a Cu grid. Samples for XPS were prepared by drop-drying 3 μL of a nominally 10 mM colloidal nanoparticle solution onto a Si wafer. ICP-MS samples were prepared by digesting 50 μL of the Pt-M solution in concentrated aqua regia for 2 days at room temperature. Assuming a 10 mM starting concentration, 100 ppb and 1 ppb solutions were then prepared through serial dilution using a 4% HCl solution. Reported ICP-MS atomic ratios were determined from 100 ppb solution measurements.

2. Electrochemical Methods

A Gamry Interface 1010B Potentiostat or a Pine WaveDriver 20 Bipotentiostat was used to perform all electrochemical experiments. The electrolyte used for all electrochemical experiments was 0.1 M KOH with pH of 13. Currents are reported with anodic current as positive and cathodic current as negative. Potentials were measured against a Ag/AgCl reference (3 M NaCl, BASi) or Hg/HgO reference (0.1 M KOH, CH Instruments) and converted to the RHE reference scale using:

E (vs RHE) = E (vs Ag/AgCl) + 0.209 V + 0.0591 V*pH

or

E (vs RHE) = E (vs Hg/HgO) + 0.165 V + 0.0591 V*pH

Cyclic voltammetry (CV) was carried out in a two-compartment glass cell containing 15 mL of 0.1 M KOH electrolyte in each compartment. The electrolyte was purged for at least 30 min. in N_2 prior to running the CV. The CVs were taken using a scan window from 0.76 V to 1.67 V and were cycled at 50 mV/s for twenty scans. The working electrode was prepared by drop-drying 1 μL of a 10 mM colloidal nanoparticle solution in DMF onto a polished glassy carbon electrode with 3 mm diameter (CH Instruments). The counter electrode was a platinum wire or platinum mesh.

Electrochemical CO stripping voltammetry was carried out after running twenty CV scans under N_2. The electrode was held at 0.126 V vs. RHE in a CO-saturated solution for 5 min. and then purged with N_2 for 15 min. The adsorbed CO was oxidatively stripped by scanning the electrode from 0.126 V to 1.67 V at 50 mV/s. Two subsequent CV scans in N_2 were carried out to provide a baseline for the CO stripping peak. After background subtraction, the CO stripping profile was integrated to determine Pt electrochemical surface area (ECSA) and fit to three peaks to estimate the coverage of distinct Pt active sites on the surface of the nanoparticle. The working electrode was prepared by drop-drying 1 μL of a 10 mM colloidal nanoparticle solution in DMF onto a polished glassy carbon electrode with 3 mm diameter (CH Instruments). The counter electrode was a platinum wire or platinum mesh. All experiments were run in triplicate, and average values for peak position and peak ratios are reported in **Figure 1.8c-d**.

Steady-state CO oxidation was carried out using a rotating disk electrode (RDE) in a single-compartment glass cell containing 120 mL of 0.1 M KOH electrolyte. The solution was purged

with CO for at least 30 min prior to the start of the experiment. Twenty CV scans under N_2 were taken prior to the CO oxidation experiment. A rotation rate of 1600 rpm and scan rate of 20 mV/s were utilized, and data from the second linear sweep voltammetry (LSV) scan is reported. LSV data was collected by sweeping from negative to positive potential because this scan direction most resembled steady state behavior. The kinetic current density (j_k) at a given potential is obtained via the Koutecky-Levich equation:

$$\frac{1}{j} = \frac{1}{j_k} + \frac{1}{j_d}$$

The diffusion-limited current density (j_d) is determined from the plateau current density in the high overpotential regime of the LSV. The half-wave potential ($E_{1/2}$) is obtained by finding the potential at which the current density is 50% of j_d. A roughness factor for each catalyst is determined through integration of the H_{upd} region of the CV under N_2 taken after the CO oxidation LSV scans. The measured area is divided by a reference value of 210 μC/cm^2 for a flat polycrystalline Pt electrode.[6] The surface-area normalized j_k is obtained by dividing the unnormalized j_k by the roughness factor for each sample (**Table A.1**). All j_k and $E_{1/2}$ values are obtained from an average of three sample runs to account for variability in the electrode drop-drying process, and the error bar reflects the standard deviation (**Figure 1.8f, 1.9**).

Table A.1. Roughness factors for each Pt-M sample calculated from Pt-H_{upd} integration.

Sample	Roughness Factor
Cr	1.15
Mn	3.96
Ni	2.51
In	2.81
Pt	2.45

Oxygen reduction reaction (ORR) voltammetry was carried out using a rotating ring-disk electrode in a single-compartment glass cell containing 120 mL of 0.1 M KOH electrolyte. The solution was purged with O_2 for at least 30 min prior to the start of the experiment. For all ORR experiments, a rotation rate of 1600 rpm and scan rate of 20 mV/s were utilized. Twenty CV scans were collected prior to running a LSV scan.

A catalyst ink consisting of 20 wt% Pt or Pt-MO_x on Vulcan was utilized for all RDE experiments. To prepare the ink, 0.3 mg of Pt or Pt-MO_x was deposited onto 0.7 mg of Vulcan and suspended in a solution containing 250 μL of DMF and 10 μL of 0.5 % Nafion in IPA. The working electrode was prepared by drop-drying 10 μL of the catalyst ink onto a polished glassy carbon electrode with 5 mm diameter. The counter electrode was a graphite rod.

3. Physical Characterization Data

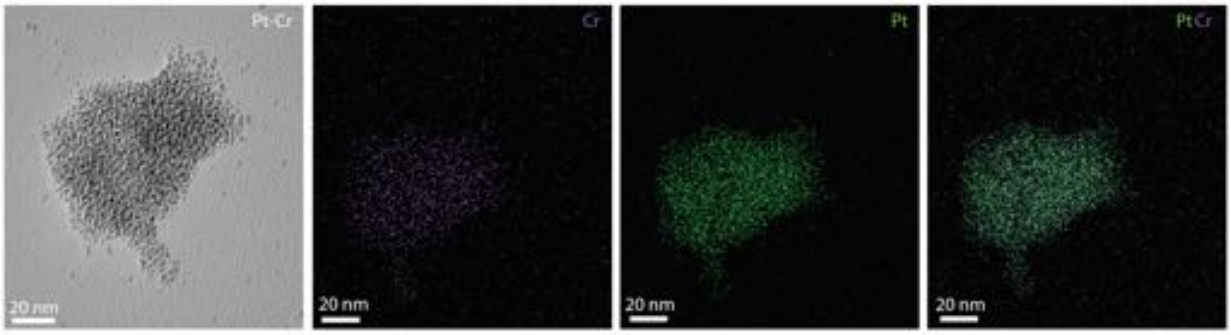

Figure A.1. EDS mapping of Pt and Cr atomic distributions for Pt-CrO_x nanoparticles before catalysis.

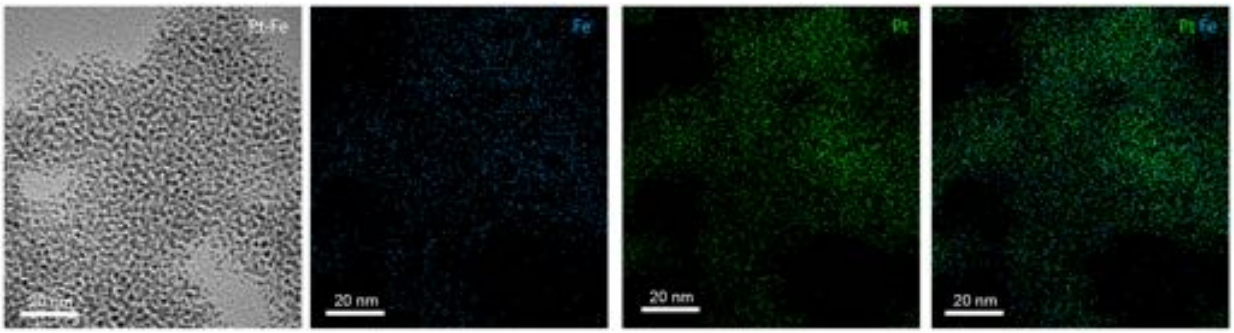

Figure A.2. EDS mapping of Pt and Fe atomic distributions for Pt-FeO_x nanoparticles before catalysis.

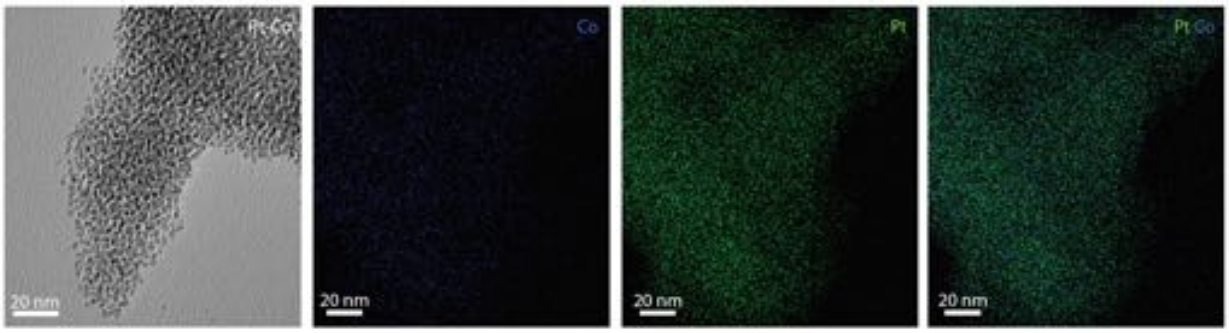

Figure A.3. EDS mapping of Pt and Co atomic distributions for Pt-CoO_x nanoparticles before catalysis.

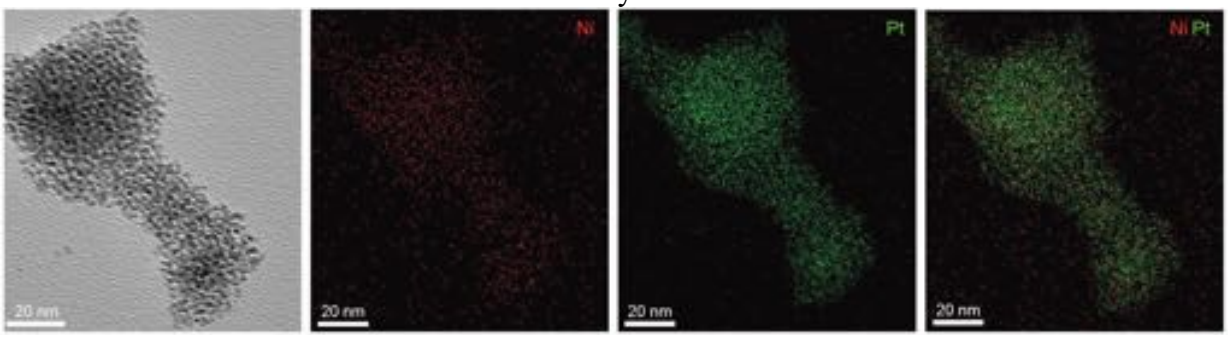

Figure A.4. EDS mapping of Pt and Ni atomic distributions for Pt-NiO_x nanoparticles before catalysis.

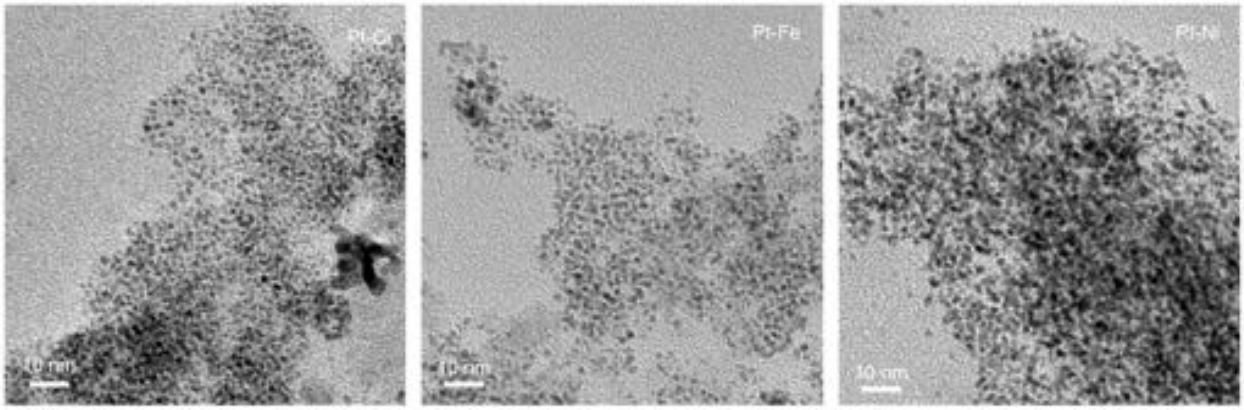

Figure A.5. TEM images for Pt-CoO_x, Pt-NiO_x, and Pt-CrO_x after electrochemical CO stripping voltammetry. All scale bars are 10 nm.

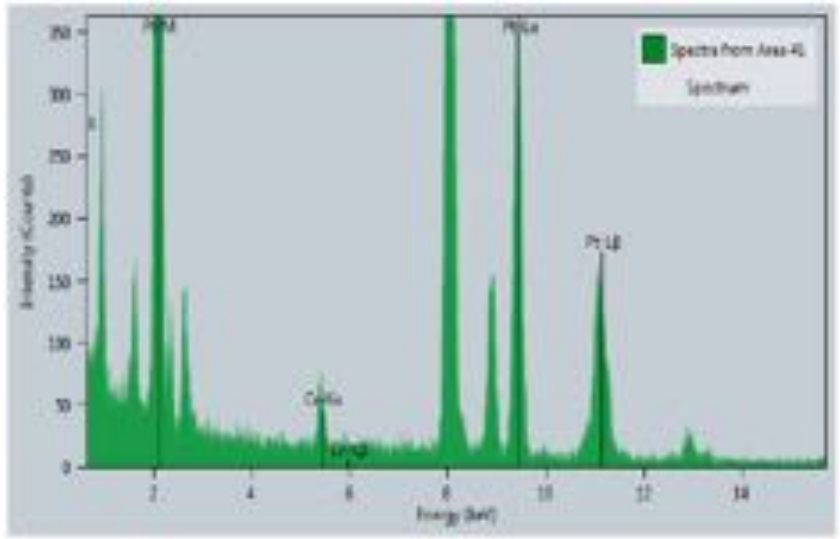
Spectra from Area #1
Spectrum
Pt Lβ
Energy (keV)

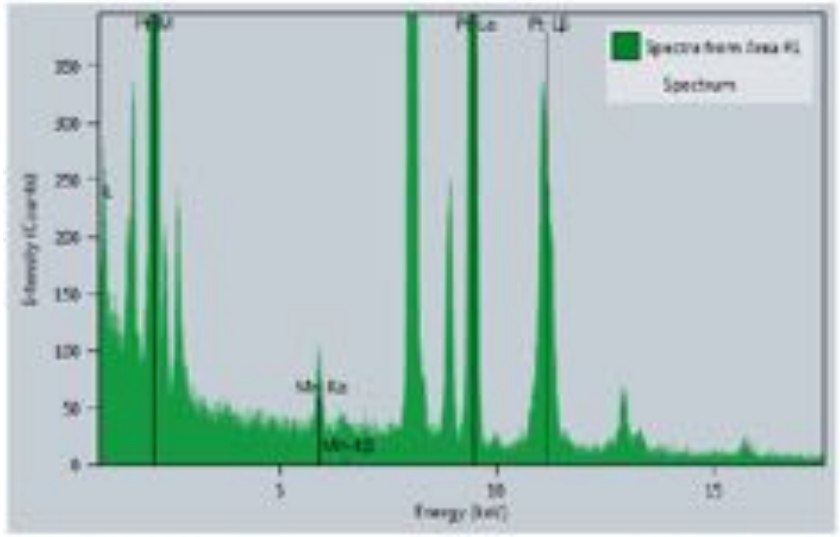
Spectra from Area #1
Spectrum
Energy (keV)

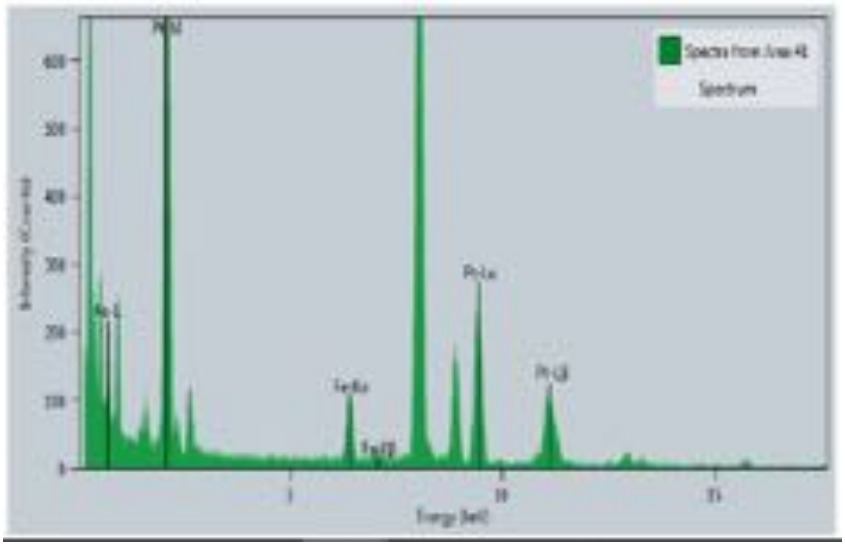
Spectra from Area #1
Spectrum
Pt-La
Pt-Lβ
Energy (keV)

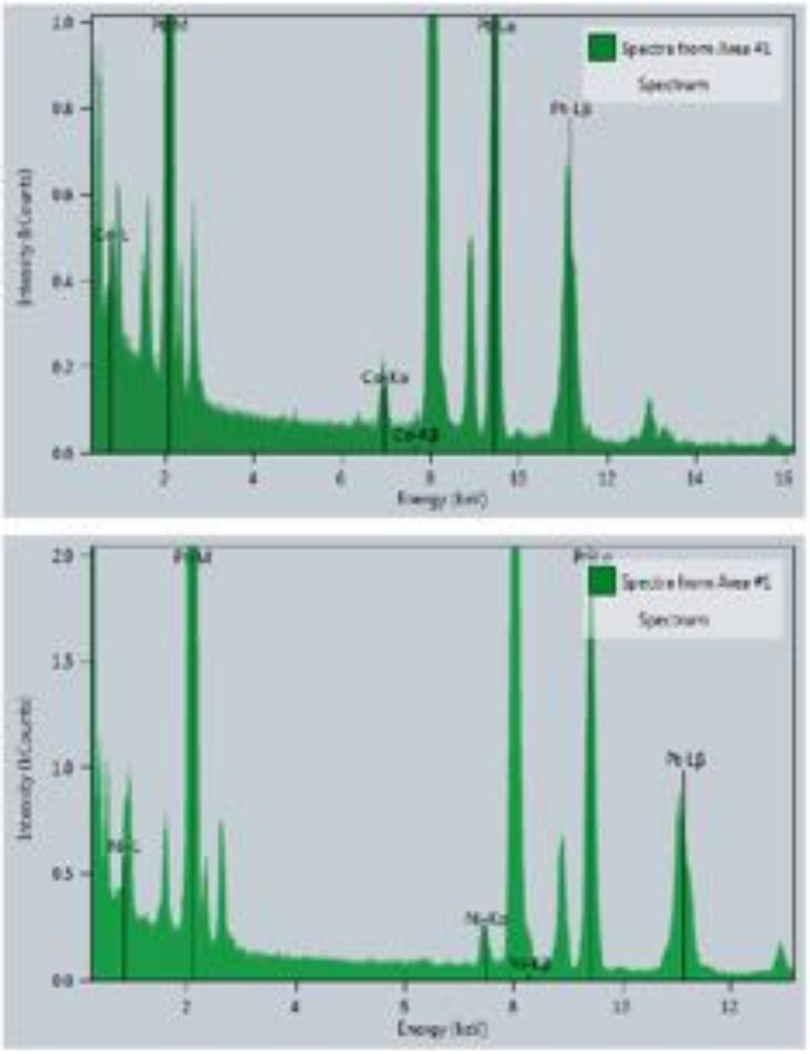

Figure A.6. Energy-dispersive X-ray spectra (EDS) Pt-CrO_x, Pt-MnO_x, Pt-FeO_x, Pt-CoO_x, and Pt-NiO_x. Quantification of atomic ratios was carried out using the indicated Pt L, metal K (M=Sc, Ti, Cr, Mn, Fe, Co, Ni, Ga) and In L peaks.

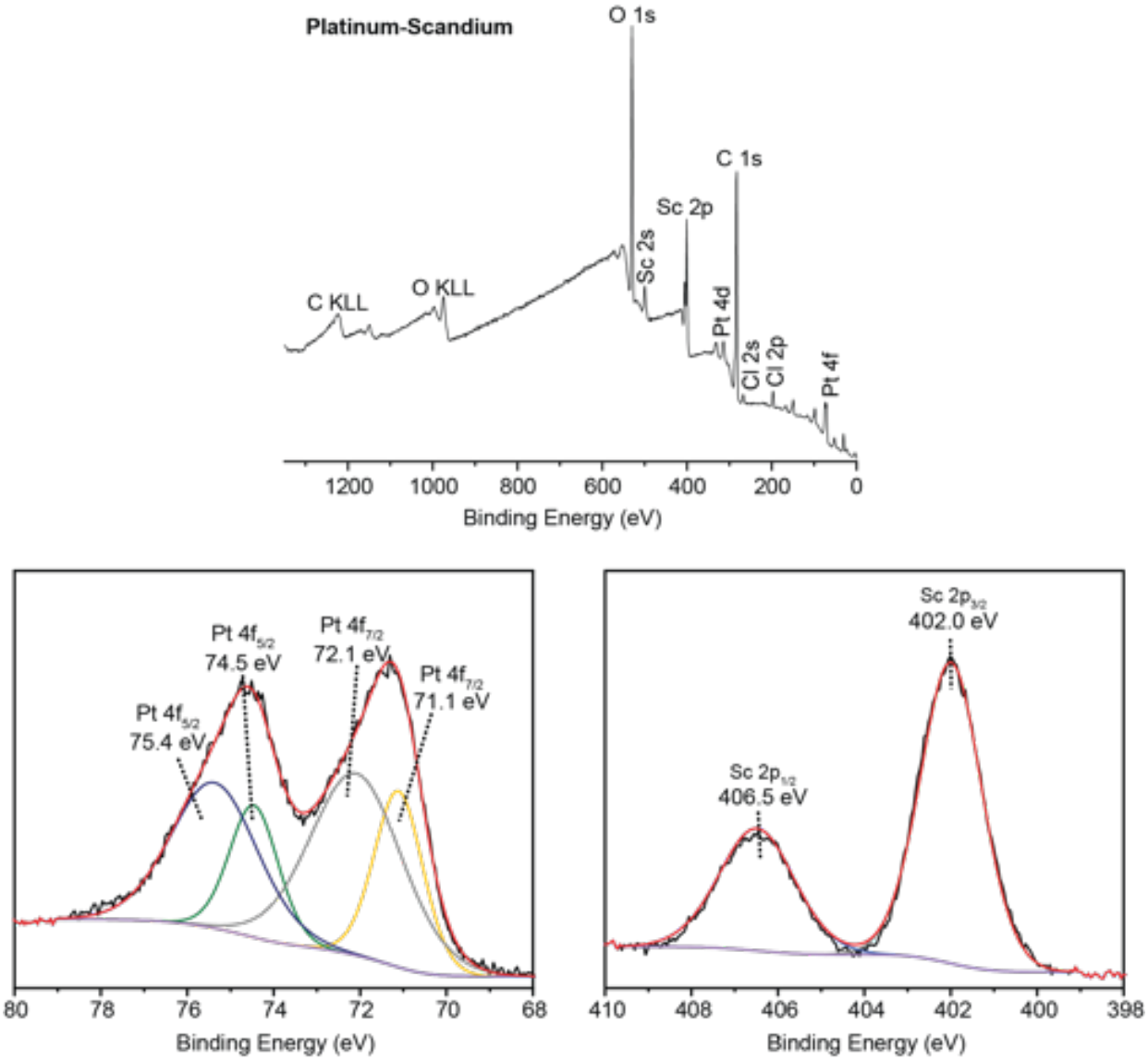

Figure A.7. X-ray photoelectron spectra (XPS) for Pt-Sc nanoparticles including survey spectrum and high-resolution spectrum of the Pt 4f and Sc 2p region.

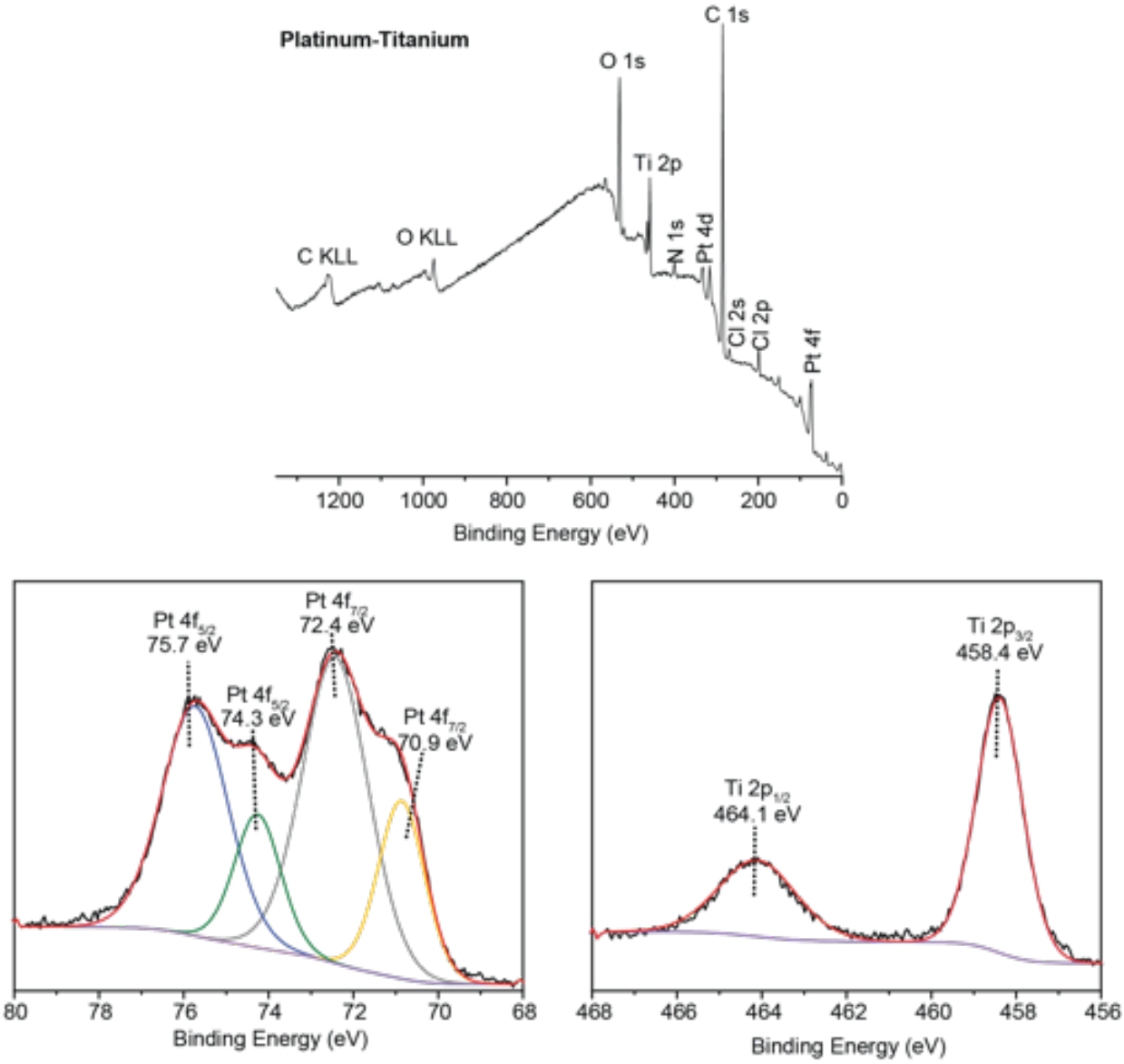

Figure A.8. X-ray photoelectron spectra for Pt-Ti nanoparticles including survey spectrum and high-resolution spectrum of the Pt 4f and Ti 2p region.

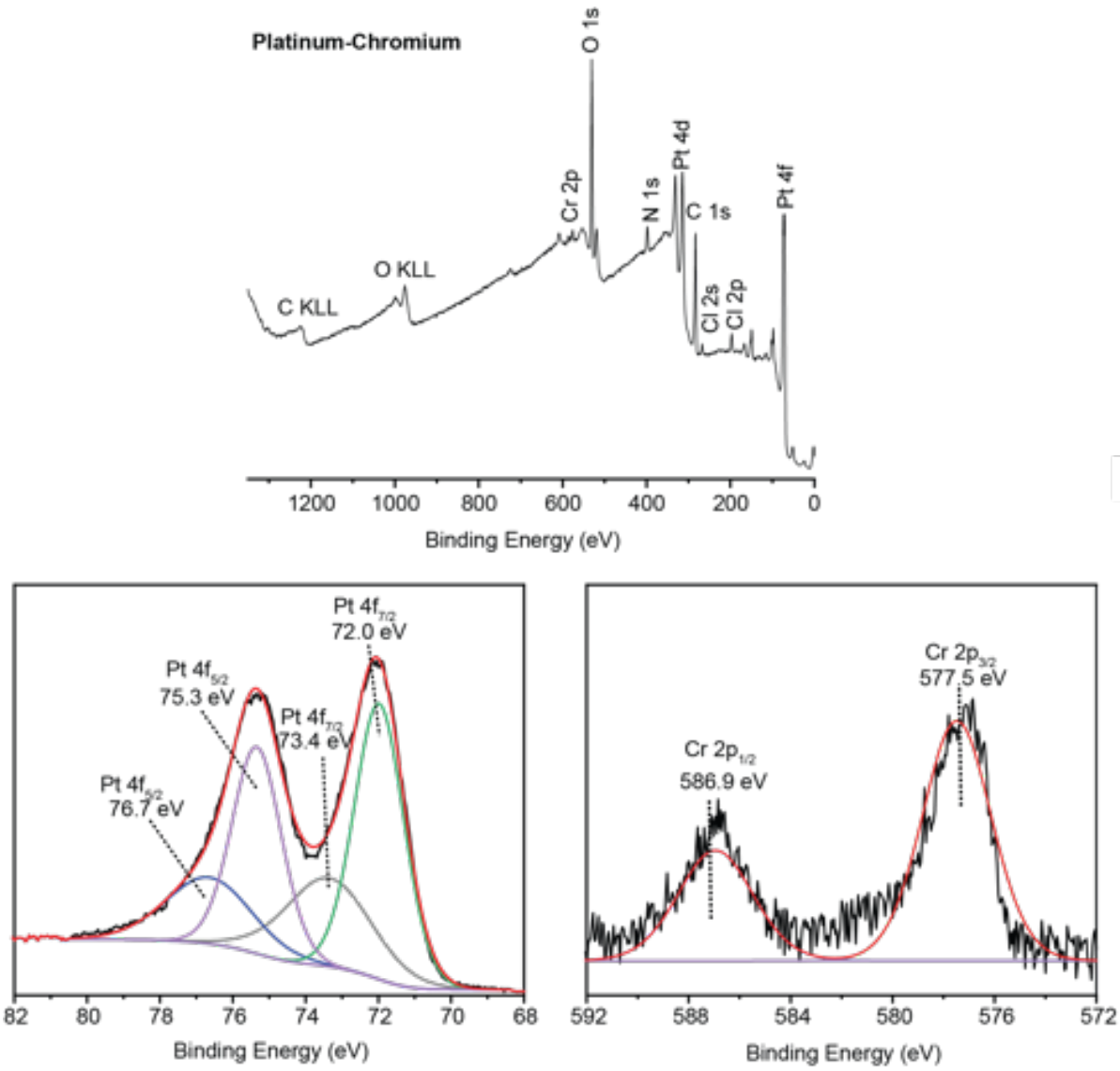

Figure A.9. X-ray photoelectron spectra for Pt-Cr nanoparticles including survey spectrum and high-resolution spectrum of the Pt 4f and Cr 2p region.

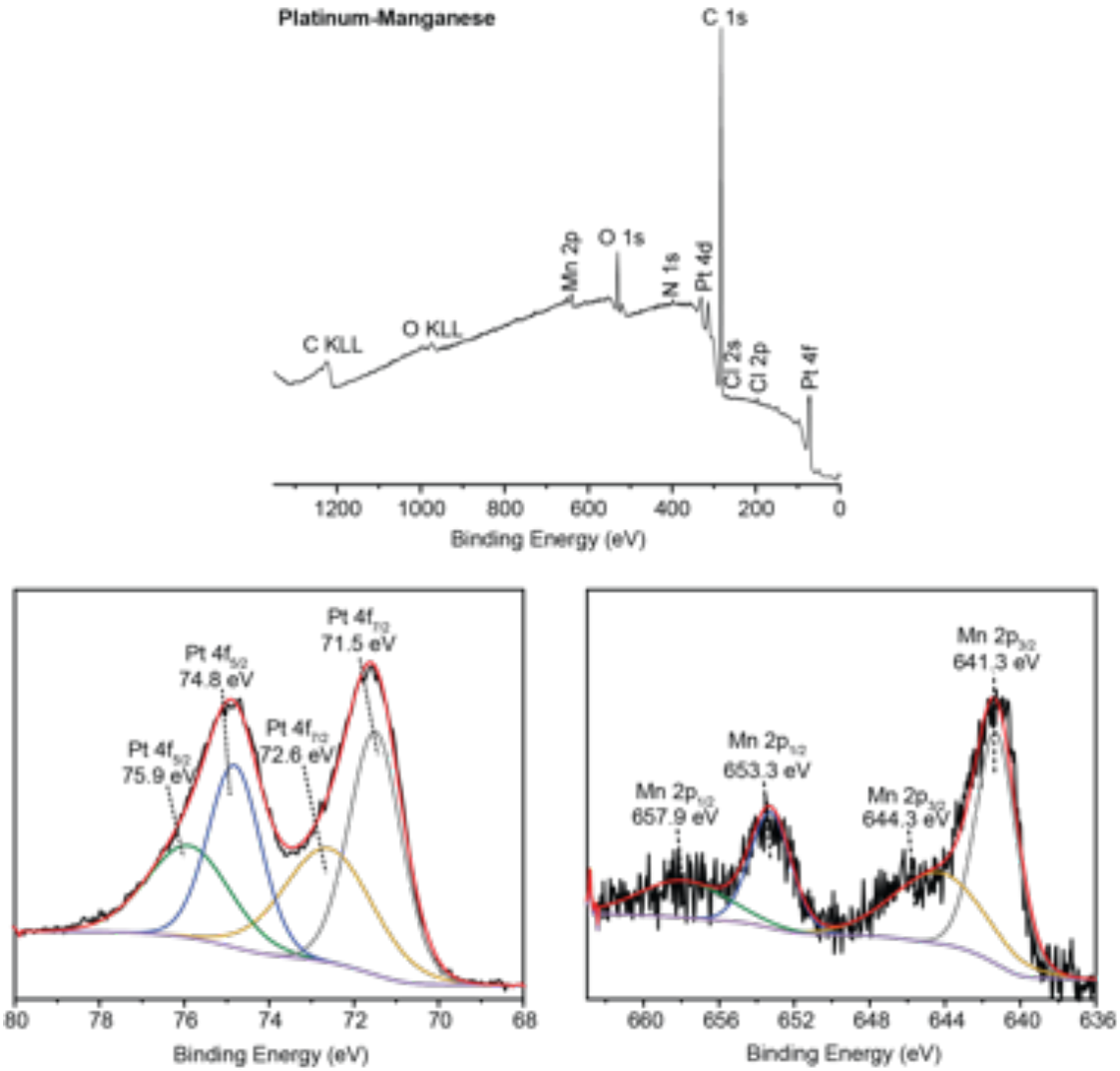

Figure A.10. X-ray photoelectron spectra for Pt-Mn nanoparticles including survey spectrum and high-resolution spectrum of the Pt 4f and Mn 2p region.

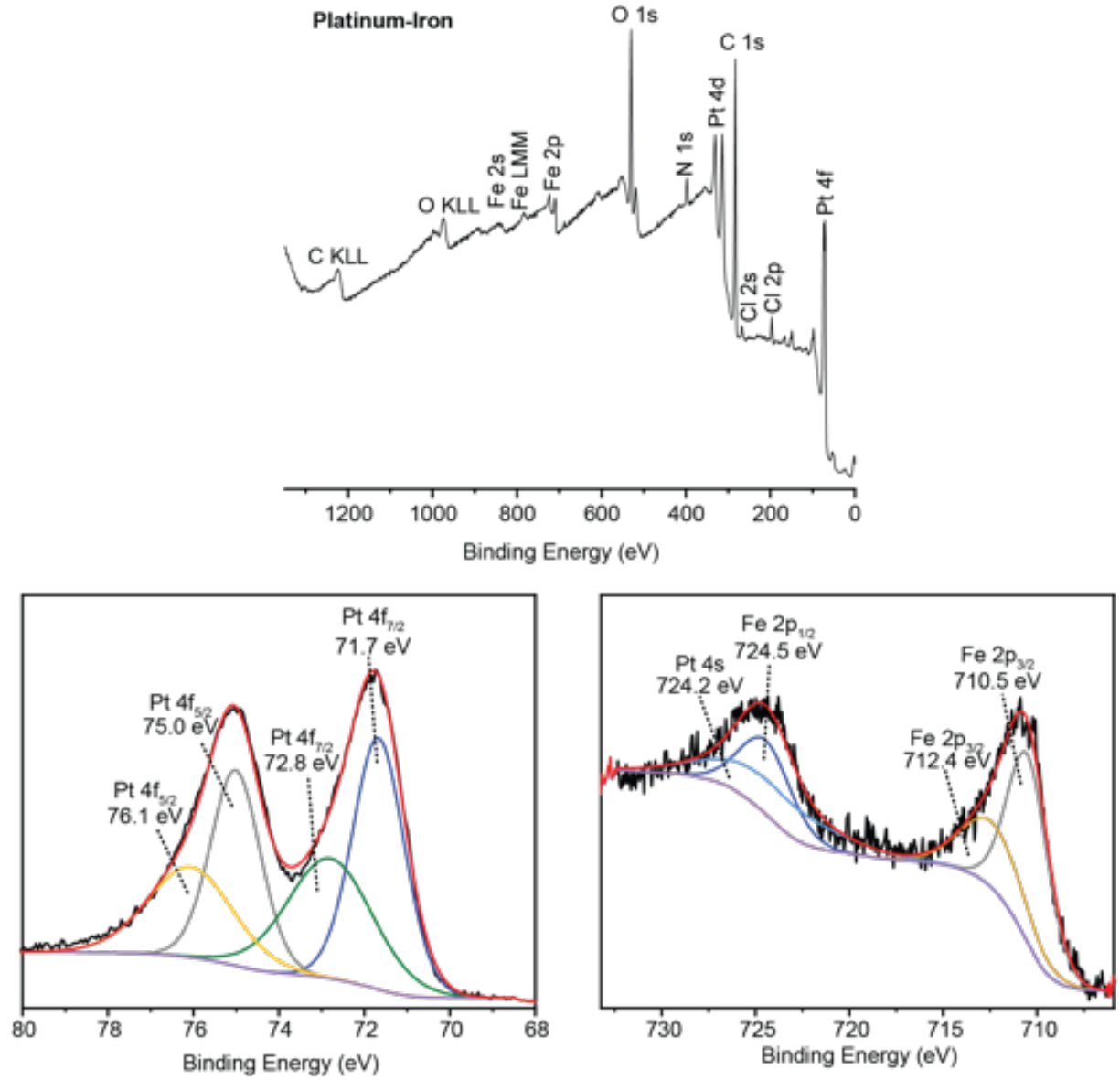

Figure A.11. X-ray photoelectron spectra for Pt-Fe nanoparticles including survey spectrum and high-resolution spectrum of the Pt 4f and Fe 2p region.

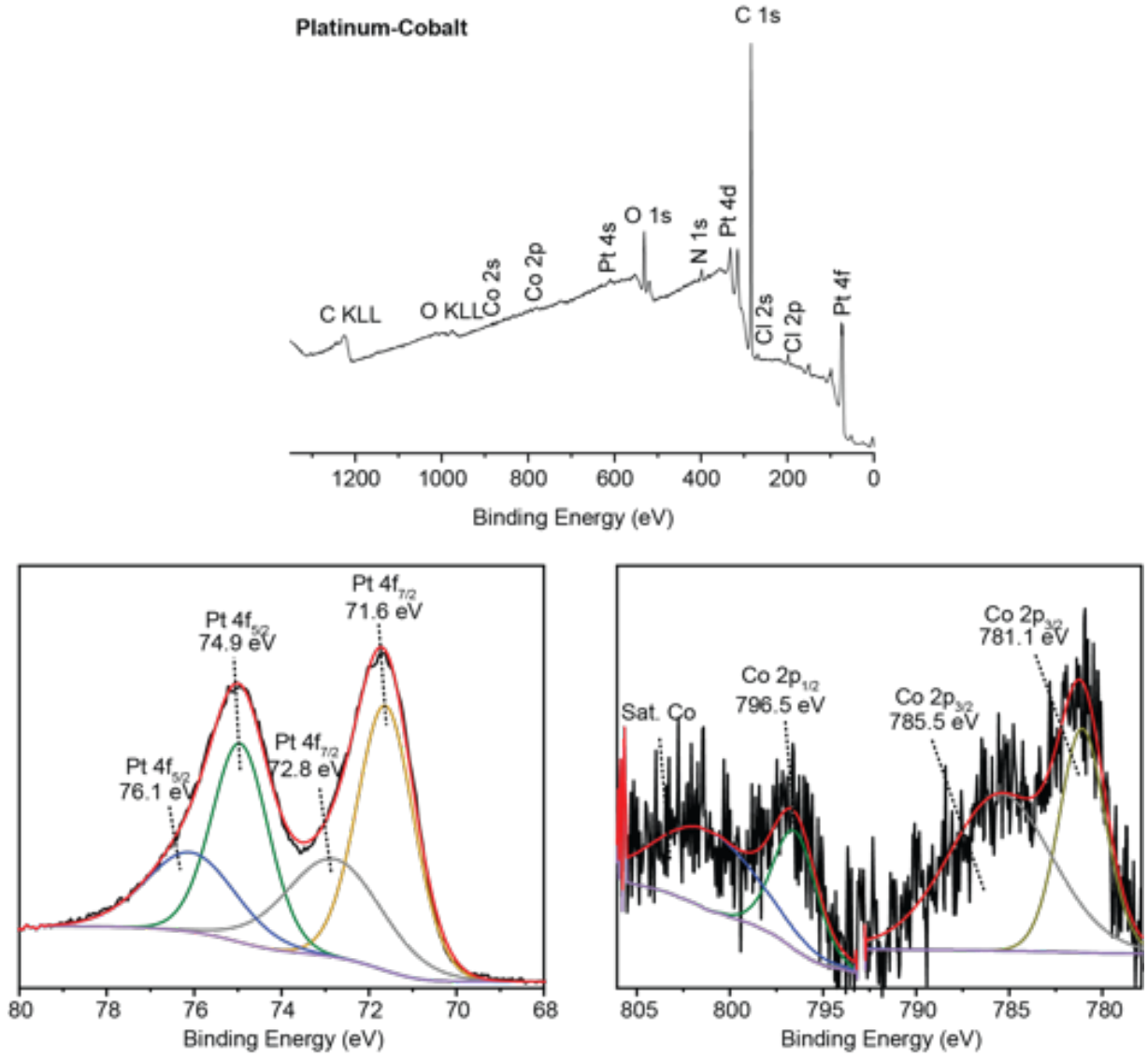

Figure A.12. X-ray photoelectron spectra for Pt-Co nanoparticles including survey spectrum and high-resolution spectrum of the Pt 4f and Co 2p region.

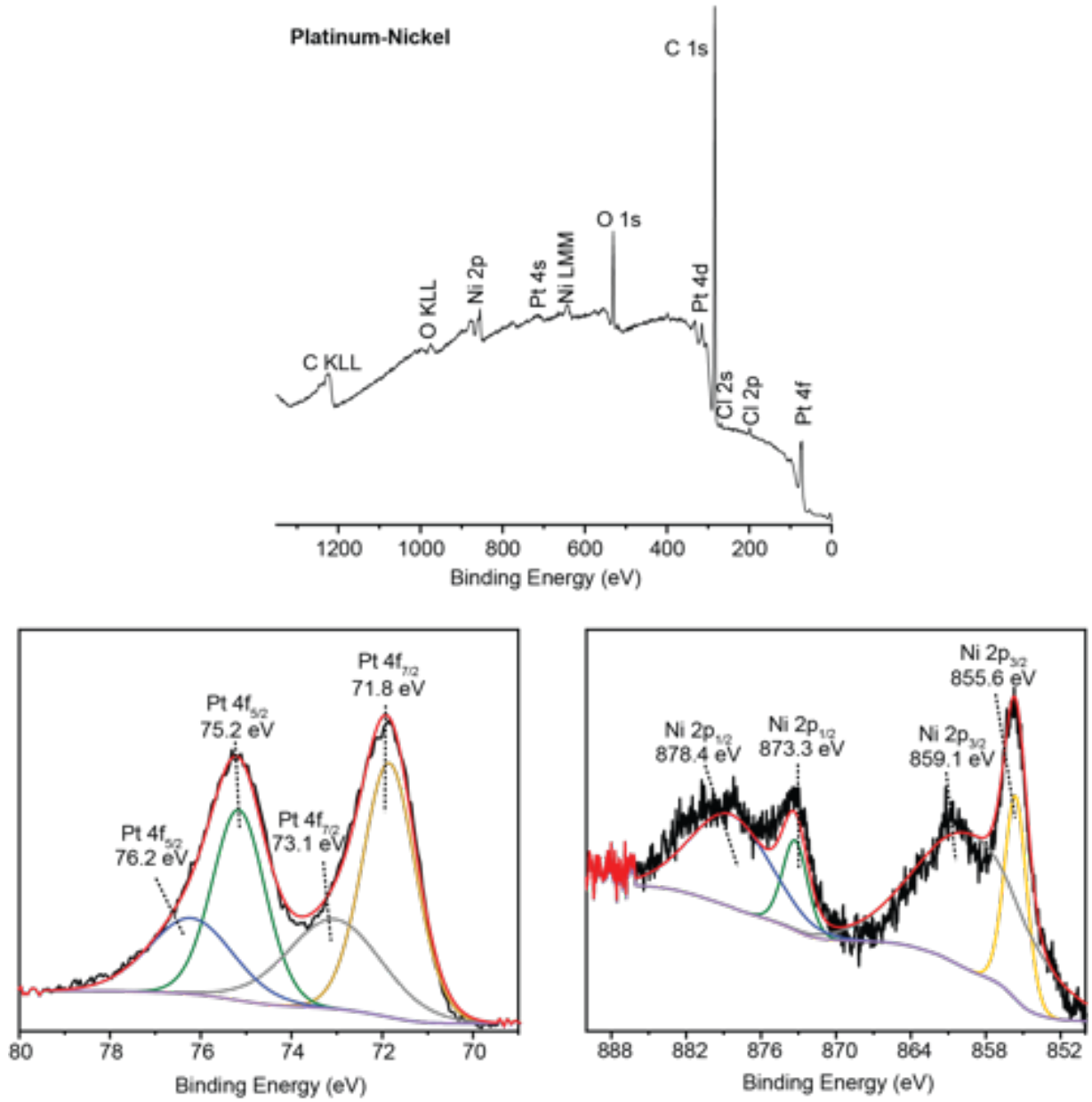

Figure A.13. X-ray photoelectron spectra for Pt-Ni nanoparticles including survey spectrum and high-resolution spectrum of the Pt 4f and Ni 2p region.

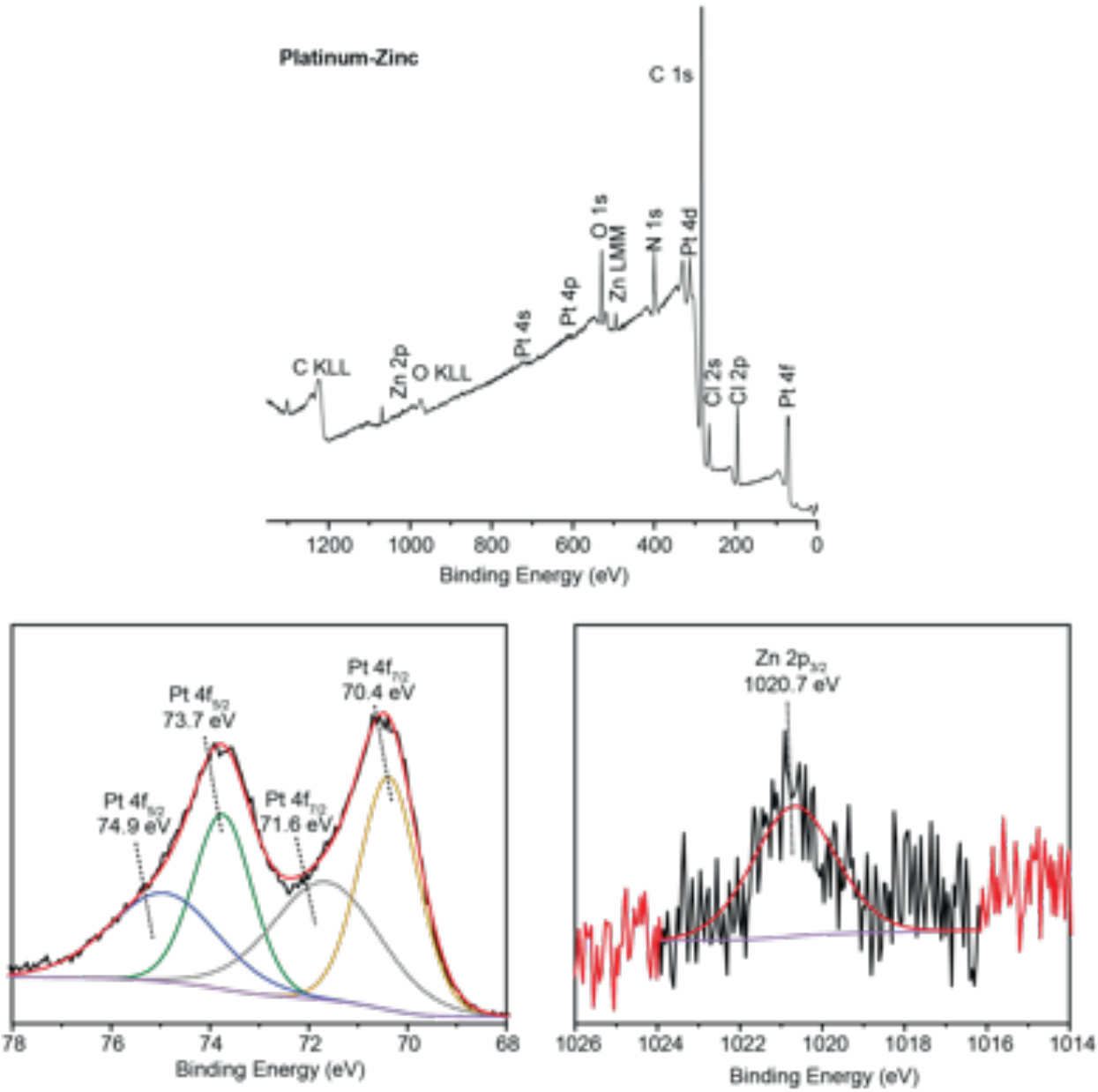

Figure A.14. X-ray photoelectron spectra for Pt-Zn nanoparticles including survey spectrum and high-resolution spectrum of the Pt 4f and Zn 2p region.

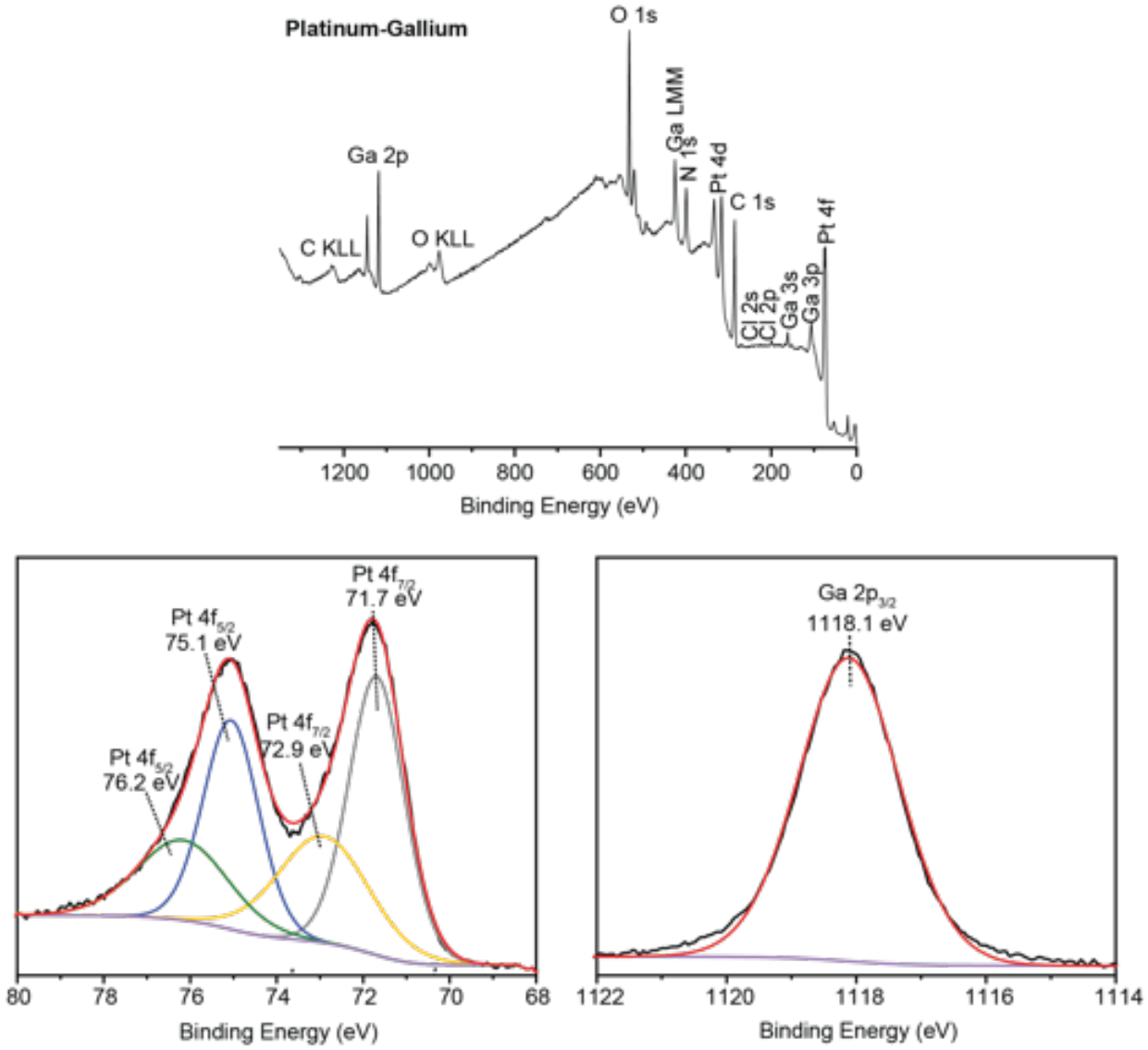

Figure A.15. X-ray photoelectron spectra for Pt-Ga nanoparticles including survey spectrum and high-resolution spectrum of the Pt 4f and Ga 2p region.

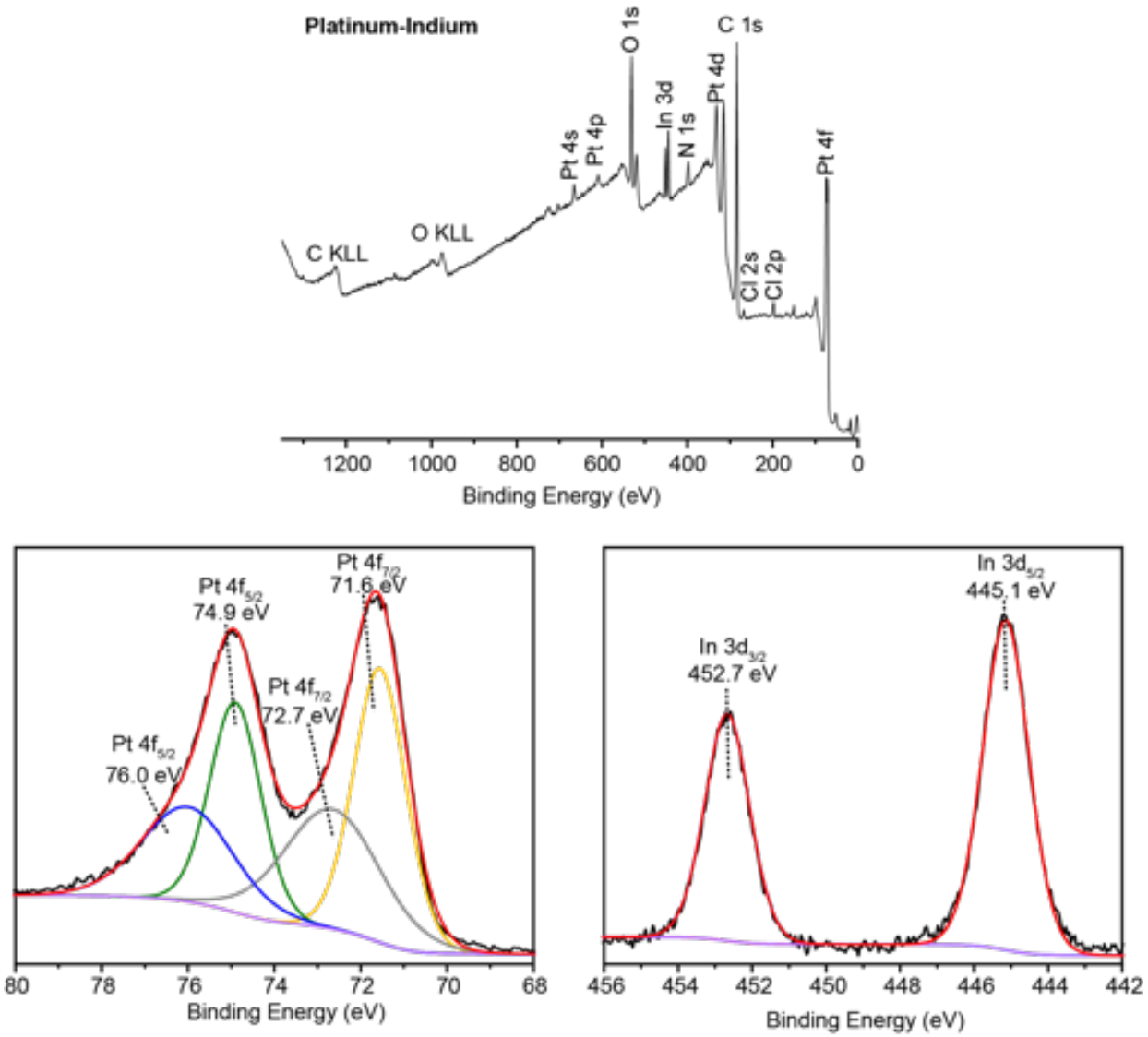

Figure A.16. X-ray photoelectron spectra for Pt-In nanoparticles including survey spectrum and high-resolution spectrum of the Pt 4f and In 3d region.

6. Electrochemical Data

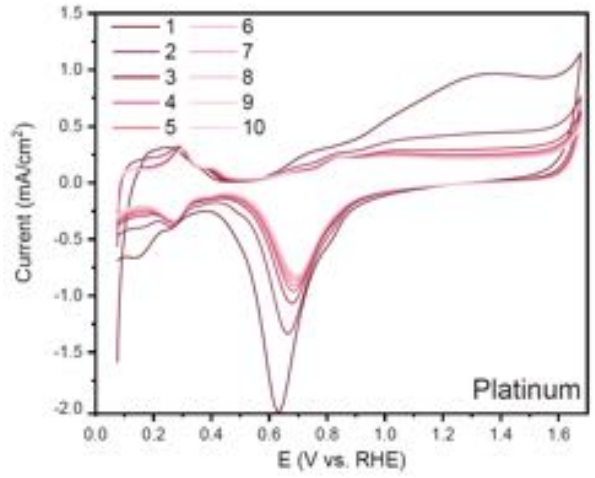

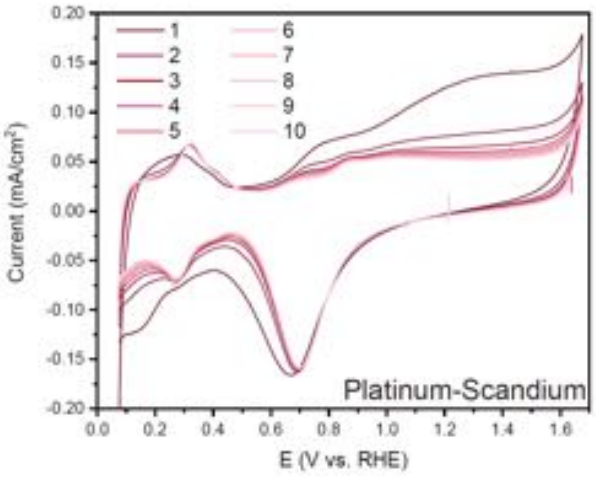

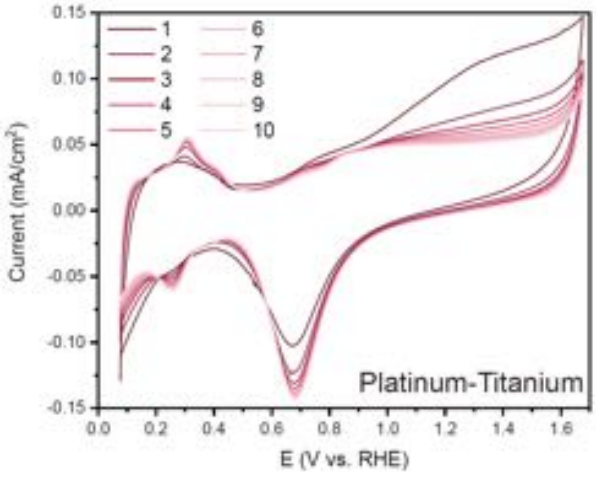

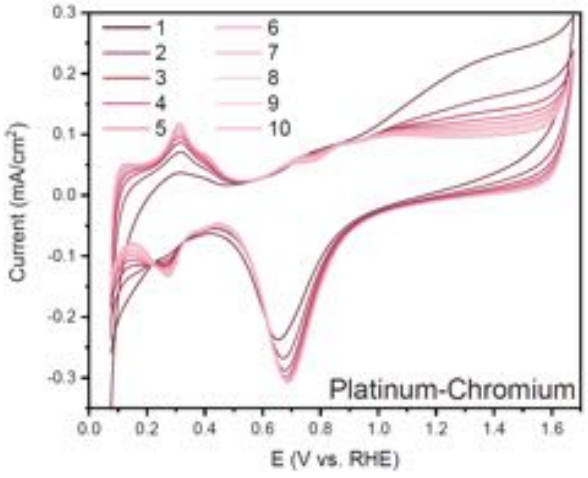

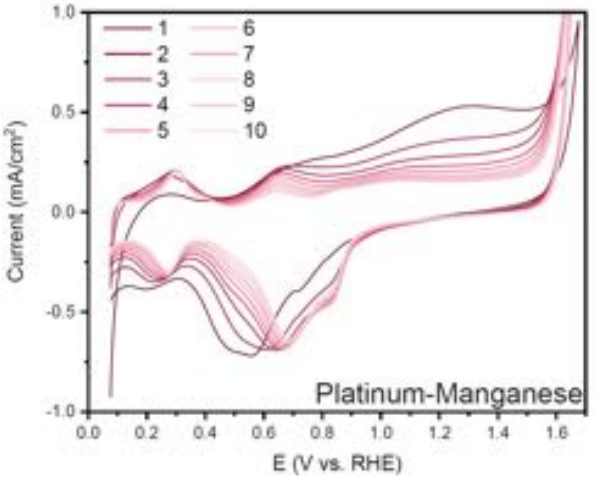

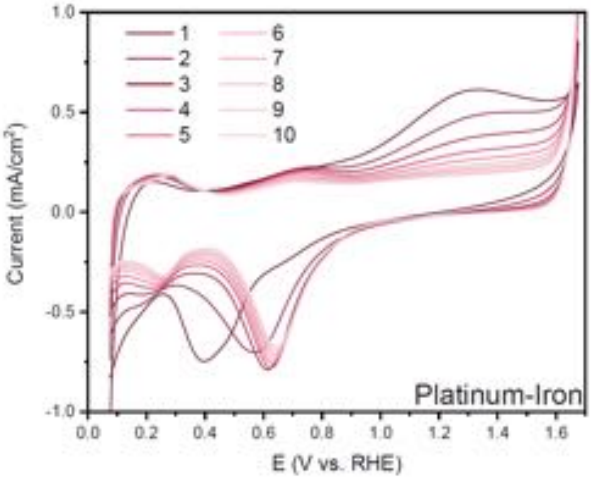

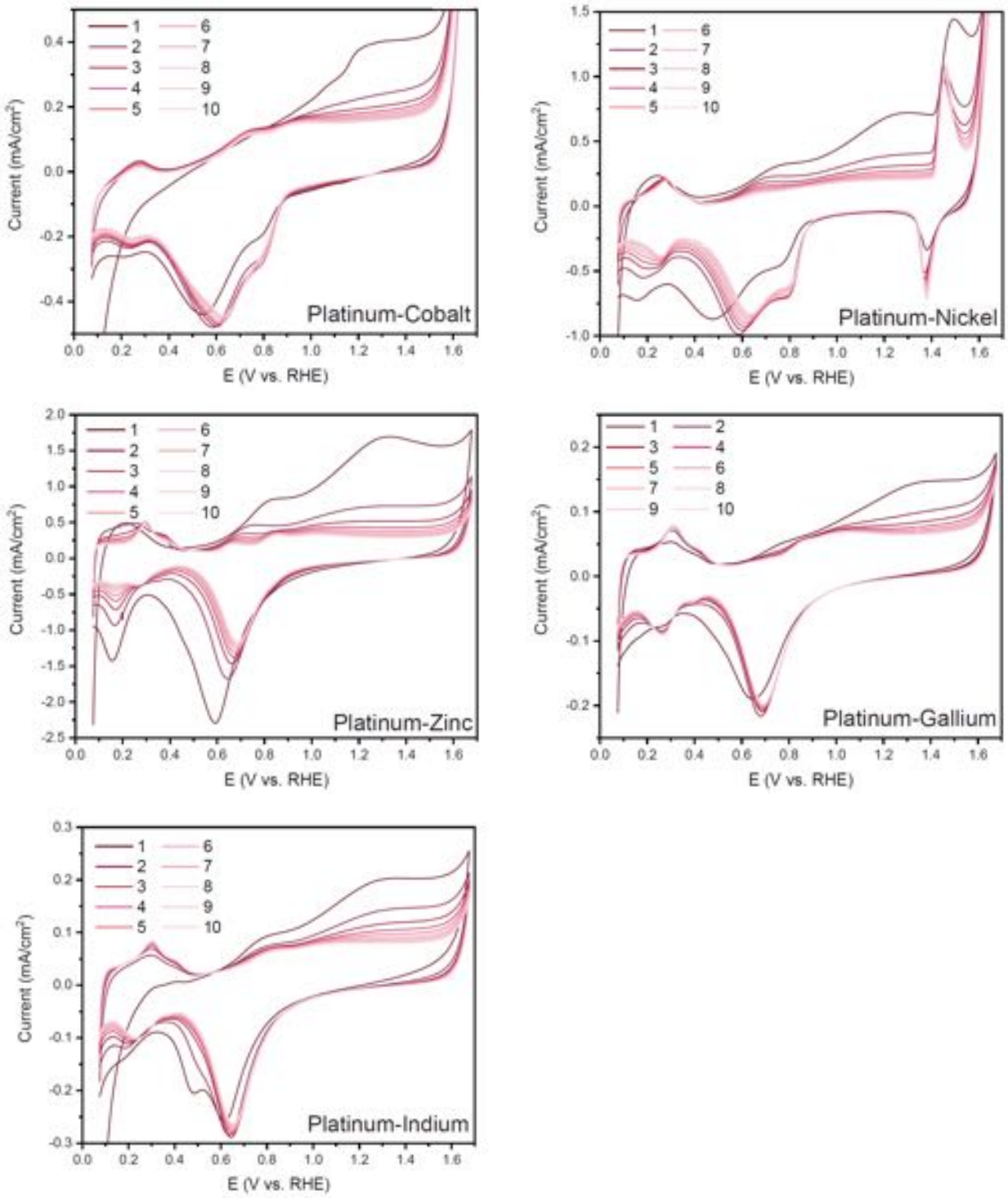

Figure A.17. First twenty CV scans taken under N_2 for all Pt-MO_x samples and pure Pt.

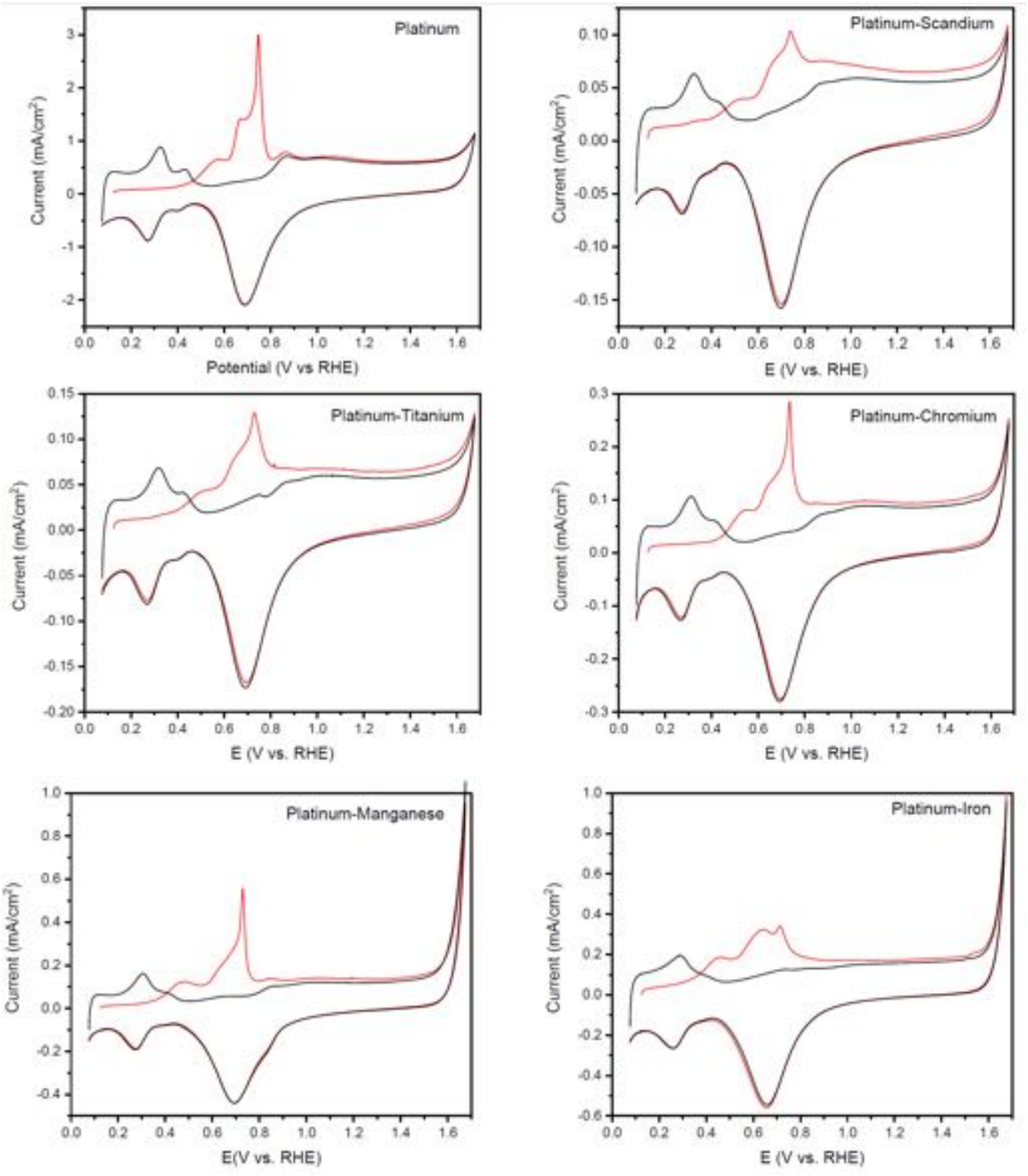
Platinum
Current (mA/cm²)
Potential (V vs RHE)
Platinum-Scandium
Current (mA/cm²)
E (V vs. RHE)
Platinum-Titanium
Current (mA/cm²)
E (V vs. RHE)
Platinum-Chromium
Current (mA/cm²)
E (V vs. RHE)
Platinum-Manganese
Current (mA/cm²)
E(V vs. RHE)
Platinum-Iron
Current (mA/cm²)
E (V vs. RHE)

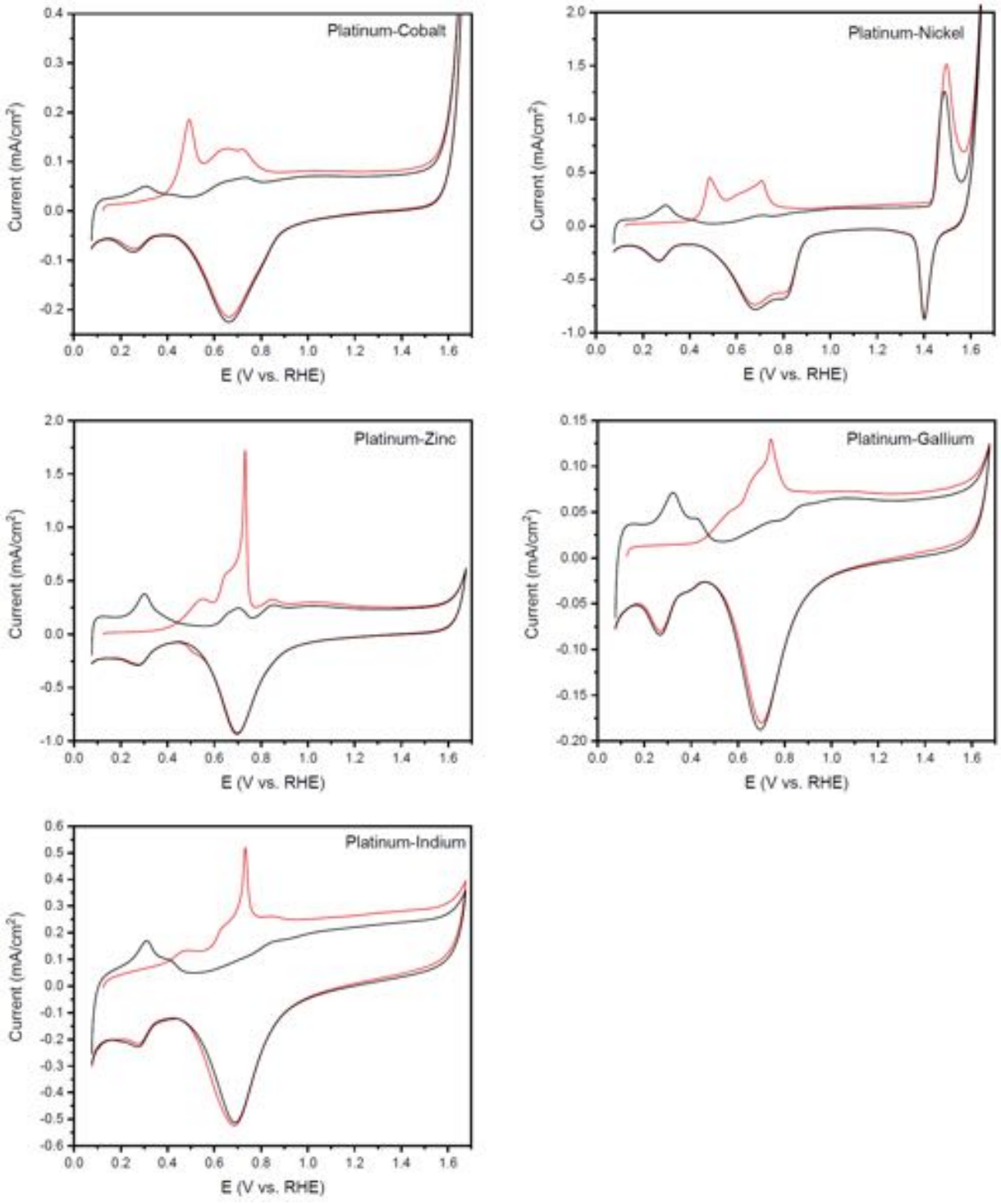

Figure A.18. Electrochemical CO stripping voltammograms (red) and second scan N_2 background (black) for all Pt and Pt-MO_x samples.

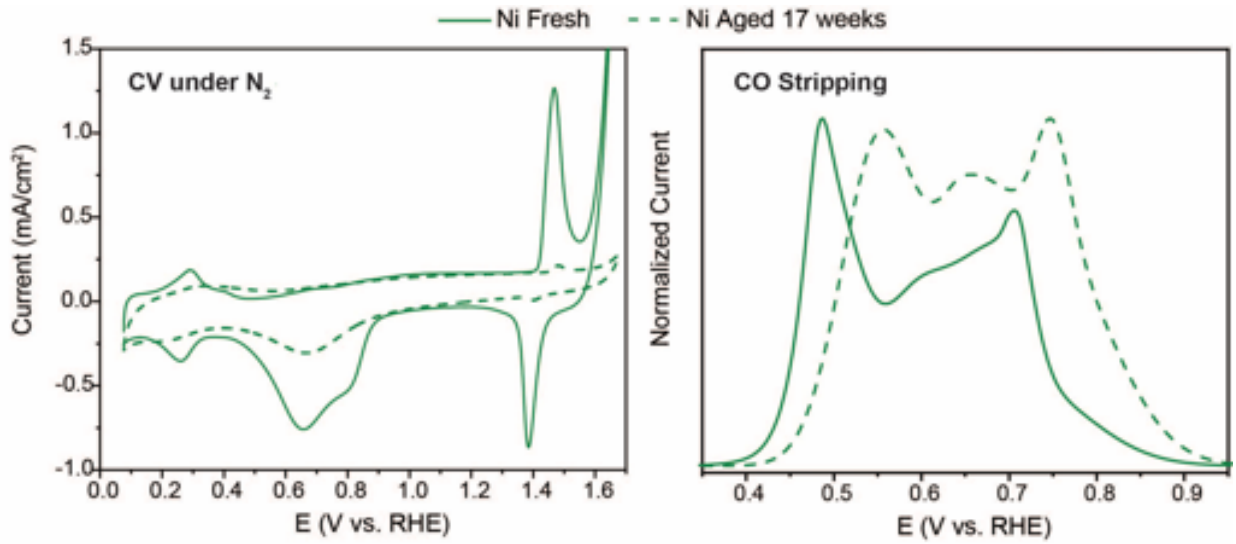

Figure A.19. CV and CO stripping for Pt-NiO_x before and after 17 weeks of sample aging.

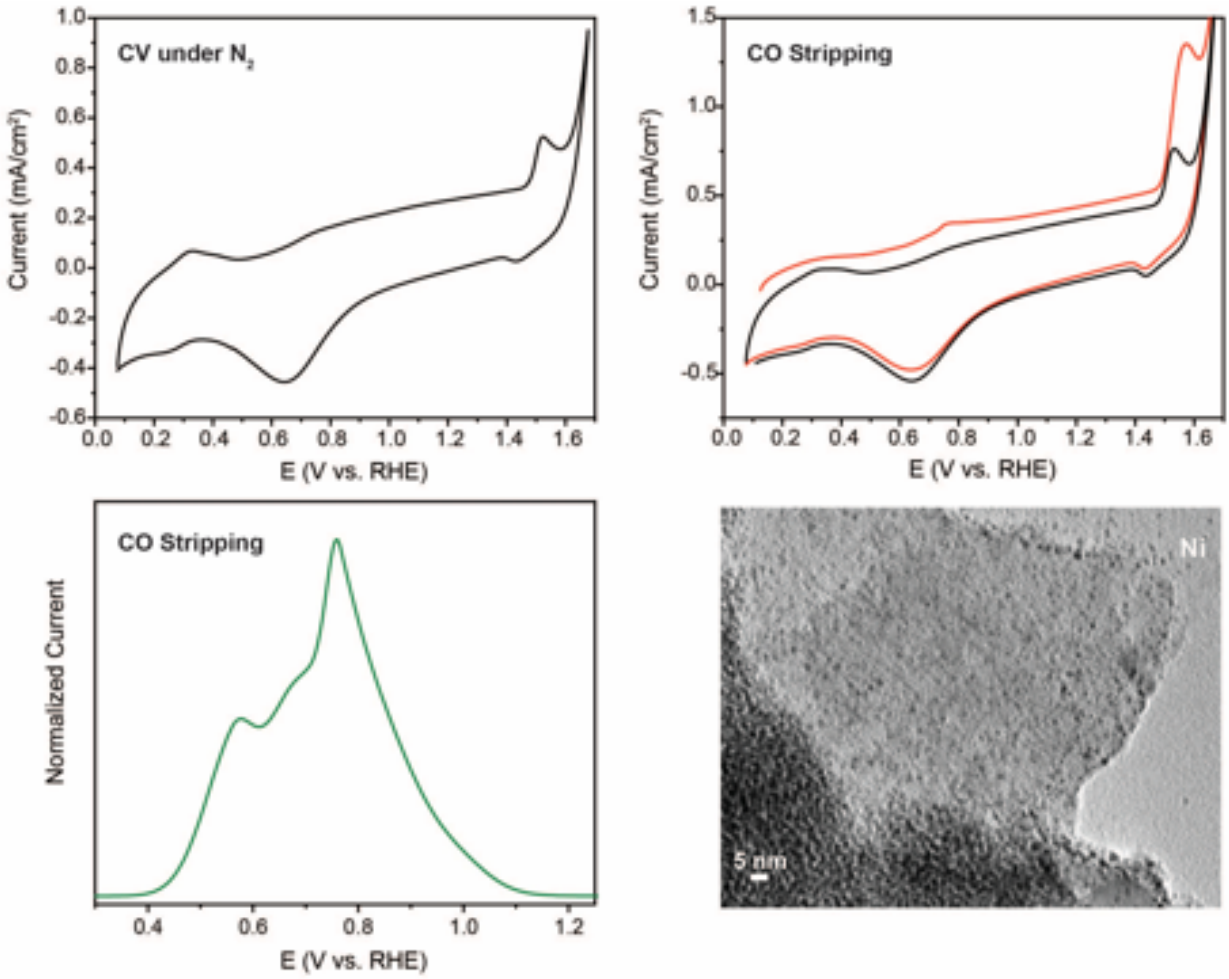

Figure A.20. TEM and CO stripping of potassium hydroxide post-treated Pt-NiO_x.

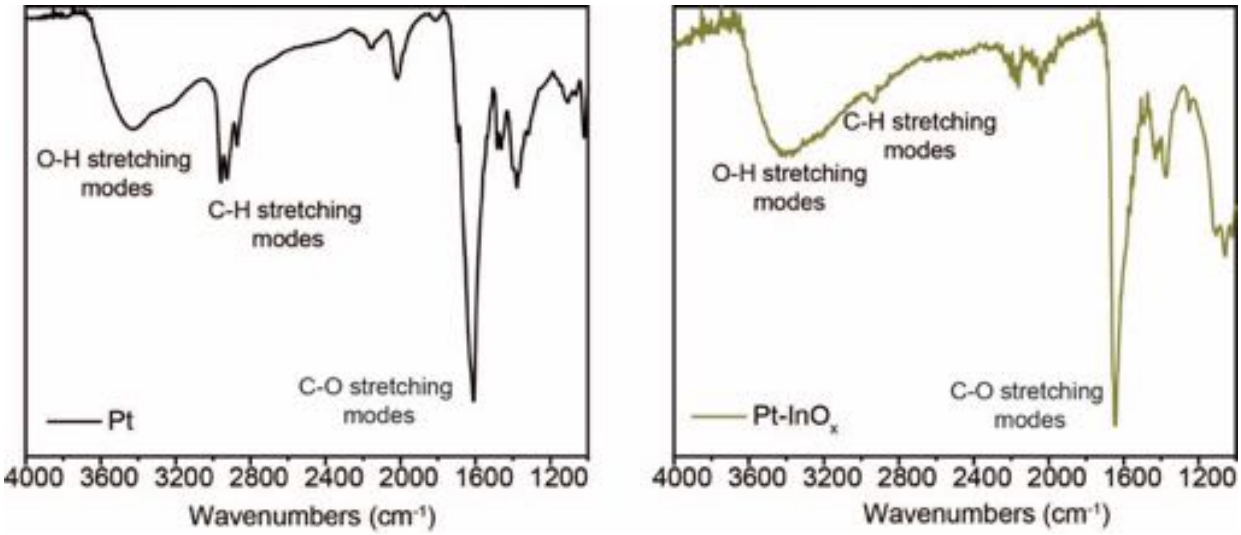

Figure A.21. Fourier-transform infrared spectra of Pt and Pt-InO_x.

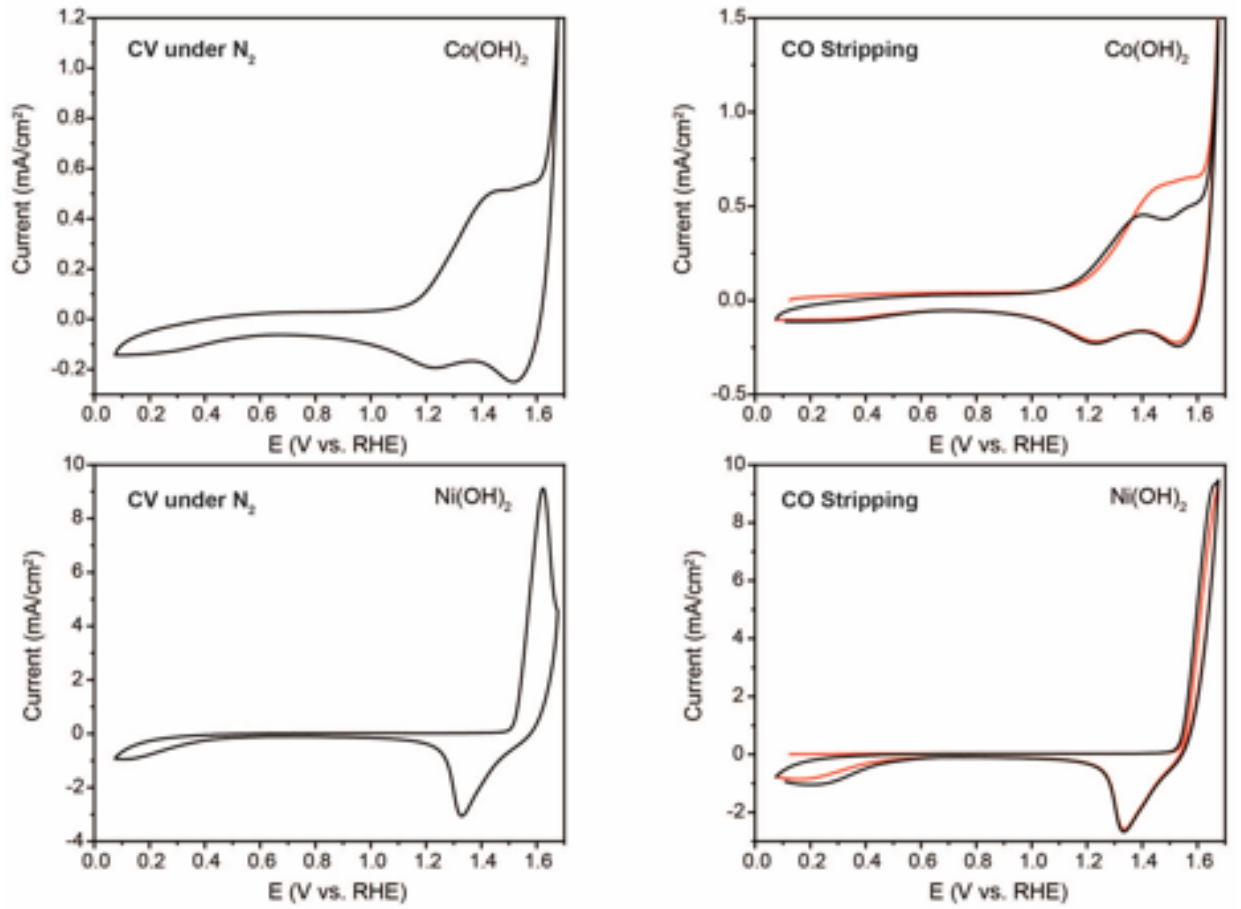

Figure A.22. CV and CO stripping of $Ni(OH)_2$ and $Co(OH)_2$ only.

4. References

(1) M. C. Biesinger, B. P. Payne, A. P. Grosvenor, L. W. M. Lau, A. R. Gerson, R. S. C. Smart, *Appl. Surf. Sci.,* **2011**, *257*, 2717-2730.

(2) M. C. Biesinger, L. W. M. Lau, A. R. Gerson, R. S. C. Smart, *Appl. Surf. Sci*., **2010,** *257*, 887-898.

(3) C. Donley, D. Dunphy, D. Paine, C. Carter, K. Nebesny, P. Lee, D. Alloway, N. R. Armstrong, *Langmuir*, **2002**, *18*, 450-457.

(4) C. V. Ramana, E. J. Rubio, C. D. Barraza, A. Miranda Gallardo, S. McPeak, S. Kotru, J. T. Grant, *J. Appl. Phys.,* **2014**, *115*, 043508.

(5) W. J. Huang, H. T. Wang, J. G. Zhou, J. Wang, P. N. Duchesne, D. Muir, P. Zhang, N. Han, F. P. Zhao, M. Zeng, J. Zhong, C. H. Jin, Y. G. Li, S. T. Lee, H. J. Dai, *Nat. Commun.,* **2015**, *6*, 10035.

(6) T. Biegler, D. A. J. Rand, R. Woods, *J. Electroanal. Chem.,* **1971***, 29*, 269-277.

APPENDIX B. SUPPORTING INFORMATION FOR CHAPTER 2

1. Physical Characterization Methods

Powder X-ray diffraction (XRD) was obtained using a Panalytical Empyrean Powder X-ray diffractometer using the reflection/transmission spinner in the Bragg-Brentano geometry. XRD patterns were measured in a two theta range of 2°–80° and 10°–70°, using a step size of 0.013°. All of the samples were sealed under Kapton tape and packaged under a nitrogen atmosphere. The phases reported were matched to β-$Co(OH)_2$ (JCPDS card No. 00-030-0443), β-$Ni(OH)_2$ (JCPDS card No. 00-014-0117), metallic Co (JCPDS card No. 00-001-1278), metallic Ni (JCPDS card No. 00-004-0850, CoO (JCPDS card No. 00-048-1719) and NiO (JCPDS card No. 00-004-835). Transmission electron microscopy (TEM) images and selected-area electron diffraction patterns (SAED) were acquired using an FEI Tecnai G20 TEM equipped with a 200 kV LaB_6 filament. X-ray photoelectron (XPS) spectra were obtained with a Kratos AXIS Ultra Delay-Line Detector Imaging X-ray Photoelectron Spectrometer. Diffuse-Reflectance UV-Vis (DRUV-Vis) on powder samples was taken on a JASCO V-670 spectrophotometer using a 150 mm integrating sphere. Electron-doped materials must be stored under an inert atmosphere and transferred in air-tight vessels. Solution-phase UV-Vis was taken on a Agilent Cary 6000i UV-Vis-NIR Spectrophotometer operating in transmission mode. Atomic force microscopy (AFM) data was obtained using a Veeco Dimension 3100 AFM in tapping mode.

X-ray absorption spectroscopy (XAS) experiments were carried out at the 10-ID beamline at the Advanced Photon Source (APS), Argonne National Laboratory at the Co K-edge (7710.7 eV) and Ni K-edge (8330.8 eV) in transmission mode. Sample preparation was done under a nitrogen atmosphere. Samples were ground to a fine powder, diluted with carbon, and pressed to form a self-supported wafer. Spectra were obtained at room temperature. During each measurement, a Co or Ni foil was scanned simultaneously through a third ion chamber for internal energy calibration. XAS data fitting was performed using the Demeter software package.[4] The reference Co and Ni foil were first fit to their known crystallographic structures in order to obtain an amplitude reduction factor (S_0^2) for the Co and Ni K-edge. Co and Ni K-edge spectra were then fit to known crystallographic structures: β-$Co(OH)_2$,[5] Co metal,[6] β-$Ni(OH)_2$,[7] and Ni metal.[8] EXAFS coordination parameters were obtained by a least-squares fit in R-space of the k^2-weighed Fourier

transform data from 2.5 to 10 $Å^{-1}$. Fittings were done by refining bond distances (R), coordination numbers (CN), energy shift (E_0), and Debye Waller factor (σ^2).

2. Conductivity Methods

All conductivity measurements were taken using a home-built apparatus (**Figure 2.20**) inside of a glovebox containing a nitrogen atmosphere. The device is composed of two metal rods (diameter = 0.233 cm) and a glass tube with an inner diameter of 0.233 cm. For each sample, sufficient powder was added to ensure full coverage of the metal rod surface and the powder was pressed into a pellet between the rods using an IRWIN 3-inch C-Clamp. The pellet thickness is measured by taking the difference of the rods with and without the powder pellet using a Fisherbrand Traceable Digital caliper. The I-V experiments were conducted on a Gamry Interface 1010B potentiostat using a scan window from –1 V to +1 V with scan rate 0.01 V/s. For samples that had currents less than ~10 nA, a Keithley 236 high current source measure unit was used with a scan window of –10 V to +10 V and scan rate of 0.5 V/s.

For each sample, I-V curves were measured for at least four pellet thicknesses (L) at a constant cross-sectional area (A) in order to obtain the average resistivity (ρ) using Equiv. 1 and Equiv. 2. Average conductivity (σ) was calculated using Equiv. 3. All data is provided in Figures **B.10-B.14** and **Table 2.9**.

$$R = \frac{V}{I} \ (eq.1)$$

$$R = \ \rho \ \frac{L}{A} \ (eq.2)$$

$$\sigma = \frac{1}{\rho} \ (eq.3)$$

3. Physical Characterization Data

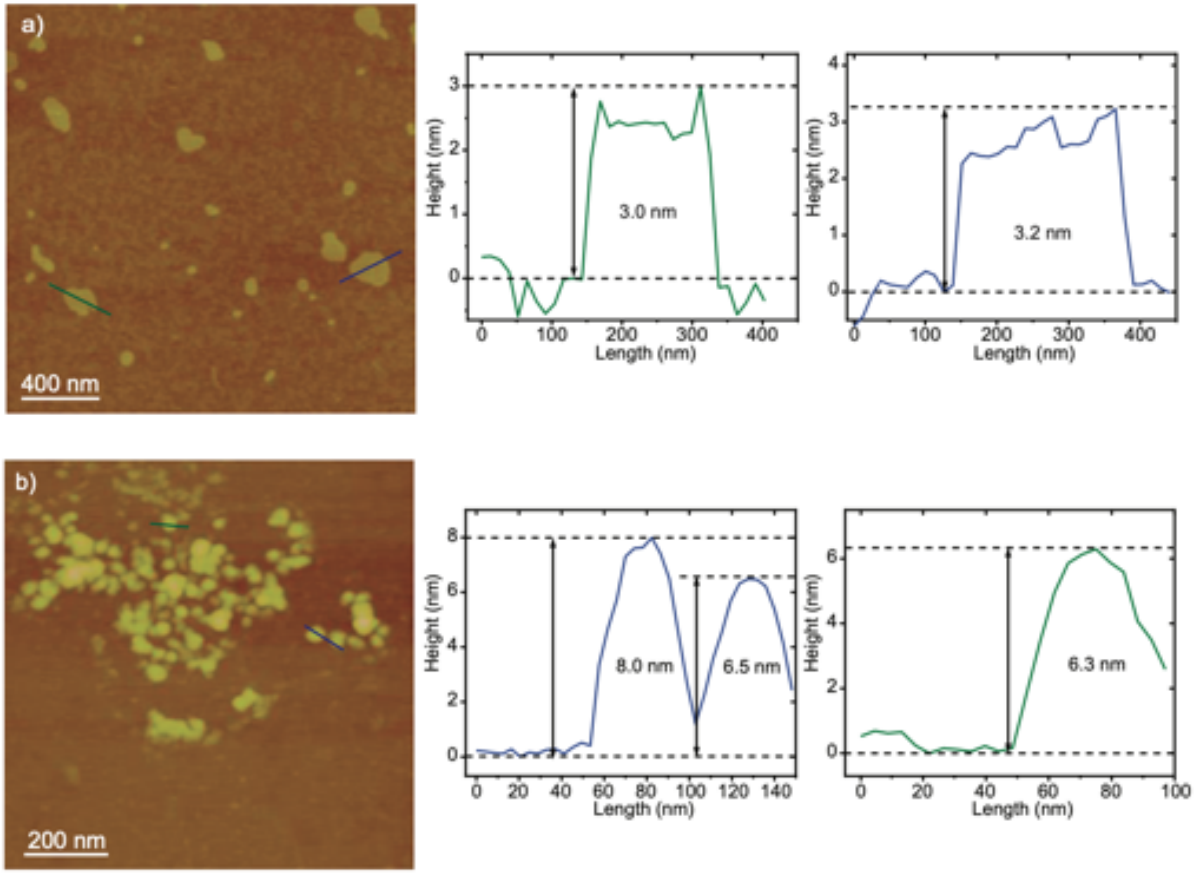

Figure B.1. Atomic force microscopy (AFM) images with height profiles on two different areas for (**a**) $Co(OH)_2$ and (**b**) $Ni(OH)_2$.

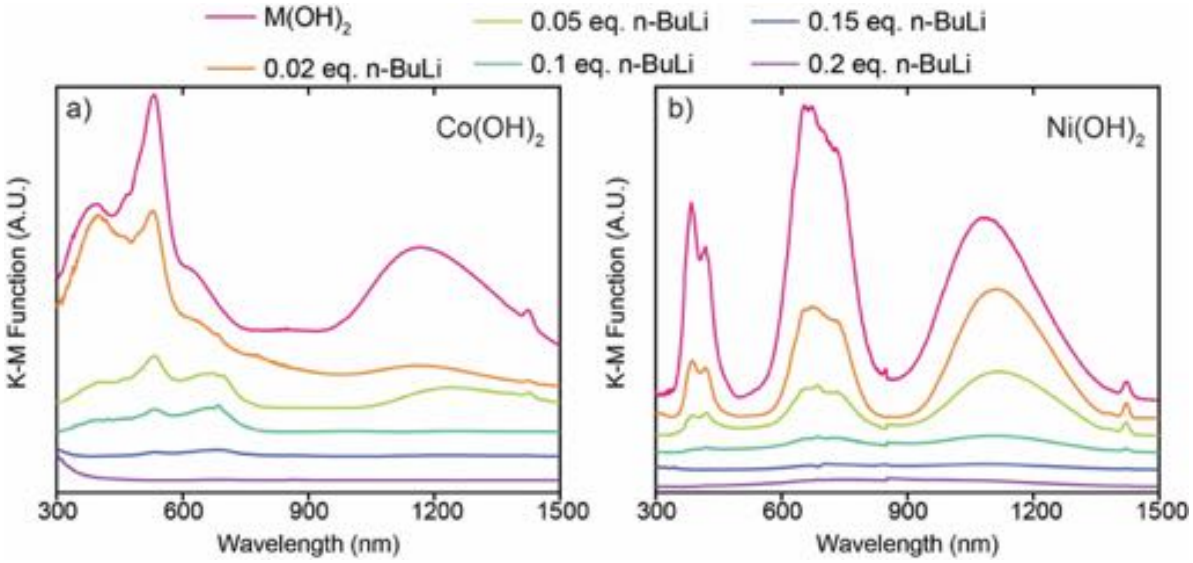

Figure B.2. DRUV-Vis of (**a**) $Co(OH)_2$ and (**b**) $Ni(OH)_2$ treated with varying equiv. of n-BuLi.

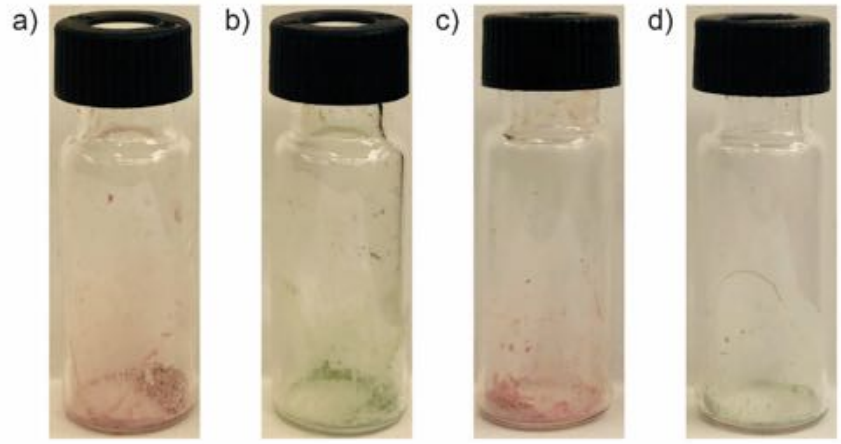

Figure B.3. Photographs of n-BuLi treated metal hydroxide powders after full recovery, i.e. protonation and electron extraction (MeOH + $*Fc^{+}$). Varying equivalents of n-BuLi were used during the electron doping step. (**a**) 0.1 equiv. n-BuLi $Co(OH)_2$, (**b**) 0.1 equiv. n-BuLi $Ni(OH)_2$, (**c**) 0.25 equiv. n-BuLi $Co(OH)_2$, and (**d**) 0.25 equiv. n-BuLi $Ni(OH)_2$.

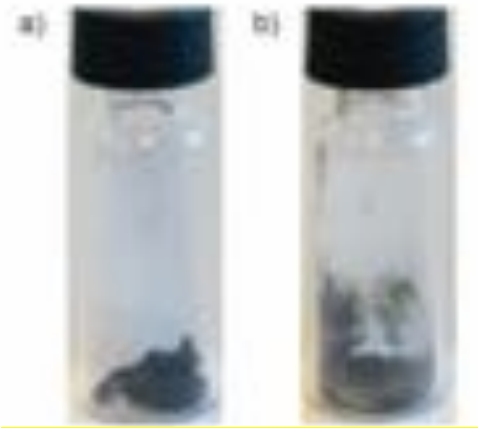

Figure B.4. Photographs of 1 equiv. n-BuLi treated (**a**) $Co(OH)_2$ and (**b**) $Ni(OH)_2$ powders after attempting a full recovery, i.e. protonation and electron extraction (MeOH + $*Fc^{+}$).

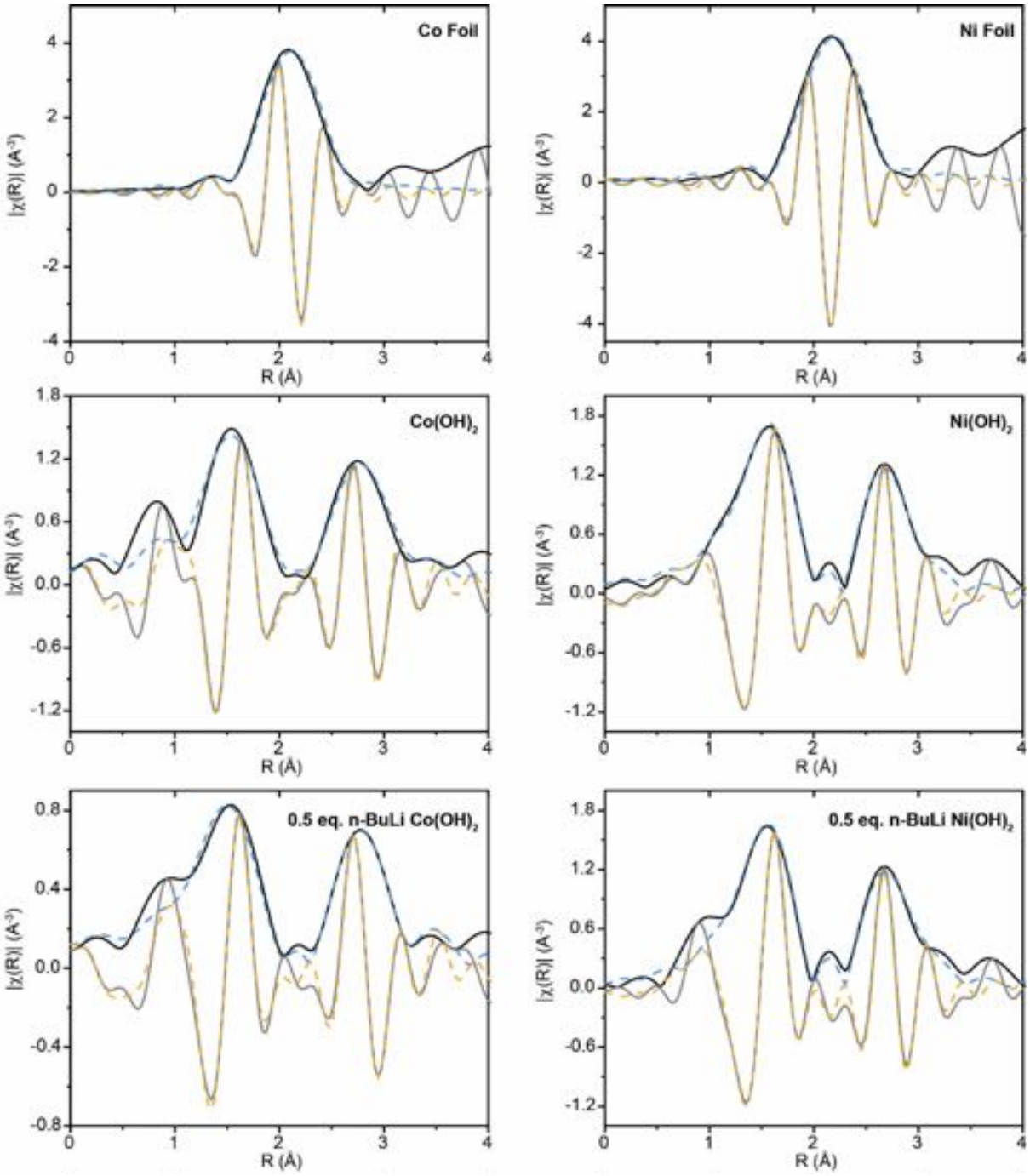

Figure B.5. Co and Ni K-edge EXAFS fitting results for the samples indicated. The black solid line is the FT magnitude, the dotted blue line is the fit to the FT magnitude, the solid gray line is the FT real part, and the dotted yellow line is the fit to the FT real part.

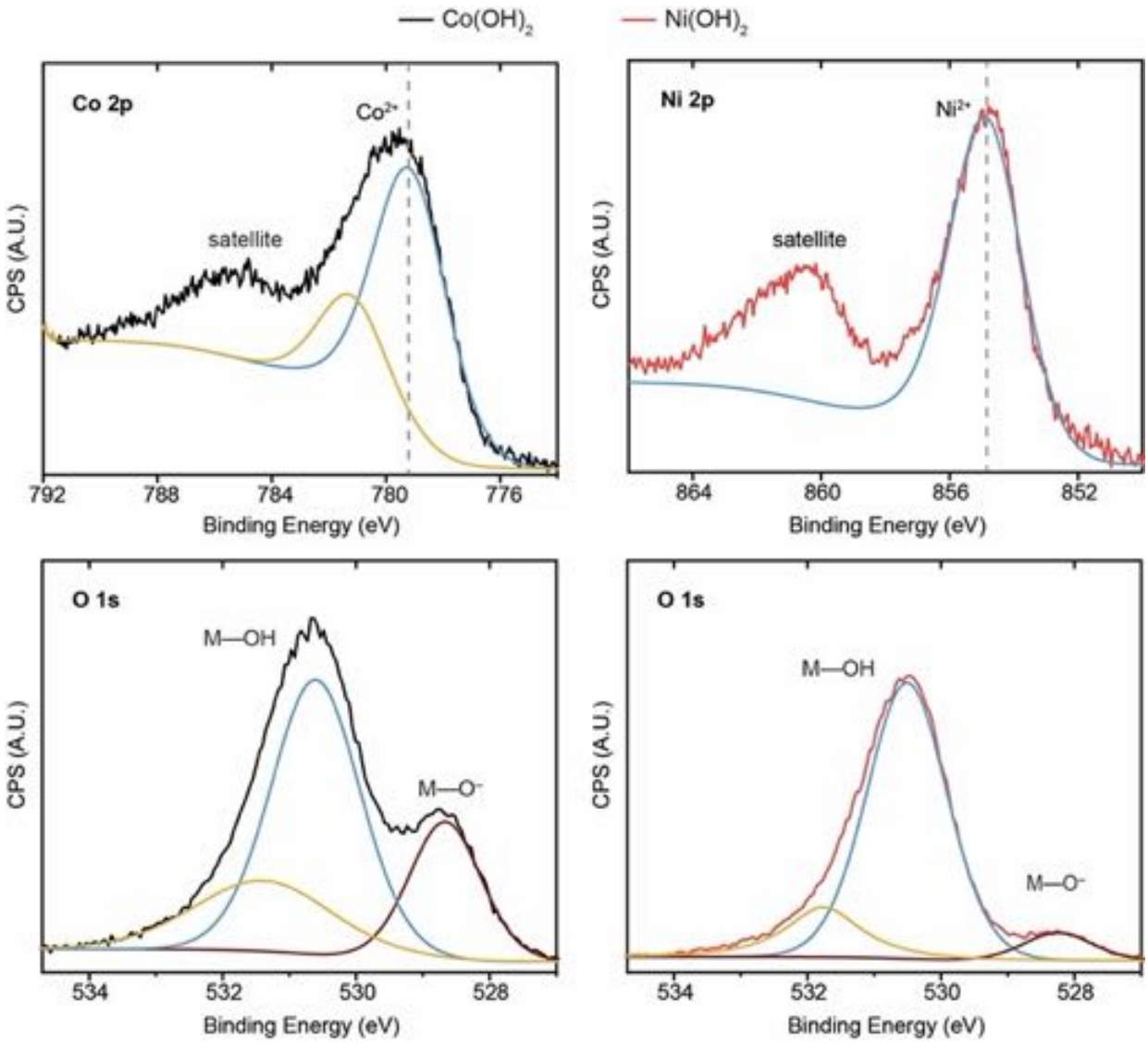

Figure B.6. High-resolution XPS of M 2p and O 1s regions for LDA treated $Co(OH)_2$ and $Ni(OH)_2$. The O 1s region is consistent with deprotonation of M–OH sites.[11]

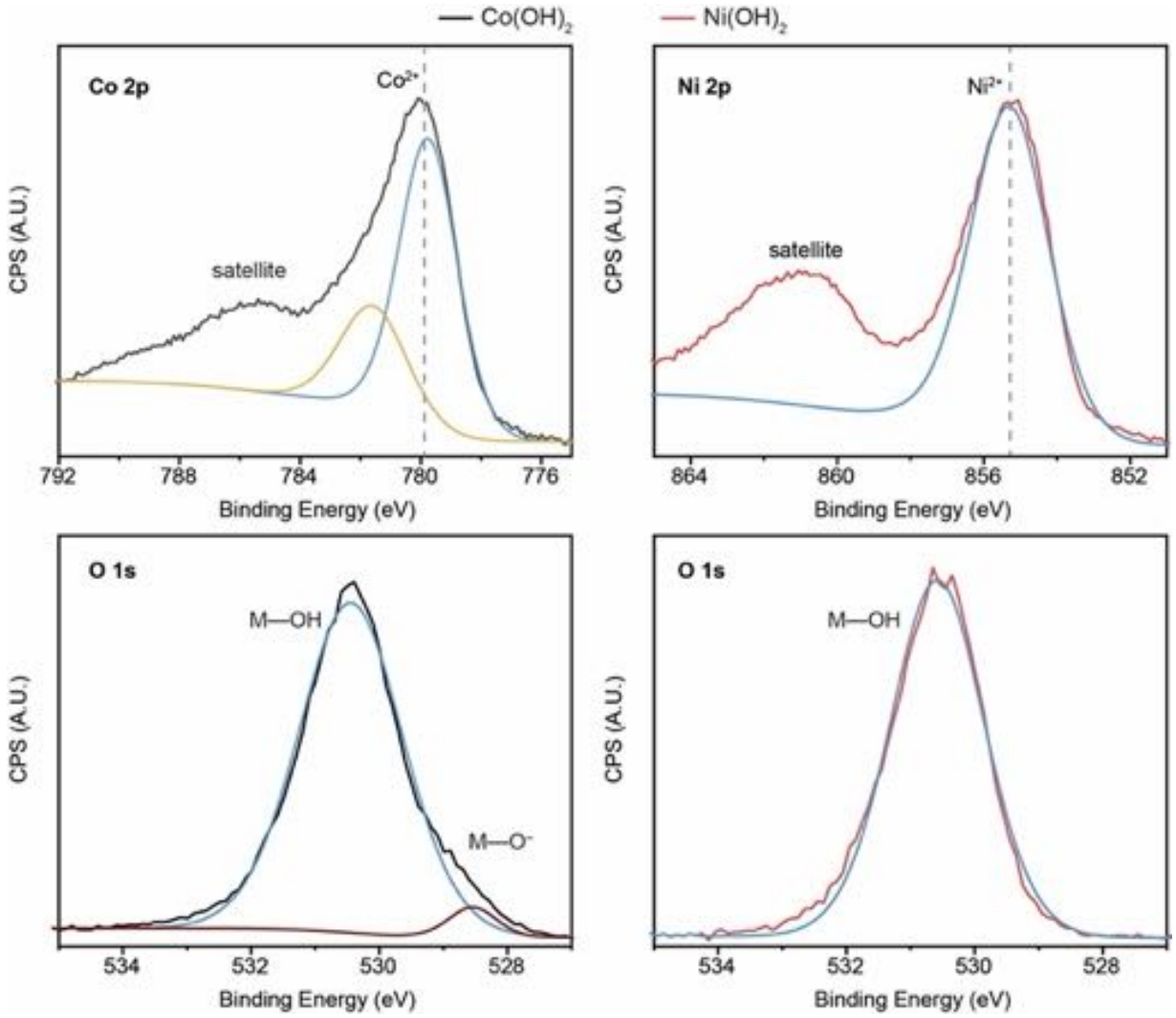

Figure B.7. High-resolution XPS of M 2p and O 1s regions for LDA treated $Co(OH)_2$ and $Ni(OH)_2$ after reprotonation with MeOH.

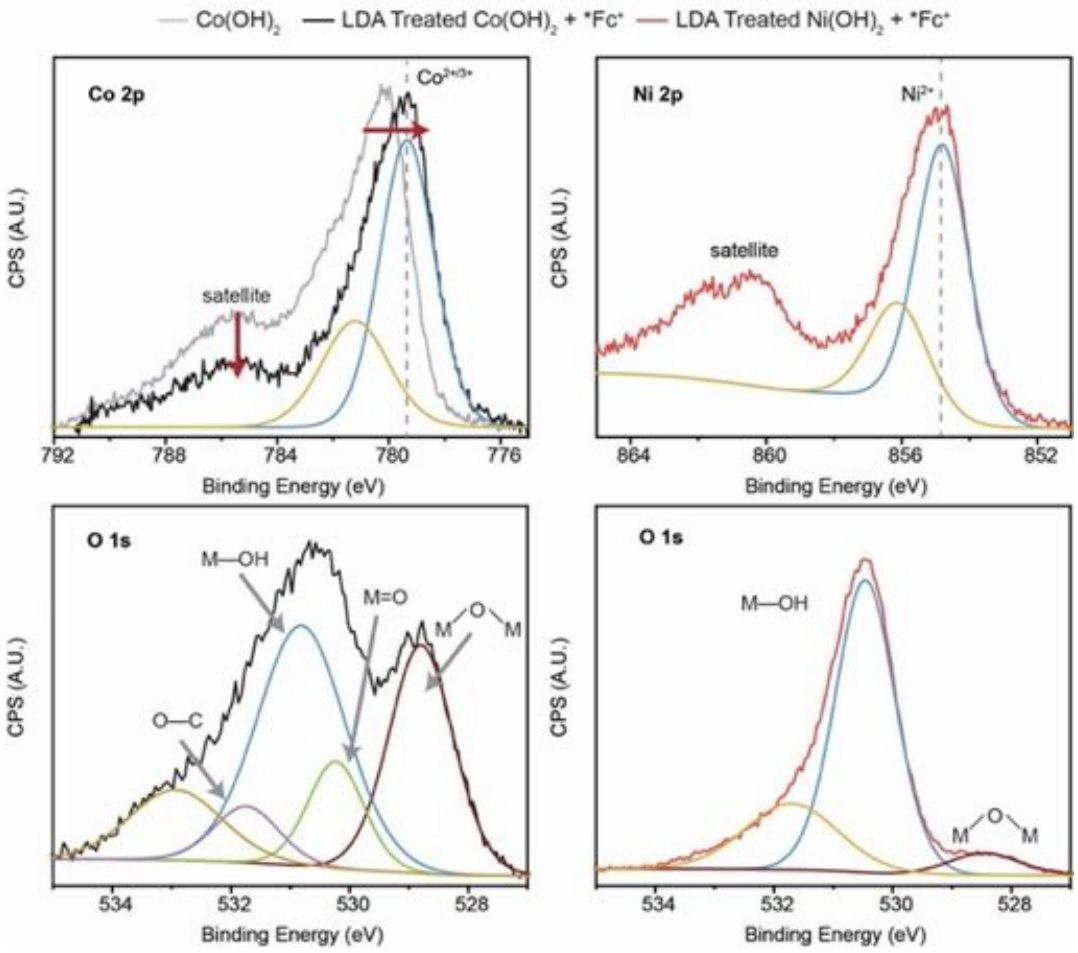

Figure B.8. High-resolution XPS of the M 2p and O 1s regions for LDA treated $M(OH)_2$ after intentional oxidation, i.e. direct $*Fc^+$ treatment without reprotonation. The differences in the M 2p and O 1s peaks compared to as-synthesized, particularly for $Co(OH)_2$, are characteristic of the formation of $M^{3+}OOH$ species.[12-14]

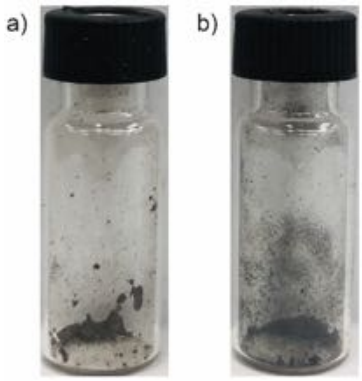

Figure B.9. Photographs of LDA-treated $M(OH)_2$ powders after intentional oxidation using $*Fc^+$. (**a**) $Co(OH)_2$, (**b**) $Ni(OH)_2$.

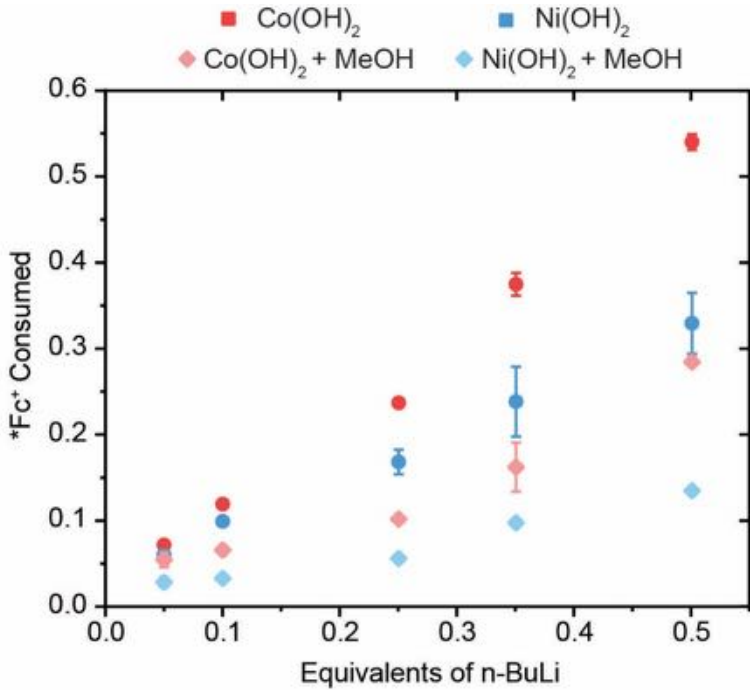

Figure B.10. Equivalents of $*Fc^+$ consumed for n-BuLi treated $Co(OH)_2$ and $Ni(OH)_2$ with and without MeOH reprotonation.

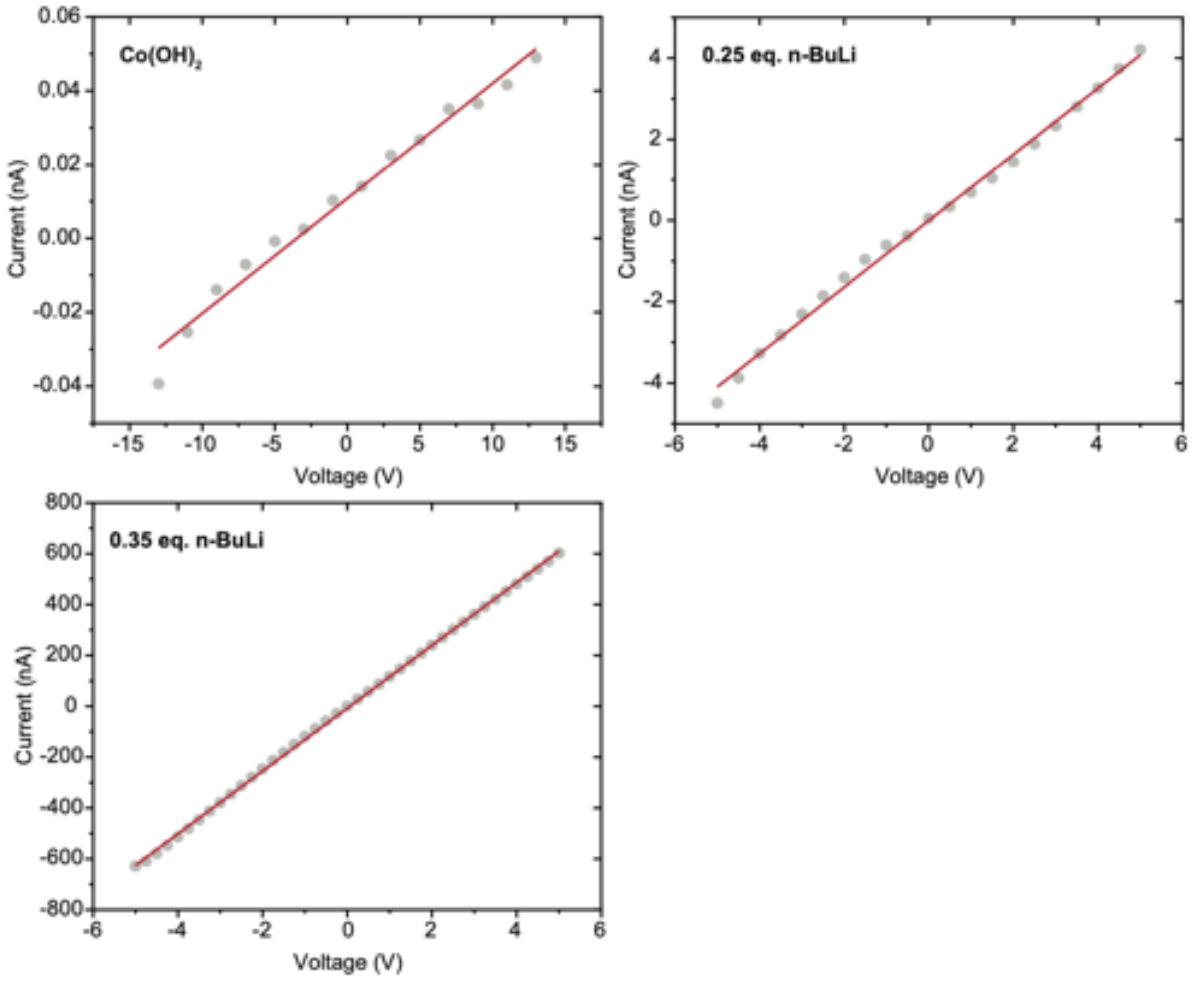

Figure B.11. Representative I-V curves for $Co(OH)_2$, 0.25 equiv. n-BuLi $Co(OH)_2$, and 0.35 equiv. n-BuLi $Co(OH)_2$. The pellets were formed *in situ*, and electrical measurements were performed under a nitrogen atmosphere at room temperature. The grey circles represent experimental data and the red line is the linear regression.

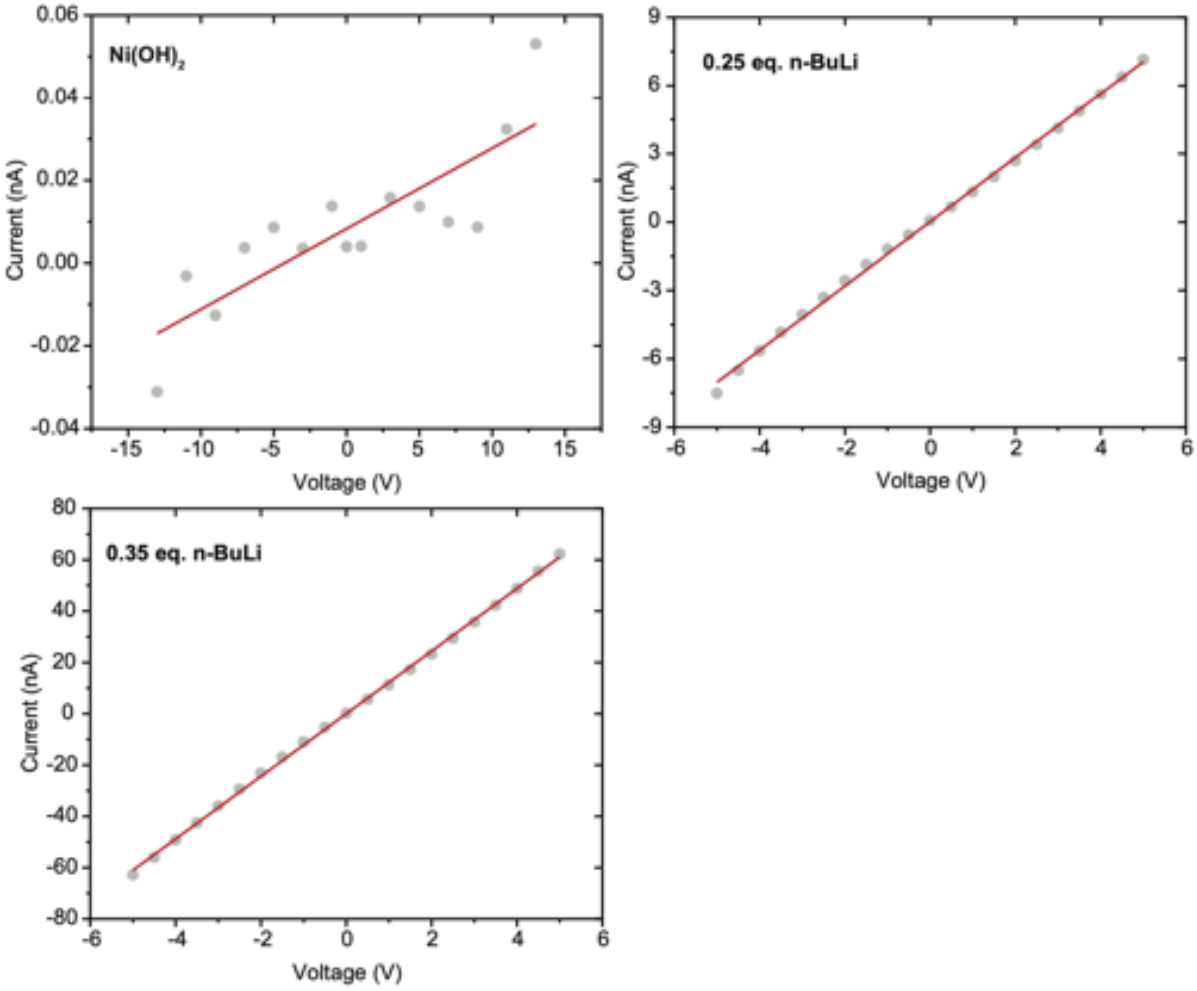

Figure B.12. Representative I-V curves for $Ni(OH)_2$, 0.25 equiv. n-BuLi $Ni(OH)_2$, and 0.35 equiv. n-BuLi $Ni(OH)_2$. The pellets were formed *in situ*, and electrical measurements were performed under a nitrogen atmosphere at room temperature. The grey circles represent experimental data and the red line is the linear regression.

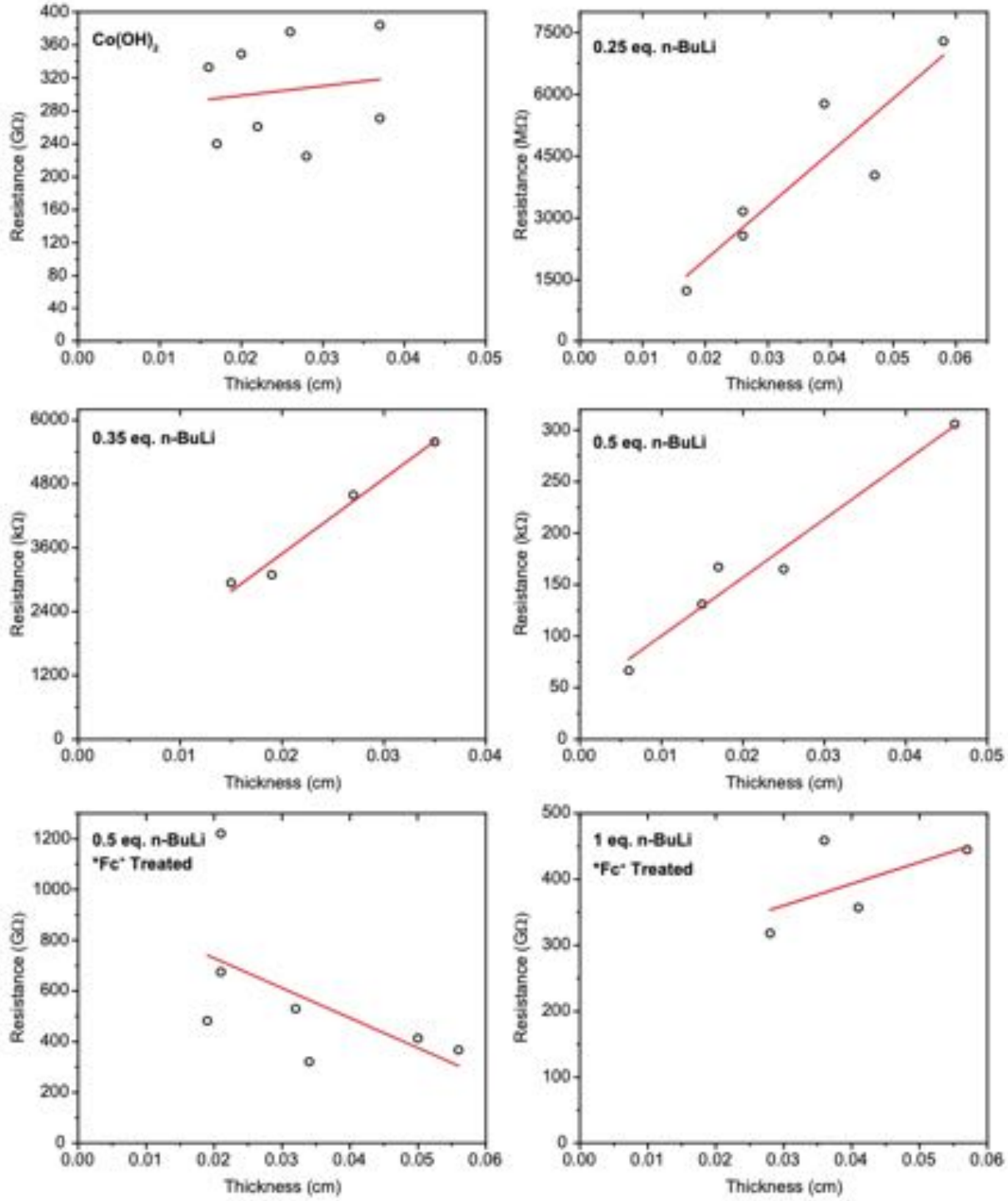

Figure B.13. Resistance vs. pellet thickness plots for representative $Co(OH)_2$ samples.

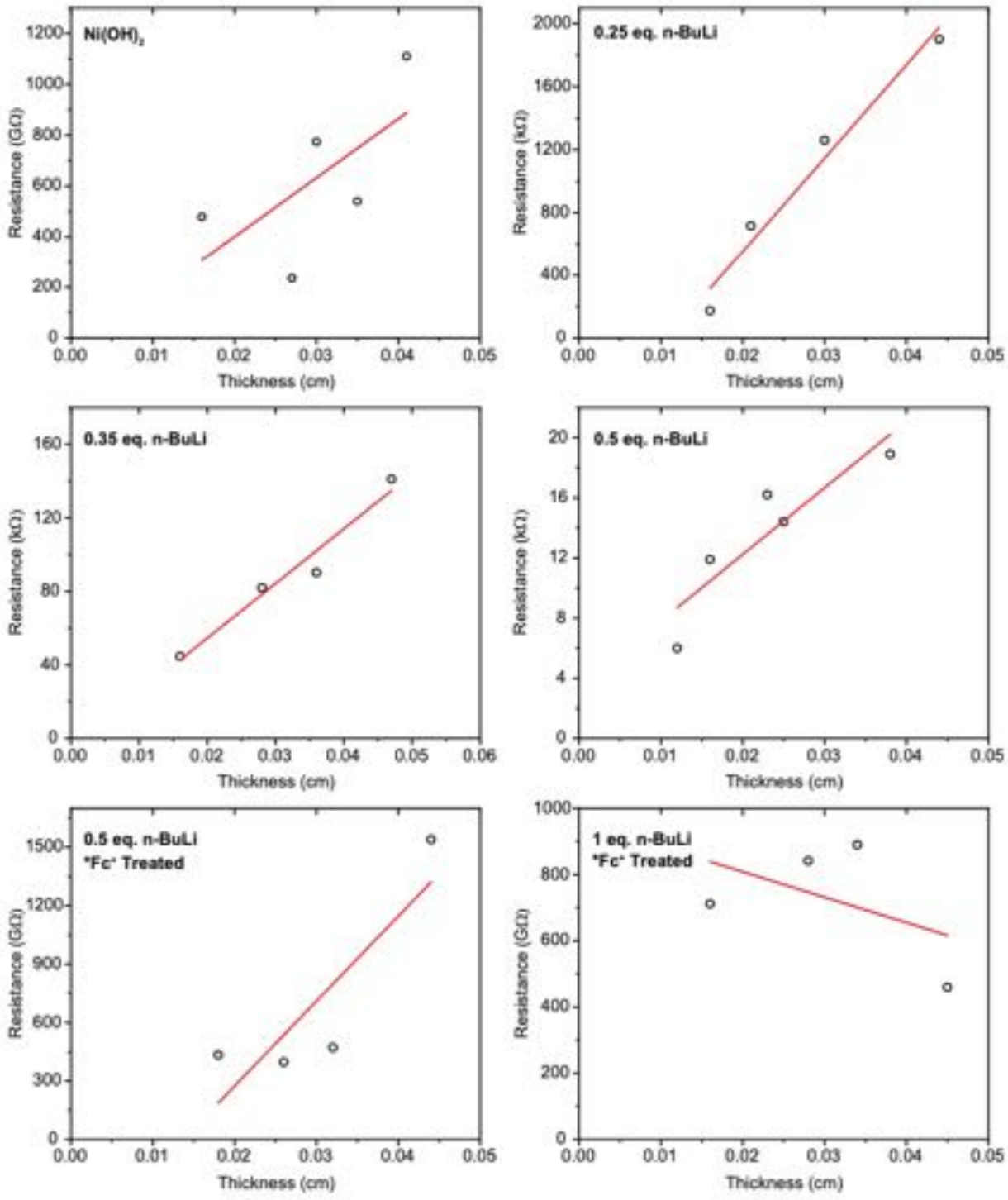

Figure B.14. Resistance vs. pellet thickness plots for representative $Ni(OH)_2$ samples.

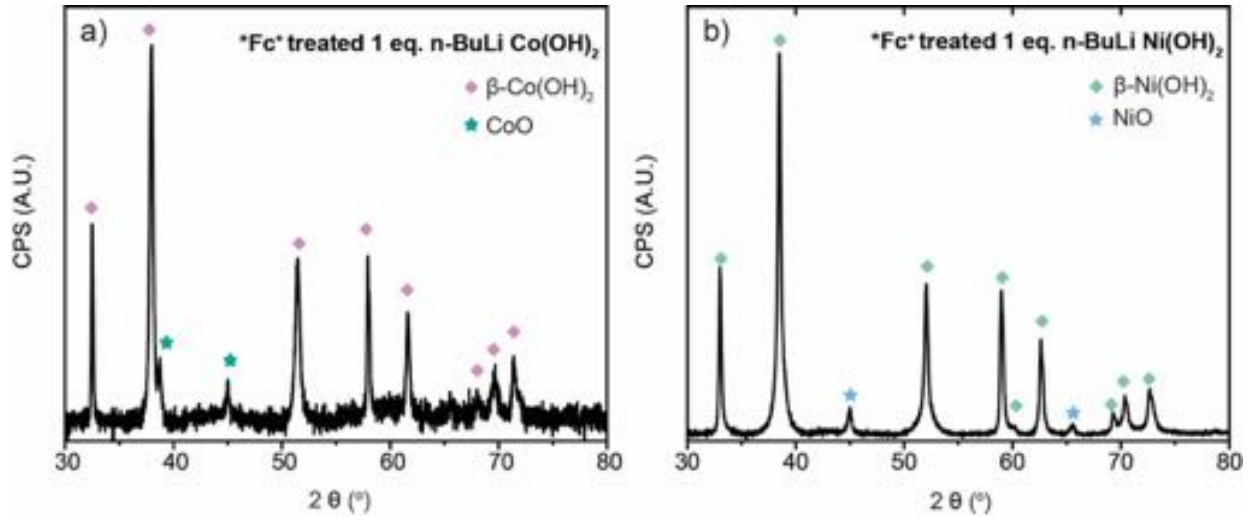

Figure B.15. Powder XRD patterns for 1 equiv. n-BuLi (**a**) $Co(OH)_2$ and (**b**) $Ni(OH)_2$ powders after intentional oxidation using $*Fc^+$. Crystalline rock salt metal oxide phases are observed.

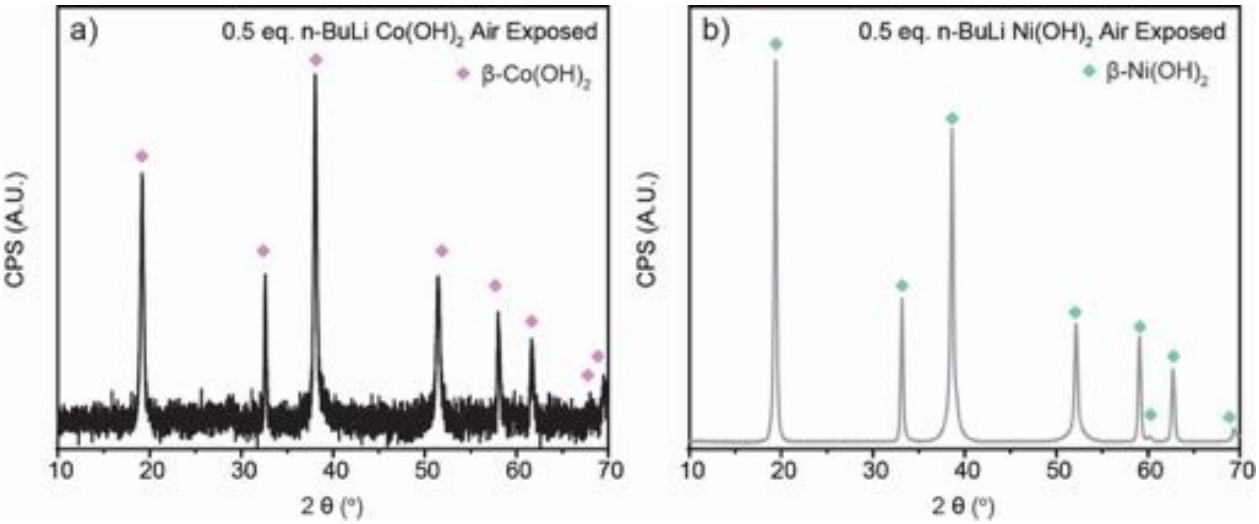

Figure B.16. Powder XRD patterns for 0.5 equiv. n-BuLi (**a**) $Co(OH)_2$ and (**b**) $Ni(OH)_2$ samples after in-situ air exposure.

6. References

(1) Miller, J. S.; Calabrese, J. C.; Rommelmann, H.; Chittipeddi, S. R.; Zhang, J. H.; Reiff, W. M.; Epstein, A. J., *J. Am. Chem. Soc.*, **1987**, *109*, 769-781.

(2) Cheng, J.; Chen, X.; Wu, J.-S.; Liu, F.; Zhang, X.; Dravid, V. P., *CrystEngComm,* **2012**, *14*, 6702-6709.

(3) Liu, X.; Qiu, G.; Wang, Z.; Li, X., *Nanotechnology*, **2005**, *16*, 1400.

(4) Ravel, B.; Newville, M., *J. Synchrotron Radiat.*, **2005**, *12*, 537-541.

(5) Hunt, D.; Garbarino, G.; Rodríguez-Velamazán, J. A.; Ferrari, V.; Jobbagy, M.; Scherlis, D. A., *Phys. Chem. Chem. Phys.*, **2016**, *18*, 30407-30414.

(6) Owen, E.; Jones, D. M., *Proc. Phys. Soc. B*, **1954**, *67*, 456.

(7) Kazimirov, V. Y.; Smirnov, M.; Bourgeois, L.; Guerlou-Demourgues, L.; Servant, L.; Balagurov, A.; Natkaniec, I.; Khasanova, N.; Antipov, E., *Solid State Ion.*, **2010**, *181*, 1764-1770.

(8) Jette, E. R.; Foote, F., *J. Chem. Phys.*, **1935**, *3*, 605-616.

(9) Schrauben, J. N.; Hayoun, R.; Valdez, C. N.; Braten, M.; Fridley, L.; Mayer, J. M., *Science*, **2012**, *336*, 1298-1301.

(10) Schimpf, A. M.; Ochsenbein, S. T.; Buonsanti, R.; Milliron, D. J.; Gamelin, D. R., *Chem. Commun*., **2012**, *48*, 9352-9354.

(11) Dupin, J.-C.; Gonbeau, D.; Vinatier, P.; Levasseur, A., *Phys. Chem. Chem. Phys.*, **2000**, *2*, 1319-1324.

(12) Yang, J.; Liu, H.; Martens, W. N.; Frost, R. L., *J. Phys. Chem. C*, **2010**, *114*, 111-119.

(13) Biesinger, M. C.; Payne, B. P.; Grosvenor, A. P.; Lau, L. W.; Gerson, A. R.; Smart, R. S. C., *Appl. Surf. Sci.*, **2011**, *257* , 2717-2730.

(14) Payne, B.; Biesinger, M.; McIntyre, N.; Phenomena, R., *J. Electron Spectrosc*., **2009**, *175*, 55-65.

(15) Sun, L.; Park, S. S.; Sheberla, D.; Dincă, M., *J. Am. Chem. Soc.,* **2016**, *138*, 14772-14782.

APPENDIX C. SUPPORTING INFORMATION FOR CHAPTER 3

1. Physical Characterization Methods

Powder X-ray diffraction (XRD) was obtained using a Panalytical Empyrean Powder X-ray diffractometer using the reflection/transmission spinner in Bragg-Brentano geometry. All of the samples were packed under nitrogen atmosphere and sealed under Kapton tape. XRD patterns were measured in a two theta range of 2°– 80° for α-$Co(OH)_2$, 2°–80° for β-$Co(OH)_2$, and 30°–80° for c-CoO using a step size of 0.013°. The phases were matched to known crystal structures: α-$Co(OH)_2$-SDS,[2] α-$Co(OH)_2$-Cl (JCPDS card No. 00-046-0605), β-$Co(OH)_2$ (JCPDS card No. 00-030-0443), metallic Co (JCPDS card No. 00-001-1278), and CoO (JCPDS card No. 00-048-1719). Transmission electron microscopy (TEM) images and selected-area electron diffraction patterns (SAED) were acquired using an FEI Tecnai G20 TEM equipped with a 200 kV LaB_6 filament. SAED patterns were indexed to known patterns from the literature.[1,3,5] High-angle annular dark-field scanning transmission electron microscopy (HAADF-STEM) images were obtained on an FEI Talos F200X S/TEM with a 200 kV X-FEG field-emission source. X-ray photoelectron (XPS) spectra were obtained with a PHI VersaProbe II Scanning X-ray Microprobe or a Kratos AXIS Ultra Delay-Line Detector Imaging X-ray Photoelectron Spectrometer. Survey spectra are collected for all samples (**Figure C.5-C.6, C.20-C.21**) as well as selected high-resolution spectra. Diffuse-Reflectance UV-Vis (DRUV-Vis) on powder samples was obtained on a JASCO V-670 spectrophotometer using a 150 mm integrating sphere.

X-ray absorption spectroscopy (XAS) experiments were carried out at the 10-ID beamline at the Advanced Photon Source (APS), Argonne National Laboratory at the Co K-edge (7708.8 eV) in transmission mode. Sample preparation was done under a nitrogen atmosphere. Samples were ground to a fine powder, diluted with carbon, and pressed to form a self-supported wafer. Spectra were obtained at room temperature. During each measurement, a Co foil was scanned simultaneously through a third ion chamber for internal energy calibration. XAS data fitting was performed using the Demeter software package.[6] The reference Co foil was first fit to the metallic Co crystal structure in order to obtain an amplitude reduction factor (S_0^2) for the Co K-edge. Co K-edge spectra were then fit to known crystallographic structures: β-$Co(OH)_2$,[7] $Co_2Cl(OH)_3$,[8] and Co metal.[9] EXAFS coordination parameters were obtained by a least-squares fit in R-space of the

k^2-weighed Fourier transform data from 3 to 9 $Å^{-1}$. Fittings were done by refining bond distances (R), coordination numbers (CN), energy shift (E_0), and Debye Waller factor (σ^2).

2. Conductivity Measurements

All conductivity measurements were made using a home-built apparatus inside of a nitrogen-filled glovebox. The device is composed of two metal rods (diameter = 0.233 cm) and a PEEK plastic tube with an inner diameter of 0.233 cm (**Figure 2.20**). For each sample, sufficient powder was added to ensure full coverage of the metal rod surface, and the powder was pressed into a pellet between the rods using an IRWIN 3-inch C-Clamp. The pellet thickness is measured by taking the difference of the rods with and without the powder pellet using a Fisherbrand Traceable Digital caliper. The I-V experiments were conducted on a Gamry Interface 1010B potentiostat using a scan window from –1 V to +1 V with scan rate 0.05 V/s. For samples with currents less than ~10 nA, a Keithley 236 high current sourcemeter was used, with a scan window ranging from ± 3 V to ± 10 V and scan rate of 0.05 V/s.

For each sample, I-V curves were measured for at least three pellet thicknesses (L) at a constant cross-sectional area (A) in order to obtain the average resistivity (ρ) using Equiv. 1 and Equiv. 2. Average conductivity (σ) was calculated using Equiv. 3. All data is provided in **Figures C.1-C.4, C.11-C.12, C.17-C.18**.

$$R = \frac{V}{I} \ (eq. 1)$$

$$R = \ \rho \ \frac{L}{A} \ (eq. 2)$$

$$\sigma = \frac{1}{\rho} \ (eq. 3)$$

3. Supplementary Figures and Tables

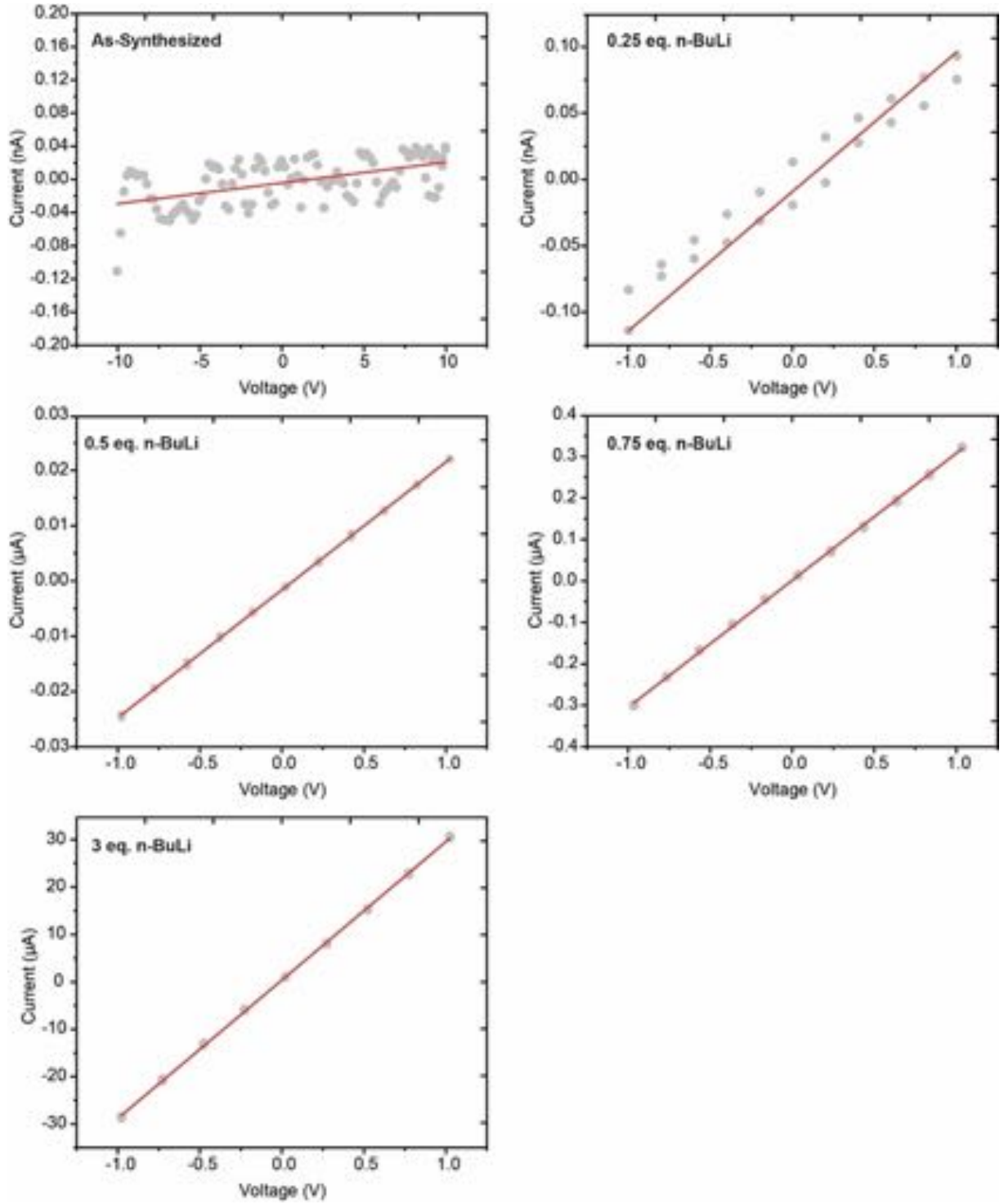

Figure C.1. Representative I-V curves for α-$Co(OH)_2$-Cl treated with varying equivalents of n-BuLi. The pellets were formed in-situ and the electrical measurements were performed under a nitrogen atmosphere. The gray lines represent the experimental data and the red line is the linear fit.

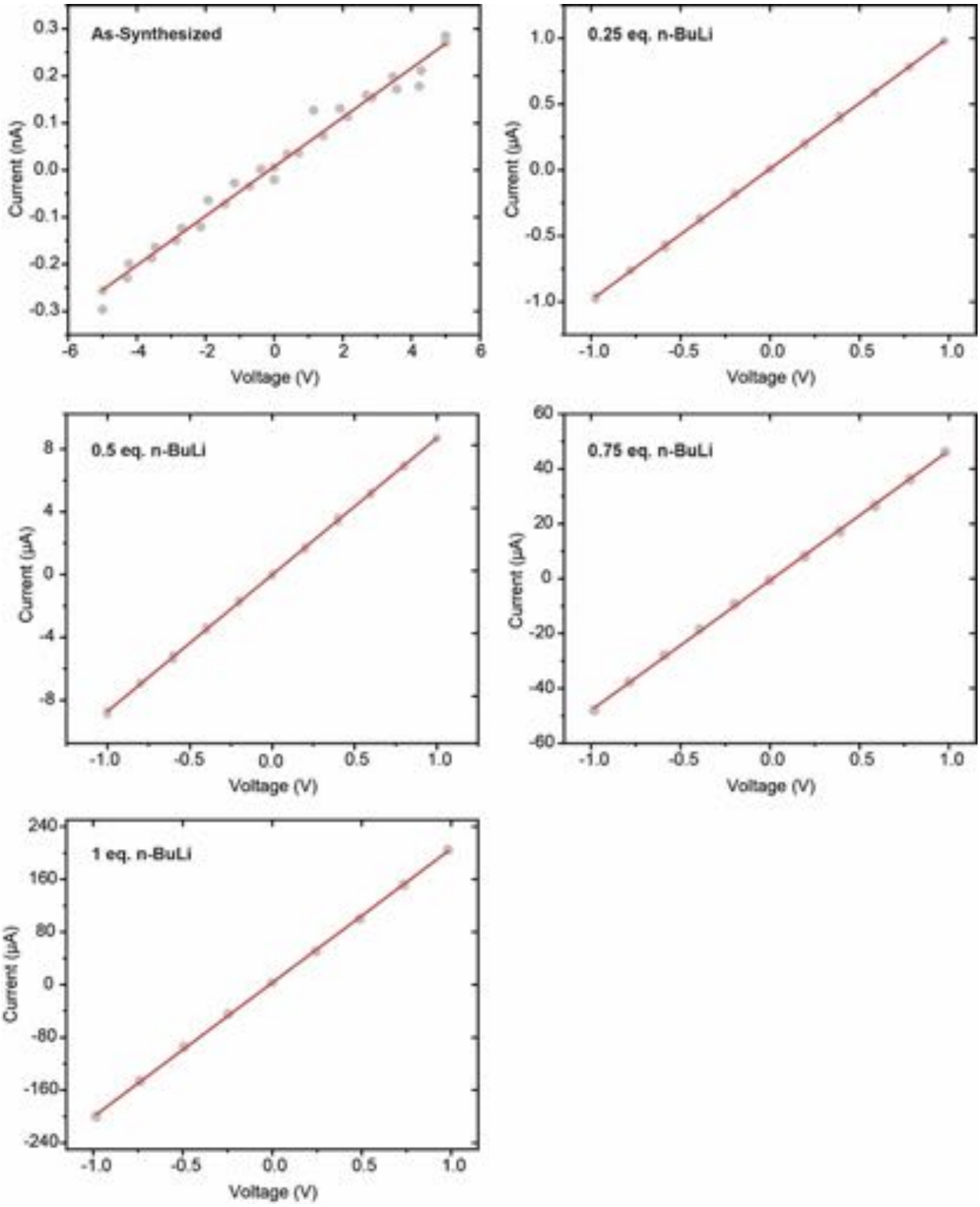

Figure C.2. Representative I-V curves for β-$Co(OH)_2$ with treated with varying equivalents of n-BuLi. The pellets were formed in-situ and the electrical measurements were performed under a nitrogen atmosphere. The gray lines represent the experimental data and the red line is the linear fit.

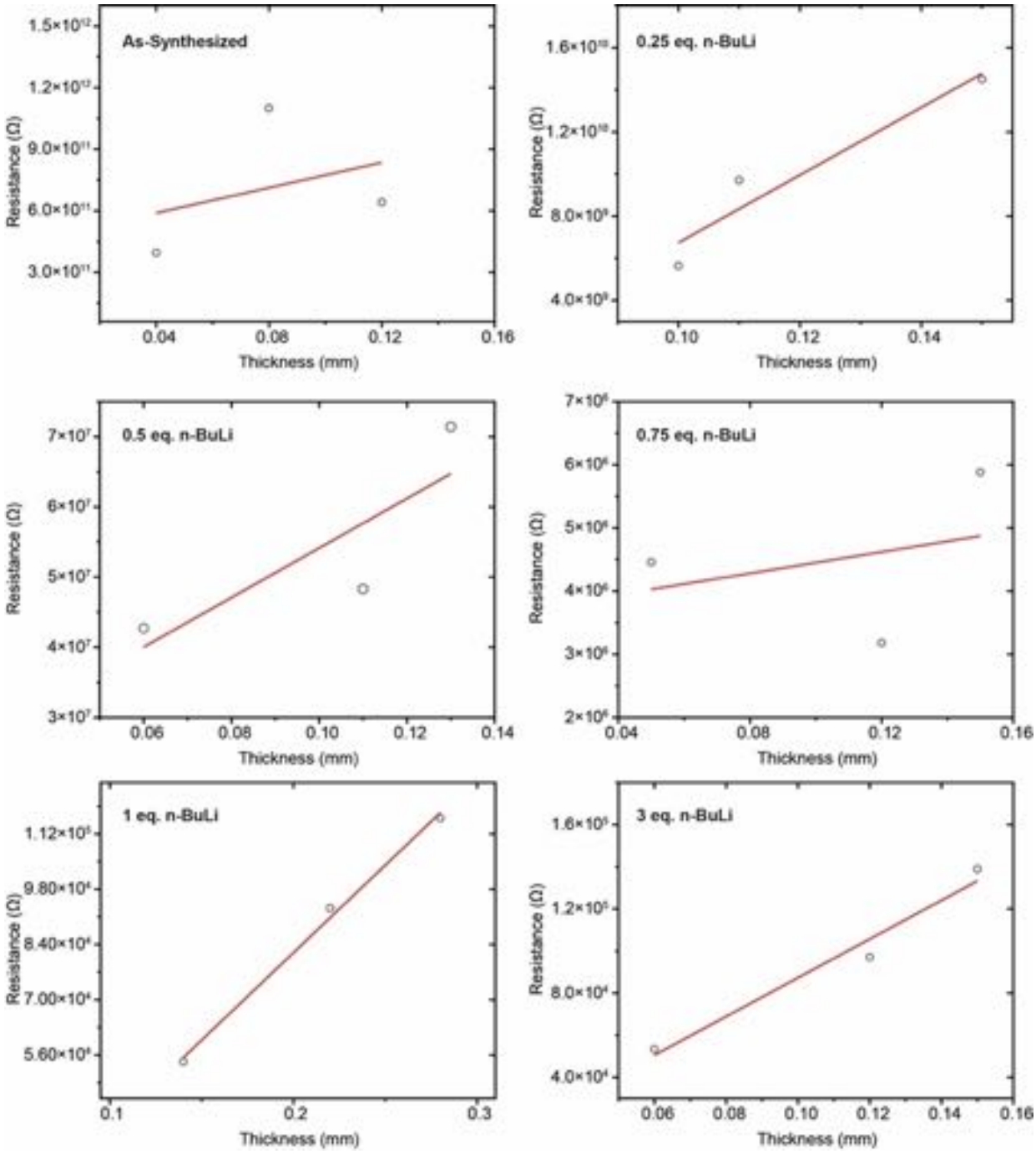

Figure C.3. Resistance vs. pellet thickness for representative α-$Co(OH)_2$-Cl samples.

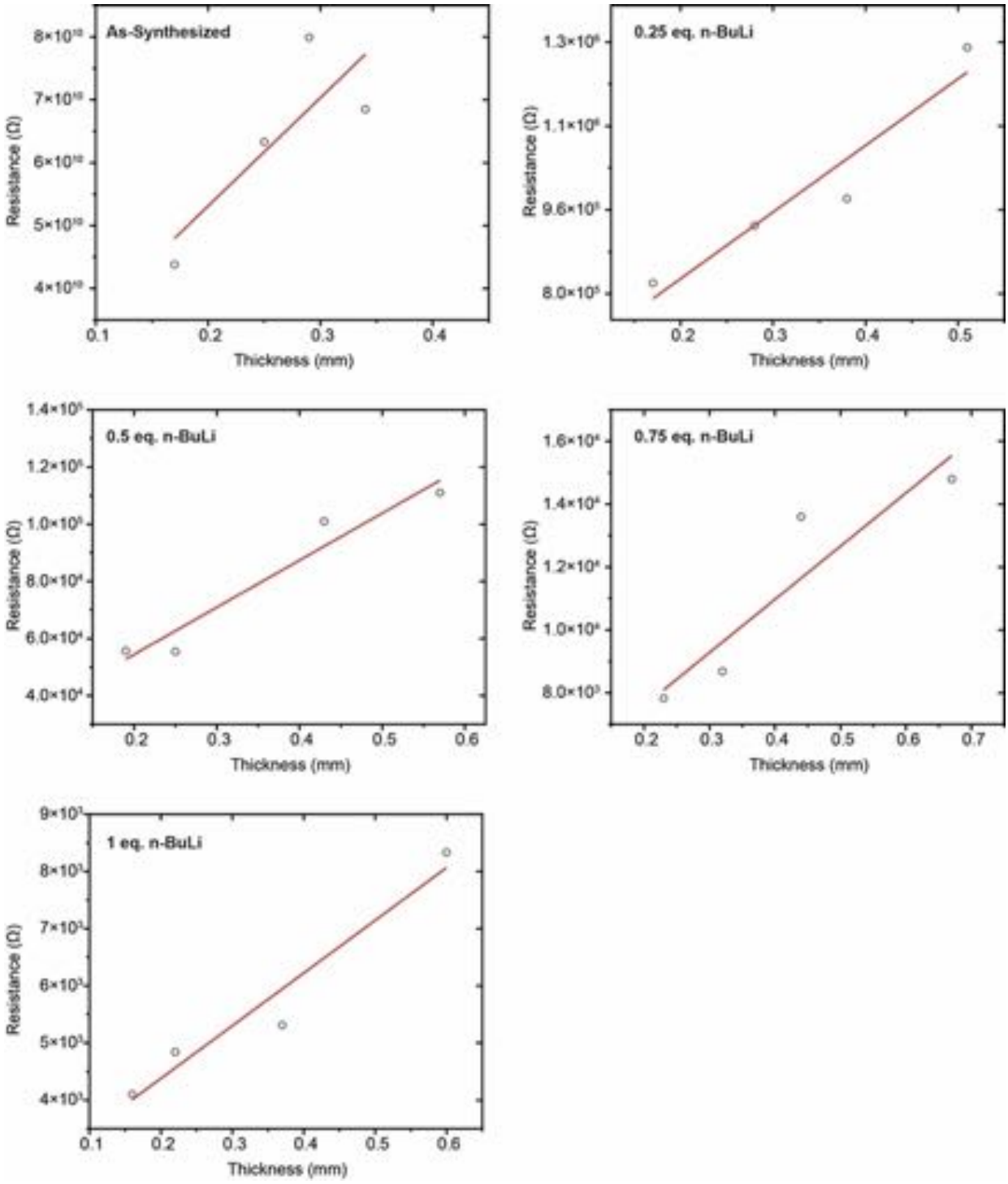

Figure C.4. Resistance vs. pellet thickness for representative β-$Co(OH)_2$ samples.

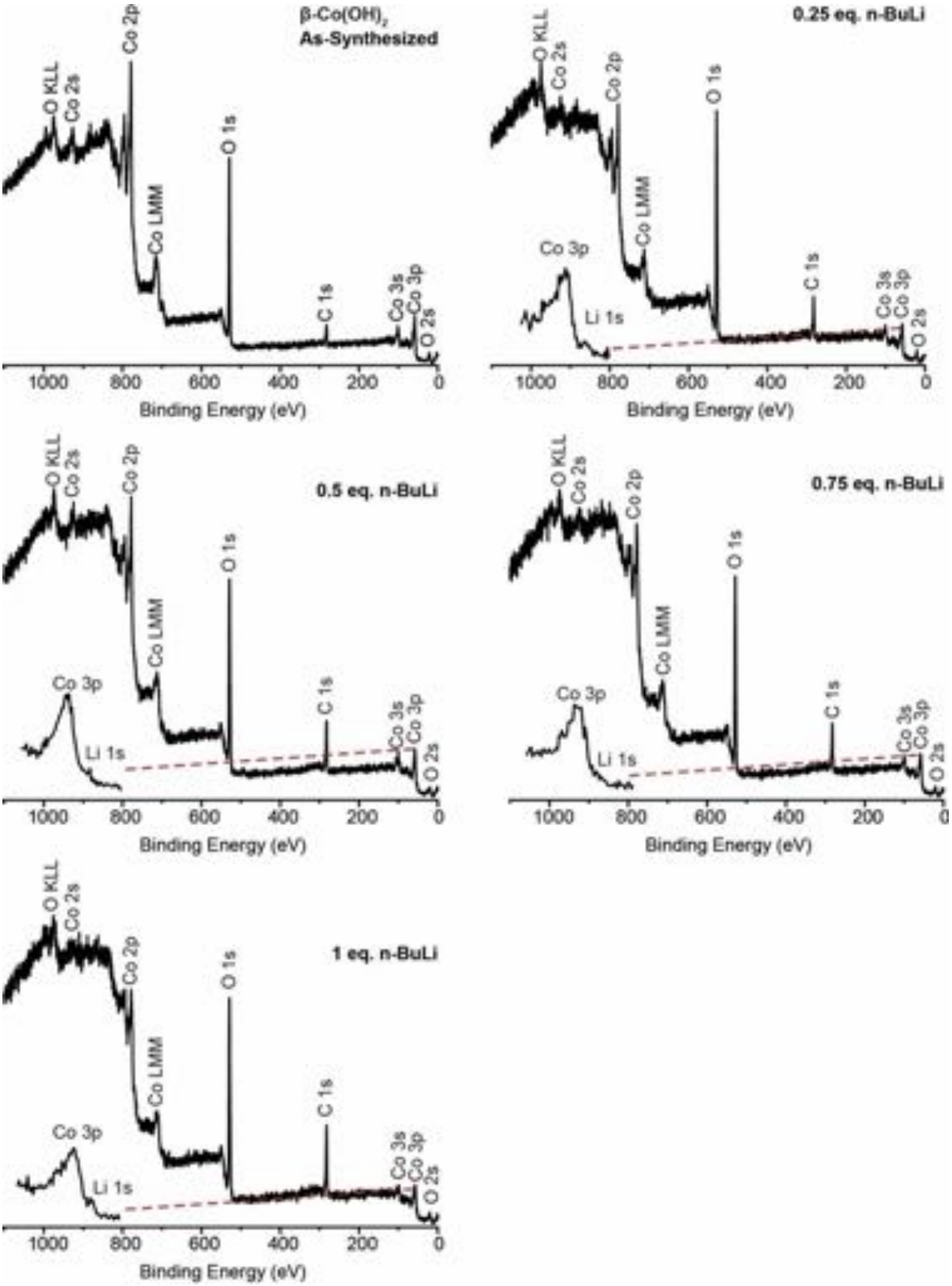

Figure C.5. XPS survey spectra of β-$Co(OH)_2$ treated with varying equivalents of n-BuLi. The high-resolution spectrum of the overlapping Co 3p and Li 1s region is provided in the inset.

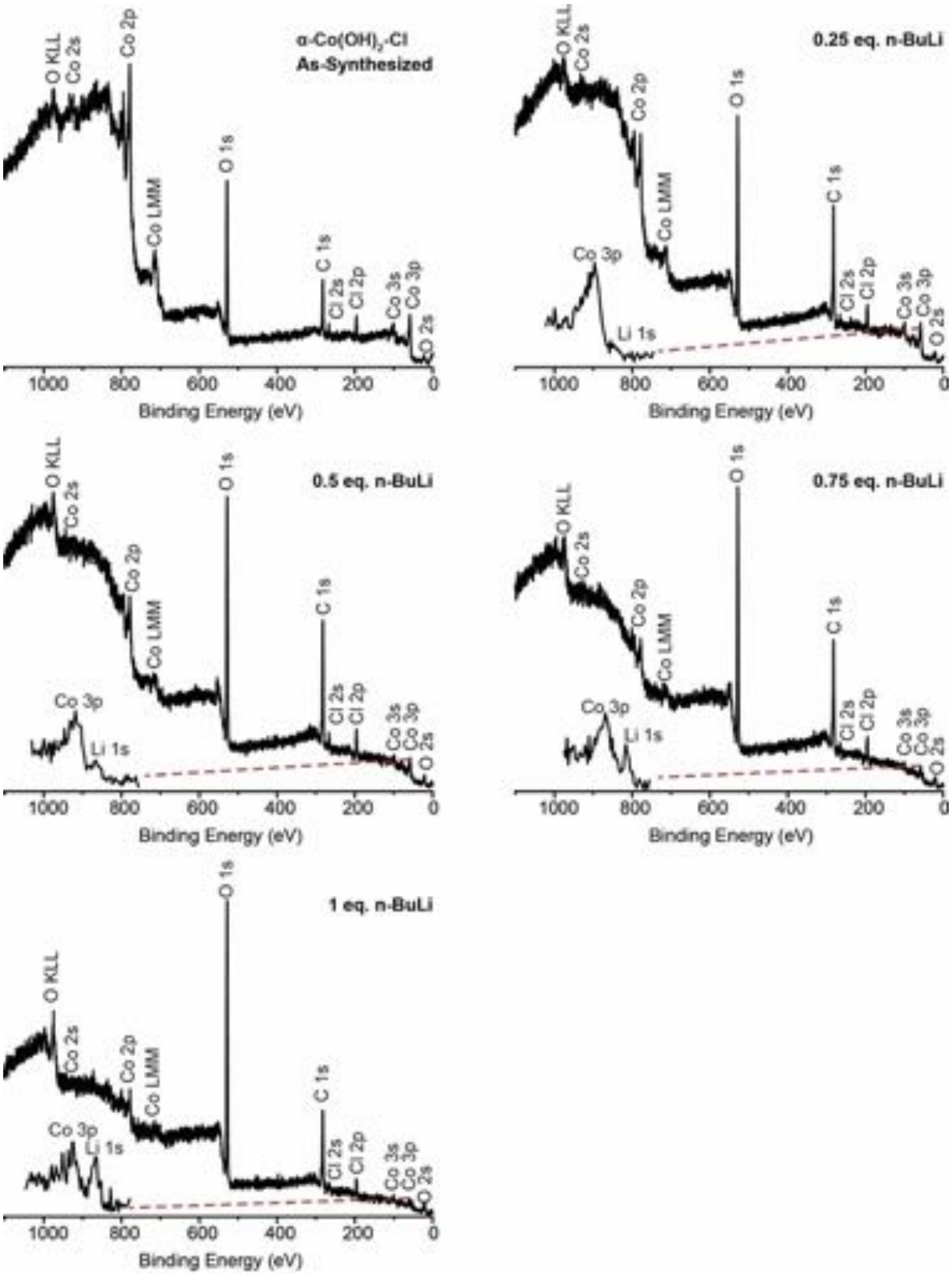

Figure C.6. XPS survey spectra of α-$Co(OH)_2$-Cl treated with varying equivalents of n-BuLi. The high-resolution spectrum of the overlapping Co 3p and Li 1s region is provided in the inset.

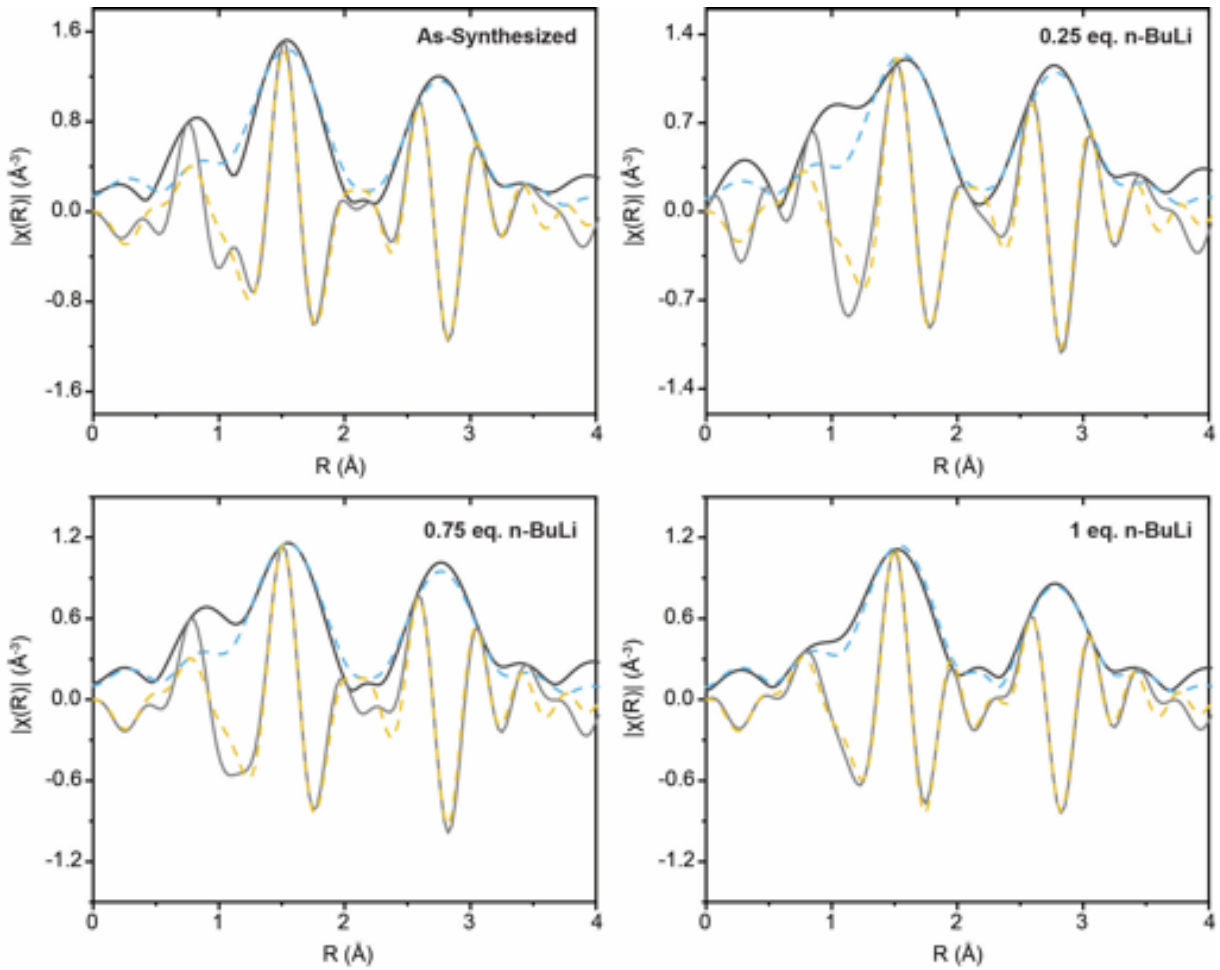

Figure C.7. Co K-edge EXAFS fitting data for β-$Co(OH)_2$ treated with n-BuLi. The black solid line is the Fourier-Transform (FT) magnitude, the dotted blue line is the fit to the FT magnitude, the solid gray line is the FT real part, and the dotted yellow line is the fit to the FT real part.

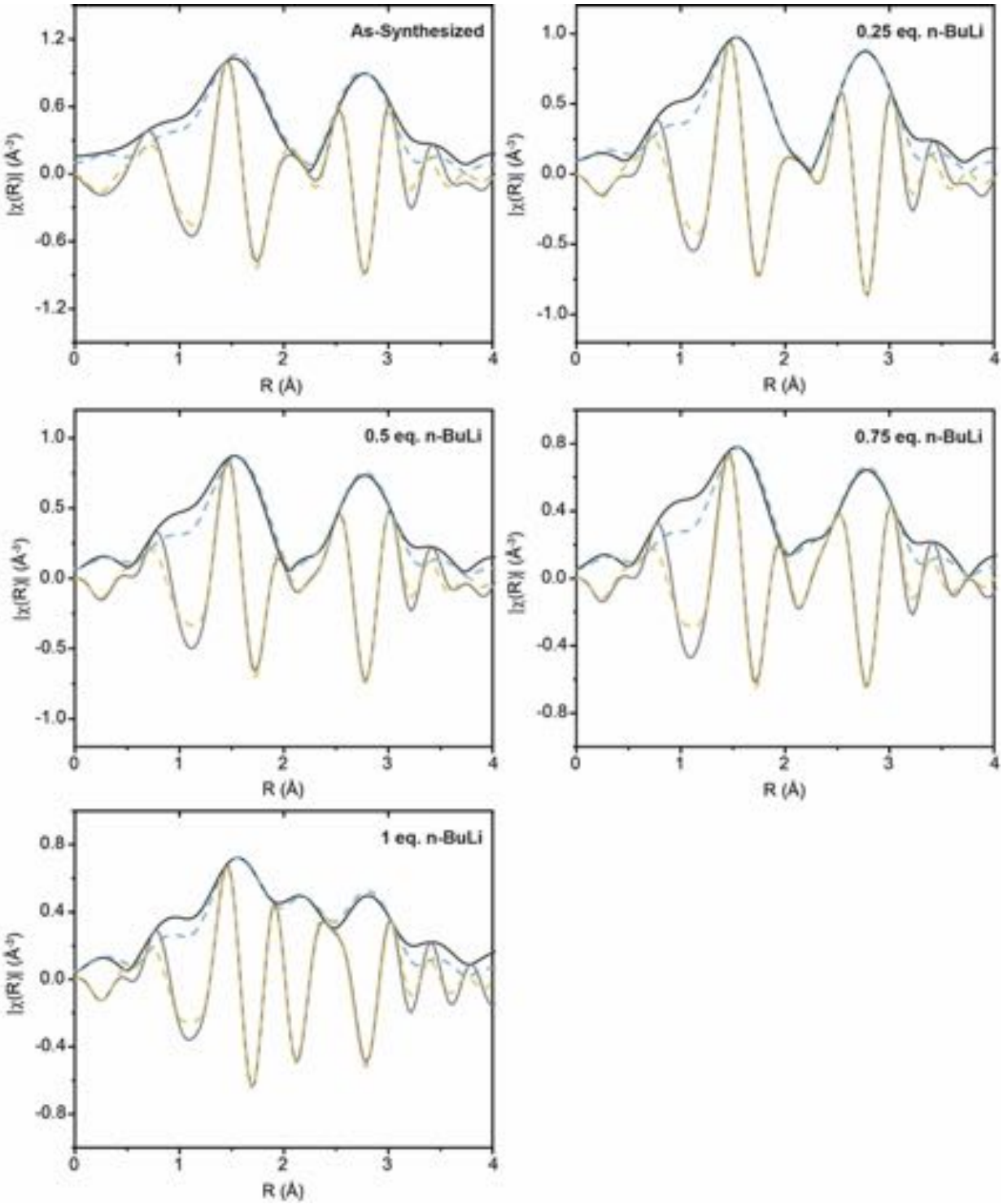

Figure C.8. Co K-edge EXAFS fitting data for α-$Co(OH)_2$-Cl treated with varying equivalents of n-BuLi. The black solid line is the FT magnitude, the dotted blue line is the fit to the FT magnitude, the solid gray line is the FT real part, and the dotted yellow line is the fit to the FT real part.

Table C.1. Co K-Edge XAS fitting parameters with error bars for β-$Co(OH)_2$ and α-$Co(OH)_2$-Cl with varying equivalents of *n*-BuLi.

Sample	Edge Edge (eV)	Scattering Pair	CN	R (Å)	σ^2 (Å^2)	E^0 (eV)
Co Foil	7708.8	Co–Co^M	12	2.50	0.008	----
β-$Co(OH)_2$ As-Synth.	7722.3	Co–O	6.1 ± 0.4	2.09 ± 0.005	0.005	–3.4
		Co–Co	5.7 ± 0.5	3.16 ± 0.006	0.005	–3.4
β-$Co(OH)_2$ 0.25 equiv. n-BuLi	7722.1	Co–O	5.1 ± 0.5	2.11 ± 0.008	0.005	–1.4
		Co–Co	5.4 ± 0.6	3.18 ± 0.008	0.005	–1.4
β-$Co(OH)_2$ 0.75 equiv. n-BuLi	7722.2	Co–O	4.7 ± 0.5	2.09 ± 0.009	0.005	–2.5
		Co–Co	4.6 ± 0.6	3.16 ± 0.009	0.005	–2.5
β-$Co(OH)_2$ 1 equiv. n-BuLi	7722.1	Co–O	4.7 ± 0.2	2.08 ± 0.004	0.005	–3.7
		Co–Co^M	1.0 ± 0.1	2.51 ± 0.004	0.005	–3.7
		Co–Co	4.2 ± 0.3	3.15 ± 0.01	0.005	–3.7
α-$Co(OH)_2$ As-Synth.	7722.8	Co–O	5.2 ± 0.2	2.08 ± 0.005	0.009	–2.0
		Co–Co	5.6 ± 0.4	3.14 ± 0.005	0.009	–2.0
α-$Co(OH)_2$-Cl 0.25 equiv. n-BuLi	7721.1	Co–O	4.8 ± 0.3	2.08 ± 0.005	0.009	–2.1
		Co–Co	5.6 ± 0.4	3.15 ± 0.005	0.009	–2.1
α-$Co(OH)_2$-Cl 0.5 equiv. n-BuLi	7721.2	Co–O	4.2 ± 0.2	2.08 ± 0.005	0.009	–1.7
		Co–Co^M	1.0 ± 0.2	2.52 ± 0.01	0.009	–1.7
		Co–Co	4.9 ± 0.4	3.15 ± 0.005	0.009	–1.7
α-$Co(OH)_2$-Cl 0.75 equiv. n-BuLi	7721.1	Co–O	3.8 ± 0.2	2.08 ± 0.005	0.009	–1.5
		Co–Co^M	1.2 ± 0.1	2.52 ± 0.01	0.009	–1.5
		Co–Co	4.3 ± 0.3	3.15 ± 0.005	0.009	–1.5
α-$Co(OH)_2$-Cl 1 equiv. n-BuLi	7721.5	Co–O	3.5 ± 0.2	2.07 ± 0.005	0.009	–2.7
		Co–Co^M	2.4 ± 0.1	2.50 ± 0.005	0.009	–2.7
		Co–Co	3.5 ± 0.3	3.15 ± 0.006	0.009	–2.7
α-$Co(OH)_2$-Cl 3 equiv. n-BuLi	7720.5	Co–O	1.1 ± 0.6	2.08 ± 0.02	0.009	–6.0
		Co–Co^M	5.6 ± 0.4	2.48 ± 0.005	0.009	–6.0
		Co–Co	0.4 ± 0.7	3.08 ± 0.14	0.009	–6.0

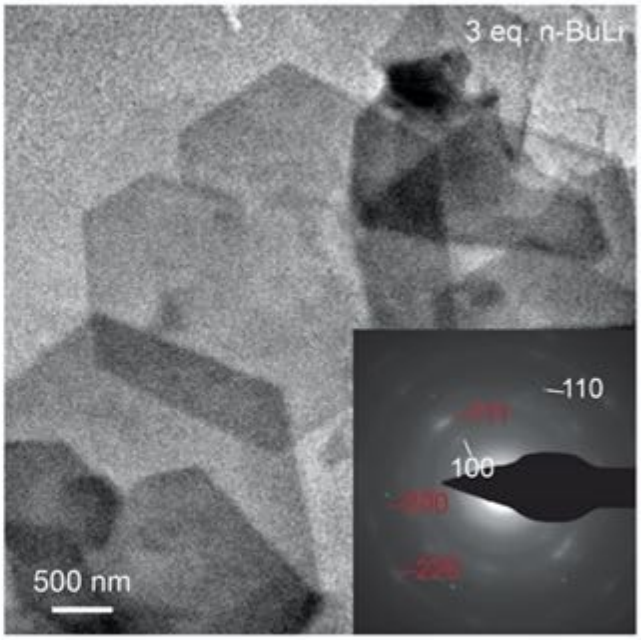

Figure C.9. TEM image and SAED pattern for α-$Co(OH)_2$-Cl treated with 3 equiv. n-BuLi. Miller indices labeled in white belong to α-$Co(OH)_2$-Cl while those in red belong to metallic Co.

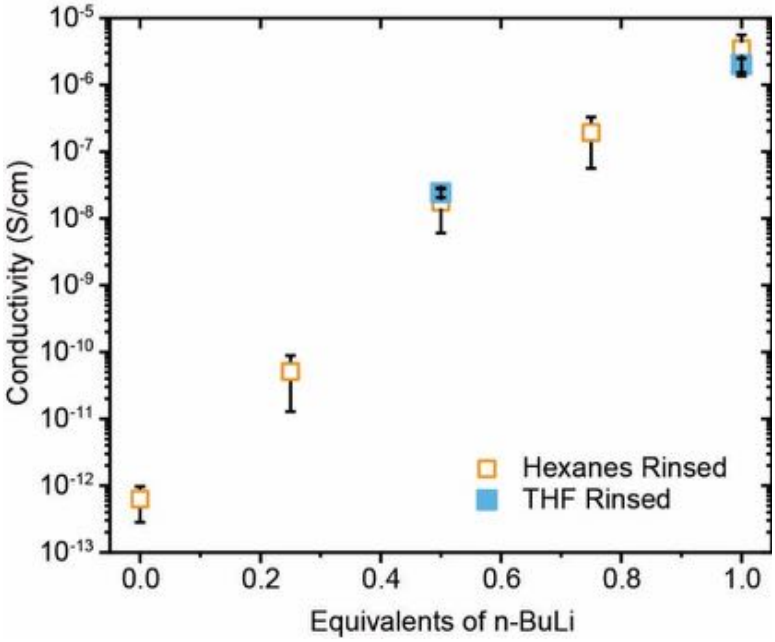

Figure C.10. Conductivity of α-$Co(OH)_2$-Cl treated with varying equivalents of n-BuLi after rinsing with either hexanes or THF.

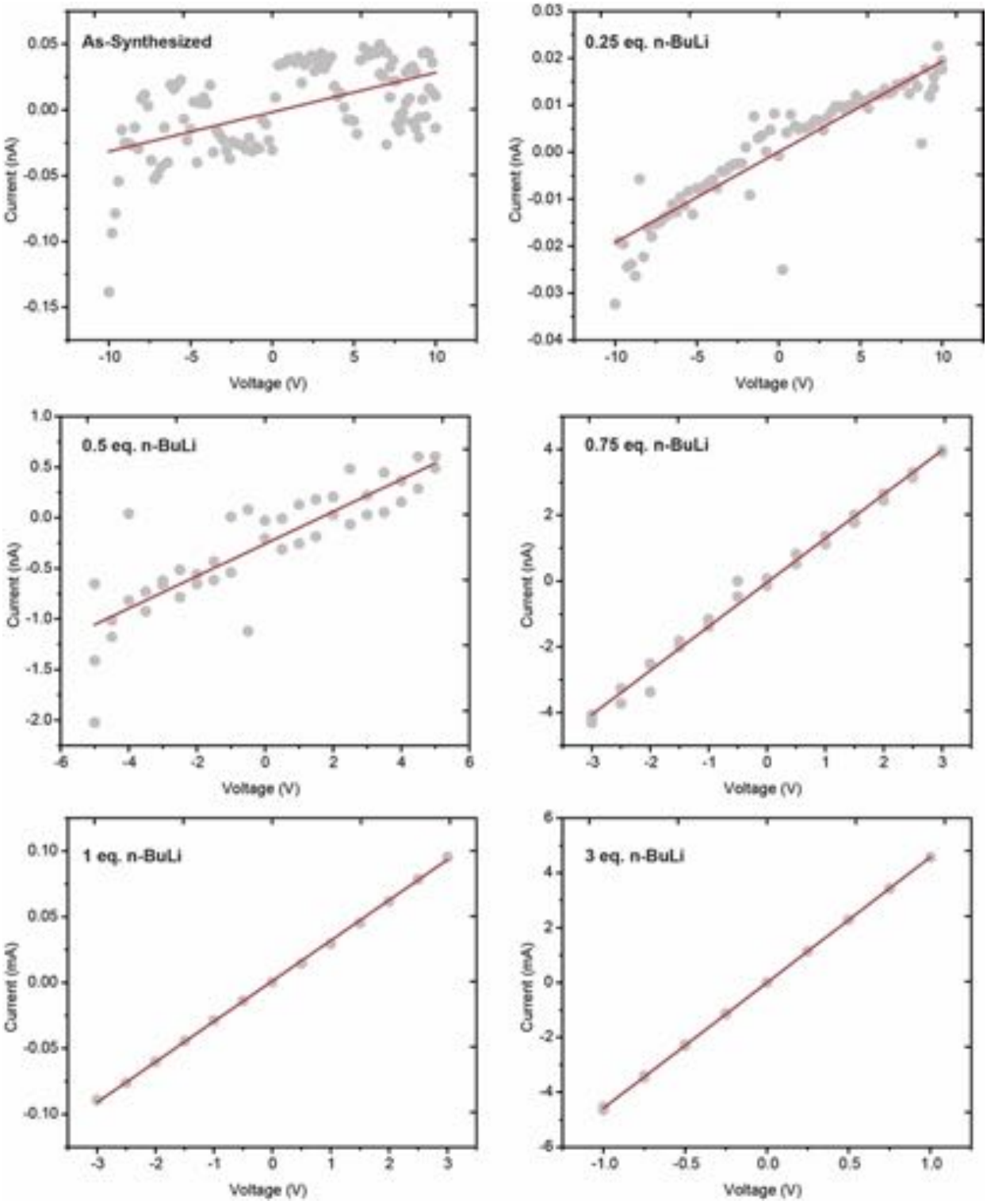

Figure C.11. Representative I-V curves for α-$Co(OH)_2$-SDS with treated with varying equivalents of n-BuLi. The pellets were formed in-situ and the electrical measurements were performed under a nitrogen atmosphere. The gray lines represent the experimental data and the red line is the linear fit.

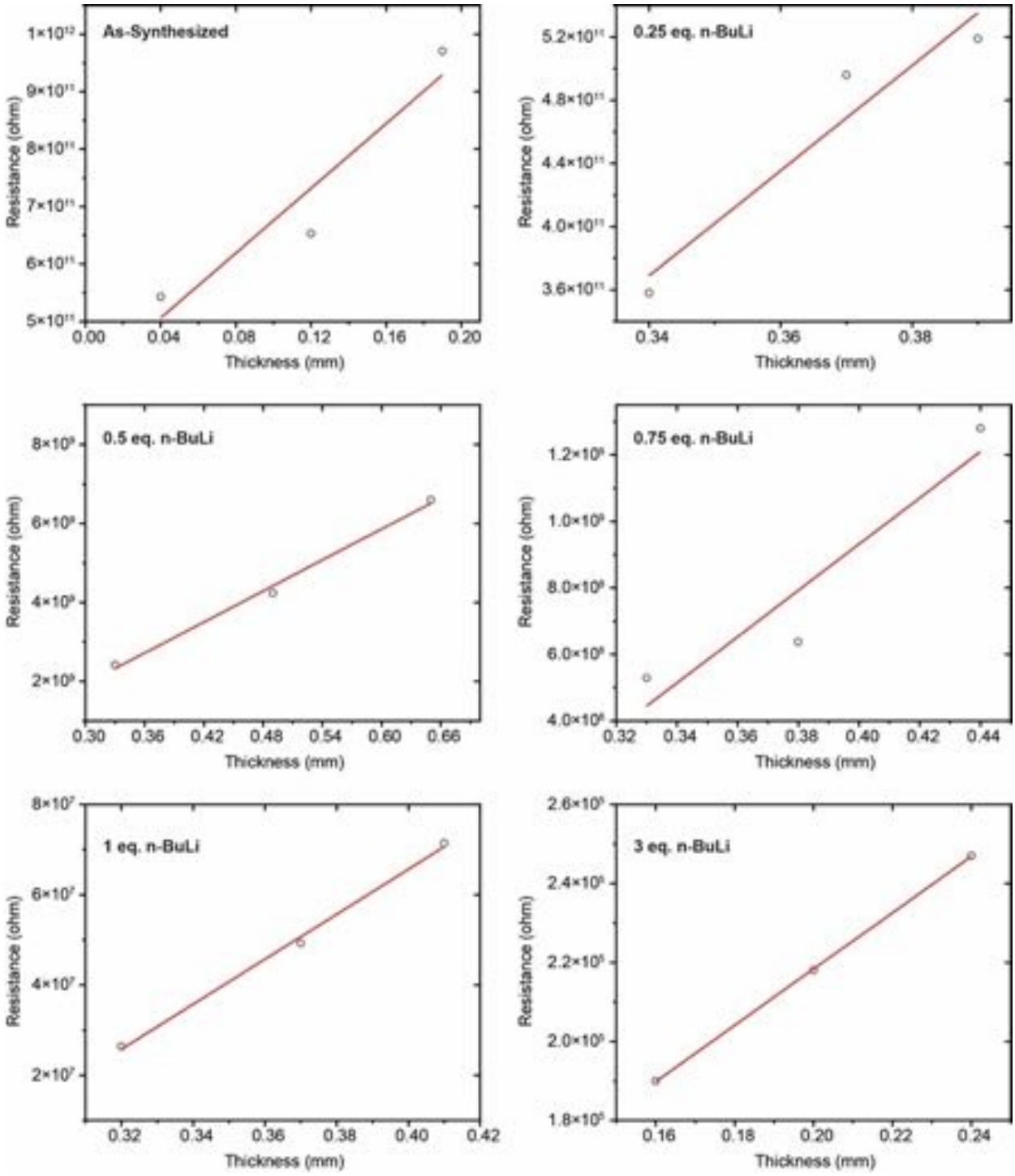

Figure C.12. Resistance vs. pellet thickness for representative α-$Co(OH)_2$-SDS samples.

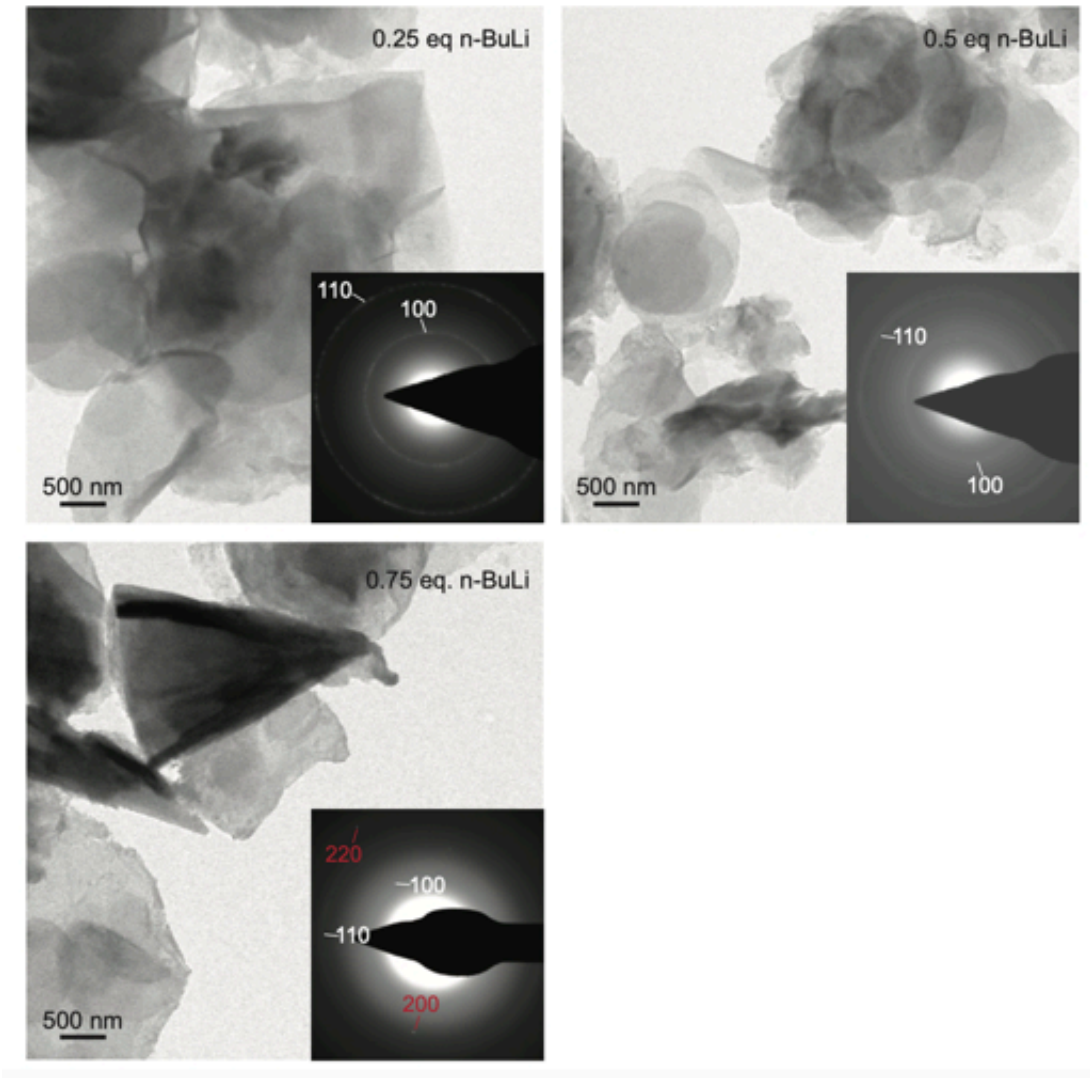

Figure C.13. TEM images and SAED patterns of α-$Co(OH)_2$-SDS treated with varying equivalents of n-BuLi. Miller indices labeled in white belong to α-$Co(OH)_2$-SDS while those in red belong to metallic Co.

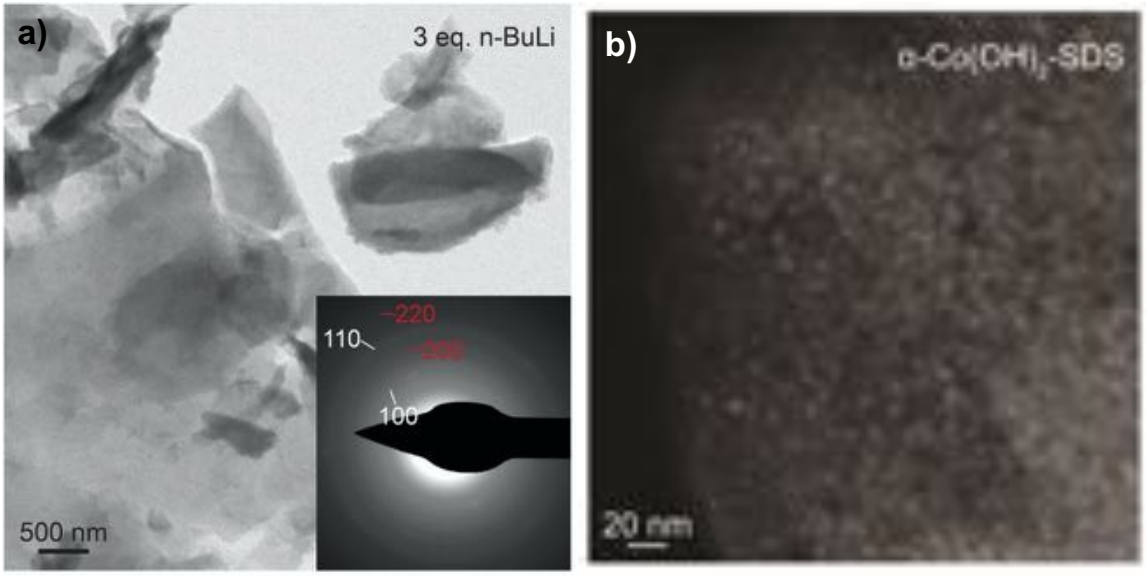

Figure C.14. (**a**) TEM and SAED images of α-$Co(OH)_2$-SDS treated with 3 equiv. n-BuLi. Miller indices labeled in white belong to α-$Co(OH)_2$-SDS while those in red belong to metallic Co. (**b**) HAADF-STEM image showing the formation of metallic Co nanoparticles (brighter spots) supported on the α-$Co(OH)_2$-SDS nanosheet.

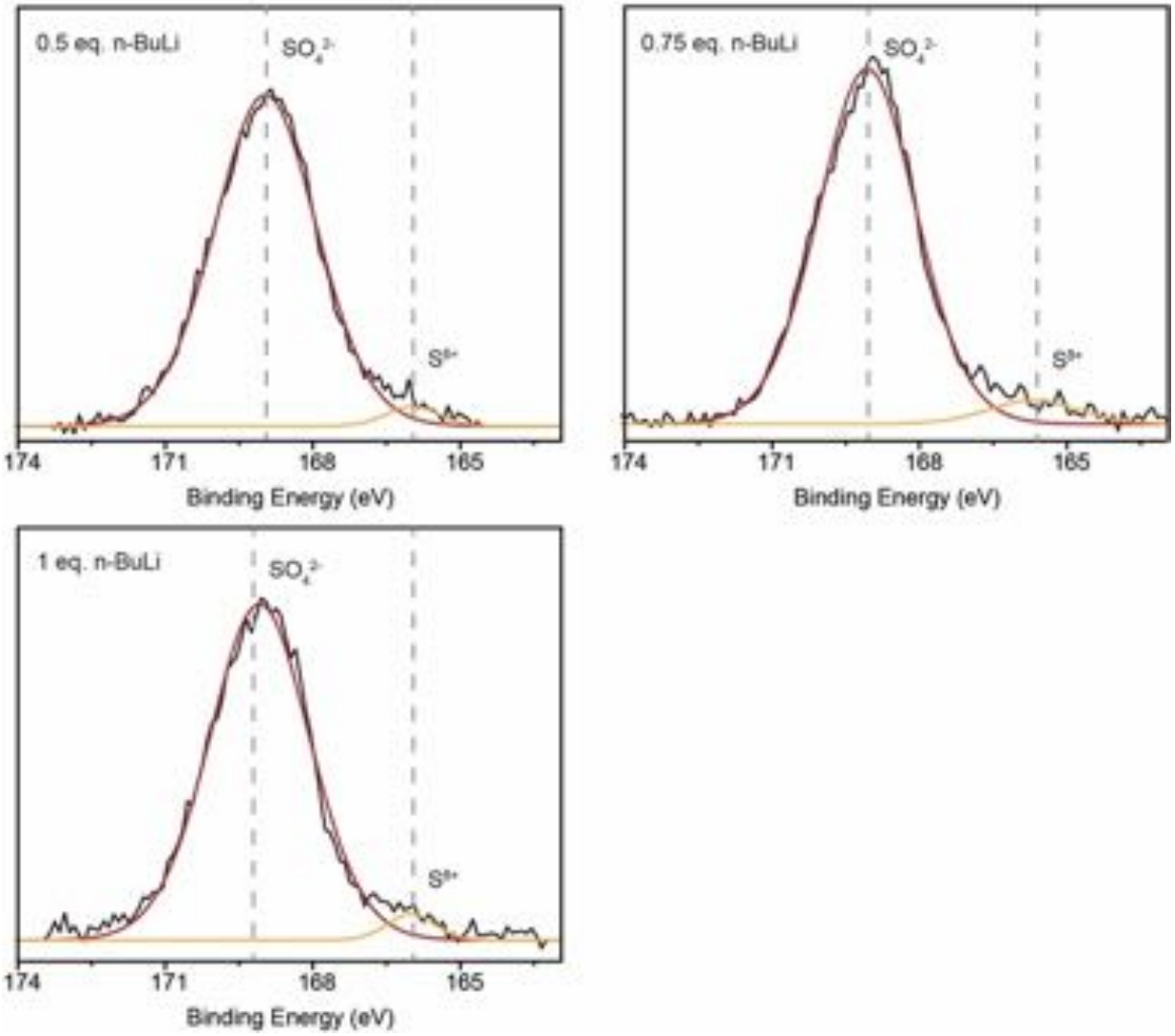

Figure C.15. High resolution XPS for the S 2p region of α-$Co(OH)_2$-SDS treated with varying equivalents of n-BuLi.

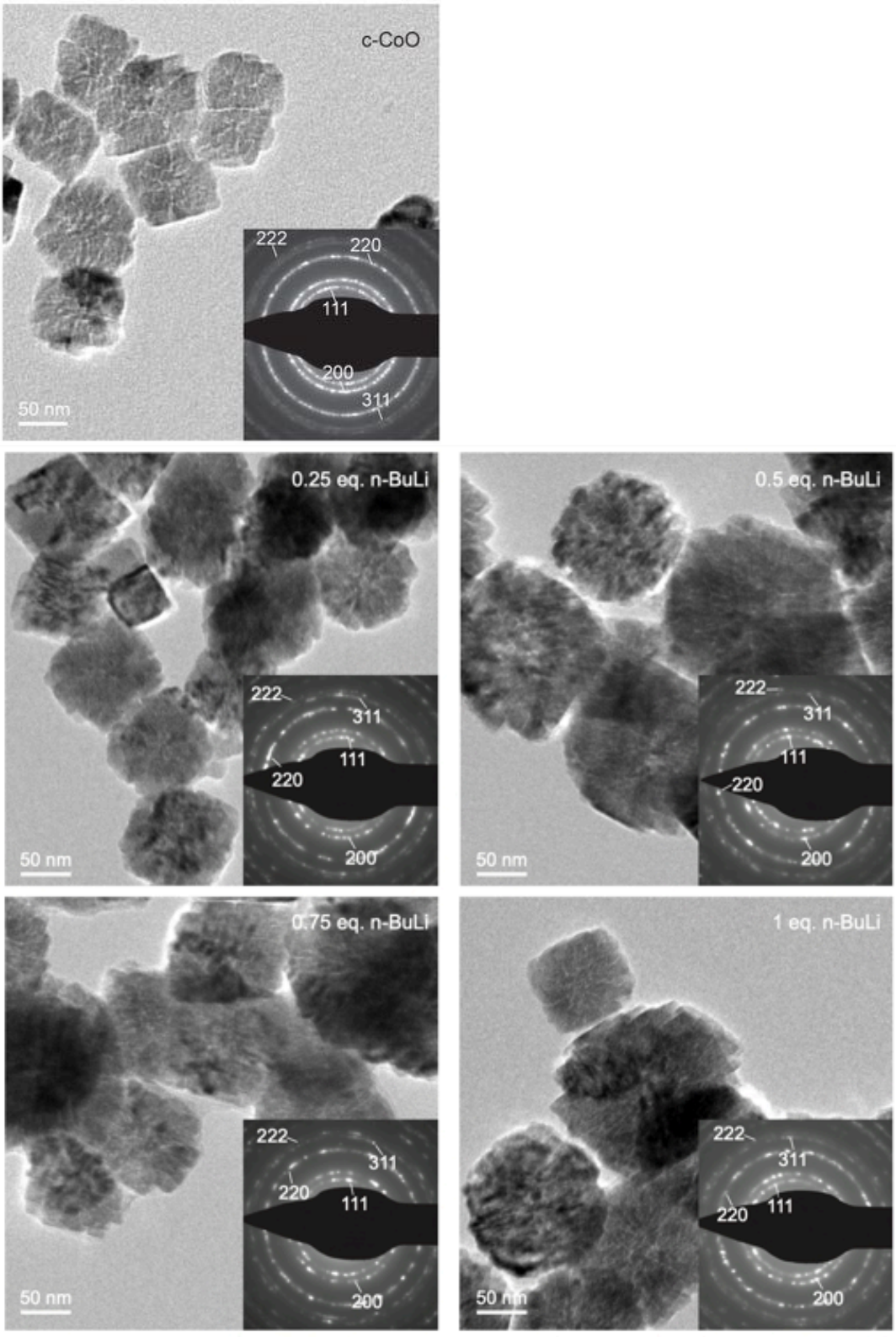

Figure C.16. TEM images and SAED patterns of c-CoO treated with varying equivalents of n-BuLi.

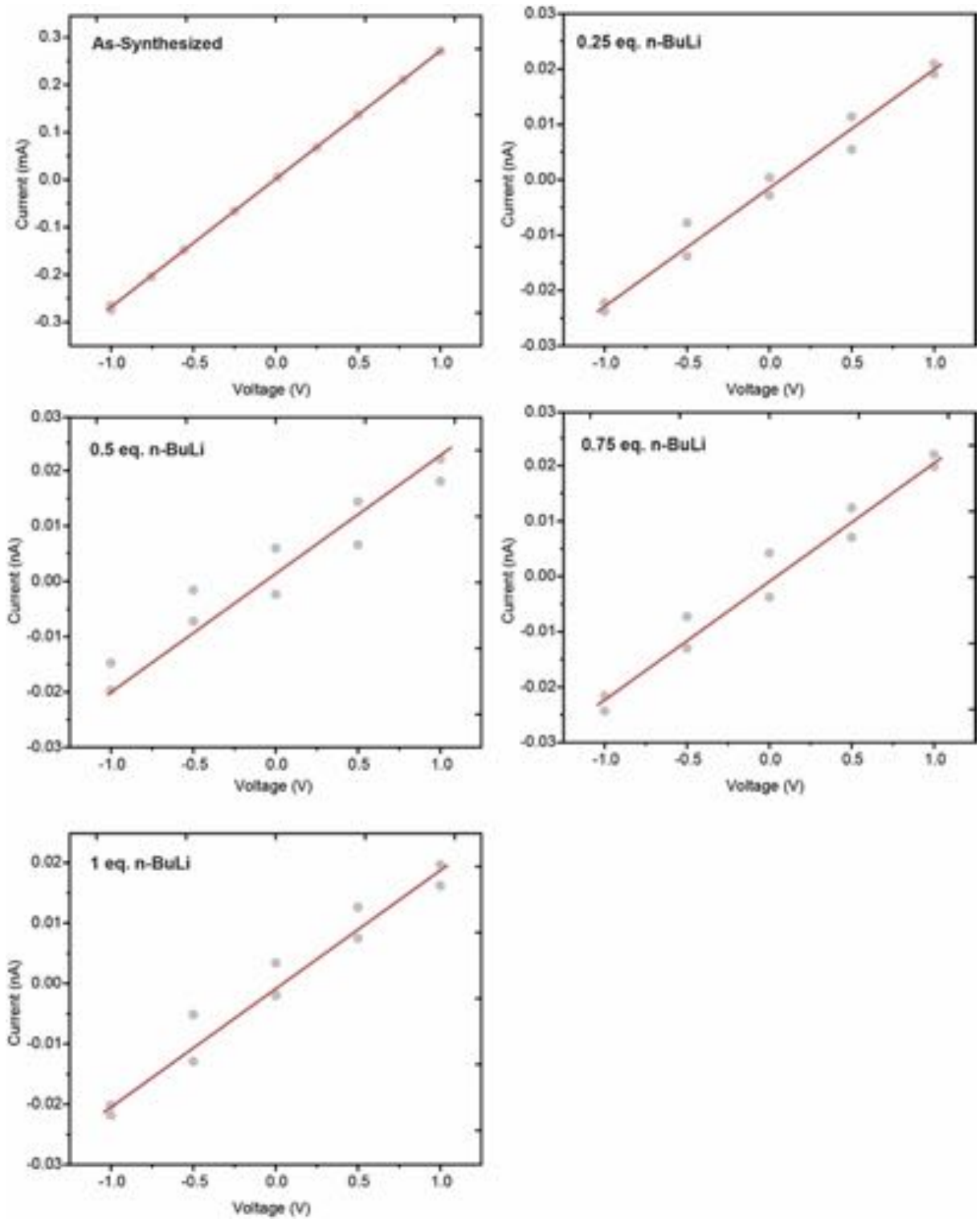

Figure C.17. Representative I-V curves for c-CoO with treated with varying equivalents of n-BuLi. The pellets were formed in-situ and the electrical measurements were performed under a nitrogen atmosphere. The gray lines represent the experimental data and the red line is the linear fit.

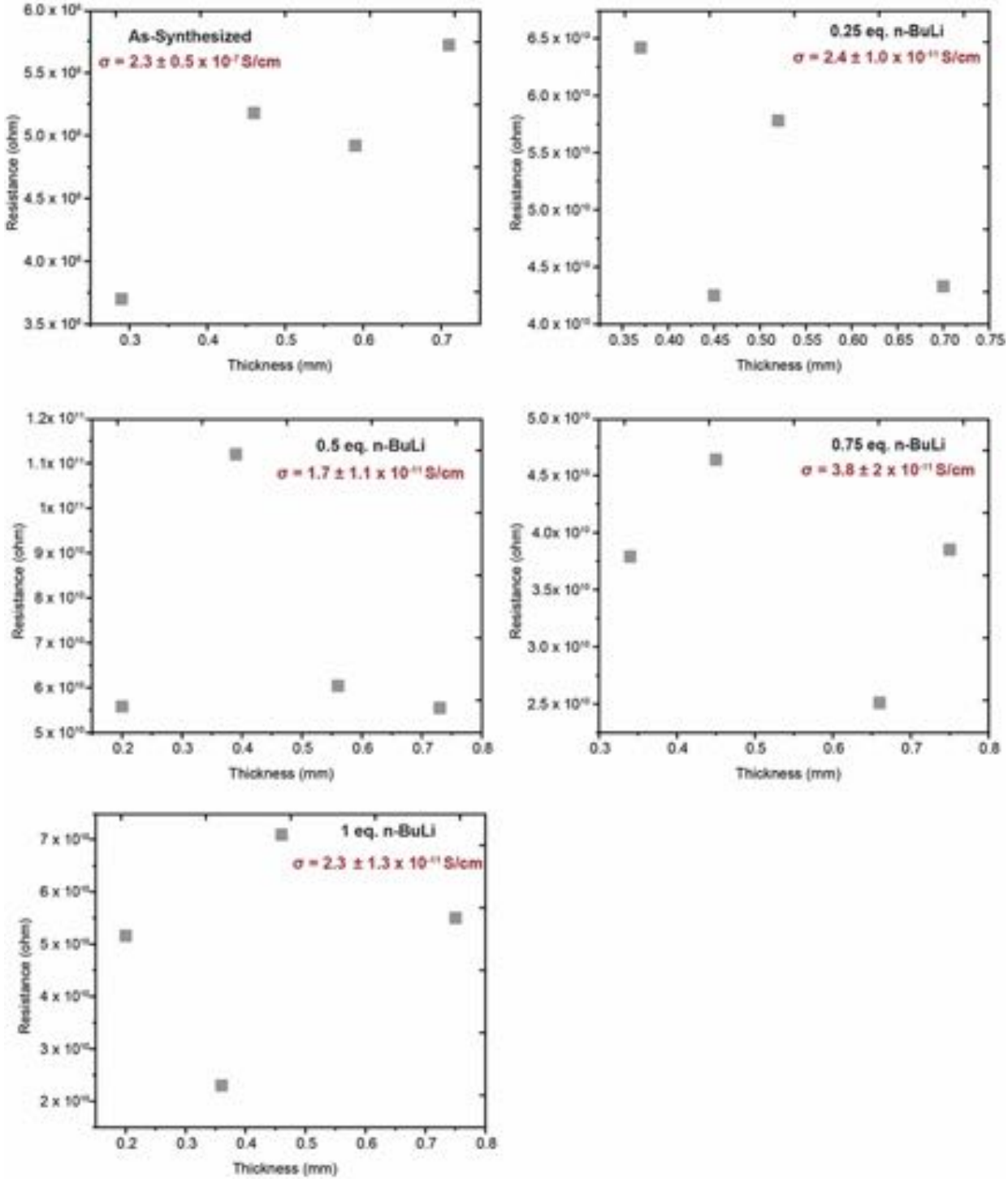

Figure C.18. Resistance vs. pellet thickness for representative c-CoO samples. Calculated average conductivity values and error bars are provided for each sample.

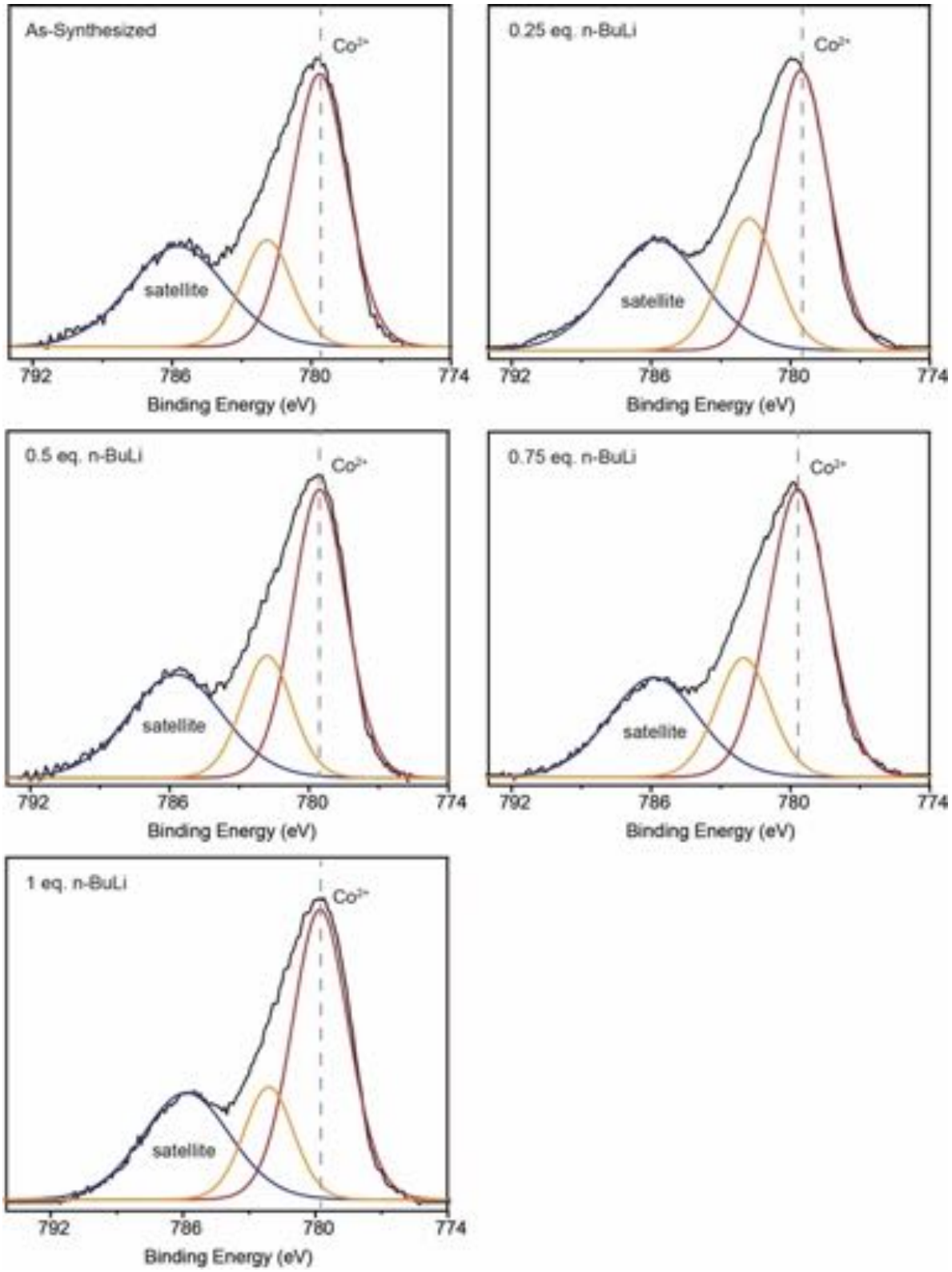

Figure C.19. High resolution XPS for the Co 2p region of c-CoO treated with varying equivalents of n-BuLi.

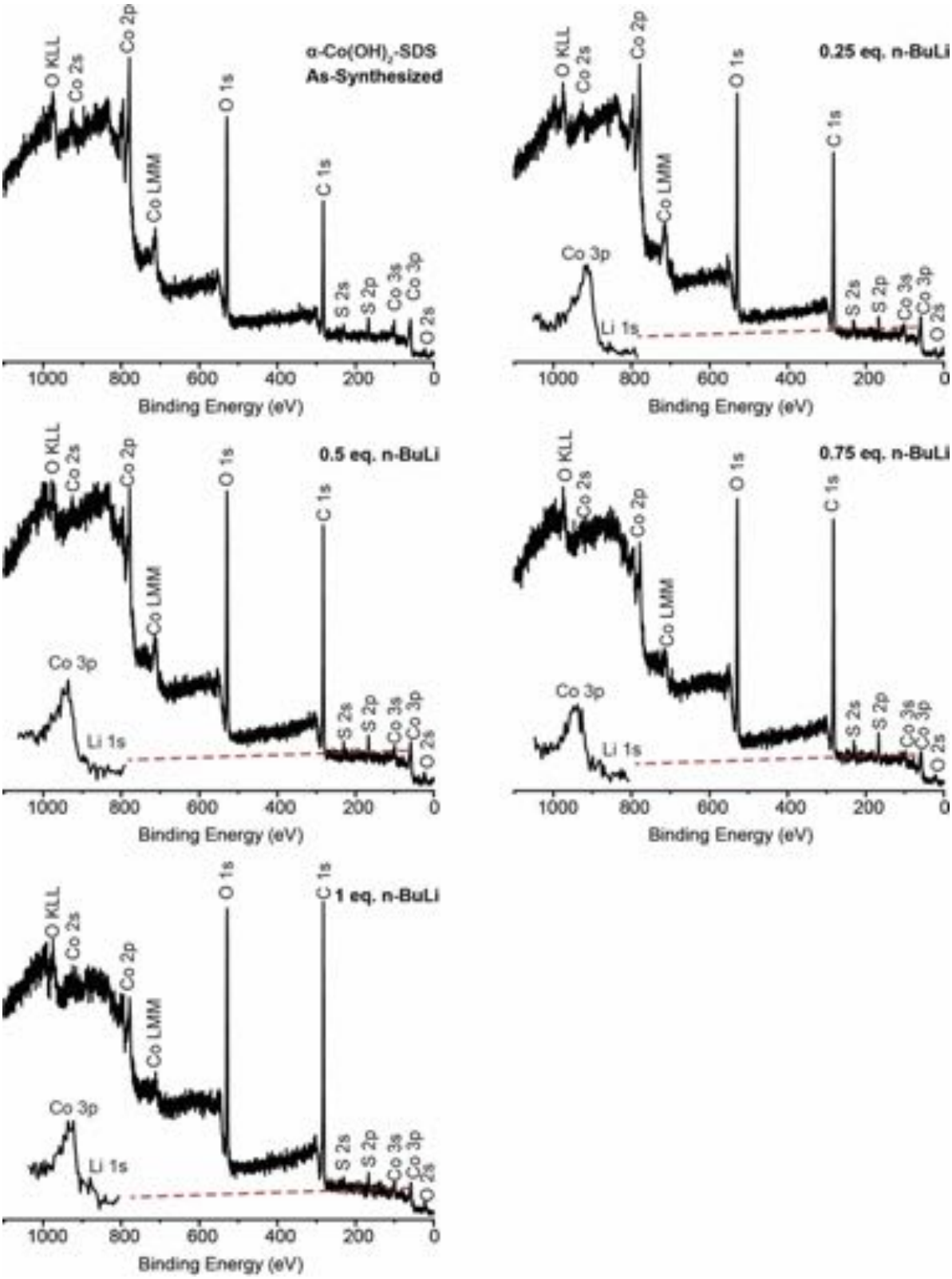

Figure C.20. XPS survey spectra of α-$Co(OH)_2$-SDS treated with varying equivalents of n-BuLi. The high-resolution spectrum of the overlapping Co 3p and Li 1s region is provided in the inset.

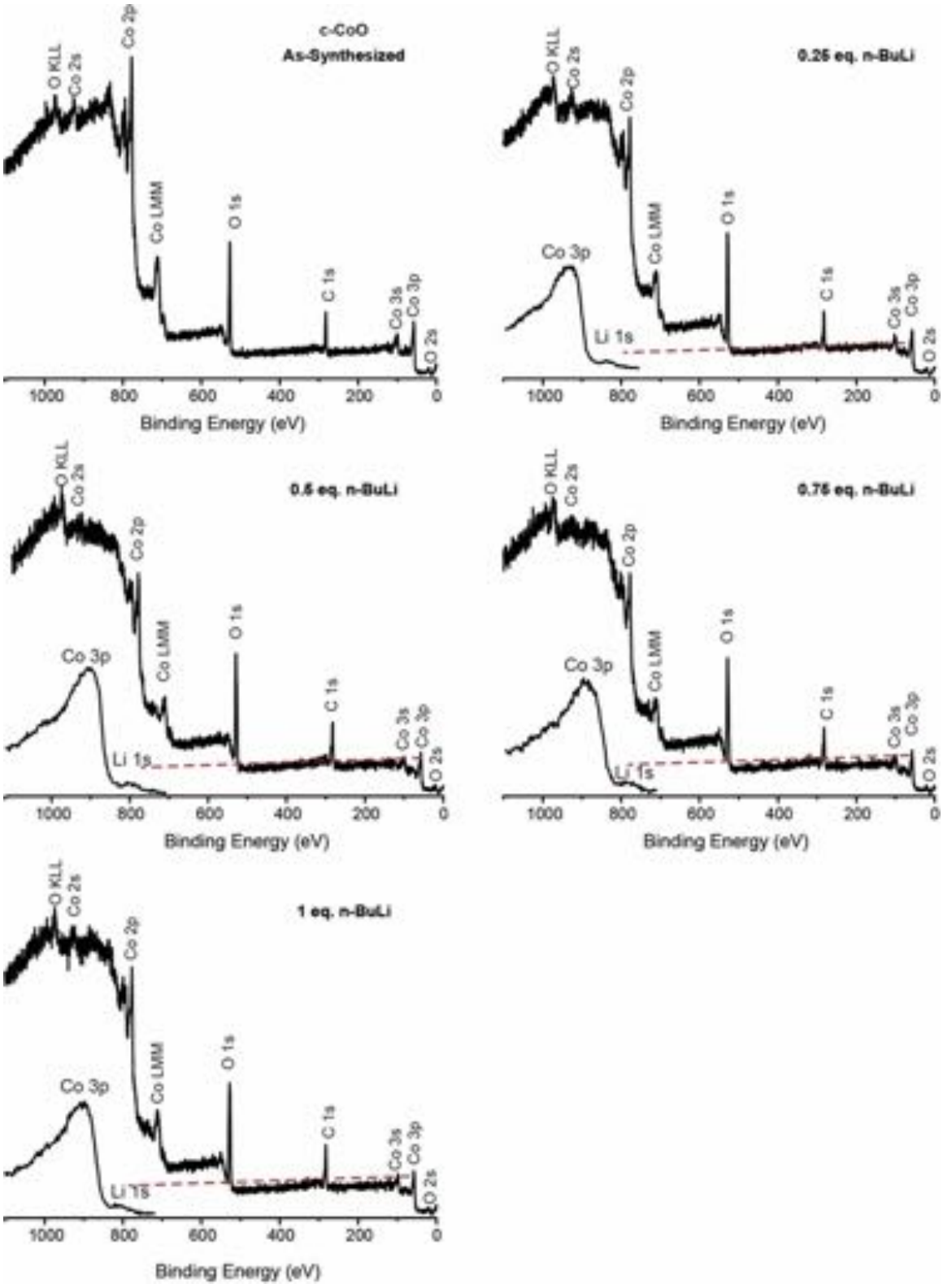

Figure C.21. XPS survey spectra of c-CoO treated with varying equivalents of n-BuLi. The high-resolution spectrum of the overlapping Co 3p and Li 1s region is provided in the inset.

4. References

(1) Liu, Z.; Ma, R.; Osada, M.; Takada, K.; Sasaki, T., *J. Am. Chem. Soc.,* **2005**, *127*, 13869-13874.

(2) Liu, X.; Ma, R.; Bando, Y.; Sasaki, T., *Angew. Chem.,* **2010**, *122*, 8429-8432.

(3) Cheng, J.; Chen, X.; Wu, J.-S.; Liu, F.; Zhang, X.; Dravid, V. P., *CrystEngComm,* **2012**, *14*, 6702-6709.

(4) Nam, K. M.; Shim, J. H.; Han, D.-W.; Kwon, H. S.; Kang, Y.-M.; Li, Y.; Song, H.; Seo, W. S.; Park, J. T.,. *Chem. Mater.,* **2010**, *22*, 4446-4454.

(5) Seo, W. S.; Shim, J. H.; Oh, S. J.; Lee, E. K.; Hur, N. H.; Park, J. T., *J. Am. Chem. Soc.,* **2005**, *127*, 6188-6189.

(6) Ravel, B.; Newville, M., *J. Synchrotron Radiat.,* **2005**, *12*, 537-541.

(7) Hunt, D.; Garbarino, G.; Rodríguez-Velamazán, J. A.; Ferrari, V.; Jobbagy, M.; Scherlis, D. A., *Phys. Chem. Chem. Phys.,* **2016**, *18*, 30407-30414.

(8) De Wolff, P., *Acta Crystallogr,.* **1953**, *6*, 359-360.

(9) Owen, E.; Jones, D. M., *Proc. Phys. Soc. B,* **1954**, *67*, 456.